Design of a mmWave channel sounder and channel model extraction in railway environment

Nicholas Attwood

COLLEGES SCIENCES
BRETAGNE POUR L'INGENIEUR
LOIRE ET LE NUMERIQUE

IMT Atlantique
Bretagne-Pays de la Loire
École Mines-Télécom

THÈSE DE DOCTORAT DE

L'ÉCOLE NATIONALE SUPÉRIEURE
MINES-TÉLÉCOM ATLANTIQUE BRETAGNE
PAYS DE LA LOIRE – IMT ATLANTIQUE

ÉCOLE DOCTORALE N° 648
Sciences pour l'Ingénieur et le Numérique
Spécialité : *Télécommunication*

Par
Nicholas ATTWOOD

Design of a mmWave Channel Sounder and Channel Model Extraction in Railway Environment.

Thèse présentée et soutenue à IMT Atlantique Campus de Brest, le 19/12/2024
Unité de recherche : Lab-STICC (UMR6285)
Thèse N° : 2024IMTA0449

Rapporteurs avant soutenance :

Sana SALOUS Professeur à Durham University
Bernard UGUEN Professeur à l'IETR

Composition du Jury :

Président :	Davy GAILLOT	Maître de Conférence - HDR à l'Université de Lille
Examinateurs :	Sana SALOUS	Professeur à Durham University
	Bernard UGUEN	Professeur à l'IETR
	Paul UNTERHUBER	Chercheur au DLR
Dir. de thèse :	François GALLEE	Professeur à IMT Atlantique
Co-dir. de thèse :	Marion BERBINEAU	Directrice de Recherche à l'Université Gustave Eiffel
Encadrant :	Patrice PAJUSCO	Directeur d'Étude à IMT Atlantique

Acknowledgements

This thesis was conducted within the Microwave Department of IMT Atlantique. First and foremost, I would like to express my gratitude to my thesis supervisor, François Gallée, and my co-supervisor, Marion Berbineau, for trusting me with the completion of this thesis, whose subject of study is rich and highly diverse. My deepest thanks go to Patrice Pajusco, a member of my thesis supervision team, whose guidance allowed me to quickly develop expertise and knowledge in propagation channels and associated signal processing. Our numerous discussions greatly improved my skills and enhanced the final outcome. In short, thank you infinitely.

I would also like to thank Sana Salous and Bernard Uguen for agreeing to be the reviewers of this thesis. Their constructive feedback significantly improved the final version of this document. Furthermore, their comments during the defense broadened my knowledge and provided new avenues for further investigation.

I also wish to thank all the doctoral students in the department who made this PhD journey much more enjoyable. I think of Guillaume Bourcin, Loïc Temdie Kom, Myssipsa Mehraz, and, of course, Grégory Gaudin, who supported me throughout the entire duration of the thesis, and even before, during my engineering studies. Thank you, Greg, for being an unwavering source of support all these years.

As mentioned earlier, this thesis was carried out within the Microwave Department. I would like to thank all the faculty members and research engineers in the department. In particular, I want to thank Alain Peden, who was always available to listen, guide me effectively, and answer my various questions. I also extend my gratitude to Daniel Bourreau for his valuable advice regarding hardware implementation and measurement techniques for the sounder characterization. Of course, a special thanks to the Vincents (Vlaminck and Castel) for both formal and informal discussions. Finally, thank you to Adrien Merlini and Clément Henry for the numerous discussions during various conferences and their time.

The Microwave Department is part of IMT Atlantique, and I would like to thank all the support staff, including human resources and the doctoral division of the Directorate of Research and Innovation, especially Delphine Lucas and Magali Gouez. I cannot forget the first level of departmental support, which helped me under all circumstances, particularly during my travel mishaps. Therefore, I wish to thank Yannick Marinette.

Lastly, this thesis could not have gone as smoothly without the support of my loved ones. I extend my heartfelt thanks to my in-laws, who were always there to help and share the ups and downs of this journey with me. I also thank my mother and father for their unwavering support during this final academic challenge. Finally, I wish to dedicate the warmest and most heartfelt thanks to the one who accompanied, encouraged, supported, and above all endured me throughout this thesis. She was the solid rock I could rely on during difficult times as well as the joyful moments of the thesis. For all these reasons, Amélie, I thank you from the bottom of my heart.

Contents

List of Figures

List of Tables

Acronyms

Notation	Description
3GPP	3rd Generation Partnership Project. ix–xi, xiv, 3, 4, 6, 22–27, 43, 46, 74, 86–88, 94, 96, 101, 102, 104–107, 109, 112, 114, 116, 117, 120–122
aASA	Azimuth Angular Spread of Arrival. 77
ABG	Alpha-Beta-Gamma. 17, 42
ADC	Analog to Digital Converter. 36
AGC	Automatic Gain Control. 70, 71, 121
ANR	National Research Agency. 2, 85, 94, 120
AoA	Angle of Arrival. ix, 15, 22, 23, 25, 41, 42, 80, 122
AoD	Angle of Departure. ix, 22, 23, 25, 41, 122
AP	Access Point. 38
APT	Asia-Pacific Telecommunity. 84
ASA	Angular Spread Arrival. xiii, 43, 46, 79
ASD	Angular Spread Departure. xiii, 43, 46, 79
AWG	Arbitrary Waveform Generator. 34, 53, 56
BBU	Baseband Processing Unit. 87
BER	Bit Error Rate. 49
BS	Base Station. 25, 62, 63
CC	City Center. 42
CDF	Cumulative Density Function. ix, 18, 19, 109, 110, 112
CDL	Cluster Delay Line. ix, 23, 25, 26
CEF	Trial Railway Center. x, 85, 87, 94, 120
CF	Crest Factor. 36, 37, 60, 120
CIR	Channel Impulse Response. ix–xi, 6, 10–13, 20–23, 27, 30–32, 34–36, 48, 57–59, 61, 64, 67, 91–93, 114
COTS	Commercial-Off-The-Shelf. 3, 30, 32, 34, 36–38, 40, 49, 52, 53, 120, 121
CS	Channel Sounder. vi, ix, x, xiii, 2, 3, 27, 29–41, 44, 48, 49, 52, 54, 55, 60–62, 64–66, 68, 70–72, 76–78, 85, 91, 94, 98, 99, 114, 116, 120–122

Notation	Description
CTF	Channel Transfer Function. x, 6, 10–12, 27, 30, 32, 33, 38, 60–62, 66–69, 120
CW	Continuous Wave. 36
DLR	German Aerospace Center. 38
DO	Disciplined Oscillator. 31, 39, 40
DP-UMCS	Dual Polarized Ultrawideband Multi-Channel Sounder. 34
DS	Delay Spread. 45, 77, 78
DSO	Digital Storage Oscilloscope. 32, 35, 36, 38
DUT	Device Under Test. 32, 33
FI	Floating Intercept. 77
FMCW	Frequency-Modulated Continuous-Wave. x, 36, 40, 59, 60
FR	Fixed Reference. 77
FRMCS	Future Railway Mobile Communication Systems. 2
FSPL	Free Space Path Loss. x, 7, 42, 61, 77, 83, 90
GNSS	Global Navigation Satellite System. x, 31, 39, 40, 56, 58, 59, 62, 63, 65, 66, 68, 71, 72, 89, 99, 116, 120
GSCM	Geometric Stochastic Channel Model. ix, 6, 24, 27, 122
GSM	Global System for Mobile Communications. 15, 21
HPBW	Half Power Beam Width. xiii, 49, 55, 79, 83, 84
HSL	High Speed Line. x, xi, xiv, 3, 74, 78, 79, 86–88, 94, 96, 104, 105, 116, 117, 120, 122
I/Q	In Phase and Quadrature Signal. 53, 54, 56, 61
IEEE	Institute of Electrical and Electronics Engineers. 38, 52
IETR	Rennes Institute of Electronics and Telecommunications. 36
IF	Intermediary Frequency. ix, 36, 53, 54
InF	Indoor Factory. 96
InH	Indoor Hotspot. 26, 96
INRAE	National Research Institute for Agriculture, Food and the Environment. 63
ITU	International Telecommunication Union. 23, 24, 26, 81

Notation	Description
KS	Kolmogorov-Smirnov. xi, 4, 96, 109, 111, 112, 117, 121
LNA	Low Noise Amplifier. ix, 53, 54
LO	Local Oscillator. 39, 57
LOS	Line-Of-Sight. xi, 8, 14, 24–26, 40–43, 45, 47, 48, 68, 69, 76, 80–83, 89, 92, 94, 96, 97, 99–116, 120
LSF	Local Scattering Function. x, 41, 48, 67, 68, 96
LSP	Large Scale Parameter. 81, 84
mDU	MHN Digital Unit. 76
MHN	Mobile Hotspot Network. 76, 81
MIMO	Multiple-Input-Multiple-Output. 15, 22, 30, 33, 38, 42, 49, 122
mmW4Rail	Millimeter-Wave For Rail. 85, 94, 120
mmWave	Millimeter-Wave. x, 2, 30–34, 37, 38, 41, 69, 76, 80, 81, 84, 86, 87, 94, 120
MPCs	Multi Path Components. x, xi, 4, 6, 7, 12–15, 18, 24, 25, 27, 31, 32, 35, 41, 43–46, 48, 60, 66, 67, 69, 76–78, 80, 90–94, 96, 97, 106, 107, 114, 121
mRU	MHN Radio Unit. 76
mTE	MHN Terminal Equipment. 76
MW	MicroWave. 52
NF	Noise Figure. 53
NLOS	Non Line-Of-Sight. x, xi, 8, 24–26, 41–43, 45, 49, 68, 76, 80, 82, 83, 86, 89, 96, 97, 99–110, 113–116, 120, 121
NTRIP	Network and Transport of RTCM via Internet Protocol. 62
OFDM	Orthogonal Frequency-Division Multiplexing. x, 36–38, 40, 59, 60, 65, 120
OLOS	Obstructed Line-Of-Sight. x, 8, 89, 102, 103, 105, 109, 114, 120
OS	Open Square. 42–44, 46
OSM	Open Street Map. 27
OTA	Over The Air. 32
P1dB	Compression Point at 1 dB. 53
P2P	Peer-To-Peer. 42–45
PA	Power Amplifier. 53, 54

Notation	Description
PC	Personal Computer. 63, 64
PDF	Probability Density Function. ix, xi, 17–19, 103, 104, 109
PDP	Power Delay Profile. x, xi, 12–14, 21, 22, 27, 41, 42, 48, 67, 69, 91, 92, 97, 98, 106, 114, 116, 122
PL	Path Loss. ix, xi, xiii, xiv, 3, 15–17, 19, 42, 47, 76–79, 81, 84, 90, 96, 101–103, 105, 106, 109, 114, 117, 120
PLE	Path Loss Exponent. 16, 42, 76, 77, 81–84, 102–106, 117, 120, 121
PLL	Phased-Locked Loop. 56, 57
PN	Pseudo Noise. 34
PPS	Pulse Per Second. 56, 58, 59
PRS	Pseudo Random Sequence. ix, 30, 34, 35
PT	Pathway. 42–45
R&S	Rohde & Schwarz. 55, 56, 58
RA	Residential Area. 42
RAM	Random Access Memory. 61
RF	Radio Frequency. 30, 38, 49, 53, 56, 120
RMa	Rural Macro-cell. xi, 24, 26, 96, 101, 102, 106
RMS	Root-Mean-Square. 4, 37, 84, 114, 116, 121
RMS DS	Root-Mean-Square Delay Spread. xi, xiii, xiv, 3, 13, 14, 27, 43, 44, 46, 76, 77, 79, 81–84, 96, 106–109, 114, 117, 121, 122
RMSE	Root-Mean-Square Error. xiv, 102, 106, 121
RRH	Remote Radio Head. 87
RTCM	Radio Technical Commission for Maritime Services. 62
RTK	Real Time Kinematic. x, 62, 63, 68, 89
Rx	Receiver. ix–xi, 6–8, 12, 14–16, 22, 23, 30–32, 34–43, 45–49, 52–57, 59–61, 64–66, 68–71, 76–78, 81, 84, 86–89, 91, 93, 97, 99, 101, 103, 105, 106, 108, 110–114, 120, 121
SC	Street Canyon. 42, 44
SCS	Sliding Correlation Sequence. ix, 34, 35
SDR	Software Defined Radio. 3, 49, 56, 77, 120–122
SF	Shadowing Factor. xi, 81–84, 101, 104, 117
SIMO	Single-Input Multiple-Output. x, xiii, 3, 53, 60, 65, 72, 88, 120
SISO	Single-Input Single-Output. 72
SMa	Suburban Macro-cell. 26
SNR	Signal-Noise Ratio. 48, 49, 59, 66, 71

Notation	Description
SOLT	Short Open Loss Termination. 32
SSA	Signal Source Analyzer. 32, 40
SSP	Small Scale Parameters. xiii, 43, 81
SV	Saleh and Valenzuela. xiii, 6, 15, 16, 20, 21, 27, 79, 80, 122
T2I	Train-to-Infrastructure. 2
T2T	Train-to-Train. 2
T2V	Train-to-Vehicle. 2
TDL	Tapped Delay Line. ix, 6, 15, 21–23, 26, 49
TRL	Through Reflected Line. 32
TS	Terragraph Sounder. 38
TWDP	Two Ways with Diffuse Power. xiii, 47, 48
Tx	Transmitter. ix, x, 6–8, 12, 14–16, 22, 23, 31, 35–43, 46, 48, 49, 52–57, 59–62, 64–66, 68, 76–78, 81, 84, 86–89, 93, 97, 99, 101, 105, 106, 108, 113, 120, 122
UI	User Interface. x, 63–65
UMa	Urban Macro-cell. 24–26, 41, 96, 101, 102, 105, 106, 109, 114, 117
UMi	Urban Micro-cell. 24, 26, 41, 43, 46, 96, 101, 102, 106, 109, 114
UPS	Uninterruptible Power Supply. 65
US	Uncorrelated Scatters. 6, 11–13, 27, 91, 96, 97
USRP	Universal Software Radio Peripheral. 56, 58, 59, 61, 64, 66
UTC	Coordinated Universal Time. 56
V2I	Vehicle-To-Infrastructure. 2, 42, 44
V2P	Vehicle-to-Pedestrian. 2
V2V	Vehicle-To-Vehicle. 2, 30, 44, 97
VNA	Vector Network Analyzer. ix, 30, 32, 33, 40, 81, 83
WSS	Wide Sens Stationary. 6, 11–13, 27, 91, 96
zASA	Zenith Angular Spread of Arrival. 77

1 General Introduction

Contents

1.1 Context

In a world increasingly focused on connectivity and sustainability, the development of communication systems dedicated to autonomous transport represents a pivotal moment for the future of mobility. This new era led to rethinking the way that vehicles communicate with each other. New scenarios such as Vehicle-To-Vehicle (V2V), Vehicle-To-Infrastructure (V2I), and Vehicle-to-Pedestrian (V2P), form an ecosystem in which vehicles interact with their environment in real-time. By leveraging the power of 5G networks, advanced sensors, artificial intelligence, and cloud computing, these vehicles can anticipate hazards, regulate traffic, and adjust their routes to optimize safety and energy efficiency. In addition, in the context of increasing demand for more efficient, safer, and environmentally friendly transport solutions. The train has to be connected to this ecosystem. In the future, the railway, subway, and other rail systems may be combined with road traffic to form an integrated transportation network, where not only V2V, but also Train-to-Train (T2T), Train-to-Infrastructure (T2I), and Train-to-Vehicle (T2V) communications will be included [1].

With the development of 5G and beyond, new communication possibilities with new available frequencies appear. In fact, the Millimeter-Wave (mmWave) bands play a crucial role in the development of vehicular communication systems by offering significantly higher data transmission capabilities compared to previous technologies. Furthermore, mmWave bands, with their high frequencies, enable breakneck data speeds, low latency, and high connection density—essential for autonomous vehicles that require near-instantaneous information exchanges with their environment.

The development of mmWave propagation channel models is essential to design and develop communication systems at these frequencies. Due to the specific characteristics of mmWave bands, such as their limited range and sensitivity to obstacles (buildings, vehicles, weather conditions), it is crucial to understand how these waves propagate in complex transport environments accurately. Without accurate channel models, it would be difficult to design robust communication systems capable of maintaining reliable connections. Additionally, these models are indispensable for optimizing spectrum resource allocation and ensuring effective coverage in various environments.

The railway sector is no exception to the trend towards millimetric frequencies, particularly because of the lack of dedicated frequencies for autonomous train command and control. In this context, and with the ongoing development of Future Railway Mobile Communication Systems (FRMCS) based on 5GNR. It will bring the railway communication system to a new level. It will answer all requirements related to safe and secure communication systems for the control and command of trains [2]. Then it is crucial to understand the behavior of mmWave in railway environments. This is the purpose of the project National Research Agency (ANR) mmW4RAIL [3] under the grant N°ANR20-CE22-0011. The PhD work was performed within the framework of the project.

1.2 Structure of the Thesis

The PhD thesis manuscript is divided into two parts. The first part concerns the realization of a new Channel Sounder (CS) able to operate in different bands and various complex environments, such as vehicular or railway ones. The other

requirement for the CS is to be able to realize measurements during a long time (more than a minute), for long-range (higher than 100 m), and for dynamic scenarios. The dynamic scenario implies being able to measure the Doppler shift induced by the dynamic measurement.

The second part is devoted to the measurement campaigns organized, first to test the correct operation and then to characterize the radio propagation channel. The measurement campaign aims to provide the behaviour of the main statistical parameters of the radio propagation channel. The extracted channel parameters obtained will be compared with the ones from existing models used, such as the 3rd Generation Partnership Project (3GPP) model.

This thesis manuscript comprises five chapters.

In the **Chapter 2**, the fundamentals of the radio propagation channel are introduced. From free space to multi-path propagation, numerous physical interactions are developed. Then, the different functions to characterize the radio propagation channel are introduced. Finally, the different modelling concepts developed over the decades are presented, such as two models used in standardization.

The **Chapter 3** presents a state-of-the-art of the different sounding techniques, and associated CS at 60 GHz. This state-of-the-art recaps measurement results for outdoor environments, leading us to introduce the specificity of the 60 GHz radio channel. The first specificities are higher losses due to oxygen peak absorption, and a sparser channel. This overview also highlighted the lack of CS able to perform dynamic measures in complex environments such as vehicular and railway ones, and also the absence of measurement results in the literature.

To overcome these issues, the **Chapter 4** is devoted to the Single-Input Multiple-Output (SIMO) CS developed from scratch in the context of this thesis at IMT Atlantique. It is capable of operating in dynamic scenarios in complex environments. The CS is based on a Commercial-Off-The-Shelf (COTS) and Software Defined Radio (SDR) platform to reduce the global cost. Moreover, its innovative architecture allows it to be used at different frequencies, and with polarimetric information. Then, the various functionalities are presented, such as an accurate localization module. Finally, two measurement campaigns are realized to validate the correct overall operation.

These test campaigns have shown that the CS works very well. Thus, we have organized a new measurement campaign in a typical marshalling yard. The **Chapter 5** describes the different elements that can be found in the railway environment, and an overview of existing measurements in the literature shows that there is a lack of measurement results. Then, the environment and the associated scenario of the measurement campaign are introduced. This campaign aims to provide measurement results data to the community and realized case studies. Finally, this chapter presents the first measurement results, which indicate the good configuration of the CS for this atypical environment.

Finally, the **Chapter 6** details the exploitation of the results of the measurement campaign realized in a railway environment, for a 3GPP High Speed Line (HSL) scenario. The first result is a discussion about the size of the local stationary region, with a stationary investigation. Indeed, the investigation of the stationary area is not commonly realized, and there is, to the best of our knowledge, no information about it at 60 GHz in the railway environment. Then, the Path Loss (PL) is modelled. The mean and standard deviation of the log value of the Root-Mean-Square

Delay Spread (RMS DS) are given, and all the parameters are compared to the 3GPP models. The best distribution to use to fit the small-scale fading is discussed, and the Kolmogorov-Smirnov (KS) test is retained as a metric to validate the final distribution choice. From this discussion, it appears that the best distribution to use, in our case, is the Rice distribution, which allows us to compare these results with 3GPP models. Finally, the Root-Mean-Square (RMS) Doppler spread is computed, and a distribution is retained to represent the spatial dispersion of the Multi Path Components (MPCs).

After the conclusion, numerous perspectives are detailed.

2 Generalities on Radio Channel

Contents

2.1 Introduction

The first step for developing a communication system is the investigation of its medium support. In wireless communications, the support medium is the radio propagation channel formed between the Transmitter (Tx) and the Receiver (Rx). From the investigation of the radio propagation channel, several properties are obtained and allow us to assess the information-theoretic capacity, in other words, the maximal data rates that a wireless system can achieve. The propagation mechanisms are various, and the main interrogation is resolved by the study of the maximum link cover distance for a wanted signal-to-noise ratio. An approximation of the received power in a free space environment, from the point of view of the Fresnel zone, is then developed and leads to the Friis equation, which will be presented in the first section. Moreover, to develop a thinner view of the propagation mechanism, it is needed to introduce the different physical interactions that occur in real-world, multipath propagation. From the simple reflection to the wave-guiding, those interactions will be introduced in the second section.

To continue, the mathematical expressions to characterize the radio channel behavior are introduced. The radio channel can be modelled as a linear filter, which is fully characterized, in the time domain, by the Channel Impulse Response (CIR) or its Channel Transfer Function (CTF), in the frequency domain. These two functions are the basics introduced by Bello in 1963 in [4].

These equations are used to characterize the radio propagation channel in the case of Wide Sens Stationary (WSS)-Uncorrelated Scatters (US) assumption, which is first introduced. In real-world cases, the distance between the Tx and the Rx can change and lead to break this assumption. This assumption violation implies an evolving description of the radio channel description and then, the characterization of the MPCs is complex to describe. In this case, a stochastic description of the radio channel is adopted.

Once the stochastic description of the radio propagation channel is made, the maximum throughput of a communication system can be estimated, via a modelling of it. In the literature, several model concepts are introduced. A historical overview of them is presented, from the well-known Saleh and Valenzuela (SV), to Tapped Delay Line (TDL), the double directional channel and the Geometric Stochastic Channel Model (GSCM). To conclude this section, two examples of standard channel models are introduced, the 3GPP and the IMT-Advanced.

2.2 Radio Channel Propagation

In simple scenarios, the radio channel can be considered in free space conditions depending on the Fresnel zone defined by the antenna height, and the obstacles in the environment, which is first presented. An estimation of the received power can be obtained from the Friis equation.

Then, the mathematical function to describe the radio propagation channel in the assumption of WSS-US is presented. Bello introduces these four functions [4] and are valid only in stationary conditions, named WSS-US. This assumption, when the distance between the Rx and Tx is changing, is valid only in a small portion, i.e., stationary area. In the case of long-range measurement, the number of this area can be high, and a deterministic description becomes complex. A stochastic approach

is then introduced, based on the auto-correlation function, and allows describing the radio propagation in a stochastic way with stochastic functions derived from the Bello functions.

From these stochastic functions, special cases are used to describe the time and frequency dispersion of the MPCs. Some special case illustrations are, finally, introduced.

2.2.1 Free Space Propagation

The free space is the simplest propagation scenario. The free space propagation is defined, from the point of view of the antennas, as the absence of obstacles inside the Fresnel zone. An approximation of the Fresnel zone radius r can be found in Eq. (2.1), where d is the distance between the Rx and Tx antenna and λ the wavelength.

$$r = \frac{1}{2}\sqrt{\lambda d} \tag{2.1}$$

At the Tx antenna, the power density, over a closed centered sphere surface with the radius r_S with an antenna radiates isotropically, is $P_{\mathrm{Tx}}/(4\pi r_S^2)$. At the Rx side, the received power at the antenna depends on this "effective area", A_{RX} defined in the Eq. (2.2), where G_{RX} is the antenna gain and λ the wavelength.

$$G_{\mathrm{RX}} = \frac{4\pi}{\lambda^2} A_{RX} \tag{2.2}$$

Finally, the received power P_{RX} in the case of the Tx antenna is not radiated isotropically can be found in Eq. (2.3), where G_{TX} is the antenna gain at the Tx side.

$$P_{\mathrm{RX}} = P_{\mathrm{TX}} G_{\mathrm{TX}} \frac{1}{4\pi d^2} A_{\mathrm{RX}} \tag{2.3}$$

With the Eq. (2.2) and Eq. (2.3), it can be obtained the received power as the function of distance in Eq. (2.4), also known as the Friis' law, where $P_{\mathrm{RX}}, P_{\mathrm{TX}}$ represent respectively the received and transmit power at the antenna, $G_{\mathrm{RX}}, G_{\mathrm{TX}}$ represent respectively the receiver and transmitter antenna gain, λ the wavelength and d is the distance between the transmitter and the receiver.

$$P_{\mathrm{RX}} = P_{\mathrm{TX}} G_{\mathrm{RX}} G_{\mathrm{TX}} \left(\frac{\lambda}{4\pi d}\right)^2 \tag{2.4}$$

From this equation, the Free Space Path Loss (FSPL) is extracted and defined as follows $\left(\frac{\lambda}{4\pi d}\right)^2$. This leads to distinguishing two cases: firstly, the propagation scenario, where we focus on the propagation channel without considering the impact of the antenna. Secondly, the transmission channel investigates the impact of the antenna on the channel. The Fig. 2.1 shows the difference between both channels.

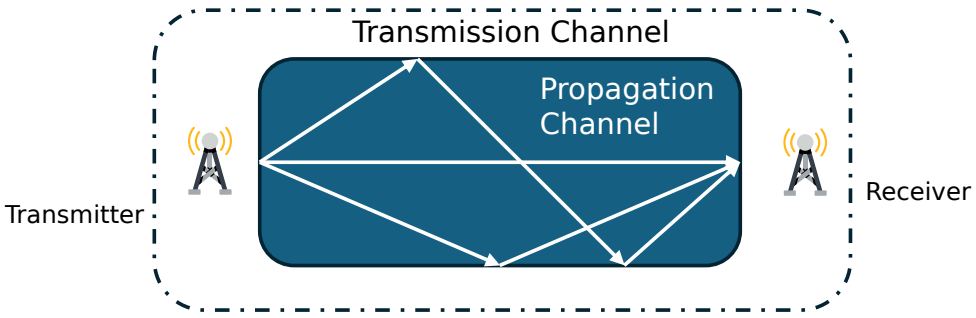

FIGURE 2.1: Difference between the transmission and the propagation channel.

To correctly use the Friis equation, the distance between a Tx and a Rx needs to be greater than the far-field distance of the antenna. The far-field distance is defined by the Fraunhofer distance and presented in Eq. (2.5), where D represent the largest size of the antenna and λ is the wavelength. It is a characteristic distance because, beyond it, the power attenuation is dependent on the inverse square of the distance and the electromagnetic wave can be considered as planar.

$$d_F = \frac{2D^2}{\lambda} \tag{2.5}$$

2.2.2 Multi-path Propagation

In a real environment, the received signal is composed of multiple replicas of the emitted signal due to interactions with various physical obstacles during propagation. The first case is when the Fresnel zone is empty of physical obstacles and named Line-Of-Sight (LOS) condition. In this case, the signal propagates in free space conditions. Furthermore, when the Fresnel zone has obstacles the signal interacts with them in multiple ways, which can heavily impact the link depending on the size of the physical obstacles relative to the wavelength. Moreover, these scenarios named Non Line-Of-Sight (NLOS) and Obstructed Line-Of-Sight (OLOS) occur when the Fresnel zone is filled by an obstacle or not, respectively. Nonetheless, even if the Fresnel zone is obstructed, due to propagation mechanisms discussed later and presented in the Fig. 2.2, a propagation path can be established.

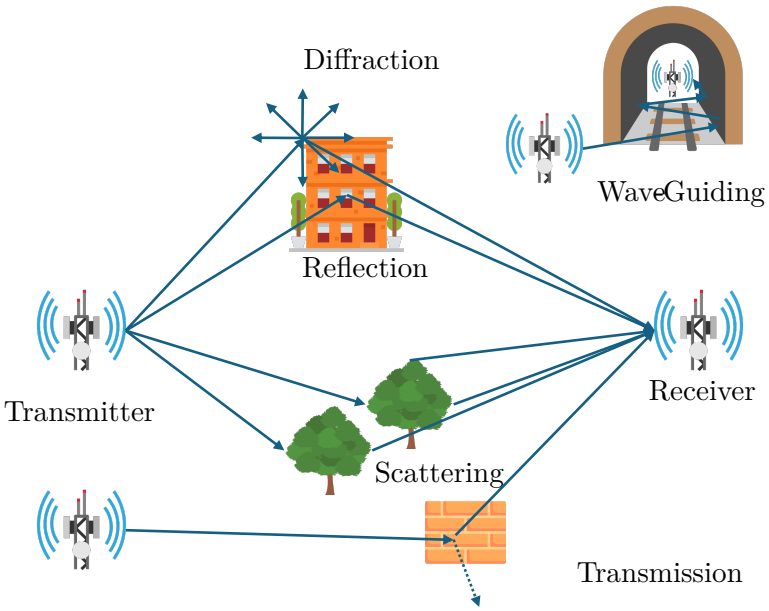

FIGURE 2.2: Illustration of the physical interaction in the real propagation environment.

Reflection In this case, the size of the object is larger than tens of the wavelengths and has limited roughness (much smaller than the wavelength).

To determine the direction and amplitude of the reflected signal, we can apply the optical physics guided by the Snell-Descartes and Fresnel equations. If the roughness is greater than the wavelength, we refer to it as diffuse reflection. In either case, the maximum amplitude is in the direction of the reflected path.

Transmission This occurs when the support does not fully reflect the signal. For example, we can consider wall transmission. The attenuation and direction of the signal depend primarily on the incident angle with the material, secondarily on the electrical composition of the transmission support and thirdly on the wavelength through variations in the refraction index. Furthermore, with thin transmission supports, multiple reflections can occur, leading to attenuated copies of the transmitted signal.

Diffraction Diffraction occurs when waves encounter an obstacle or an opening whose dimensions are comparable to their wavelength. This phenomenon causes a change in the direction of wave propagation, allowing the waves to bend around the obstacle or spread out after passing through the opening.

Scattering Scattering is the process by which a wave deviates from its straight-line path when it encounters an obstacle, a rough surface, or a medium with non-uniform properties.

Wave guided propagation This phenomenon occurs in environments, where a waveguide can be created thanks to a wall, such as in a corridor or tunnel. The multiple reflections lead to a direct electromagnetic field in the direction of the waveguide.

2.3 Radio Channel Description

2.3.1 Static Scenario: Deterministic Channel Description

To model and synthesize the aforementioned interactions, a mathematical description is required. The aforementioned interactions will serve to filter the emitted signal, thereby producing a filtered version. Furthermore, it can be stated that none of the aforementioned interactions results in non-linear behavior, and the channel can thus be considered reciprocal. This leads to the conclusion that the radio propagation channel can be considered as a linear filter with two parameters: time and delay. The filter can be measured using the Dirac delta function. To obtain the propagation response to any input signal, a convolution is applied between the input signal and the CIR. The CIR, $h(t,\tau)$, linked the received signal, $s(t)$, and the emitted signal, $e(t)$, presented in Eq. (2.6). The CIR represents the initial deterministic form of the Bello function.

$$s(t) = \int_{-\infty}^{+\infty} e(t-\tau)h(t,\tau)d\tau \tag{2.6}$$

The second function of Bello, dual of the CIR, is the CTF, which is presented in Eq. (2.7). In this equation, $h(t,\tau)$ represents the CIR, $H(t,f)$ the CTF, and the latter is computed via the Fourier transform of the CIR to obtain the frequency response of the channel. The CTF represents the variation of the radio channel propagation in the frequency domain.

$$H(t,f) = \int_{-\infty}^{+\infty} h(t,\tau)e^{-2j\pi f\tau}d\tau \tag{2.7}$$

Furthermore, the received signal from the CTF can be obtained by computing the formula presented in Eq. (2.8), where $s(t)$ is the received signal in temporal domain, $E(f)$ the spectrum of the emitted signal and $H(t,f)$ is the CTF.

$$s(t) = \int_{-\infty}^{+\infty} H(t,f)E(f)e^{2j\pi ft}df \tag{2.8}$$

The four Bello functions in the different domains can be obtained from these functions, as illustrated in Fig. 2.3. In Fig. 2.3, a black dot at the end of the link represents the implementation of the Fourier transformation, whereas a white dot indicates the application of the inverse Fourier transform.

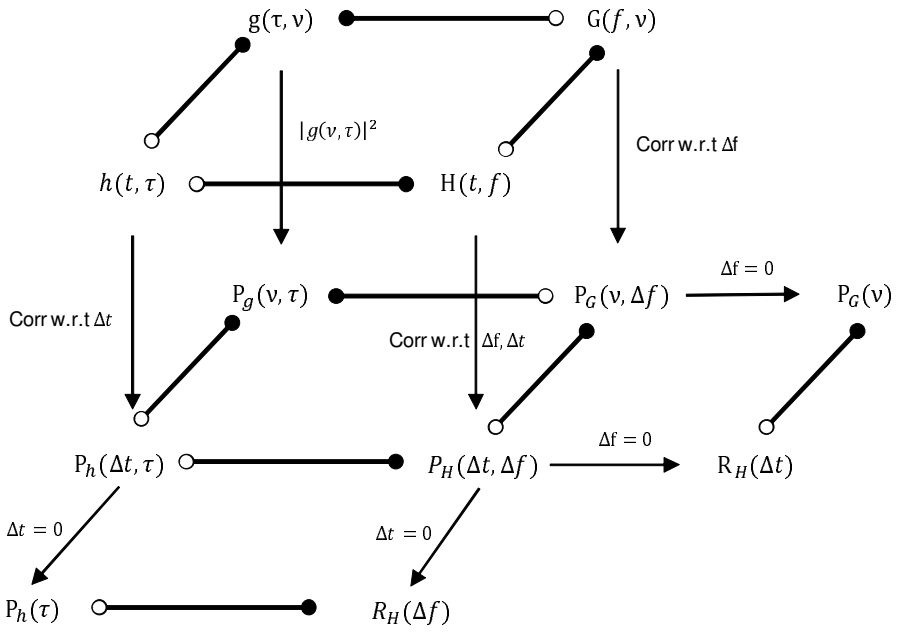

FIGURE 2.3: Representation of the Deterministic and stochastic Bello's Functions and the special cases associated.

The delay-Doppler spread function provides information about the Doppler at each delay. The computation of this function is presented in Eq. (2.9), where $g(\tau, \nu)$ is the delay-Doppler function and $h(t, \tau)$ the CIR. Finally, the CIR can be retrieved by performing the inverse Fourier transform on this delay-Doppler spread function.

$$g(\tau, \nu) = \int_{-\infty}^{+\infty} h(t, \tau) e^{-2j\pi\nu t} dt \tag{2.9}$$

The Doppler spread function is the Fourier transform counterpart of the CIR, representing the frequency and Doppler domains, whereas the CIR describes the time and delay domains. This function may represent the received signal spectrum as a summation of the Doppler-shifted emitted signal. Furthermore, the Fourier transformation establishes a relationship between the delay-Doppler spread and CTF as illustrated in Eq. (2.10), where $G(f, \nu)$ is the Doppler spread function. The function $H(t, f)$ is the CTF as defined in Eq. (2.11), where the delay-Doppler spread function is given by $g(\tau, \nu)$.

$$G(f, \nu) = \int_{-\infty}^{+\infty} H(t, f) e^{-2j\pi f t} dt \tag{2.10}$$

$$g(\tau, \nu) = \int_{-\infty}^{+\infty} G(f, \nu) e^{2j\pi f \nu} df \tag{2.11}$$

The equations mentioned above are employed to delineate the temporal evolution of the radio propagation channel. Nevertheless, this description describes its evolution in the assumption of WSS-US.

2.3.2 Moving Scenario: Stochastic Channel Description

2.3.2.a WSS-US Channel

In a dynamic scenario, this condition is only validated in a restricted area, designated as the stationary area, where the WSS-US conditions are satisfied. This assumption is comprised of two distinct parts. Firstly, the term WSS signifies that the second-order statistical properties of the channel remain unaltered with respect to distance. Furthermore, the definition of WSS states that different MPCs with varying Doppler shifts are uncorrelated. In the case of relative movement between the Rx and the Tx, this assumption is not fulfilled throughout the entire measurement interval. However, it is possible to define a region in which this assumption remains valid. The extent of the stationary region may vary considerably depending on the specific measurement type, encompassing hundreds of wavelengths in some cases and just a few in others.

Secondly, the assumption of US is based on the premise that MPCs with different delays are uncorrelated. Moreover, this implies that MPCs are associated with different scatterers in the propagation channel.

When describing the radio propagation channel over long distances, it is divided into distinct stationary regions. The deterministic description of each region generates a substantial amount of data, particularly at high frequencies where the wavelength is small. A deterministic description of each region is not optimal. It is preferable to describe each region with stochastic functions.

2.3.2.b Stochastic Channel Description

The stochastic functions are derived from the Bello deterministic function and will be introduced in this section. In practice, the stochastic description is limited to the second order due to the knowledge of the auto-correlation functions. Similarly, the four stochastic functions are each linked through Fourier transformations, as is the case with the deterministic part.

In the stochastic domain, the counterpart of the CIR is the delay cross-spectral density, denoted as $P_h(\Delta t, \tau)$, which is computed by correlation w.r.t Δt. From this function, the Power Delay Profile (PDP) can be derived, representing the power evolution of the MPCs. The time dispersion of the MPCs can then be extracted from the PDP.

The scattering function, denoted $P_s(\nu, \tau)$, is defined as the square modulus of the delay-Doppler spread function. This function describes the frequency dispersion of the MPCs in terms of power. From this, the frequency dispersion of the MPCs can be extracted.

The time-frequency correlation function, denoted as $P_H(\Delta t, \Delta f)$, is computed by correlation w.r.t Δf of the CTF. This function can be used to derive the frequency correlation function, denoted $R_T(\Delta f)$, with $\Delta t = 0$ and the time correlation function, denoted as $R_T(\Delta t)$ with $\Delta f = 0$.

The final step is to obtain the Doppler cross-spectral density $P_G(\nu, \Delta f)$, through correlation w.r.t. Δf on the Doppler-variant transfer function $H(\nu, f)$.

In order to obtain the stochastic variation of the radio propagation channel, the special cases of the stochastic functions are employed. As previously stated, the PDP

is utilized to characterize the time spread of the MPCs, and the scattering function represents the frequency dispersion of the MPCs.

2.3.3 Statistic Parameters in Time and Frequency Domain

This section will present the principal statistical parameters derived from the special cases of the stochastic function. As previously stated, two main functions will be introduced: the PDP for the temporal dispersion of the MPCs and the scattering function for the frequency dispersion of the MPCs.

2.3.3.a Power Delay Profile

In order to characterize the power distribution of MPCs as a function of delay, it is necessary to extract the average PDP from a stationary zone. The PDP can be obtained via special cases of the delay cross-power spectral density, denoted as $P_h(\Delta t, \tau)$, where $\Delta t = 0$. This is illustrated in Fig. 2.3. The PDP is computed via CIR power averaging, as presented in Eq. (2.12), where N represents the number of CIRs in a stationary zone and $h(x, \tau)$ is the CIR. The size of the stationary region is contingent upon the WSS-US characteristics of the channel, which will be discussed subsequently. However, it can be stated that this area size is typically between 20 and 40 times the wavelength. An illustrative example of a PDP example is presented in Fig. 2.4.

$$PDP(x, \tau) = \frac{1}{N} \sum_{k=1}^{N} |h(x_k, \tau)|^2 \tag{2.12}$$

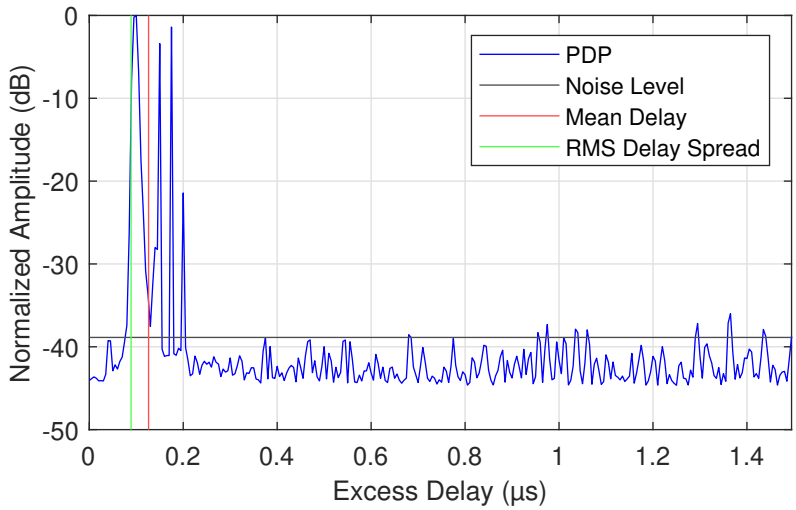

FIGURE 2.4: Example of a PDP with typical parameters.

2.3.3.b Delay Spread and Coherence Bandwidth

As demonstrated by the earlier presentation of the PDP function, the existence of MPCs can be discerned and delineated by examining the first moment of the PDP. The square root of the second-order moment of the PDP function provides the RMS DS, which characterizes the delays of MPCs around the mean delay. The RMS DS

is presented in Eq. (2.13), where τ and P represent, respectively, the delay and the PDP value associated.

$$D_s = \sqrt{\frac{\int_{-\infty}^{+\infty}(\tau - \tau_m)^2 P}{\int_{-\infty}^{+\infty} P}} \text{ with } \tau_m = \frac{\int_{-\infty}^{+\infty} \tau P}{\int_{-\infty}^{+\infty} P} \tag{2.13}$$

Typically, the RMS DS is calculated with a threshold to minimize the impact of noise on the computation. This is achieved by first computing the PDP and then removing the noise identified by the noise threshold, as illustrated in Fig. 2.4. The subsequent step is to select an appropriate threshold value, which can be either a fixed value or dependent on the PDP dynamic.

From the PDP, several values can be defined, beginning with the first arrival delay, which corresponds to the shortest distance between the Rx and the Tx. This is typically assimilated with the LOS component, if present. Subsequently, the maximum excess delay is defined as the delay between the first arrival delay and the last delay above the noise threshold.

The coherence bandwidth, denoted by B_c, is defined as the bandwidth over which all the frequencies experience similar effects in terms of gain and phase. The estimation is based on the frequency correlation function. An alternative approach, as outlined in [5], is to estimate it through the average PDP and perform a Fourier transform. The estimation presented in Eq. (2.14) is as follows: $R_H(\Delta f)$ is the frequency correlation function, $E\{|h(\tau)^2|\}$ represents the averaged PDP, and $e^{-2j\pi\Delta f\tau}$ is the part corresponding to the Fourier transformation. Nevertheless, in [6], an approximation is provided in which the coherence bandwidth is defined as the bandwidth over which the frequency correlation function exceeds a threshold, typically set at 0.9. This is estimated using the relation $B_c \approx \frac{1}{50\sigma_t}$, where σ_t is the RMS DS.

$$R_H(\Delta f) = \int_{-\infty}^{+\infty} E\{|h(\tau)^2|\} e^{-2j\pi\Delta f\tau} d\tau \tag{2.14}$$

The coherence bandwidth provides information regarding about the frequency selectivity of the channel. If the signal bandwidth of a communication system (B_s) is significantly smaller, $B_s << B_c$ than the coherence bandwidth, the channel is deemed non-frequency selective. Conversely, if B_s is comparable to or larger than B_c, the channel is regarded as frequency selective.

2.3.3.c Doppler Spread and Coherence Time

The phenomenon of Doppler shift occurs when there is a relative movement between the Rx and Tx. Nevertheless, in the context of radio propagation channel characterization, instances have been observed where a Doppler shift occurs even when the Rx and Tx remain stationary. This phenomenon can be attributed to the movement of scatterers, which may be caused by external factors such as the wind on the leaf or the passage of a moving object through the Rx and Tx. Such movement results in a Doppler shift of the MPCs.

The maximum Doppler shift resulting from relative motion between Rx and Tx is a function of both the relative displacement and the wavelength. The MPCs Doppler shift is a function of the relative displacement between the Rx and Tx as well as the angle between the scatters and the Rx. This relationship is illustrated in Eq. (2.15)

$$f_d = \frac{v}{\lambda} \cos\theta \tag{2.15}$$

The distribution of the Angle of Arrival (AoA) of MPCs in the environment and the characteristics of the Tx and Rx antennas determine the shape of the Doppler spectrum. The most well-known shape is the 'Jakes' spectrum, which occurs when the AoA distribution follows a uniform distribution between $[-\pi, +\pi]$. This is defined in Eq. (2.16), where σ^2 is the variance of the signal and f_d is the maximal Doppler spread.

$$f(x) = \begin{cases} \frac{\sigma^2}{\pi f_d} \frac{1}{\sqrt{1-\frac{f}{f_d}^2}} & , -f_d \leq f \geq +f_d \\ 0 & , \text{otherwise} \end{cases} \tag{2.16}$$

In the time domain, the Doppler effect gives rise to variations in the coherence time, which is defined by the time correlation function. This is the Fourier transform of the Doppler spread function. The coherence time can be estimated using the equation $T_c = \frac{1}{16\pi DP_s}$, where DP_s represents the Doppler spread of the channel, as outlined in [6]

2.3.4 Conclusion

This section has introduced the various ways in which an electromagnetic wave can interact with its surrounding environment, which can be considered as either free space or multipath. It then goes on to present the principal interaction between the electromagnetic wave and the environment. Following this, the different scales of channel description are presented, which ultimately lead to the channel being represented as a linear filter that varies over time. This time-varying nature of the channel then introduces a stochastic description of the radio propagation channel, with some special cases of this description being presented.

Once the aforementioned introduction has been made, the channel stochastic parameters are to be modelled to estimate the feasibility of a communication system. The following section will present the main model concept, which has been developed from the PL to a geometrical stochastic description.

2.4 Channel Modelling Concepts

This section presents the principal concept employed in the modelling of the radio propagation channel. The initial model component is the PL. The initial information required to ascertain the viability of a communication system is the received power and the estimated coverage distance. Subsequently, a more comprehensive concept was introduced by SV in 1987, which is still in use today. However, due to the limitations in computational power at the time, it was not explicitly implemented. With the subsequent evolution of the communication systems and with the advent of the Global System for Mobile Communications (GSM) standardization in 1993, a model with a greater number of parameters was required, leading to the introduction of the TDL model.

The TDL model lacks angular information, and the endorsement of Multiple-Input-Multiple-Output (MIMO) system has prompted the necessity for a novel model.

The double-directional channel model, which considers the antenna diversity on both sides, (Rx and Tx), was subsequently introduced in the early 2000s.

The link between the geometric configuration of the environment and the modelling is then made with a geometric stochastic channel model. This model uses the concept introduced by SV and links the cluster to the scattering in the environment.

Finally, two examples of existing models are presented to illustrate the use of the presented concept, even today.

2.4.1 Path Loss Model

The PL represents the attenuation suffered by the transmitted signal during its propagation through the radio channel. This attenuation is divided into three scales, firstly, the large scale represents the power variation over a long distance, higher than the wavelength. The large scale is modelled by a linear curve as a function of the separation distance between the Rx and Tx.

Nonetheless, on a smaller scale, minor variations occur due to various interactions between the electromagnetic field and the environment. These variations are called small-scale fading and happen over a range of several wavelengths. This fluctuation is modelled differently depending on the visibility conditions.

Finally, between large- and small-scale variations, there is another type of fluctuation, and the distinction between small and large is subtle. However, this fluctuation still needs to be modelled. To address this, a case called shadowing is introduced, representing the remaining fluctuations. This variation is modelled with Gaussian distribution. An illustration of the different scales of the PL is proposed in Fig. 2.5.

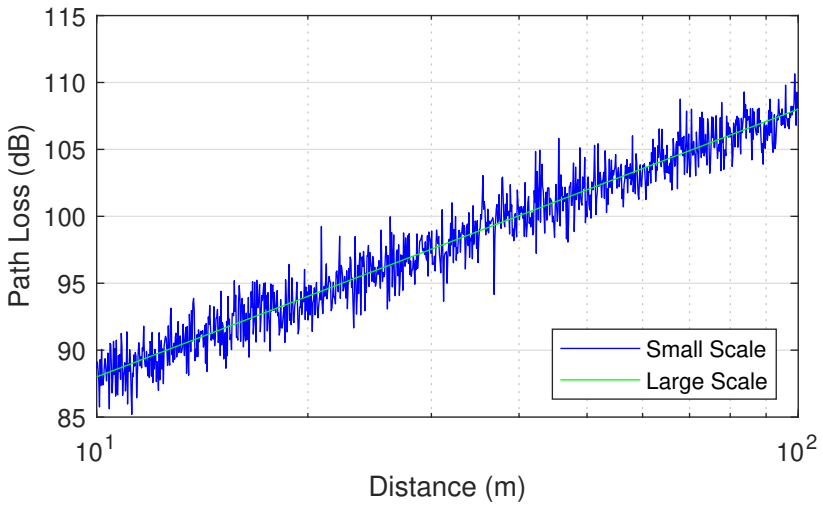

FIGURE 2.5: Illustration of the different scale of the PL.

2.4.1.a Large Scale

The initial large-scale PL model is described by the Friis equation, presented in Eq. (2.17), where λ represents the wavelength and d_r the distance between the Tx and the Rx. In this case, the Path Loss Exponent (PLE) is considered to be equal to 2.

$$PL_{Friis} = 20\log_{10}\left(\frac{\lambda}{4\pi d_r}\right) \tag{2.17}$$

However, not all scenarios in wireless communication occur in free-space conditions. Various scatterers have different impacts on propagation, depending on their size relative to the wavelength, λ. This observation necessitates the development of a model to easily characterize power attenuation in these diverse scenarios.

The model that incorporates the most comprehensive information about measurements is known as the Alpha-Beta-Gamma (ABG) model [7], which is defined in Eq. (2.18). In this model, α represents the free space attenuation, β denotes the path loss exponent, γ signifies the frequency dependency of the path loss, f represents the carrier frequency in GHz and X_σ^{ABG} corresponds to the large-scale shadowing fading, as detailed in Sec. 2.4.1.c.

$$PL_{ABG}(f,d) = \alpha + 10\beta\log_{10}\left(\frac{d}{d_0}\right) + 10\gamma\log_{10}\left(\frac{f}{1\text{GHz}}\right) + X_\sigma^{ABG} \tag{2.18}$$

From Eq. (2.18), various models are derived, including the floating-intercept and single-frequency close-in models, where the frequency dependency is not considered. In contrast, for the close-in model, the carrier frequency influences the computation of the α parameter, derived from the Friis space path loss. Additionally, a multi-frequency model is proposed, incorporating a frequency-dependent term that uses a weighted average of all frequencies to account for frequency dependency.

Moreover, PL in railway environments often exhibit a two slopes characteristic, especially in scenarios with curved track in tunnels [8] or multiple scenes within a single scenario [9]. The model defining this behavior is presented in Eq. (2.19), where $\beta_{1,2}$ represent the path loss exponents of the first and second slopes, $\alpha_{1,2}$ represent the interception points, X_{σ_1,σ_2} represent the shadowing factors, following a centered normal distribution with parameters σ_1 and σ_2 and d_b represents the break distance.

$$f(d) = \begin{cases} 10\beta_1\log_{10}\left(\frac{d}{d_0}\right) + \alpha_1 + X_{\sigma_1} & d \le d_b \\ 10\beta_2\log_{10}\left(\frac{d}{d_0}\right) + \alpha_2 + X_{\sigma_2} & d > d_b \end{cases} \tag{2.19}$$

2.4.1.b Small Scale

Fast fading is caused by scatterers with dimensions comparable to the wavelength. The variation in these scatterers, combined with their movement during the communication, leads to constructive and destructive interference, resulting in rapid variations of the received signal envelope. The most commonly used distribution to model the fast fading is the Nakagami-m distribution. This distribution, introduced in 1960 by Minoru Nakagami, better fits measurement results. The Probability Density Function (PDF) of this distribution is presented in Eq. (2.20), where Γ represents the gamma function, m controls the shape of the curve, and Ω controls the spread parameter.

$$\rho_r(r;m,\Omega) = \frac{2m^m}{\Gamma(m)\Omega^m} r^{2m-1}\exp\left(-\frac{m}{\Omega}r^2\right), \forall r \ge 0 \text{ with } m \ge \frac{1}{2}, \text{ and } \Omega > 0 \tag{2.20}$$

From the Nakagami-m distribution, special cases commonly used to model small-scale variations are the Rayleigh and Rician fading models. The Rayleigh model's PDF is presented in Eq. (2.21), where σ^2 represents the second moment, $E[R^2]$. The Fig. 2.6 shows the PDF and the Cumulative Density Function (CDF) of this distribution. The Rayleigh distribution is used to model the scenarios where the MPCs arrive with equal power.

$$\rho_r(r;\sigma^2) = \frac{r}{\sigma^2}\exp\left(-\frac{r^2}{2\sigma^2}\right), r \geq 0 \tag{2.21}$$

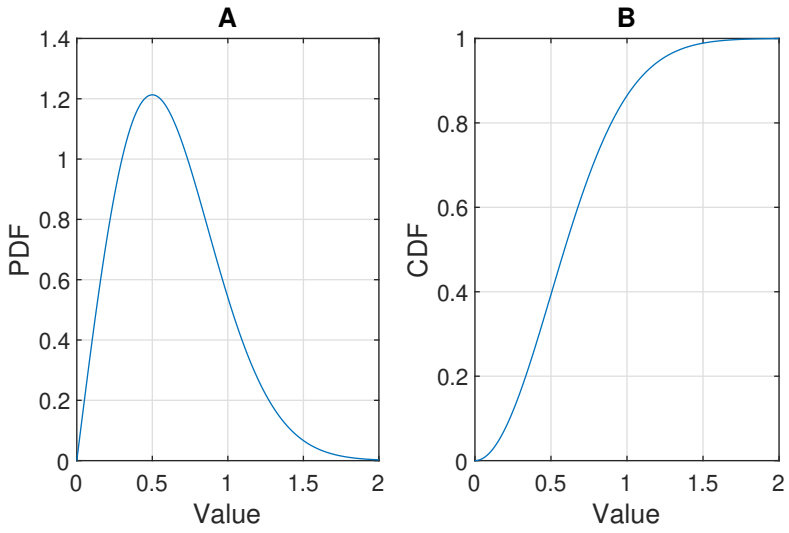

FIGURE 2.6: Illustration of the Rayleigh distribution with, **A**, the PDF and in **B** the CDF.

In scenarios where one path arrives with higher power than the other paths, the most widely used model is the Rician fading model. Its PDF is presented in Eq. (2.22), where $K = \frac{\nu^2}{2\sigma^2}$ represents the ratio between the power of the direct path and the power in the MPCs, and $\Omega = \nu^2 + 2\sigma^2$ represents the total power from all paths, acting like a scaling factor. I_0 is the 0^{th} order modified Bessel function of the first kind. The Fig. 2.7 shows the PDF and the CDF of the Rice distribution.

$$\rho_r(r;K,\Omega) = \frac{2(K+1)r}{\Omega}\exp\left(-K-\frac{(K+1)r^2}{\Omega}\right) I_0\left(2r\sqrt{\frac{K(K+1)}{\Omega}}\right) \tag{2.22}$$

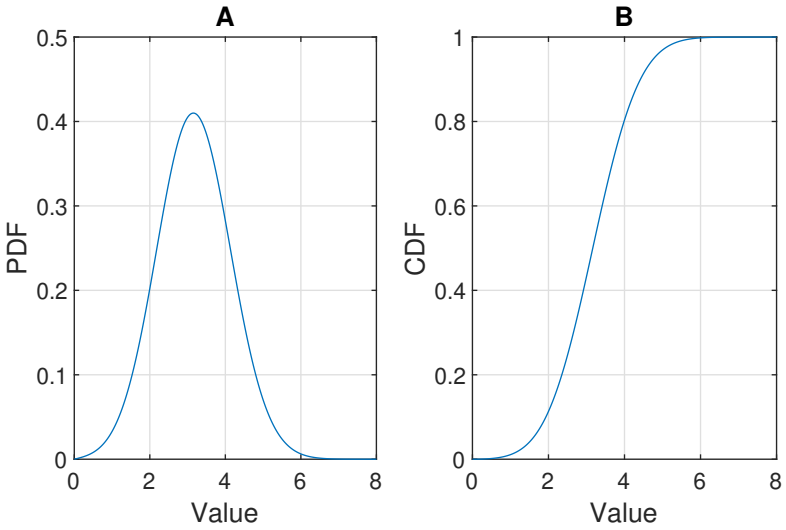

FIGURE 2.7: Illustration of the Rice distribution with, **A**, the PDF and in **B** the CDF.

2.4.1.c Shadowing

As mentioned earlier, another scale is proposed to model PL due to the thin boundary between small and large scales. The shadowing model accounts for all the attenuation that is not modelled in the other cases. In dB scale, these variations occur around the mean value of the PL, and can be modelled with a zero-mean Gaussian random variable, where σ_S^2 represents its variance. The PDF equation of a normal distribution is given in Eq. (2.23), where σ denotes the standard deviation and μ denotes the mean value. The Fig. 2.8 shows the PDF and the CDF of the normal distribution.

$$\rho_S(r;\mu,\sigma) = \frac{1}{\sigma\sqrt{2\pi}} e^{-\frac{1}{2}\left(\frac{r-\mu}{\sigma}\right)^2} \tag{2.23}$$

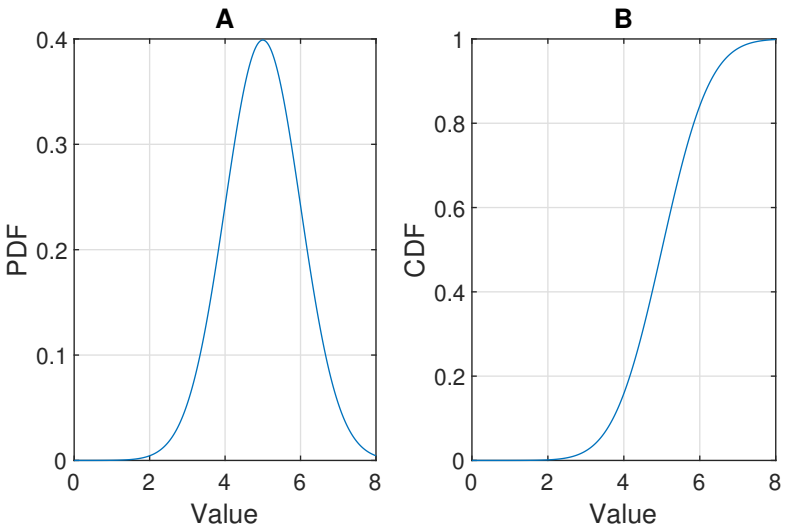

FIGURE 2.8: Illustration of the Normal distribution with, **A**, the PDF and in **B** the CDF.

The second-order statistics of shadowing fading describe the joint distribution between different points within the same cell. As previously mentioned, shadowing is often modelled using a Gaussian random variable, which prompts an investigation into correlation functions. A simple yet effective model for this correlation is the exponential correlation model presented in Eq. (2.24), where D_c represents the correlation distance of the process.

$$R_S(\Delta) = \sigma_S^2 \exp\left(-\frac{|\Delta|}{D_c}\right) \tag{2.24}$$

2.4.2 Saleh And Valenzuela Model

Saleh and Valenzuela were the first to introduce the basic concepts still used today in 1987 [10], such as clusters, rays and stochastic modelling. The CIR is modelled with multiple groups of rays. Each group represents a cluster, which has its own power decay, either exponential or linear in dB, in the time domain. Eq. (2.25) presents the CIR in the SV model, where $\beta_{k,i}$ is the amplitude of the k^{th} rays on the i^{th} cluster, $\theta_{k,i}$ represent the phase which follows a uniform distribution in $[0, 2\pi)$, T_i the time arrival of the i^{th} cluster and $\tau_{k,i}$ the excess delay of the mentioned path. Regarding intra-cluster interactions, the power decay between clusters (inter-cluster) follows either an exponential decay or linear decay on the dB scale. The Fig. 2.9 shows a SV CIR example.

$$h(\tau) = \sum_{i=0}^{L} \sum_{k=0}^{K_L} \beta_{k,i} e^{j\theta_{k,i}} \delta(\tau - T_i - \tau_{k,i}) \tag{2.25}$$

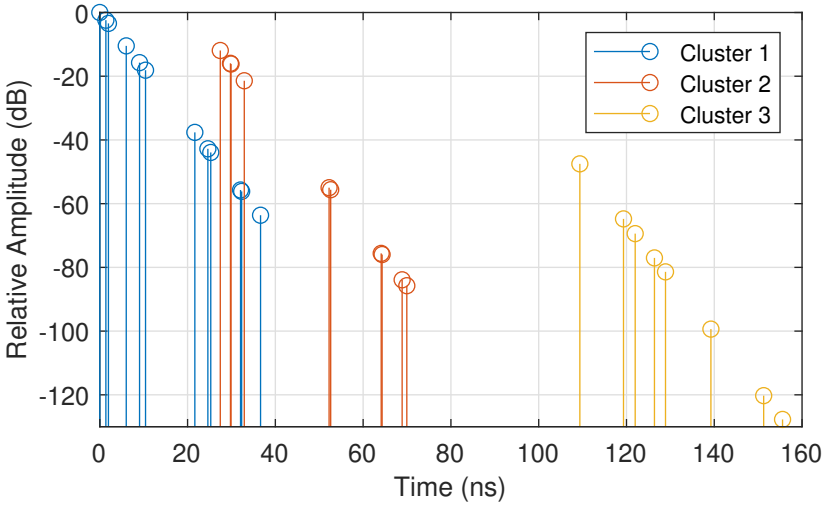

FIGURE 2.9: Saleh and Valenzuela channel model principle.

As mentioned earlier, the SV model includes a stochastic component in the arrival times of intra-cluster or inter-cluster rays. The arrival times of the clusters and intra-cluster rays follow a Poisson distribution with different parameters. Eq. (2.26) presents the probability of the arrival time of the i^{th} cluster, where Λ is the fixed rate of the cluster arrivals. Eq. (2.27) presents the probability of the occurrence of the k^{th} ray in the i^{th} cluster, where λ is the fixed rate for the arrival of the rays.

$$p(T_i|t_{i-1}) = \Lambda \exp\left(-\Lambda(T_i - t_{i-1})\right), i > 0 \tag{2.26}$$

$$p(\tau_{ki}|\tau_{(k-1)i}) = \lambda \exp\Big(-\lambda(\tau_{ki} - \tau_{(k-1)i})\Big), k > 0 \tag{2.27}$$

The Eq. (2.28) present the computation of the mean square amplitude for the k^{th} rays in the i^{th} cluster, where $\overline{\beta_{0,0}^2}$ represent the power of the first arrival path in the first cluster, and Γ and γ are the power delay time constants for respectively the clusters and rays.

$$\overline{\beta_{k,i}^2} = \overline{\beta_{0,0}^2} e^{\left(\frac{-T_i}{\Gamma}\right)} e^{\left(\frac{-\tau_{k,i}}{\gamma}\right)} \tag{2.28}$$

This model presents the fundamental concepts still used today; however, when it was introduced, computer power was not sufficient to implement it. To simplify the model, a different type of model was developed.

2.4.3 Tapped Delay Line

This model is developed within the framework of GSM development, dividing the CIR into a limited number of paths. The spacing between two paths is determined by the available bandwidth. Eq. (2.29) presents the definition of the CIR in the TDL model, where N represents the number of taps or paths in the response, and $g_i(t)$ and τ_i are, respectively, the amplitude and the delay of the i^{th} path. The path amplitudes evolve and follow distributions that depend on the characteristics of the radio channel.

$$h(\tau, t) = \sum_{i=1}^{N} g_i(t)\delta(\tau - \tau_i) \tag{2.29}$$

This model was compatible with the computer processing speeds and the material simulation capabilities of the 1900s and was first introduced in the COST207 [11] channel model for GSM. In this model, the amplitudes follow a Rayleigh distribution that varies according to a Doppler spectrum. The model categorizes the environment into three categories:

1. Rural area, where the PDP is modelled with one cluster having a maximum number of 6 taps.
2. Urban, the PDP is modelled with one cluster having a maximum number of 12 taps with a reduced version of 6 taps.
3. Hilly urban, the PDP is modelled by two clusters, having a maximum number of 12 taps.
4. Hilly, the PDP is modelled by two clusters, having a maximum number of 12 taps.

This model represents the first example of a TDL model used in mobile communication. It retains the main ideas developed by the SV model but adapts them to the computational power available at that time. This modelling concept was utilized for

fifteen years and is still used in various projects such as the 3GPP [12] and IMT2000 [13]. An illustration of this concept can be found in Fig. 2.10.

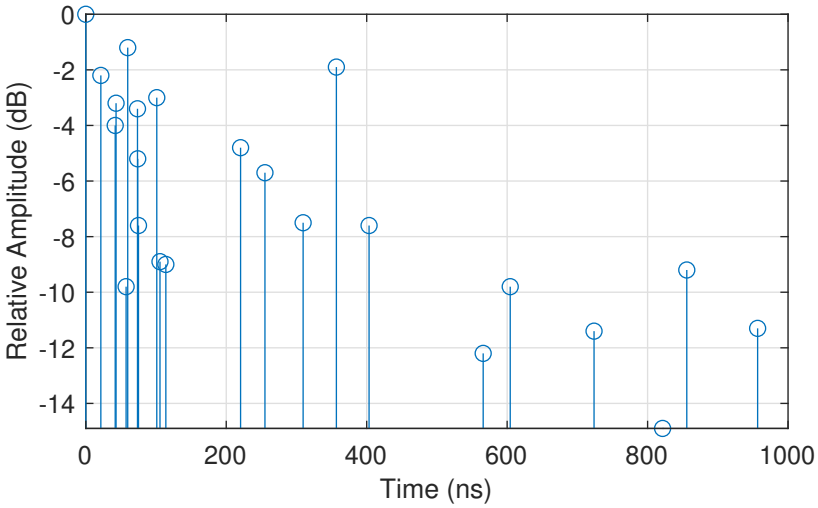

FIGURE 2.10: TDL model B from 3GPP 39.801 v17.0.0 [12].

However, while this model simplifies and facilitates implementation, it categorizes environments into specific cases, which can limit its applicability. Additionally, each environment is represented by a single PDP with a restricted number of paths, further constraining the model. Finally, with the emergence of MIMO technology, limitations in existing models became apparent, necessitating the development of directional models.

2.4.4 Double Directional Model

The MIMO technique enhances communication link coverage and throughput by employing multiple antennas at both the Tx and the Rx sides. To accommodate this advanced technique, channel models that incorporate antenna diversity needed to be developed. One such model, the double directional model introduced in 2001 [14] was designed with this objective. All the concepts presented above focus on modelling the time-dependent CIR or PDP. These time-dependent functions represent the summation of all components travelling from the Tx antenna to the Rx antenna. However, the propagation channel can be viewed as having a dual angle dependency, originating from both the Rx and Tx perspectives. Eq. (2.30) presents the formula which links the double directional CIR $h(\tau, t, \theta_R, \theta_T)$ and the time-dependent CIR $h(\tau, t)$, where $G_R(\theta_R)$ and $G_T(\theta_T)$ represent the complex antenna pattern at the Rx and Tx, respectively.

$$h(\tau, t) = \int_{-\pi}^{\pi} \int_{-\pi}^{\pi} h(\tau, t, \theta_R, \theta_T) G_R(\theta_R) G_T(\theta_T) d\theta_T d\theta_R \tag{2.30}$$

In practical cases, the propagation channel is modelled as N paths, each characterized by its excess delay τ_k and complex amplitude, $H_k e^{j\psi_k}$. The number of paths, denoted as $N(t)$, can vary over time depending on measurements. Additionally, each Angle of Departure (AoD) is associated with an AoA, allowing the function $h(\tau, \theta_R, \theta_T)$ to be expressed as shown in Eq. (2.31).

$$h(\tau, \theta_R, \theta_T) = \sum_{k=1}^{N} H_k e^{j\psi_k} \delta(\tau - \tau_k)\delta(\theta_R - \theta_{R,k})\delta(\theta_T - \theta_{T,k}) \tag{2.31}$$

Moreover, this model considers the polarization of the antenna. Although the cross-polarization factor is not directly introduced in [14], it is presented in International Telecommunication Union (ITU) [15] report just after the introduction of this model. Eq. (2.32) presents the antenna contribution to the CIR matrix, denoted as $\mathbf{A}_{u,s}$, where u represents the u^{th} Rx antenna element and s represents the s^{th} Tx antenna element. Additionally, this equation uses the antenna pattern for each element on Rx side, $F_{rx,u,V}(\phi)$ and $F_{rx,u,H}(\phi)$ for vertical and horizontal polarization, respectively, along with its counterpart on the Tx side, $F_{rx,u,V}(\phi)$ and $F_{rx,u,H}(\phi)$. The cross- and co-polarization factors, noted α_{VH}, α_{HV} and α_{VV}, α_{HH}, respectively, are also used, where H and V represent the horizontal and vertical polarization, respectively.

$$\mathbf{A}_{u,s} = \begin{bmatrix} F_{rx,u,V}(\phi) \\ F_{rx,u,H}(\phi) \end{bmatrix}^T \begin{bmatrix} \alpha_{VV} & \alpha_{VH} \\ \alpha_{HV} & \alpha_{HH} \end{bmatrix} \begin{bmatrix} F_{tx,s,V}(\phi) \\ F_{tx,s,H}(\phi) \end{bmatrix} \tag{2.32}$$

This approach can be integrated into the TDL view to form the Cluster Delay Line (CDL) model. Angular information is then introduced with a Laplacian angular distribution within the cluster. Paths inside a cluster are generated to match the appropriate intra-cluster angular spread in both azimuth and elevation. Similar to the TDL model, this model has some limitations [16], such as the frequency selectivity of the wireless channel and weak consideration of mobility and time variability when the channel changes rapidly, especially in scenarios with a high building density.

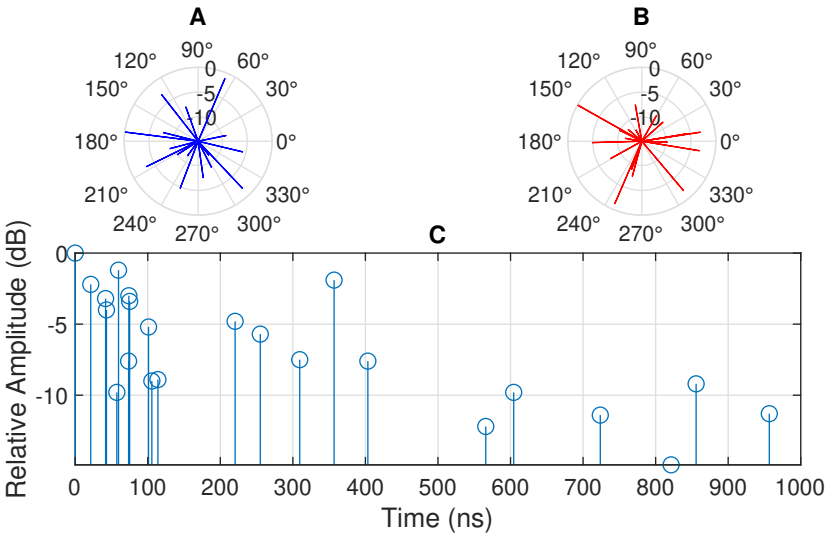

FIGURE 2.11: Illustration of CIR of CDL model (C), with for each cluster the AoD (A) and AoA (B).

This model is used in standardization bodies such as the ITU or 3GPP standard because it enables a broad representation of the channel through simulated propagation scenarios. However, a significant limitation of this model is the challenge of accurately matching the distribution of measurement data.

2.4.5 Geometric Stochastic Channel Model

The GSCM was first introduced by COST Action 259. The initial idea behind this model is to combine MPCs from the same scatterers within a single cluster. The model addresses scatterers, allowing for a flexible approach that ranges from a simple theoretical framework to a complete reproduction of real channels [17]. These MPCs can be obtained through geometrical construction simulations, which include their characteristics. Within the simulation scene, the number and the position of the clusters and isolated reflectors are statistically determined, and each simulation of the channel represents a different propagation scenario. The cluster principle of the model is presented in Fig. 2.12.

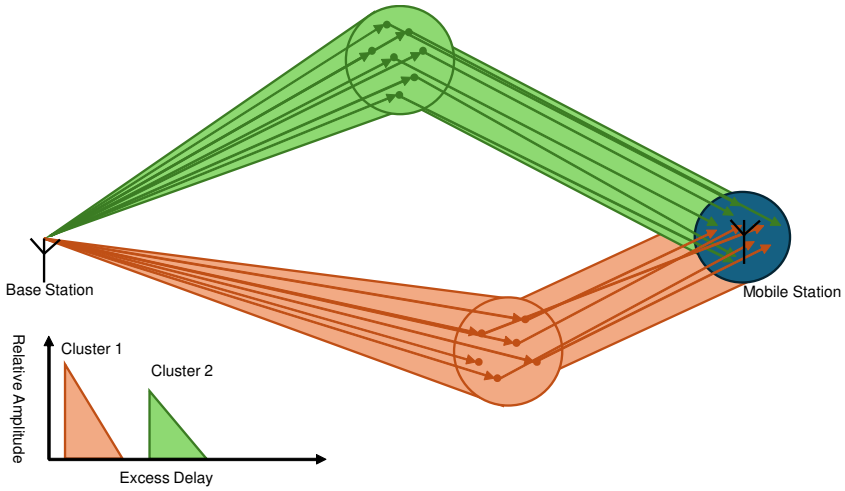

FIGURE 2.12: GSCM model and cluster principle.

To illustrate the current use of the channel model concept introduced before, the next section will present examples of channel models from the standardization bodies. The first is the well-known 3GPP, and the second is the ITU.

2.4.6 Example of Channel Model in Standardization

2.4.6.a 3rd Generation Partnership Project channel model

The 3GPP [12] is a group that proposes a technical framework for 3D channel models spanning from 0.5 to 100 GHz with an available bandwidth up to 10% of carrier frequency. In this framework, all the concepts presented previously are included. The 3GPP divides the environment into 4 categories, each of which is further divided into LOS and NLOS scenarios:

1. Urban Micro-cell (UMi)-street canyon and Urban Macro-cell (UMa) represent the urban micro and macro-cell environments, respectively. The main differences between them include cell size, the intersite distance, and the base station antenna height.

2. Indoor-office environments are categorized into two types: open office and mixed office. The primary difference between them lies in the LOS probability.

3. Rural Macro-cell (RMa) represents the rural macro-cell scenario, characterized by a maximum frequency of 7 GHz. It shares similarities with the UMi and

UMa scenarios in terms of Base Station (BS) characteristics such as antenna height and cell size but typically features a larger intersite distance.

4. Indoor Factory, which represents the environment inside factories with varying levels of machinery and assembly lines. This scenario is typically categorized into five levels of density, ranging from low to high, with corresponding variations in the installation heights of base stations.

The Fig. 2.13 illustrates the procedure for generating the channel coefficients in the stochastic channel model, considering antenna characteristics and multiple interactions. However, the exact locations of MPCs cannot be determined solely by geometric considerations.

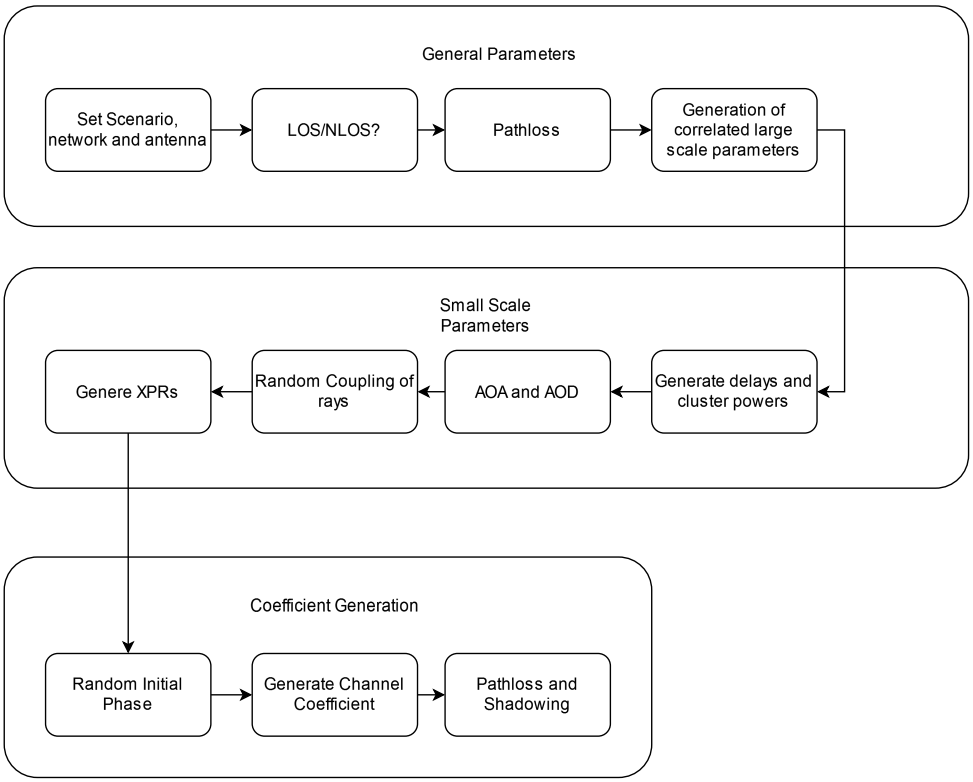

FIGURE 2.13: 3GPP procedure to generate channel coefficient for the fast fading model.

In this case, the cross-polarization coefficient is modelled as a variable generated for each ray that follows a log-normal distribution, while the co-polarization factor is modelled only as a phase variation during propagation.

Moreover, the 3GPP proposed models for link-level evaluation include two types: first, the CDL models, which characterize the propagation channel for frequencies from 0.5 to 100 GHz and with a maximum bandwidth of 2 GHz. Unlike previous models, CDL models are divided to represent different NLOS channels for CDL-A to C and LOS channels from D to E. To estimate the channel coefficient from this model, the last step in the Fig. 2.13 must be replaced with the CDL parameters. In this model, each cluster comprises several rays with angular dependency, but the cluster size is small, and each cluster tap represents an area with closely spaced rays, each with different AoA and AoD.

The second type of model used for simple evaluation is the TDL model. Like CDL, it operates within the frequency range of 0.5 to 100 GHz, with a maximum bandwidth of 2 GHz. The TDL model is also divided into three categories for NLOS and two for LOS scenarios. In all cases, the Doppler spectrum of each tap follows a classical spectrum shape with a maximum shift of $F_D = \frac{\overline{v}}{\lambda}$, where $\overline{v}$ represents the speed vector.

For LOS scenarios, the first tap has a fading distribution that follows a Ricean distribution with a specified K-factor, while the other taps follow a Rayleigh distribution. In NLOS scenarios, all taps follow a Rayleigh fading distribution.

2.4.6.b IMT Advanced Channel Model

The IMT-Advanced channel model [15] is developed by the ITU but at a lower frequency than the 3GPP until few GHz. But as the 3GPP divide the environment into different cases and for each case, the distinction between LOS and NLOS visibility is made. The environment is divided into different areas, presented in the following:

1. Indoor Hotspot (InH) focuses on the smallest cell and high user throughput in buildings.
2. UMi represents an urban area where the base station and the users are outdoors located and below the tops of the surrounding buildings. This scenario also includes the outdoor-to-indoor part.
3. UMa represents the typical urban area with a base station located above the surrounding building, which has over four floors. The density and the height of the buildings are homogenous in this area.
4. RMa represents propagation in large areas with low building density. The height of the base station antenna is typically higher than the average building height. In this scenario, the user can reach a speed in the range from 0 to 350 km/h
5. Suburban Macro-cell (SMa) represents a wide coverage area, where the base stations are located above the rooftops.

The procedure to obtain the channel coefficient is like the 3GPP and presented in Fig. 2.13. As for the 3GPP version, the cross-polarization is considered as a factor following a normal distribution. Moreover, a CDL is also proposed but only used for calibration purposes and not for a link-level evaluation as for the 3GPP.

2.4.6.c Differences

To conclude, the channel model proposed is derived from the concept presented in this section. The differences between both models are various but centered into similar points such as the area division, the maximal carrier frequency and velocity. For example, the IMT-Advanced model allows a high-speed scenario with speed until 350 km/h but a frequency below 6 GHz.

2.5 Conclusion

In this section, the fundamentals of radio channel propagation are presented, starting from the theoretical case of free-space propagation to multi-path propagation and its physical interactions. These physical interactions can be analyzed by solving Maxwell's equations, which involve several time computations to obtain the final

electromagnetic field. Nonetheless, geometric optics can simplify these interactions, reducing complexity and allowing wave propagation to be approximated with rays. Several ray-based simulators exist and can be used in various environments. The first is the Matlab ray tracing tool, which uses open data from Open Street Map (OSM) to generate scenes with buildings. Another example is NYUSIM implemented by the New York University [18]. As engineering tools for coverage, Siradel and Altair WinProp ray launching simulators can also be cited. Other ray-based simulators have been developed for railway simulations, such as Rap Lab [19], and Cloud RT [20], developed by Beijing Jiaotong University, which is the primary simulator used for railway environment characterization.

Once the physical basics are introduced, the mathematical foundations presented by Bello are discussed. First, deterministic functions are introduced, allowing for the representation of the CIR and CTF in the time and frequency domains, as well as their dual in the Doppler domain. These functions are applicable in stationary areas, where the WSS-US assumption holds. This assumption validates the fact that different MPCs have their own Doppler shifts and scattering characteristics.

Moreover, this assumption allows the introduction of the Bello stochastic function and special cases used to characterize the distance evolution of the channel, such as the PDP, and its associated RMS DS, as well as the scattering function and the associated Doppler spread, to name a few.

From these functions, modelling concepts are then presented, including path loss modelling and its different scales, the GSCM, the clustering principle of the SV model, and the double directional model. Two well-known standard models, IMT-Advanced and 3GPP, are then introduced, building upon the previously presented concepts.

To develop such stochastic channel models, it is necessary to measure the radio propagation channel by the means of CS. The next chapter will introduce the various methods for performing channel sounding and provide a state-of-the-art overview of CS operating at 60 GHz and its associated measurement results.

3 Measuring the Radio Propagation Channel at 60 GHz

Contents

3.1 Introduction

3.1.1 Channel Sounding Evolution

The modelling of radio propagation channels is an important issue in the development of wireless communication systems. Before modelling the radio channel, it is necessary to perform a measurement, known as channel sounding, to extract the channel characteristics. Thanks to the evolution of the capabilities of the measuring equipment, the modelling of radio channels has evolved considerably in terms of the number of estimated characteristics. From measuring only received power in the 1960s, to space-time directional propagation characteristics in the 1990s with the development of the MIMO architecture. The channel sounders have changed, and the environment and measurement scenarios have also changed from macro cells to micro-cells, especially for indoor propagation.

These changes can also be seen in the mmWave band, where the frequency ranges from 30 GHz to several hundred GHz. The available environments for such systems vary from indoor office environments to outdoor V2V links with the deployment of 5GNR and then the 6G standard. Despite this, the theoretical channel search techniques have not changed over time.

The techniques for performing channel sounding are varied, from those that are easy to implement to those that require the processing of the received signal to obtain either the CIR or the CTF of the radio propagation channel. The simplest and oldest way to measure the CIR is the pulse technique, then to increase the bandwidth without adding heavy equipment it is possible to use a Radio Frequency (RF) instrument such as a spectrum analyzer or a Vector Network Analyzer (VNA) with sufficient dynamics.

To overcome the limitations of using such systems, it is possible to directly use a data sequence also known as a Pseudo Random Sequence (PRS).

In addition, PRS techniques have some limitations, such as Doppler estimation at relatively high speeds. To overcome these issues, it is possible to use some advanced techniques with different sounding sequences that provide the CTF of the radio propagation channel. These advanced techniques mainly use Wiener inversion to compute the CTF, where the transmitted spectrum is compared to the received spectrum.

Finally, with the development of 5G and beyond, communication standards at 60 GHz are provided, and COTS can be found based on this communication standard. This type of equipment can be used to perform channel sounding at a lower cost than developing a complete architecture.

An overview of existing measurement results at 60 GHz is then presented.

These results allow the presentation of the different scenarios considered and validate the possible use of the CS to perform long-range dynamic measurements outdoors in a vehicular environment. Finally, the characteristics of the CS are summarized, and we discuss the possible use of existing CS for our objectives.

3.1.2 Channel Sounder Requirements for Dynamic Scenarios

In order to discuss the possible use of a CS, it is necessary to introduce the CS requirements for performing dynamic outdoor measurements in vehicular environment. Firstly, the dynamic scenario is defined by a relative displacement between the Rx

and the Tx. This means that both or one of the CS elements should be able to move at different speeds and distances. Moreover, the measure will be realized at mmWave frequency more precisely at 60 GHz and this implies some constraints that will be presented in this section.

3.1.2.a Scenarios Requirements

The first requirement for dynamic measurements in vehicular environments is the need for synchronization between the Rx and the Tx. In fact, the synchronization is necessary to provide absolute time to ensure a good measurement quality. In dynamic scenarios, the Rx and Tx cannot be connected by a cable carrying a reference signal. It is necessary to have an independent synchronization unit in both Tx and Rx, achieved by a clock of good quality, in terms of spectrum and phase stability for Doppler resolution. The phase stability can be achieved with an atomic clock such as a rubidium clock. However, another option is to use a Global Navigation Satellite System (GNSS) Disciplined Oscillator (DO) as the reference clock.

The recording time is an important factor when it comes to long-distance measurements. Indeed, in a vehicular domain, the communication link may last several minutes and pass through different environments. In order to correctly study these environmental changes, it is necessary to have a CS with a long recording time.

Finally, the dynamic range of the channel sounder is important for the realization of long-range measures. Indeed, vehicular communication implies to go along to short-range link and to estimate the maximum distance to ensure a link, it is necessary to have a CS able to measure distances higher than 100 m.

3.1.2.b Requirements for Measurements at Millimeter Wave Band

The measurements will be realized at 60 GHz and the size of the wavelength involved implies interaction with many obstacles in the environment. The first affected factor is polarization, so the CS must be able to perform measurements with polarization diversity.

Another feature to be measured is the Doppler. To measure it, it is necessary to perform measurements with a spatial sampling with a minimum value of $\lambda/2$, which results in a measurement every 2.5 mm minimum. Furthermore, the dynamic measurements imply speed, and the CIR rates must be high enough or adjustable to resolve the maximum Doppler shift.

Finally, the bandwidth is an additional feature, and it needs to be as high as possible in order to check all the features mentioned above.

3.2 Existing Channel Sounders at 60 GHz

3.2.1 Pulse-based CS

In the temporal domain, the first technique that can be explored is pulse emission. The idea behind this technique is to emit a pulse that is as short as possible in order to come as close as possible to a Dirac function.

In this technique, the distance resolution, the minimum distance between two MPCs, is linked to the pulse width as shown in Eq. (3.1), where τ_P represents the

pulse duration and c_0 the speed of light, and the maximum path distance can be estimated by the pulse repetition.

$$\Delta R = \tau_P c_0 \tag{3.1}$$

This type of CS makes it easy to measure the CIR of the radio propagation channel with a Digital Storage Oscilloscope (DSO). This technique is technologically limited by pulse generation and amplification. The amplification of short pulses requires a power amplifier capable of handling a high 1 dB compression point. Finally, this amplification problem limits the maximum distance range.

An example of a CS using the pulse technique can be found in [21, 22]. It allows a resolution distance of 3 m, resulting in a bandwidth of 100 MHz. The Rx of this CS is a DSO, which limits the data storage and the measurement time to 10 s.

3.2.2 Spectrum Analyser-based or Vector Network Analyser-based CS

3.2.2.a Spectrum Analyser

The Signal Source Analyzer (SSA) is an instrument capable of measuring the magnitude of a signal, i.e. the phase information is not available. In order to carry out a channel sounding, it is necessary to obtain the phase of the received signal to obtain information about the MPCs.

The author in [23] presents a method to estimate the phase from a magnitude measurement. The demonstration in [23], presents the argument of the CTF as a Hilbert transformation, $\mathcal{H}[\cdot]$, of the CTF magnitude, $H(j\omega)$ as presented in Eq. (3.2).

$$\arg[H(j\omega)] = \mathcal{H}[\log_e(|H(j\omega)|)] \tag{3.2}$$

The use of a SSA CS has the advantage of removing the synchronization module, since the measurement consists of measuring the magnitude of the received signal and estimating the phase. This equipment and technique was the basis of the VNA equipment. A last CS with a spectrum analyser and COTS was developed and presented in [24], which only measures the magnitude of the received signal up-and-down converted by the Vμbiq card.

3.2.2.b Vector Network Analyser

A VNA is an instrument capable of measuring the S-parameters of a device under test, called a Device Under Test (DUT). The DUT can be anything, from a coupler to an amplifier. The S_{21} parameter measurement between two antennas allows the CTF of the transmission path to be measured. The VNA works with the excitation signal swept in the band of interest.

In order to take into account the VNA effect, a calibration process is required. This calibration process can be different, from Over The Air (OTA) or Through Reflected Line (TRL) to Short Open Loss Termination (SOLT). These types of calibration are usually included on every VNA and in most cases a wire link is used, which can be difficult to realize at mmWave band. Once the calibration process is complete, the reference planes are established and the CTF of the VNA is measured.

The measurement of the radio propagation channel is then carried out by comparing the frequency response of the DUT, with the CTF of the VNA.

The VNA has the advantage of being able to measure the CTF of the radio propagation channel simply by only connecting its input and output to antennas. Moreover, there is no need to realize any additional up or down conversion, since everything is realized inside the VNA. Furthermore, since the calibration process is included in the VNA, there is no need to ask about power correction, the calibrated CTF is directly available. The final advantage of using a VNA is the ability to measure over a wide bandwidth, but with the assumption that the environment is static during the frequency sweep time.

[25, 26] is a basic example of VNA used for channel sounding. As mentioned above, MIMO systems are commonly used nowadays, this requires angular information of the radio propagation channel, which can be given with VNA system by adding multiple switched antennas as mentioned in [27, 28].

This setup has several limitations, starting with the low repetition rates that result in a slow measurement. The dynamic environments, for example where the channel changes rapidly, are not suitable for this instrument. Moreover, both antennas have to be connected to the instrument, which reduces the maximum measurable distance. To overcome this limitation, different architectures can be used, such as [29, 30] by using a VNA operating at a lower frequency, which reduces the wire attenuation, and adding a mmWave conversion unit. Another architecture replaces the wire link between the VNA and the mmWave converter with a fibre optic link as presented in [31]. The Fig. 3.1 shows the different architecture possibilities on VNA CS to increase the measurement range.

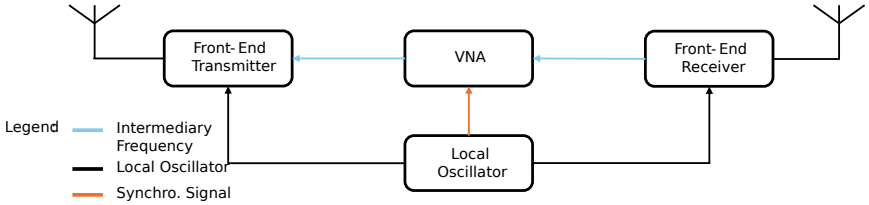

(A) VNA at a lower frequency with up and down converter to achieve the desired carrier frequency.

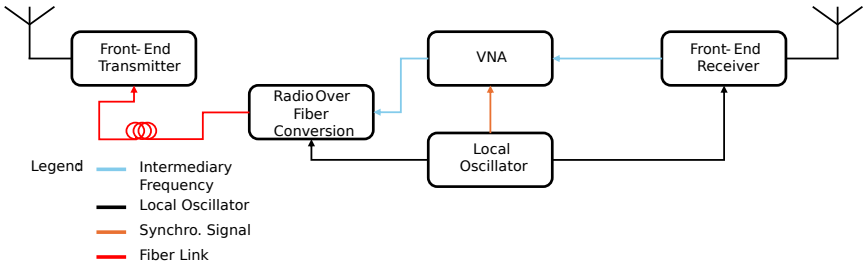

(B) VNA at a lower frequency with Radio-Over-Fibre link to increase the maximum measurable distance.

FIGURE 3.1: Different architectures of VNA CS to increase the measurement range.

3.2.3 Correlation Based

3.2.3.a Pseudo Random Sequence Correlation

This section presents the PRS technique and an overview of existing CS operating at 60 GHz. This technique exploits the good autocorrelation properties of random sequences. The PRS is modulated at the desired frequency, transmitted and then down-converted to compare with the transmitted sequence. The Fig. 3.2 presents the architecture of a CS using the PRS technique.

This technique is easy to implement from a hardware point of view. In fact, the PRS can be realized with a shift register that avoids the use of Arbitrary Waveform Generator (AWG), which can lead to the emission of a signal with a high bandwidth. As an example of a high bandwidth CS, the Italian CS presented in [32, 33] has a bandwidth of 5 GHz with carrier frequency translation, resulting in a bandwidth of 10 GHz. This technique of concatenating different bands to give a high bandwidth measure is also used in [34]. In addition, the CIR can be easily estimated with hardware (sliding correlation). However, this technique does not take into account the filter imperfection.

Several CS use this technique for different purposes in the literature. The first one is the Dual Polarized Ultrawideband Multi-Channel Sounder (DP-UMCS) developed by the Technical University of Ilmenau [35, 36]. Thanks to its dual receivers, this CS can be used in different bands and carry out polarimetric measurements.

There are several techniques for performing polarimetric measurements, the first is to use multiple receivers with a dedicated antenna on each, and the second is to use a phased array antenna as mentioned in [37, 38]. In this CS, the phased array has twelve elements active at the same time, resulting in a vertical beam of $\pm 10°$ and a horizontal beam of $\pm 45°$. The third possibility is to use an antenna array with different antennas to cover $360°$ in the azimuth plane and switch on one antenna to have only one receiver as mentioned in [39–43]. Moreover, this CS can perform elevation diversity measurements with the same antenna array by integrating between two antennas in the azimuth plane and a tilted antenna in the elevation plane.

Moreover, this technique can be used in different environments, such as vehicular, as presented in [44, 45], but this CS lack of recording time. This problem has been addressed by the Fraunhofer Institute, which has developed two CS, presented in [46, 47] and in [48]. Both architectures are home-grown, which increases the complexity for external use and also the overall price of the CS. Another university has developed a lower cost CS by using COTS and presented in [44, 45]. The use of COTS reduces the overall cost of the CS and allows measurements at 60 GHz to be realized in the vehicle domain as presented in the literature.

Finally, a hybrid architecture can be considered with an already developed CS [49] at a lower frequency with the development of a mmWave converter [50].

3.2.3.b Sliding Correlation Sequence

The Sliding Correlation Sequence (SCS) takes advantage of the auto-correlation properties of the same Pseudo Noise (PN)-sequence as for the PRS. The CIR are obtained by calculating the correlation between the transmitted PN-sequence and the received signal. The main difference between SCS and PRS difference is that the Rx of the SCS CS operates with a different clock frequency. The frequency between

the Tx and Rx is dilated by a factor k, this factor is defined as follows $k = \frac{f_{\mathrm{Tx}}}{f_{\mathrm{Rx}} - f_{\mathrm{Tx}}}$, where f_{Tx}, f_{Rx} are the clock frequencies of the Tx and Rx, respectively.

The advantage of this technique is its simple hardware implementation, which requires a shift register to realize the PRS and a DSO to store the obtained CIR analogously.

The CIR computation time with this technique is increased by a factor of k, due to the need to drift for a sounding period to measure all the MPCs. The characterization of the Doppler shift is then limited by the long time between two CIR, even if a solution can be found to increase it. As mentioned in [51], the authors present a maximum measurable Doppler shift of 25 kHz with $k = 5000$. The Fig. 3.2 presents the architecture of a CS using the PRS and the SCS techniques.

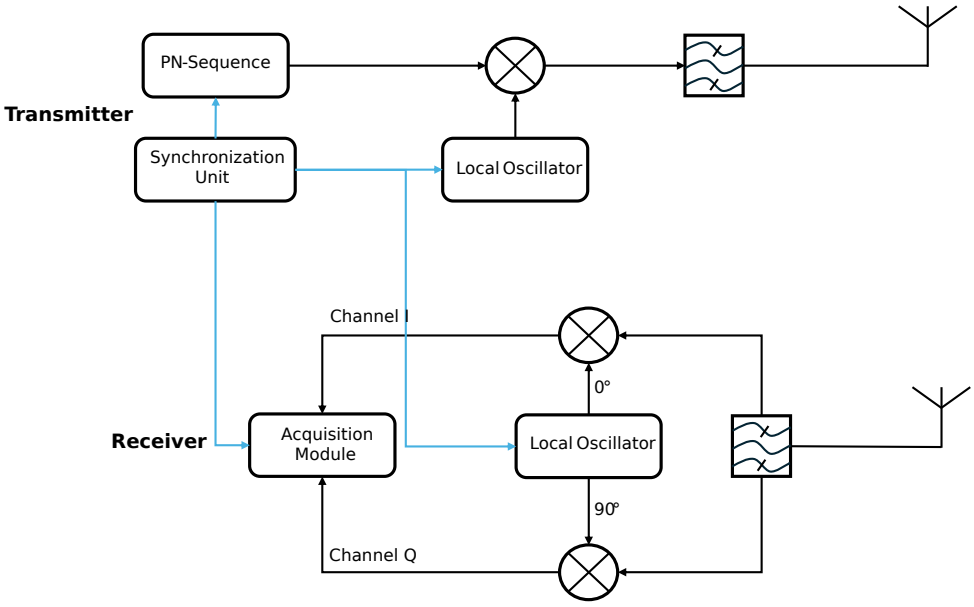

(A) Architecture for PRS technique.

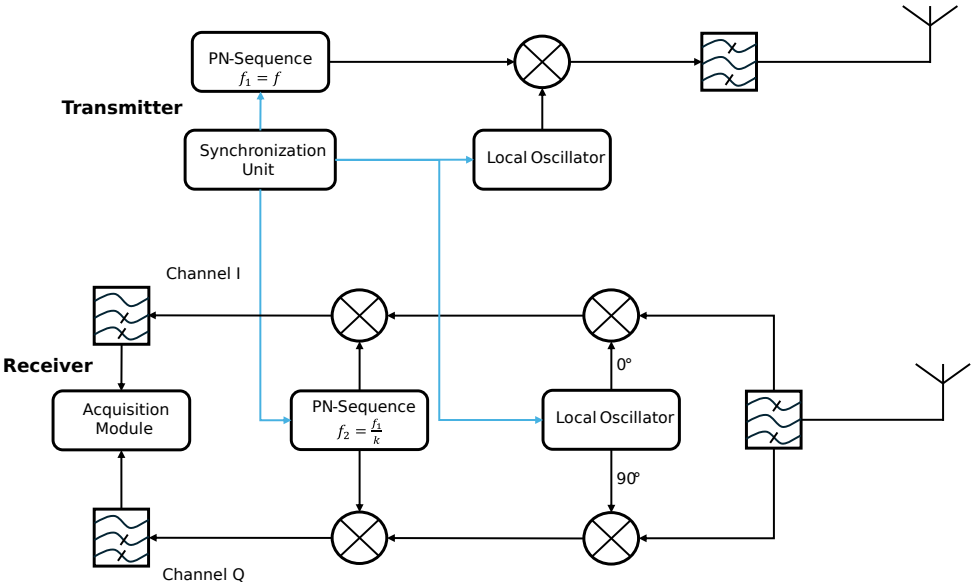

(B) Architecture for SCS technique with L is the code length and T_c is the bit duration.

FIGURE 3.2: Architecture comparison between PRS and SCS.

The second example of an existing CS using this technique is the New York University sounder can be cited [52], the k factor in this case is 20 000, but the Doppler cannot be extracted from the measurement data.

Nevertheless, a CS with a long recording time has been developed at the Rennes Institute of Electronics and Telecommunications (IETR) and presented in [51, 53], with a variable k from 1 000 to 100 000.

Finally, a last CS with a different architecture can be found in [54]. This sounder digitizes the Intermediary Frequency (IF) directly instead of the baseband signal, which makes it possible to increase the CIR rates.

3.2.4 Advanced Technics

As mentioned above, the main calculation in advanced techniques uses Wiener inversion. This computation compares the received spectrum with a spectrum obtained after the calibration process. This principle has the advantage of taking into account the effect of the different stages of the whole chain, from Tx to Rx.

In the literature there are two main sounding sequences, firstly the Frequency-Modulated Continuous-Wave (FMCW) or chirp signal, which has the advantage of having a perfect Crest Factor (CF) but a non-square spectrum. Instead of the unmodulated Orthogonal Frequency-Division Multiplexing (OFDM) signal, which is the second type of sounding sequence.

3.2.4.a Frequency-Modulated Continuous-Wave

The first type of sounding sequence is the FMCW, where the frequency of a Continuous Wave (CW) is swept for a limited time. This modulation, known as chirp, is defined in Eq. (3.3), where f_0 is the carrier frequency, Δf is the frequency step, and T_{chirp} is the signal duration.

$$s(t) = \exp\left[2\pi j(f_0 t + \Delta f \frac{t^2}{2T_{chirp}})\right], \text{ for } 0 \leq t \leq T_{chirp} \tag{3.3}$$

An example of a chirp signal with $T_{chirp} = 2$ µs and a bandwidth of 180 MHz can be found in Fig. 3.3. The chirp spectrum is flat over virtually the whole bandwidth, as seen in Fig. 3.3, there is ripple exists in every part of the birder spectrum. A way to overcome these limitations is presented in [55], where the authors realized a chirp signal with a higher bandwidth and filtered it to obtain a flat spectrum in the band of interest. Moreover, this CS is interesting because it is made of COTS components, which reduces the overall cost. The digitization of the transmitted and received signal is performed by a DSO, which limits the time recording, and the rotation motor of both antennas is controlled by an independent computer. However, the maximum measurement distance is limited by the lack of amplifiers in the Tx and Rx.

Another CS using COTS can be found in [56], the up and down conversion is done with SiversIMA components and the baseband signal is realized with a generator and digitized at the Rx side, with a Texas Instrument Analog to Digital Converter (ADC).

A final CS made with COTS can be found in [57]. The up-and-down conversion is realized using the Hittite HMC6450 device, which provides a full heterodyne structure

with variable gain chains on both sides. Another COTS card exists to realize this conversion and is presented in [58].

A homemade CS is developed by Durham University and presented in [59], which uses a version at a lower frequency and develops a mmWave up and down converter. In addition, in [60], the authors indicate that the Tx number is increased by two and the antenna at the Rx is rotated to obtain angular information.

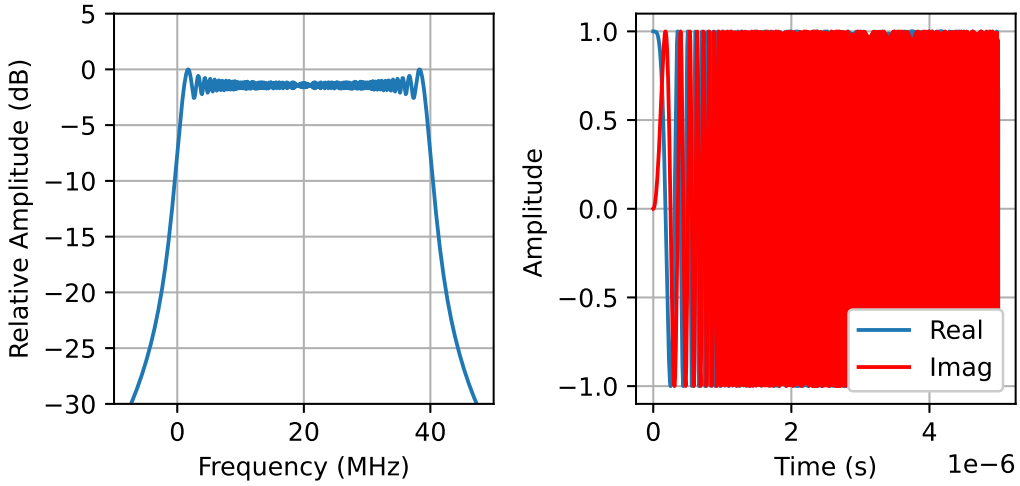

FIGURE 3.3: Chirp signal spectrum, on the left, and in the time domain, on the right.

3.2.4.b Orthogonal Frequency-Division Multiplexing

The principle is to sound the channel at different frequencies at the same time. To achieve this, the sounding sequence is made up of a summation of sinusoids with different phases and transmitted simultaneously on the Tx side. This type of sounding sequence is well-known in telecommunications and is called OFDM. The difference between the OFDM telecommunications signal and the sounding sequence is the absence of modulation in each subcarrier. The definition of the unmodulated OFDM sequence can be found in Eq. (3.4), where N_{tones} is the number of subcarriers, f_0 the carrier frequency, Δf the space between the subcarriers, ϕ_i is the phase of the i^{th} subcarrier and T_S is the duration of the OFDM symbol.

$$s(t) = \sum_{i=1}^{N_{\text{tones}}} \exp\left[2\pi j t \left(f_0 + i\frac{\Delta f}{N_{\text{tones}}} + j\phi_i\right)\right], \text{ for } 0 \leq t \leq T_S \tag{3.4}$$

An important parameter for the unmodulated OFDM signal is the CF, defined as the ratio of the peak amplitude to the RMS amplitude value. There are several techniques for increasing the CF, the most common of which is to use the phase value of the subcarrier. The best-known phase distribution is the Newman distribution, originally presented in [61] and defined in Eq. (3.5), which gives a CF of 2.

$$\phi_i = \frac{\pi\,(i-1)^2}{N_{\text{tones}}} \tag{3.5}$$

As a first example of CS using a OFDM technique is presented in [62], featuring a homemade architecture which allows it to characterize the radio propagation channel variously with different antenna configurations, up to ten, with different settings for the Doppler characterization, and with multi-band capability. Another home-grown architecture CS is being developed at the German Aerospace Center (DLR) and is called RUSK. This version was initially developed to perform measurements in the sub-6 GHz band, but an upgraded version was developed with a mmWave front-end to reach the 60 GHz frequency [63].

The CS made by the Tokyo Institute of Technology is presented in [64], built around COTS for up and down conversion and a baseband unit on each side, Tx and Rx to realize and digitize the sounding sequence. This CS has been upgraded to perform MIMO measurements with a COTS phased array, which divides the 360° azimuth plane into eleven and twelve for Tx and Rx, respectively [65]. Another CS built around COTS is presented in [66–68], with an updated version that integrates another Tx tilted in elevation for scenario need. This sounder has a limited maximum recording time of 3 s.

3.2.5 Based on Existing Communication Standard

With the development of the mmWave band for the communication system, an upgrade of the standard communication protocol is developed for these specific bands. One of them is the Institute of Electrical and Electronics Engineers (IEEE) 802.11ad which provides 6 different channels around 60 GHz with 2.16 GHz bandwidth. From this standard, manufacturers have developed COTS to realize communication systems in the mmWave band frequency. In the IEEE 802.11ad, a periodic beacon frame is planned to announce the presence of a Access Point (AP), and this periodic beacon can be estimated before it is transmitted. This beacon can be used to perform channel sounding at the mmWave frequency with a bandwidth of 2.16 GHz.

A first CS using this method is presented in [69]. The architecture of this CS is made with COTS set as an AP, for the Tx part, and the Rx is composed of a COTS down-converter connected to a DSO to store the radio channel CTF.

Another example of a CS using the IEEE 802.11ad standard is presented in [70]. This CS, also known as Terragraph Sounder (TS), has an antenna array consisting of 36 RF feeders in the azimuth plan for 8 distributed antennas in the elevation plan. The TS can perform channel sounding, interference analysis with the possibility to beam custom for nulling, and performance analysis of a 60 GHz link at a maximum distance of 440 m.

3.2.6 Discussion

In this section, the different CS operations have been presented. In each case, examples of existing CS operating at 60 GHz have been presented. Finally, the required features presented before are synthesized in the Tab. 3.1 and Tab. 3.2.

The first conclusion of this survey is the variety of existing CS, with different operating systems at 60 GHz. However, the first limitation of the CS for our purposes is the inability to perform independent external synchronization.

Of the remaining CS, another limitation is the inability to perform dynamic measurements with a resolvable maximum Doppler shift high enough to cope with the measurement speed. Furthermore, this overview shows the lack of CS available

for long recording time, for most of them the maximum recording time is limited to less than one minute, which is not suitable for our purpose.

Finally, if a CS ticks all the boxes as for the RUSK, the limitation comes firstly to the diversity polarization ability. Secondly, the possibility of setting and using it to measure in our way for our purposes.

TABLE 3.1: Comparison settings of the presented CS for pulse and instrument based category.

CS type	**Reference**	**University**	**Bandwidth**	**Tx-Rx Synchronization**	**Dynamic Measurement**	**Tx Antenna**	**Rx Antenna**
Pulse	[22]	Technical University of Athens	100 MHz	Linked	No	1	1
Pseudo Random Sequence	[35, 36, 71–76]	Technical University of Ilmenau	4-7 GHz	GNSS DO	No	2 Parallel	2 Parallel
	[37, 38]	NYU Tandon School of Engineering	1 GHz	Linked	No	1 Beamforming	1 Beamforming
	[39–43, 77–84]	National Institute of Standards and Technology	2 GHz	GNSS DO	Yes	1	8 by elevation angle Commutable
	[46, 47, 85–88]	Fraunhofer Heinrich Hertz Institute	250 MHz	GNSS DO	Yes	2 Parallel	2 Parallel
	[48, 89]	Heinrich-Hertz-Institut	1 GHz	Independent LO	Yes	1	1
	[44, 45, 66, 90–97]	Brno University of Technology	4 GHz	GNSS DO	Yes	1	1
	[32, 33, 98]	University of L'Aquila	5 GHz	Linked	No	1	1
	[49, 50]	Elektrobit OY, Espoo	100 MHz	GNSS DO	Yes	1	1
	[34]	Siemens VDO Automotive AG	5 GHz	GNSS DO	No	1	1
Sliding Correlation	[52, 99, 100]	New York University Tandon School of Engineering	800 MHz	Independant Synchronized Sources	No	1	1
	[51, 53, 101]	INSA Rennes	500 MHz	Linked	No	1	1
	[54]	University of Vigo	500 MHz	GNSS DO	No	1	1

TABLE 3.2: Comparison settings of the presented CS for correlation, advanced technics and based on existing communication standard.

CS type	Reference	University	Bandwidth	Tx-Rx Synchronization	Dynamic Measurement	Tx Antenna	Rx Antenna
VNA	[25, 26]	Delft University of Technology	5 GHz	VNA	No	1	1
	[27, 28, 102–105]	Quebec University in Outaouais	7 GHz	VNA	No	1	1
	[29–31, 106]	Aalto University	4 GHz	VNA	No	1 with Rotator	1
	[107]	Helsinki University of Technology	3.5 GHz	VNA	No	1 virtual array	1
	[108]	Cartagena University	9 GHz	VNA	No	1 virtual uniform rectangular array	1 virtual uniform linear array
	[109]	Orange Labs	2.047 GHz	VNA	No	1	1 with Rotator
	[110]	Brno University of Technology	10 GHz	VNA	No	1	1
	[111]	Huawei Technologies Co.	2 GHz	VNA + wire extension	No	1 with Positioner	1
SSA	[23, 112]	Brno University of Technology	8 to 10 GHz	Not Needed	No	1	1 with Rotator
FMCW	[10, 59, 60, 113–117]	Durham University	2.2 to 6 GHz	DO	No	2 parallel	2 parallel
	[56, 118]	The University of Auckland	1 GHz	Linked	No	1	1 with rotator
	[57]	SINTEF	368.4 MHz	GNSS DO	No	1	1
	[55]	Mondragon University	2.16 GHz	Linked	No	1 with rotator	1 with rotator
	[58]	Gustave Eiffel University	1.2 GHz	GNSS DO	No	1	1 with rotator
OFDM	[62, 119]	Orange Labs	250 MHz	GNSS DO	No	1 with rotator	1 with rotator
	[64, 65, 120–122]	Niigata University	400 MHz	GNSS DO	No	4 with beamforming on each	4 with beamforming on each
	[66–68, 123, 124]	Technological University of Vienna	500 MHz	Linked	Yes	2	1
	[63, 125–128]	DLR	120 MHz	GNSS DO	Yes	1	1
	[24]	University of Bedfordshire	1 GHz	Linked	No	1	1
Communication Standard	[69]	2.5 GHz	N.A	No	1 with 6 antennas (COTS)	1	
	[70, 129–140]	Facebook Terragraph Radios	2.16 GHz	N.A	No	36 × 8 parallel	36 × 8 parallel

3.3 Existing Measurement Results at 60 GHz

This section introduces the characteristics of the radio propagation channel at 60 GHz will be introduced. First, a comparison between a lower frequency and 60 GHz is presented, which results in a sparser channel. Then, the necessary parameters to realize a channel model extracted from measurement campaigns are presented.

Moreover, some results highlight the clustering and fading models. The fading models are specially made for 60 GHz radio channel propagation, in which there are two main components. The two main components are the main one, which is the LOS when it exists, and a reflected one in a close scattering such as a road, for the vehicular domain.

Finally, the sparsity of the radio channel at 60 GHz is mainly explained by the higher power losses due to the higher frequency and also by the oxygen peak absorption. To overcome this problem, several techniques are presented in the literature.

3.3.1 Sparsity of the 60 GHz Radio Channel Propagation

The first element that differs at 60 GHz from lower frequencies, is the sparsity of the radio propagation channel. Indeed, in [74], the authors present a measurement in a vehicular environment, in a "T" intersection. The measurements are performed at 6 and 60 GHz and the influence of different elements of the environment is studied with an azimuth scan on both sides, Tx and Rx. The PDP with a fixed dynamic over the distance is presented and shows that it is richer at 6 GHz than at 60 GHz. Also, some scattering is only visible at 6 GHz.

This conclusion also holds at higher frequency. In fact, in [73], the authors present another measurement in a vehicular environment at 6.75, 30 and 60 GHz with and without blockage with different cars. The measurements are also performed with a full azimuth scan at both Tx and Rx sides. From these measurements, the synthetic omnidirectional PDP is presented at both frequencies and shows that some scattering is present at 6.75 GHz but absent at mmWave frequency. There are also no scatters between 30 and 60 GHz. Finally, the power bi-azimuth profile is calculated by integrating the received power in the delay domain for each combination of Tx and Rx scan directions at 6, 30 and 60 GHz is presented. This plot shows an increasing sparsity with increasing frequency.

Another measurement campaign made at 38 and 60 GHz is presented in [100]. Two measurements are realized: a peer-to-peer link in a pedestrian walkway, following the same procedure as above and a cellular network. In the first measurement, the Rx is placed at 10 localizations and the power angle information is examined, resulting in different MPCs due to the walkway environment allowing multiple reflections. This is in contrast to the second measurement, where the Tx is placed at the top of a 6-storey building, and the Rx is placed at the ground level. In these measurements, an azimuth scan is also performed to characterize the different AoA and AoD of the scattering. The results are presented as a scatter plot of the Rx and Tx azimuth angles that resulted in successful links, and show the presence of scatter at 38 GHz that is not present at 60 GHz.

A measurement campaign at different frequencies has been carried out in [65]. The measurements were made in two typical urban environments, UMi and UMa. An example of the results is made at a specific position in the UMa environment is made, with azimuth scans at both Tx and Rx. From this measurement, the azimuth delay power spectrum is plotted on both sides and shows, again showing the sparsity evolution of the channel as the frequency increases.

Even in a vehicular environment, the radio propagation channel is sparse, as presented in [123]. Indeed, the measurement in the campaign took place in a city street, with two Tx placed on the top of a car and the Rx placed at the same level as a traffic light. From the measurements, the Local Scattering Function (LSF) is shown at different measurement times and shows how sparse the channel is.

Finally, a measurement at different frequencies is presented in [119], where the authors use the CS developed by Orange to investigate the impact of antenna aperture on the channel for outdoor environments in urban scenarios. The carrier frequencies of the measurements are 17 and 60 GHz, and the measurements were performed at the Orange campus in Belfort, France. In this campaign, several positions are investigated for different distances in both LOS and NLOS situations. The conclusion is made by comparing the azimuth-delay power profiles for both frequencies and confirms the sparser radio channel propagation at 60 GHz than at 17 GHz.

3.3.2 Parameters of the 60 GHz Radio Channel

3.3.2.a Stationarity

Before presenting the different parameters of the 60 GHz radio channel, it is necessary to introduce the size of the stationary area derived from the measurements. In fact, as mentioned earlier, the small-scale parameters are derived from a stationary area. This stationary area can be determined in several ways. The first possibility is to use the Pearson coefficient as presented in [97]. This coefficient is calculated with the PDP, which is calculated on a lower range, most commonly a dozen wavelengths. This coefficient computed in [97] for a dynamic vehicle scenario in which two cars, with the Tx and Rx placed on the roof of each, pass each other. Once the Pearson factor has been calculated, it is necessary to set a threshold below which the radio propagation channel is no longer stationary. In this paper, the threshold is set at 0.5. The average stationary time for seven passes is 50 ms, which gives 140λ at a speed of 50 km/h as mentioned in the paper.

3.3.2.b Received Power

The first large-scale parameter estimated is the power evolution as a function of the Tx-Rx distances, known as PL. The first example of a measurement where the PL is estimated, can be found in [117]. The outdoor measurements in this paper have been performed with co and cross-linear polarization with different Tx-Rx distances up to 60 m. The first investigation is made around the received power as a function of the AoA, which shows that there is no real indication that the environment affects the polarization.

In [141], the authors present a measurement made in an outdoor environment at various distances, with a maximum value of 200 m. From these MIMO measurements, the PL is modelled with a path loss exponent of 1.93 which is lower than the free space due to the corridor environment of the measurements.

Another campaign is realized in [85] in the City Center (CC) environment for Open Square (OS), Street Canyon (SC) and Residential Area (RA) scenarios. The PL is modelled with the ABG model, where in this case γ is equal to zero, and α is the mean losses at the reference distance d_0 equal to 1 m. All the results for PL can be found in Tab. 3.3. It can be seen that the PLE is very close to the FSPL under the LOS condition.

Table 3.3: PL model obtain from measurements in [85].

Scenario	Condition	$\alpha(d_0)$	β (dB)	σ (dB)	Validity Range (m)
OS-CC	LOS	69.2	1.88	1.03	5-50
SC-CC	LOS	67.0	2.13	2.03	5-50
SC-RA	LOS	67.0	2.07	2.53	10-210
	NLOS	69.7	2.67	4.93	10-80

In [52, 100], a V2I link in a car park and Peer-To-Peer (P2P) link in an urban area and pedestrian Pathway (PT) environment are investigated. The PL is estimated for each environment, following the ABG model where, α is the FSPL value at the reference distance of 3 m, γ is equal to zero and β is estimated with the measured data as σ for the shadowing value. All the results are presented in Tab. 3.10.

TABLE 3.4: Value obtain for path loss estimation and delay spread for measurement performed in [52, 100].

Scenario	Visibility Case	β	σ (dB)	$E[\sigma_{RMS}]$ (ns)
Vehicle	LOS	2.66	-	2.73
	NLOS	7.17	-	2.73
P2P	LOS	2.25	2	0.8
	NLOS	3.76	10.16	7.4
P2P PT	LOS	2.23	-	6.02
	NLOS	4.19	-	6.02

3.3.2.c Delay Spread

From the measurements made in [60], the RMS DS is extracted and the median value for each polarization is presented in the Tab. 3.5. The conclusion from the low RMS DS is that there is a presence of MPCs around the dominant received power, which is explained by the sparsity of the channel. This tendency towards low RMS DS is also confirmed by the measurements made in [117], where its median value is 12.3 ns for a noise threshold value and 7.5 ns for a calculation made with a threshold of 18 dB below the maximum component. Furthermore, in this case, the polarization has no real effect on the RMS DS.

TABLE 3.5: Power decay of cluster obtained from [60, 141].

Reference	Polarization Tx/Rx	median RMS DS [ns]
[60]	V/V	25
	V/H	19
	H/V	30
	H/H	40
[141]	-	0.6

The small value of RMS DS is also shown presented in [141] for a typical corridor outdoor environment, with a median value for a threshold of 20 dB, which is shown in the Tab. 3.5.

In [121], the authors present a measurement campaign to perform outdoor static measurements in the OS environment. From the measurement, some positions are extracted for investigation, and the angular delay power profile for each position is discussed. Furthermore, the RMS DS, Angular Spread Departure (ASD) and Angular Spread Arrival (ASA) are presented, resumed in Tab. 3.6, and compared with the 3GPP UMi model. The higher value of the ASD is explained by the environment, which is an open square area but with a low antenna height. In addition, the average value of the ASA is due to strong reflections in the environment.

TABLE 3.6: Presentation of the Small Scale Parameters (SSP) obtained from measurement in [121].

Parameter	μ	σ	3GPP UMi
RMS DS	31.06 ns	13.22 ns	27.01 ns
ASD	27.9°	4.95°	13.20°
ASA	29.29°	19.31°	38.65°

Another campaign in vehicular environment with a static CS is summarized in [67]. The goal is to investigate the impact of different categories of vehicles in a V2V link while varying distances up to 12 m. The RMS DS comparison between the two vehicles does not vary much, as shown in the Tab. 3.7. The increasing RMS DS for a truck is due to a larger reflector due to its larger size than a conventional car, which implies a higher MPCs number and an increase in RMS DS.

TABLE 3.7: Presentation of the RMS DS obtained for cars, and trucks in [67].

Vehicle	1 m	2 m	3 m	4 m	5 m	6 m	7 m	8 m	9 m	10 m	11 m	12 m
Car	3.7 ns	3.7 ns	3.7 ns	4.1 ns	3.7 ns	3.7 ns	3.6 ns	3.8 ns	4 ns	4.5 ns	4.3 ns	4.5 ns
Truck	3.2 ns	3.1 ns	3.5 ns	4 ns	4.1 ns	4.1 ns	4 ns	4.4 ns	5 ns	5.2 ns	5.2 ns	4.9 ns

Another type of vehicle is considered in the results presented in [68]. An SUV is added for comparison with the previous results. Also, the stationary time for the RMS DS calculation is slightly different than before, which explains the different results, but the conclusion for cars and trucks remains identical, such as presented in the Tab. 3.8.

TABLE 3.8: Presentation of the RMS DS obtained for cars, trucks, SUV in [68].

Vehicle	1 m	2 m	3 m	4 m	5 m	6 m	7 m	8 m	9 m
Car	2.6 ns	2.6 ns	2.9 ns	2.4 ns	2.2 ns	2.2 ns	2.2 ns	2.5 ns	2.7 ns
Truck	2.4 ns	2.1 ns	2.4 ns	2.5 ns	2.7 ns	3.3 ns	3.5 ns	3.2 ns	3.5 ns
SUV	2.5 ns	2.5 ns	2.9 ns	3.4 ns	3.2 ns	3 ns	3.1 ns	3.2 ns	3.5 ns

Nevertheless, the statistical parameters of the RMS DS are given for urban scenarios and environments like OS, SC are presented in [85] and summarized in the Tab. 3.9. A distance dependence of the delay spread is also presented and fitted with a linear regression as in the Eq. (3.6), where α represents the intercept, β the slope, and Γ a zero-mean random variable with a standard deviation of ϵ. The value for each parameter obtained from the measurement is presented in the Tab. 3.9.

$$\log_{10}(\frac{\tau_{RMS}}{1s})(d) = \alpha + \beta d + \Gamma_{\epsilon} \tag{3.6}$$

TABLE 3.9: Statistical Parameters of the RMS DS and fitting value of the distance dependency of the Delay Spread for various outdoor scenarios [85].

Scenario	**Condition**	μ_{DS}	m_{DS}	σ_{DS}
Open Square - City Center	LOS	26.5 ns	27.3 ns	16.9 ns
Street Canyon - City Center	LOS	26.6 ns	23.2 ns	19.1 ns
Scenario	**Condition**	α	β	Γ_{ϵ}
Open Square - City Center	LOS	-8.54	0.0322	0.262
Street Canyon - City Center	LOS	-8.13	0.0170	0.287

Finally, in [52, 100], the RMS DS of a V2I link in a parking lot and P2P link in an urban area and pedestrian PT environment are investigated. All the results are presented in Tab. 3.10.

TABLE 3.10: Value obtain for path loss estimation and delay spread for measurement performed in [52, 100].

Scenario	Visibility Case	$E[\sigma_{RMS}]$ (ns)
Vehicle	LOS	2.73
	NLOS	2.73
P2P	LOS	0.8
	NLOS	7.4
P2P PT	LOS	6.02
	NLOS	6.02

3.3.2.d Doppler Spread

In this section, the effect of the Doppler shift on the radio propagation channel extracted from measurement campaigns is presented. The first measurement, where a Doppler shift is performed, is presented in [67]. The setup of this measurement is presented in the previous section, with the presentation of the Delay Spread (DS) results. As mentioned before, the results are divided into two vehicle categories, cars, and trucks. In addition, the Doppler shift is rescaled with respect to the top speed and the results are presented in Tab. 3.11.

The results for distances below 4 m are mainly due to the phase noise of the equipment. However, between 7 and 8 m, the vehicles show the strongest effect on the Doppler shift. The difference in the Doppler spread between the two vehicles is mainly due to the larger size of the truck compared to the car, which leads to a higher dispersion and a higher number of reflected MPCs.

Finally, the Doppler spread decreases as the vehicles move away from the Rx. Furthermore, the Doppler spread is less than 12% of the maximum Doppler shift. This value can be compared to the value obtained with a typical Doppler spectrum, such as a uniform distribution which gives to a Doppler spread of 30% of the maximum Doppler, or a half-Jakes distributed Doppler which gives to 40%, and a Jakes distributed Doppler to a 70%. This observation led to finding another distribution to fit the Doppler shift distribution on this channel. It is important to note that this distribution is not discussed in the paper.

TABLE 3.11: Presentation of the Doppler spread obtain for cars and trucks in [67].

Vehicle	1 m	2 m	3 m	4 m	5 m	6 m	7 m	8 m	9 m	10 m	11 m	12 m
Car	90 Hz	85 Hz	90 Hz	110 Hz	125 Hz	150 Hz	150 Hz	140 Hz	125 Hz	125 Hz	125 Hz	125 Hz
Truck	150 Hz	155 Hz	210 Hz	160 Hz	190 Hz	160 Hz	140 Hz	150 Hz	150 Hz	130 Hz	100 Hz	125 Hz

The difficulty in finding the right distribution to fit the Doppler shift in a vehicle overtaking scenario is not the only effect on the radio propagation channel. Indeed, in [68], the authors present another Doppler effect on the power evolution. The frequency of power fluctuations, due to fading, is higher with the higher Doppler shift. This information leads to a very fast changing channel with high power fluctuation, which affects the communication link by reducing the data rates. In addition, this paper presents the Doppler spread obtained with another stationary time window with another type of vehicle, an SUV, using the same measurement campaign mentioned above. The results are presented in the Tab. 3.12. The conclusion with these results remains identical to the one mentioned before.

TABLE 3.12: Presentation of the Doppler spread obtained for cars, trucks, and SUV in [67].

Vehicle	1 m	2 m	3 m	4 m	5 m	6 m	7 m	8 m	9 m
Car	110 Hz	105 Hz	170 Hz	150 Hz	150 Hz	160 Hz	160 Hz	150 Hz	140 Hz
Truck	180 Hz	180 Hz	240 Hz	260 Hz	290 Hz	350 Hz	360 Hz	300 Hz	310 Hz
SUV	110 Hz	110 Hz	170 Hz	200 Hz	200 Hz	160 Hz	160 Hz	160 Hz	165 Hz

3.3.3 Extracted Model

3.3.3.a Cluster Modelling

In this section, cluster models extracted from measurement results are presented. As a first example, a measurement campaign made in [60] can be presented. These measurements are made in an outdoor environment at different distances, with a maximum value of 50 m. There are two routes in this measurement campaign, each with ten different positions for the Rx for both linear polarization, vertical and horizontal, respectively. These measurements show, first, that the vertical polarization has stronger delayed components and the power decay over the delay is used for each polarization with the following.

$$P_i = \alpha_0 - 10\alpha_1 \log(\tau_i) \tag{3.7}$$

where P_i is the average received power at delay τ_i, and α_0, α_1 are the model parameters. The result for each polarization can be found in the Tab. 3.13, it can be noted that the cluster power is normalized, which implies $\alpha_0 = 0$.

TABLE 3.13: Power decay of cluster obtain from [60].

Polarization Tx/Rx	α_1
V/V	5.3
V/H	4.9
H/V	4.0
H/H	3.1

In [121], the authors present a measurement campaign to perform outdoor static measurements in the OS environment. For all the positions, several cluster estimates obtained by the scattering process are presented, varying from seven to twelve. From this estimation, the cluster parameters are estimated and compared with a 3GPP UMi, and presented in the Tab. 3.14. The cluster RMS DS is lower from the measurement than from the 3GPP UMi model due to the sparsity of the radio channel at 60 GHz and from the MPCs extraction and clustering.

TABLE 3.14: Presentation of the cluster parameters obtain from measurement in [121].

Parameter	μ	σ	**3GPP UMi**
No. Clusters	$7 \sim 12$		12
Cluster RMS DS	0.45 ns	0.79 ns	5.00 ns
Cluster ASD	4.48°	8.98°	3.00°
Cluster ASA	10.73°	20.07°	17.00°

3.3.3.b Fading Model

This section highlights the different ways to model the fading extracted from the measurement campaign. As a first example, the measurements made in [65], present the fading evolution with a two-ray model. The two-ray model is set up with a simple Gaussian beam of the same half-power beam width as the measurement. This comparison shows similarity, but the PL are larger than the model for a small distance.

In an overtaking scenario in a vehicular environment, a new fading model can be adopted when a strong reflected signal is included in the main component due to physical interactions that cannot be distinguished due to the limited bandwidth of the equipment, as presented in [68]. The model, named Two Ways with Diffuse Power (TWDP), proposed a fading description with deterministic amplitudes of the non-fluctuating specular components, $V_1 > 0$ and $V_2 \geq 0$, with uniformly distributed phases, ϕ_1, and ϕ_2. Moreover, the diffuse components, $X + jY$, where $X, Y \sim \mathcal{N}(0, \sigma^2)$ are independent Gaussian random variables. The complex-valued baseband is represented in Eq. (3.8).

$$r_{\text{complex}} = V_1 e^{j\phi_1} + V_2 e^{j\phi_2} + X + jY \tag{3.8}$$

This fading is modelled with two parameters, the K-factor, describes the power ratio between the specular and the diffuse components.

$$K_{\text{TWDP}} = \frac{2V_1V_2}{2\sigma^2} \tag{3.9}$$

The second parameter is the Δ parameters, which describe the amplitude relationship among the specular components. This parameter is bounded between 0 and 1. If the parameter equals 0 that means the TWDP fading degenerates to Rician fading.

$$\Delta_{\text{TWDP}} = \frac{2V_1V_2}{V_1^2 + V_2^2} \tag{3.10}$$

The K-Factor and the Δ parameters obtained for cars, trucks, and SUVs are shown in the Tab. 3.15. The K-Factor shows a lower value when the vehicle is close to the Rx antenna, when the vehicle passes the Rx antenna then the LOS tap does not fade anymore, resulting in a high K-Factor. For the Δ, the size of the vehicle affects the evolution of this parameter, with a longer vehicle leading to a longer TWDP model. The zero value of the SUV at a small distance is due to a negative bias in the estimation of the parameter.

Nonetheless, it can be noted that the Akaike criteria is chosen to select a Rician fading or the TWDP. This criterion validates the use of a Rician fading in most cases after a certain distance, which depends on the size of the vehicle.

TABLE 3.15: Presentation of the TWDP parameters for cars, trucks and SUVs, obtained in [68].

Type	Vehicle	1 m	2 m	3 m	4 m	5 m	6 m	7 m	8 m	9 m
K-Factor [dB]	**Car**	28	31	34	37	42	42	43	43	43
	Truck	21	24	24	26	30	32	39	42	42
	SUV	26	25	32	35	36	37	40	42	42
Δ	**Car**	0.18	0.1	0	0	0	0	0	0	0
	Truck	0.25	0.1	0.2	0.2	0	0	0	0	0
	SUV	0.05	0	0.05	0	0	0	0	0	0

Moreover, the inclusion of the strong reflection from the moving vehicle in the main component, which in this case is the LOS, is presented in [66]. This paper presents the PDP and the LSF for two different cars and a truck. These figures show the absence of MPCs on the PDP, due to the moving vehicle. Instead of the LSF, where these components can be seen.

From the measurements presented in [87, 94], the most important second component in a 60 GHz link in a vehicular environment is the ground reflection. In fact, in [94], a measurement is performed with a Tx placed on the top of a car and a Rx placed on a room at the 6^{th} floor of a building. The direct optical connection between Tx and Rx is made by an angular motor controlled by a camera treatment. From these measurements, it appears that the second main component after the direct one is the component reflected from the street.

A similar conclusion can be drawn from the results presented in [87]. Indeed, a measurement campaign was carried out in an airfield and the path loss for a varying distance from 40 to 1000 m is presented. Then, the CIR are modelled with a two-ray model, taking into account the ground reflection factor and the oxygen absorption taken into account. The CIR model is presented in Eq. (3.11), where i selects the path and l_i the total length of the path. $G_i = \frac{\lambda}{4\pi l_i} 10^{\left(-\frac{l_i l_{Ox}}{1000 \cdot 20}\right)} R_i$ is the path gain with the oxygen absorption l_{Ox} in dB/km and R_i the ground reflection. In this case, the value of l_{Ox} that gives the best result is 14 dB/km.

$$h(t) = \sum_{i=1}^{2} G_i e^{\left(-\frac{2\pi j l_i}{\lambda}\right)} \delta\left(t - \frac{l_i}{c_0}\right) \tag{3.11}$$

In [95], two measurements are presented, the first is realized in a highway road with a static position for the CS. The Tx is placed on a bridge above the highway, and the Rx is placed on a tripod standing on the ground below the bridge. The second measurement represents a dynamic scenario in which two cars, on which the Tx and Rx are placed, pass each other. From these measurements, it can be concluded that the metallic body of the car also affects the fading distribution, without giving a real distribution to match this fading.

3.3.4 Overcome the Excessive Losses

As mentioned before, the 60 GHz radio propagation channel has higher power losses due to the higher frequency, which leads to higher propagation losses and secondly, due to an oxygen peak absorption. To overcome these limitations, several techniques are proposed. The first one is based on the Signal-Noise Ratio (SNR)

obtained on the Rx side. This technique is proposed in [123], and is based on measurements made in a vehicular environment for dynamic scenarios. The measures are made with two Tx. The first is to use the correct antenna based on the geometry of the environment. The second is to use the maximum instantaneously available SNR. Finally, if two Tx chains are available, the choice can be made with the maximum transmission ratio, which leads to the highest average SNR.

Another technique is to use an antenna with a higher gain, which implies a lower Half Power Beam Width (HPBW). However, a lower HPBW, increases the possibility of beam misalignment possibilities. The effect of the beam misalignment is shown in [112] and shows that a misalignment of more than 10° can increase the Bit Error Rate (BER) by a factor of 100. This value is obtained from a Monte-Carlo simulation performed with a TDL model made for two different misalignment ranges, 0° to 10° and from 10° to 25°.

3.3.5 Advantages of a 60 GHz Communication System

As mentioned before, the radio propagation channel at 60 GHz suffers from severe drawbacks, such as higher power losses, higher sparsity leading to difficulties in characterizing paths in NLOS visibility. Even adding antennas with higher gain implies a higher impact of beam misalignment.

However, this high attenuation allows the channel band to be reused with multiple user interfaces, even in small cells. This could be useful in many situations, such as resource sharing in the vehicular domain, where the number of users can be high in a small area, or train command in a restricted area, from marshalling yards to stations for example, and so on. In addition, the available bandwidth at 60 GHz is much higher, resulting in high data rate communication with low latency.

Finally, the size of the communication system will be reduced, since the wavelength at 60 GHz is 5 mm. This size will reduce the antenna arrays in MIMO system but also the RF chain with the development of integrated COTS.

3.4 Conclusion

This chapter has presented an overview of existing CS operating at 60 GHz and the various sounding techniques associated with them. It appears that there are no existing CS that are easy to use for our purposes. However, this overview highlights the development of COTS at 60 GHz which will allow the development of a low-cost CS.

From this review, the 60 GHz radio propagation channel characteristics and parameters are extracted. This review highlights the lack of measurement data in dynamic outdoor scenarios, especially in vehicular environments.

To fill this gap, a low-cost CS based on COTS and SDR platforms have been developed at IMT Atlantique, and measurement campaigns have been performed in different environments to validate the correct operation of the CS.

4 Development of IMT Atlantique Channel Sounder

Contents

4.1 Introduction

As mentioned on the state-of-the-art, there is a lack of CS capable of performing outdoor dynamic measurements for vehicular scenarios with a long recording time. To fill this gap, a CS has been developed at IMT Atlantique, in two versions. Both of them have a Rx and Tx unit, made with COTS to reduce the overall cost of the CS and to increase the ease of use.

The architecture of the IMT Atlantique CS, for both Rx and Tx, follows the same principle. The CS is divided into three parts, but two of them, the front-end and the synchronization unit, are critical. First, the up-and-down conversion of the baseband sounding sequence is realized in the front-end unit, and the challenge is to do it at 60 GHz. Second, the independent synchronization of the Rx and Tx is required to perform dynamic measurements, since a direct link to a reference signal is not allowed. The Tx and Rx modules of the IMT Atlantique CS can be seen in Fig. 4.1.

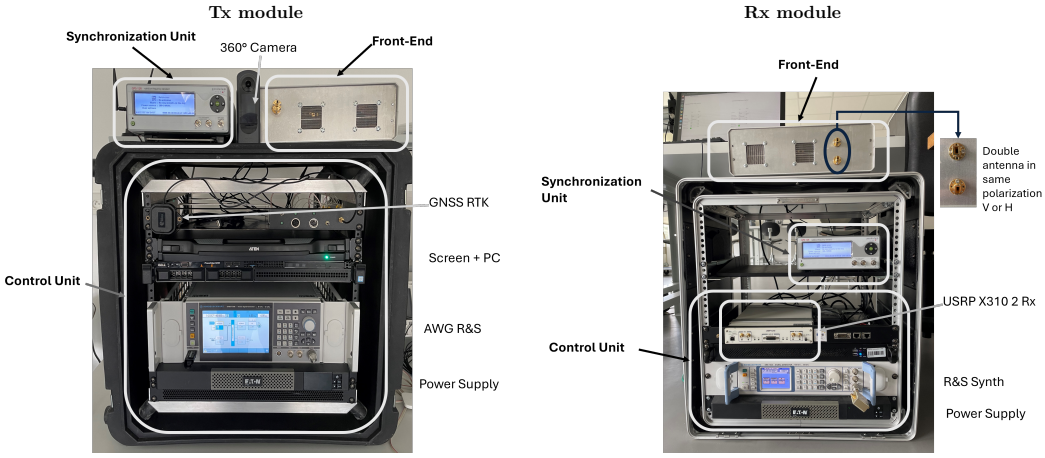

FIGURE 4.1: Integration of the IMT Atlantique CS.

In the following, the complete architecture of the CS is presented. Then, test campaigns will be performed in front of the MicroWave (MW) department of IMT Atlantique for vehicular scenarios to validate the operation of all the CS functionalities. Finally, from these test campaigns, some limitations appear and are presented.

4.2 IMT Atlantique SIMO Channel Sounder

4.2.1 Front-End

4.2.1.a Up-and-Down Conversion

As mentioned above, the use of COTS makes it possible to develop a low-cost CS. With the development of standards such as IEEE 802.11ad, some vendors are offering plug-and-play solutions to running communication links at 60 GHz. One of them is Analog Device, which provides a demonstration board that operates in the V-band, from 57 to 64 GHz with the reference EK1HMC6350 [142]. This demonstration board contains a Tx module referenced HMC6300 [143], with a heterodyne architecture for the up-conversion to the V-Band from 57 to 64 GHz, presented in Fig. 4.2.

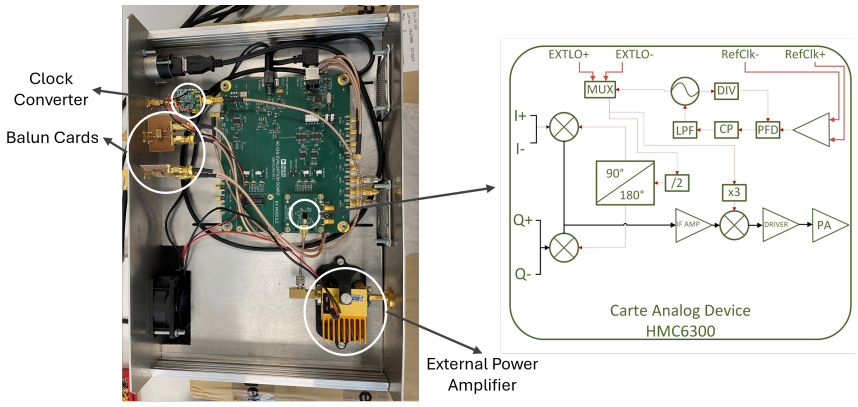

FIGURE 4.2: Tx front-end integration and architecture of the HMC6300.

This demonstration board allows the use of a differential In Phase and Quadrature Signal (I/Q) signal, I^+, I^-, Q^+, Q^-, but the AWG, in which the baseband signal is realized, does not have differential I/Q output. To convert the single-ended signal into a differential signal, an electronic card with an integrated balun is used.

Once the baseband signal is converted to differential I/Q, it is transmitted to the demonstration board and up-converted to the IF stage. The signal passes through a first amplification stage with a maximum gain value of 17 dB. Finally, another up-conversion is performed to obtain a 57 to 64 GHz RF signal, with another amplification stage to adjust the emitted power with a maximum gain of 17 dB, resulting in a maximum emitted power of 12 dBm.

Moreover, an external Power Amplifier (PA) is integrated to extend the measurement range. The output Compression Point at 1 dB (P1dB) of the PA is limited to 23 dBm, which results in limiting the transmit power of the HMC6300 to 0 dBm. Finally, the PA output is connected to the horn antenna.

The down-conversion is then realized by COTS, also developed by Analog Device referenced as HMC6301, which is the counterpart of the HMC6300. The HMC6301 [144], can operate from 57 to 64 GHz and down-convert the signal with heterodyne structure as presented in Fig. 4.3. The number of demonstration boards is two in the Rx front end, which allows to perform SIMO measurements. Multiple attenuators can be set to achieve a maximum gain of 69 dB. The first stage is a Low Noise Amplifier (LNA) is provided with a variable gain of 18 dB. The attenuation will increase the overall Noise Figure (NF) but it is useful to reduce the signal power to avoid saturation of the Rx chain. The signal is down-converted to the IF band with the same frequency as the up-converter. Another attenuator is available in the IF stage with a maximum attenuation value of 17 dB. Finally, the IF signal is down-converted to baseband and a final attenuation stage is proposed with a maximum value of 36 dB.

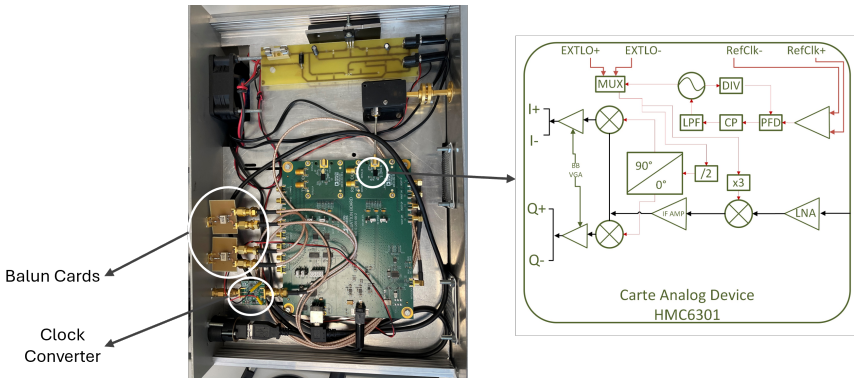

FIGURE 4.3: Rx front-end integration and architecture of the HMC6301.

Finally, the different attenuators are characterized on the Rx side. The study is done only on the Rx side because on the Tx side a fixed setting is implemented to ensure a 0 dBm output to avoid the saturation of the external PA.

To characterize the gain of the Rx chain, a pure sinusoidal signal is used. This signal is passed through the Tx and Rx chains, and then the baseband signal is analyzed with a spectrum analyser. For each attenuator value, the power value of the signal is stored and then compared to the case where all the attenuators are set to zero. The results of this measurement are displayed in Fig. 4.4.

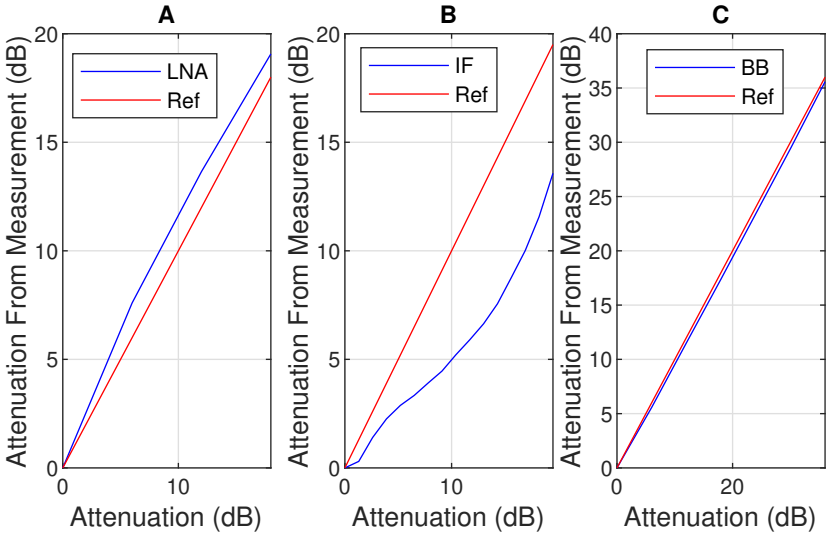

FIGURE 4.4: Results of the Rx attenuators for stage, **A**, LNA **B**, IF and **C** Baseband.

As for the Tx, an electronic card will be developed and used to power the demonstration board, and balun cards will be used to convert the differential I/Q to single-ended I/Q.

4.2.1.b Available Antennas

The CS has three antenna possibilities: a high gain (15 dBi), a medium gain (10 dBi) and finally a low gain (5 dBi). The antenna's 3D patterns are presented in Fig. 4.5.

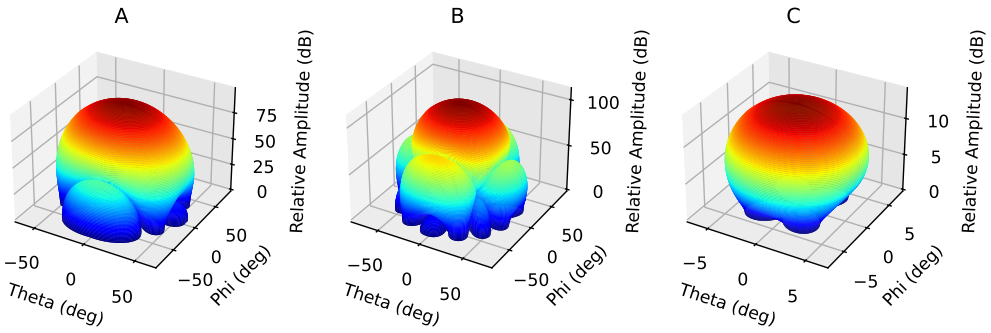

FIGURE 4.5: 3D antenna pattern for, **A** the 10 dBi antenna gain reference 261V/10, **B** the 15 dBi antenna reference 261V/15 and **C** for the 5 dBi antenna reference 260V/15 from Mi-Wave.

On the Rx side, the front-end box is modified to add another demonstration board with the HMC6301 wired on it. Finally, the HPBW of each antenna will be noted on Tab. 4.1. We also plan to use an orthomode to perform polarimetric measurements. The orthomode is a system that gives the two polarizations, horizontal and vertical, obtained from a circular horn antenna, as shown in Fig. 4.6.

TABLE 4.1: HPBW parameter of the available antennas.

Parameter	**5 dBi Antenna**	**10 dBi Antenna**	**15 dBi Antenna**
HPBW [°]	74.14	50.60	33.37

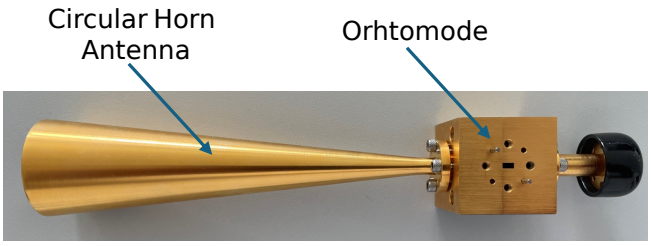

FIGURE 4.6: Orthomode with its circular horn antenna to obtain both linear polarizations.

4.2.2 Synchronization Unit

4.2.2.a Baseband

A synchronization unit is used to synchronize all the CS components in time and frequency. As mentioned before, the front-end is synchronized by a reference signal obtained from a Rohde & Schwarz (R&S) synthesizer. On both sides, the synthesizer is synchronized by a 10 MHz reference signal obtained from a synchronized reference. The synchronization scheme for both Rx and Tx is shown in Fig. 4.7.

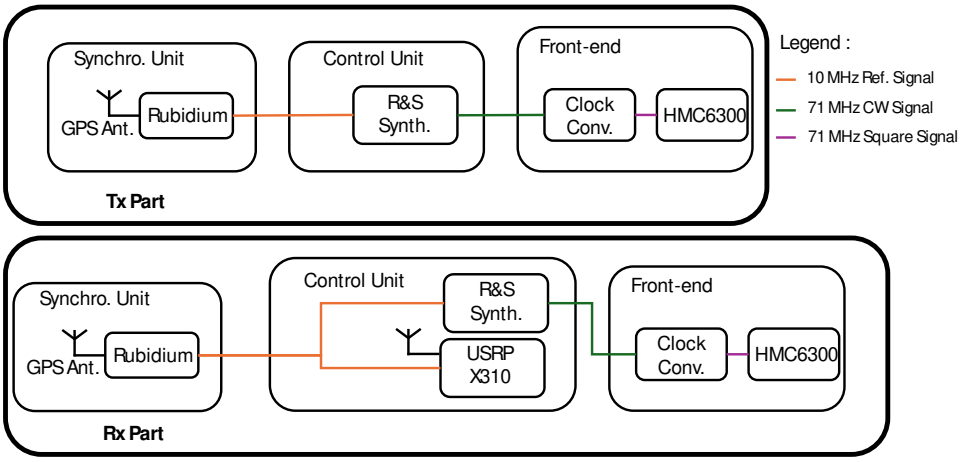

FIGURE 4.7: Synchronization schematic for both Rx and Tx part.

Also, on the Tx side, the synthesizer is a R&S AWG SMBV100A, which allows to transmit a RF with or without modulation up to 6 GHz and at the same time a modulated baseband signal with I/Q signal at the same time. This AWG is used to transmit the baseband sequence and the reference signal to the Tx front end.

Furthermore, on the Rx side, the architecture is almost the same as it can be seen in Fig. 4.7. There is also a R&S synthesizer synchronized by a 10 MHz reference signal. The main difference is the integration of a SDR platform to digitize the analog baseband signal. The SDR platform retained is a Universal Software Radio Peripheral (USRP) of National Instruments reference X310 [145], which can digitize two channels simultaneously from baseband to 6 GHz with a bandwidth of 200 MHz. Furthermore, it is easy to use thanks to many open-source programs.

As for USRP synchronization, it can be done externally in both time and frequency domains, using a Pulse Per Second (PPS) or 10 MHz reference signal provided by the rubidium reference clock. Or, it can be done with GNSS data. This feature allows setting the correct Coordinated Universal Time (UTC) time on the USRP, which is used to date the measurement data.

4.2.2.b Front-End

There are two ways to synchronize the up and down components. First, both the Tx and Rx conversion electronics have an input that can be used as an external oscillator. These inputs are called $\text{EXTLO}^-, \text{EXTLO}^+$ and are not used for our purposes.

Secondly, another solution exists and consists of fixing the reference clock of the internal Phased-Locked Loop (PLL) of both components. To achieve this aim, two inputs are available on both components and are named $\text{RefClk}^-, \text{RefClk}^+$.

On the demo board, which is used to easily use the up and down conversion components, there is an input for the RefClk signal. As seen in the Fig. 4.8, this input is controlled by a multiplexer that can choose between an external reference and a quartz signal. In our case, the external reference input is used. The reference sine signal with a frequency of 71.4286 MHz is provided by a R&S synthesizer and then converted to a square wave in the front end.

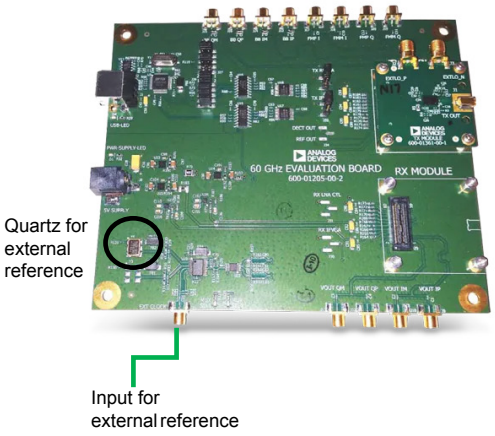

FIGURE 4.8: Pictures of the EK1HMC6350, with the external reference clock input and the quartz.

The quartz plays an important role in the synchronization quality. Indeed, test measurements highlight phase shifts that occur at random times but repeatedly. To characterize these shifts, a measurement is proposed which consists in measuring the CIR with a cable connection between Rx and Tx. From these measurements, the peak values in each case are kept such as the phase, and the evolution is plotted. The Fig. 4.9 shows this evolution, and it can be seen that the peak attenuation sometimes reaches 8 dB. The zoomed part in the Fig. 4.9 shows that each phase shift implies a decrease in the CIR peak.

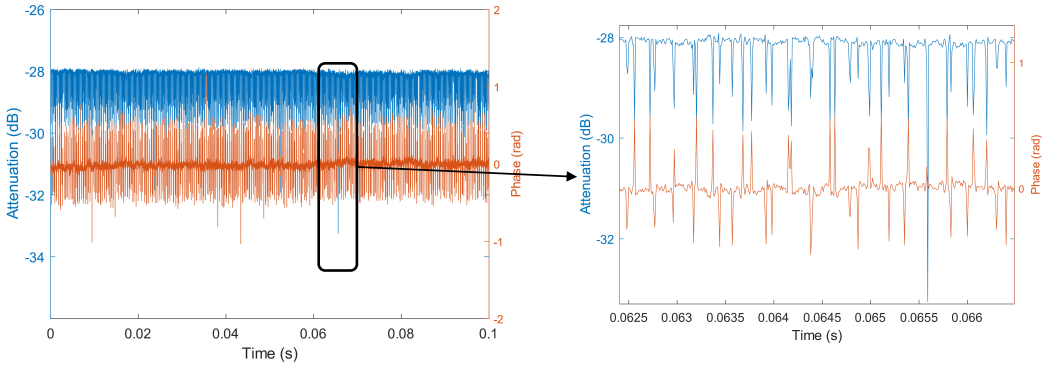

FIGURE 4.9: Phase shift and attenuation peak on the CIR.

As seen in Fig. 4.3 and Fig. 4.2, the LO is generated with a PLL. This PLL is referenced with an external clock, i.e. not implemented inside the HMC6300 or HMC6301, and can be selected in the demo board, quartz, or input port on the board. Indeed, the Fig. 4.8 shows the demonstration board and the two possibilities of the external clock on it. To illustrate the effect of the quartz on the external sync signal, its power supply is removed.

Once the action is realized, a pure sinusoidal signal is used as a narrowband-sounding sequence. The Fig. 4.10 shows that the phase shifts disappear.

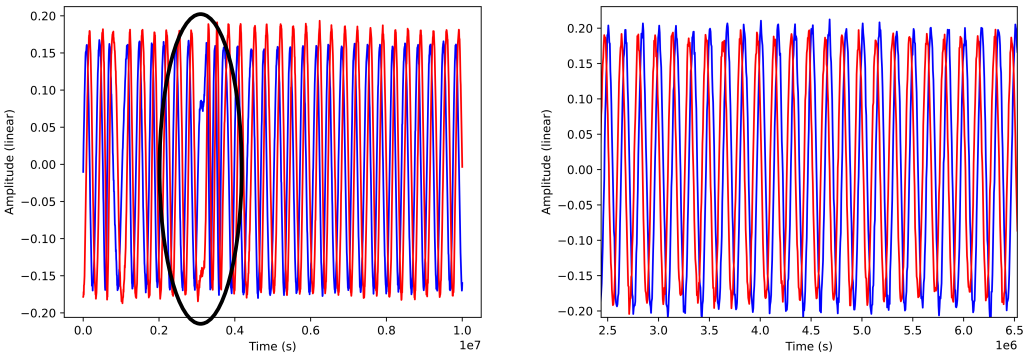

FIGURE 4.10: Evolution of the sinusoidal signal. The left figure represents the evolution of the sinusoidal signal and, the right figure the evolution without the quartz.

Then, it is necessary to verify the disappearance of the phase shift in the measurement case. To do this, the same measurement as in the first case is carried out, the CIR maximum value and its phase are plotted in the Fig. 4.11, which demonstrates the disappearance of the phase shift. It can be concluded that the problem is solved.

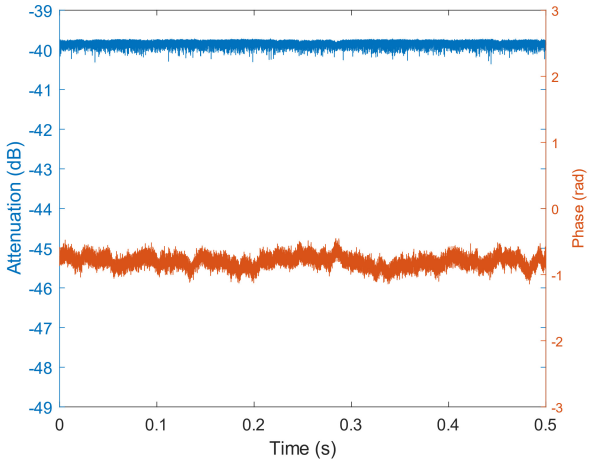

FIGURE 4.11: Results of quartz disconnection on the CIR maximum value and phase. The blue line represents the evolution of the CIR maximum value, and the orange line its phase.

4.2.2.c Clock Reference

As mentioned before, the synchronized reference clock must provide a 10 MHz signal and PPS. The first option is to use the USRP. Indeed, there is a GNSS module for the USRP, which has the advantage of synchronizing the USRP directly. Moreover, the USRP has an output with a 10 MHz reference that can be given to the R&S synthesizer. This solution is a low-cost solution compared to the atomic clock, even though it requires one USRP per module.

This solution is not maintained because the continued phase synchronization with GNSS implies phase shifts during the measurement. To achieve this purpose, two rubidium clocks are used. This clock can be externally synchronized by external

PPS or GNSS data and has the advantage of having good phase stability (for several hours). This allows us to firstly synchronize all, USRP and rubidium.

As mentioned before, maintaining the GNSS synchronization implies a slaving process in the rubidium clock or in the USRP, which affects the measurement with oscillations on the phase and the power value, as it can be seen in the Fig. 4.12. The measurement is realized with Rx and Tx connected by wire, and the evolution of the CIR maximum value and its phase is plotted.

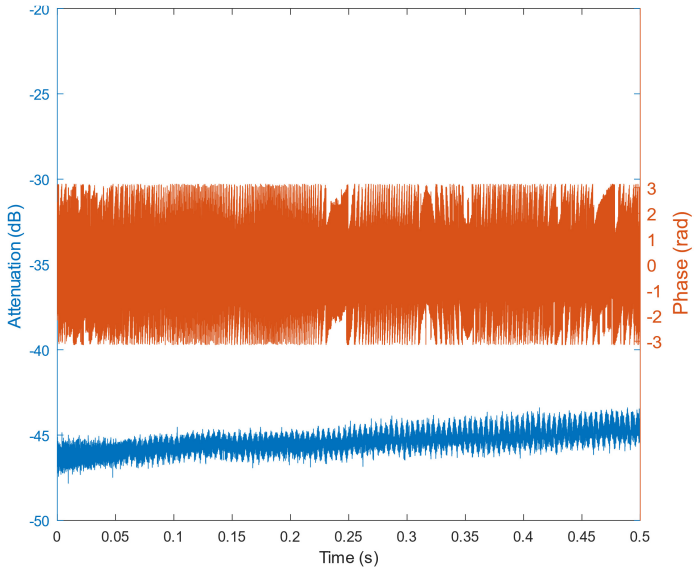

FIGURE 4.12: Impact of the rubidium clock disciplined by GNSS on the measurement quality. The blue line represents the variation of the CIR maximum value, and the orange line represents its phase.

To deal with this variation due to the slaving process, the rubidium clock is first disciplined by GNSS data as for the USRP. Then, the rubidium clock is put into free-run mode and the rubidium phase stability, which lasts for several hours, ensures the synchronization during the measurement. This configuration is not the cheapest, but gives better phase stability, which is an important factor, especially at 60 GHz.

4.2.3 Operations of the Channel Sounder

4.2.3.a Sounding Sequence

The first sounding sequence developed is the unmodulated OFDM sequence, where the phase between the sub-carrier follows a uniform distribution and has a bandwidth of 80 MHz. This sequence has a very high noise in the bandwidth and the SNR cannot be increased due to saturation in the Rx part.

This sounding sequence is not retained because the available SNR limit the dynamics. A new sounding sequence is then proposed to increase the SNR and the spectral quality. A FMCW signal is proposed, with a time duration of 10 µs and repeated continuously. The signal provides the desired gains, but the extreme ripples reduce the square characteristics of the spectrum signal.

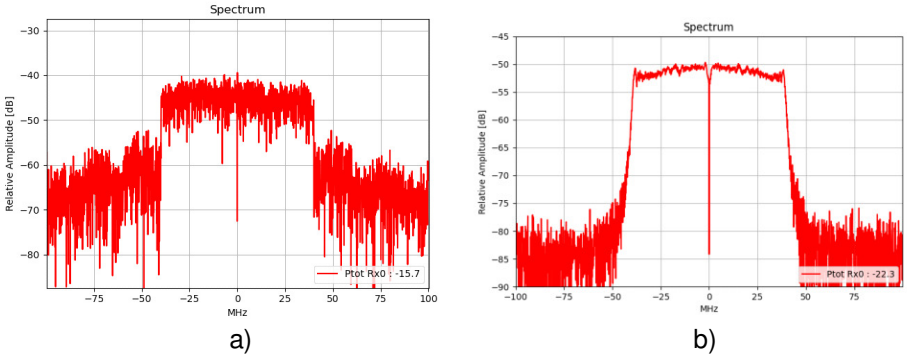

FIGURE 4.13: Spectrum of a) OFDM signal with phase following a uniform distribution, b) FMCW signal.

Finally, a new sounding sequence is realized to reduce or eliminate the ripple on the FMCW sequence and increase the sequence bandwidth. The proposed new sequence is an unmodulated OFDM sequence with Newman phase between each sub-carrier. The Newman phase distribution, originally presented in [61] to reduce CF and used in [146], is chosen and defined by the following equation $\phi_k = \frac{\pi(k-1)^2}{N}$, where N denotes the number of tones.

Another aspect of the new sounding is its time reduction. Indeed, test measurements and the state-of-the-art show that the maximum excess delay was too long and no MPCs were extracted after a few microseconds. The sounding sequence is now reduced to 2 µs and has a bandwidth of 180 MHz with a sub-carrier space of 1 MHz. The comparison between the FMCW sounding sequence and the new sounding sequence is shown in Fig. 4.14, both are obtained with Rx-Tx linked by wire.

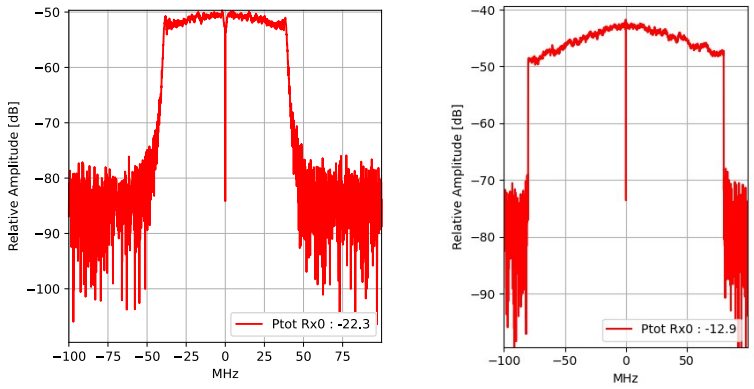

FIGURE 4.14: The left curve represent a FMCW spectrum and on the right, the unmodulated OFDM sequence for SIMO version of the CS.

This sequence has the advantage of deleting the ripple on the spectrum extreme, and with an equivalent CF.

4.2.3.b Measurement Process

This section introduces the measurement procedure is introduced. The CS measures the CTF, H, of the radio propagation channel by comparing the received spectrum with a reference spectrum obtained from the calibration process.

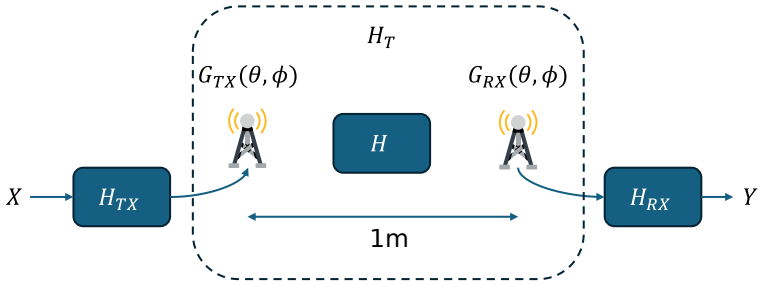

FIGURE 4.15: Measurement schematic of the CS.

The measure of the complex CTF is given in Eq. (4.1), where Y is the spectrum of the received signal during the measurement. The CIR is then computed by performing a Fourier transform on the CTF and an example is given in Fig. 4.20.

$$\frac{Y}{Y_{\text{Cal}}} = H_T = G_{\text{Tx}}(\theta,\phi) \times H \times G_{\text{Rx}}(\theta,\phi) \tag{4.1}$$

4.2.3.c Calibration Process

The calibration process aims to estimate the reference spectrum mentioned above. This reference is obtained by over-the-air measurements at a distance of 1 m. This distance validates the absence of obstacles in the Fresnel zone and is greater than the Fraunhofer distance to validate the far field from the antenna point of view.

An advantage of this technique is that it takes into account the complex CTF of the Rx and Tx, denoted H_{Tx}, H_{Rx} respectively. Moreover, the antennas are considered, in this process, as a pure gain value, which leads to $G_{\text{Tx}}(\theta,\phi) \approx G_{\text{Tx}}$ and $G_{\text{Rx}}(\theta,\phi) \approx G_{\text{Rx}}$. The calibration is done at a distance of 1 m, where H can be approximated with FSPL, $H \approx G_H$. The Fig. 4.15 shows the measurement principle in the case of calibration. The spectrum of the received signal, Y_{Cal}, in the calibration process, is shown in Eq. (4.2).

$$Y_{\text{Cal}} = X \times H_{\text{Tx}} \times G_{\text{Tx}} \times G_H \times G_{\text{Rx}} \times H_{\text{Rx}} \tag{4.2}$$

4.2.3.d Recording Time

The received sequence is sampled on the Rx side by the USRP at a rate of 200 MSamples/s, and both I/Q are digitized. Each file has a size of 80 MBytes, and, for link speed reasons, the file is first stored in the Random Access Memory (RAM) part of the computer, which has a limited size of 20 GBytes.

Without any modification, the maximum recording time is 10 s at CTF rate of 10 MHz. To increase the recording time, it is possible to decimate the data by a factor of 5, which results in 50 s but at the expense of the CTF rates. The CTF recorded continuously except in the case of decimation, where a large part of the data was lost.

The objectives are to increase the recording time, reduce the amount of decimated data, and maintain a spatial sampling rate high enough to resolve the Doppler shift. To achieve this, the CTF rate can be fixed, by changing the time delay between two consecutive CTF. The CTF rate is chosen to give a spatial sampling rate of $\lambda/10$ at a maximum measurement speed. In our case, the maximum speed is set to 30 km/h, which results in measurements of several minutes instead of 50 s. The Fig. 4.16 shows

an abacus of the data size as a function of the measurement time for different speeds, with a black line plotted on it representing the maximum size of the CS memory. To realize this, the CTF size is 3.2 kBytes, and the desired spatial sampling rate is $\lambda/10$.

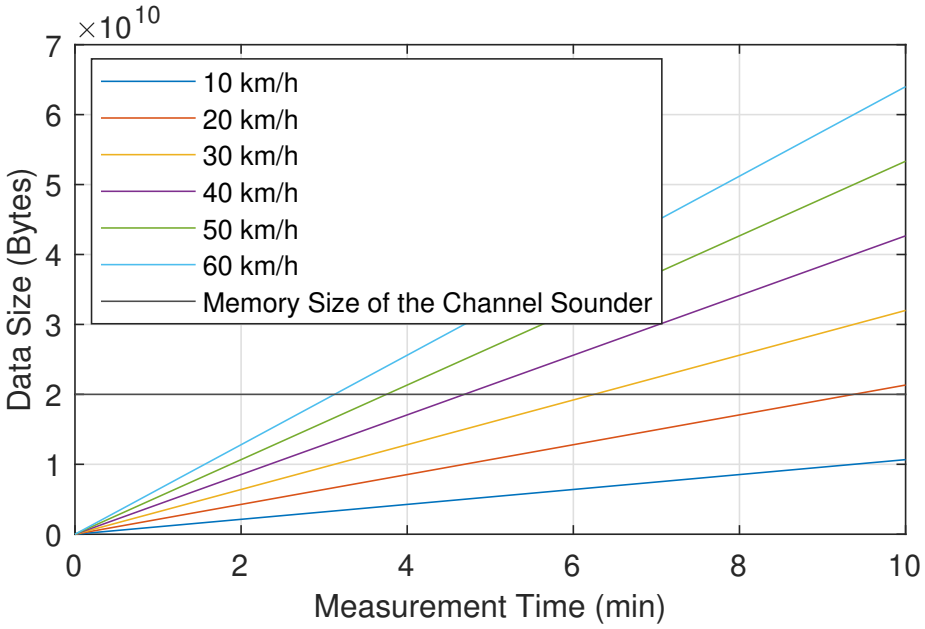

FIGURE 4.16: Abacus of maximum measurement time in function for various speed.

4.2.3.e Localization and Camera

The localization is done with a GNSS module. The accuracy of a GNSS module is limited to a few meters, which is too high for our purposes. As a reminder, the wavelength at 60 GHz is 5 mm, so an estimation error of a few meters means thousands of wavelength errors. Nowadays, it is possible to increase the accuracy of the GNSS localization by using a GNSS extended module or Real Time Kinematic (RTK). The principle of this module is to compare the raw GNSS data, with an accurate localization called BS. Then, the BS send the corrected data via Radio Technical Commission for Maritime Services (RTCM) protocol through the internet until an Network and Transport of RTCM via Internet Protocol (NTRIP) caster. The NTRIP caster is a data server, that collects the correction data from all the BS in a network. Finally, the correction data from the NTRIP is sent over a 4G connection to the GNSS module of the CS on the internet, and the module corrects the GNSS information. The Fig. 4.17 represents the operation to obtain the corrected data on the CS. This module is only implemented in the Tx, since it is the moving element in our dynamic measurements.

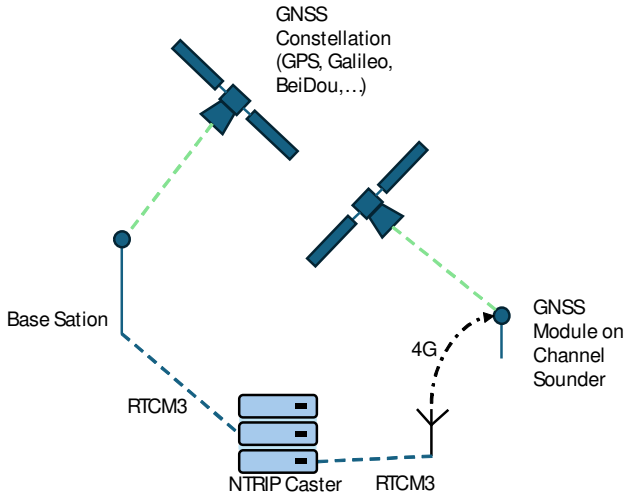

FIGURE 4.17: Operation of the RTK module.

There are several databases of BS, most of them require a subscription, but an open source solution developed by the National Research Institute for Agriculture, Food and the Environment (INRAE) and called Centipede [147], allows us to use several BS for free. To check the accuracy of this system, a test was carried out in a car park. For each configuration, with and without correction, three journeys were performed in the car park. The results are shown in Fig. 4.18.

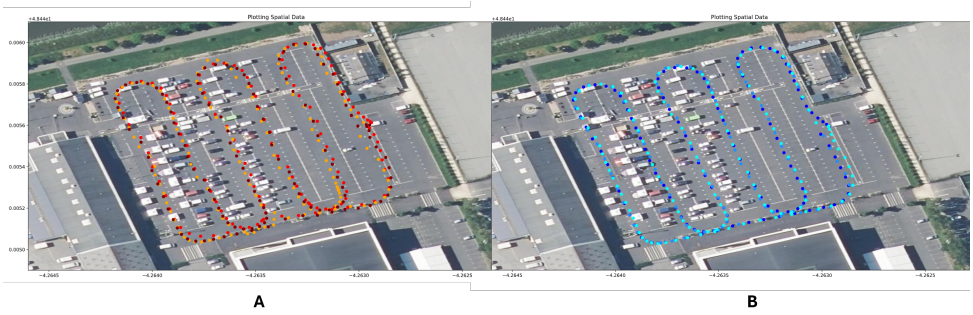

FIGURE 4.18: Result of comparison measurement campaign, **A**, without correction and **B**, with RTK correction.

The results indicate that the localization result is more accurate with the RTK module. In addition, the actions are repeatable, which allows different actions to be performed on the same track, and the localization remains accurate.

Secondly, a 360° fisheye camera is implemented. This camera is controlled by the Personal Computer (PC) and takes pictures every second, synchronized by the GNSS module. In fact, in the control unit, the User Interface (UI) developed ensures that the camera is triggered by the appearance of a new localization frame that arrives every second.

Thirdly, to improve the quality of the speed indication, two setups were implemented. The first used an incremental encoder developed by Peiseler. This encoder can be mounted on a car wheel and has an accuracy of 0.36°. The second possibility is to use the speed information obtained from the GNSS data, this solution is retained for our case.

4.2.4 Control Unit

4.2.4.a Transmitter Part

The Tx side of the CS is controlled by a PC in which a UI is developed to control the Analog Device demonstration board. The UI is written in Python and controls all the attenuators inside the HMC6300, and sets the carrier frequency. The UI is based on the Analog Device UI, which does not fit our proposal. Also, in this UI it is possible to check the value of each register to see if the card is set correctly. A screenshot of the UI for the Tx is presented in Fig. 4.19.

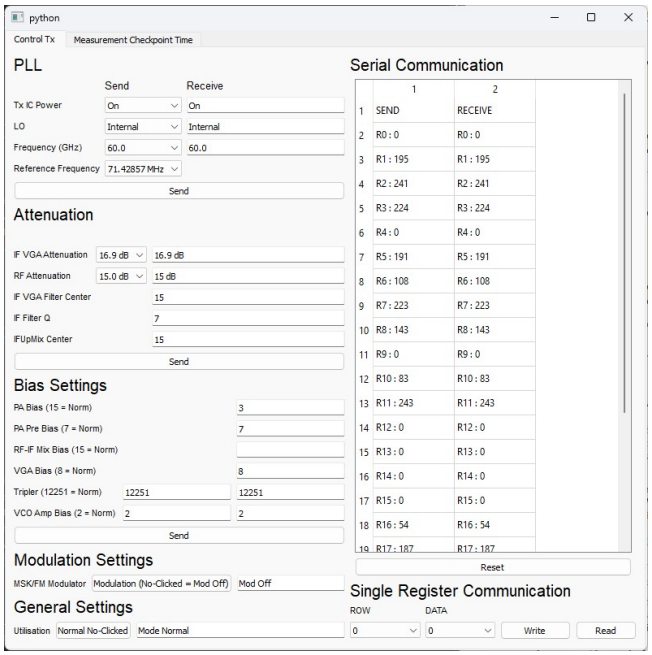

FIGURE 4.19: Screenshot of the developed UI for the Tx side.

4.2.4.b Receiver Part

The Rx control part has a PC in order to control both the front-end and the USRP. As far as the Tx is concerned, a UI has been developed to deal with the peculiarities of the demonstration board but also with two other features. The first is the possibility of visualizing the spectrum, amplitude, CIR and phase of the received signal, with a live mode that allows the user to see the evolution of the spectrum and other plots if selected. A screenshot of this UI part is presented in Fig. 4.20. This UI is also implemented to start and stop a measurement and to save the measurement data.

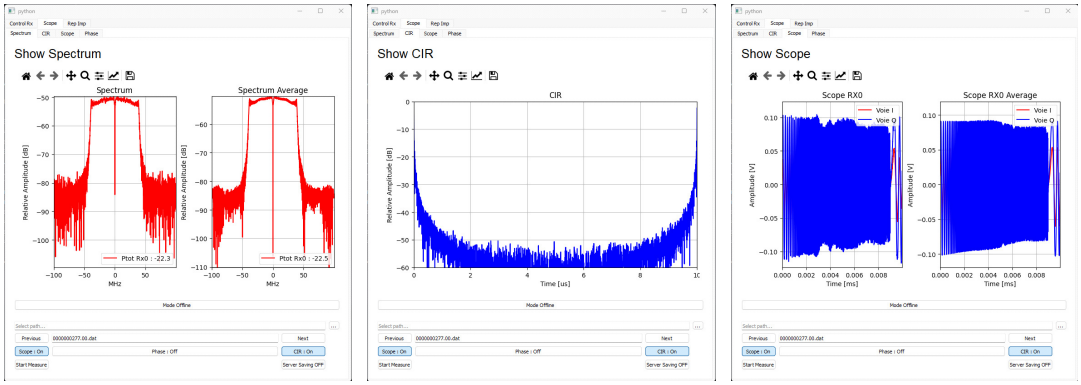

FIGURE 4.20: Debug window plot in Rx UI.

4.2.5 Integration

Finally, all of the above components are integrated into a box that is easy to transport and install in different environments. In addition, an electronic card for power conversion and supply is realized and integrated inside the box. The purpose of this card is to allow the use of a signal power supply plug on a sector socket to supply all the components of the box.

Finally, all these components are connected to a Uninterruptible Power Supply (UPS), which is used in two cases. Firstly, in the event of power failure, the UPS provides power until the end of the measurement so that the CS can be switched off properly. Secondly, it is used to ensure a quality power signal to all the components of the Tx side. A picture of the final box integration is presented in Fig. 4.1.

4.2.6 Specifications

The specifications of the developed CS are presented in Tab. 4.2.

TABLE 4.2: Specifications of the SIMO CS.

Parameter	Value
Carrier Frequency	60 GHz
Bandwidth	160 MHz
Time Resolution	6.25 ns
Max Excess Delay	2 µs
Power	23 dBm
Antennas	5-10-15 dBi
Polarization	Vertical & Horizontal
Synchronization	GNSS Disciplined Rubidium
Sounding Sequence	Unmodulated Newman OFDM
Max Recording Time	6 mins

4.3 Test Campaigns

4.3.1 Corridor Dynamic Scenario

Once the CS has been developed, measurements are carried out to validate its correct operation. These first measurements took place in a 20 m corridor long at

IMT Atlantique and the Tx-Rx synchronization is performed with a 10 MHz reference signal transmitted by wire, since it is impossible to obtain GNSS data. The measurement environment and installation are described in Fig. 4.21.

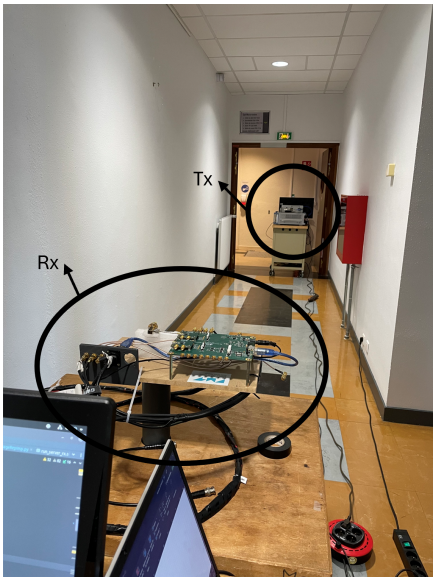

FIGURE 4.21: Environment and CS installation for the first version operation testing campaign.

In addition, this measurement campaign allows the presentation of the preprocessing applied to the file in order to reduce the amount of data. As mentioned before, a measurement repository has 20 GBytes of data, and to increase the SNR, a first coherent averaging is achieved. The size of the average depends on the speed of the measurement. The aim is to keep at least one CTF per $\lambda/10$. The CTF is then calculated and stored in a structured Matlab file. From this file, it is first possible to plot the evolution of the averaged CTF gain as a function of time, as shown in Fig. 4.22. The aim is to present the average power over the available bandwidth and to overcome the difficulty of measuring a power value at the carrier frequency, since it is the continuous value digitized by the USRP. In our case, this bandwidth is limited to 180 MHz, which allows the hypothesis of a narrowband power evolution. The Fig. 4.22 shows the presence of fading can be seen, but further investigation is needed to validate its origin, which could be from system noise or MPCs.

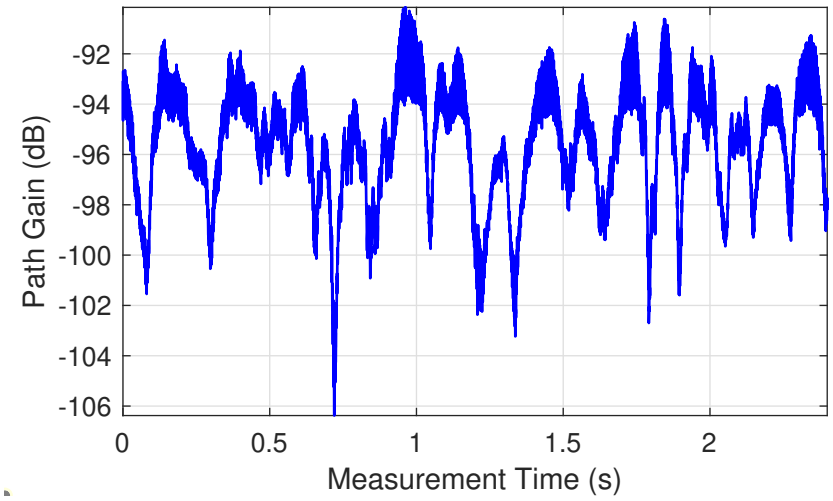

FIGURE 4.22: Evolution of the CTF gain during the measurement.

Secondly, the CIR are extracted from the CTF by a Fourier transform. The CIR are then power-averaged over on a stationary domain to obtain the PDP. A window of size 40λ is used for this measurement. The window is also overlapped by 20λ, to avoid discontinuities. The obtained PDP is presented in Fig. 4.23, and due to the limited bandwidth, the MPCs are included in the main contribution.

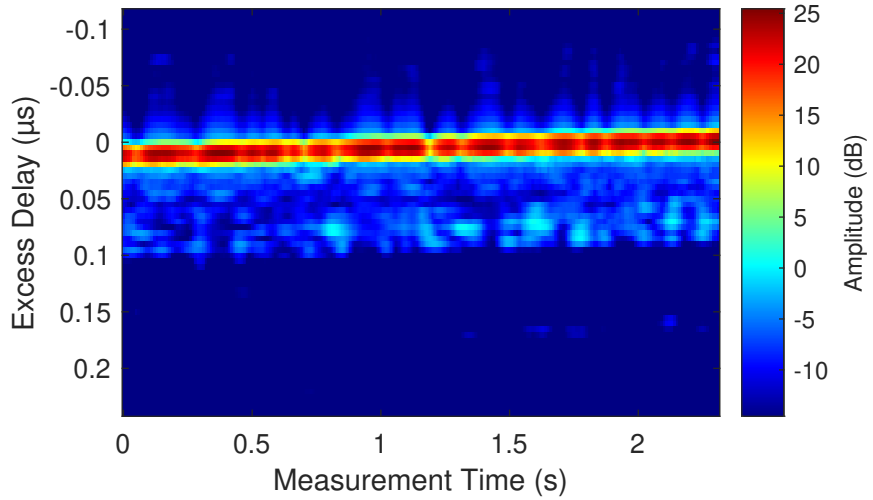

FIGURE 4.23: Evolution of the PDP during the measurement.

To detect the presence of MPCs, the Doppler function must be calculated. As with CIR, this function can be incoherently averaged to give a representation of Doppler in terms of the evolution of the power plot over time. This function, called LSF, is represented in Eq. (4.3), where $g(\tau, \nu)$ is the Doppler variant impulse response and N_τ is the number of excess delays in the measurement.

$$P_g(\nu, \tau) = \frac{1}{N_\tau} \sum_{k=1}^{N_\tau} |g_k(\tau, \nu)|^2 \tag{4.3}$$

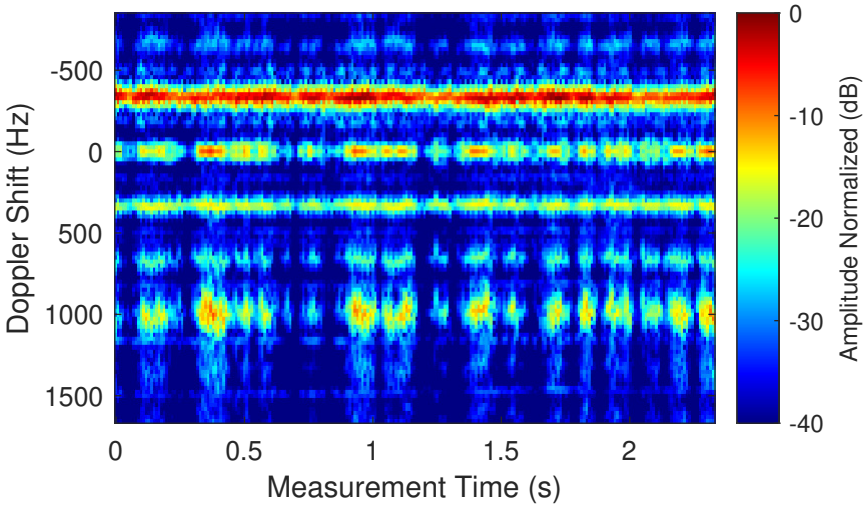

FIGURE 4.24: Evolution of the LSF during the measurement.

The Fig. 4.24 shows the evolution of the LSF during the measurement. This figure shows the evolution of the velocity during the measurement (red component just below -500 Hz). Moreover, the sign of the Doppler shift is coherent, since the Tx is moving away from the Rx. Finally, some components can be seen in the line of 1000 Hz line, oscillating around this value during the measurement.

4.3.2 Dynamic vehicular Scenario

To test the final version of the CS, a measurement campaign is planned in a vehicular environment for dynamic scenarios. To test its operation in real conditions, the Tx part of the CS will be installed on the top of a car and the Rx will be placed in the middle of a road at IMT Atlantique. Moreover, the RTK module is installed on the Tx part on the top of the car. The CS installation on the car, the measurement track obtained from the RTK module and a fisheye image taken during the measurement are presented in Fig. 4.25.

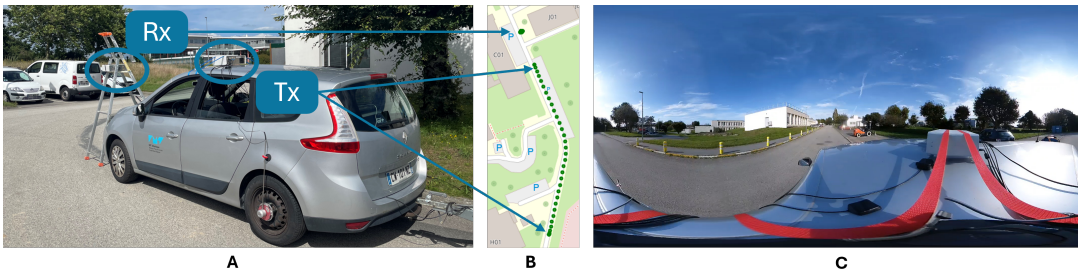

FIGURE 4.25: **A**, installation of the CS in the environment. **B**, localization data obtain from the RTK module for the Tx part and from GNSS data for the Rx part. **C**, fish eye picture of the environment during the measurement.

The road used to carry out the measurement is located on the campus of IMT Atlantique campus and only 150 m are used for our purpose. The measurement starts from the NLOS situation due to the little hill at the beginning and finishes to LOS situation. As a first result, the evolution of the CTF gain, for the two receivers as

a function of the measurement distance is shown in Fig. 4.26. Both channels are quasi-identical and highlight a significant reflector in the mmWave band. Indeed, the green line in Fig. 4.26 represents the evolution of the path gain of a two-ray model, indicating a good fit. This measurement is similar to the one presented in [87], where the author indicates that the ground reflection is the main scattering of their measurement.

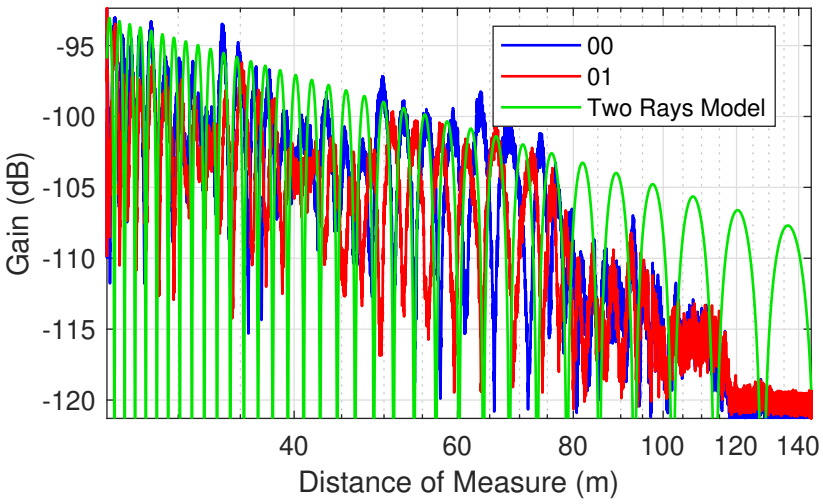

FIGURE 4.26: Evolution of the CTF gain during the measurement.

After studying the evolution of the path gain, the PDP is calculated. The Fig. 4.27 shows the evolution of the PDP for the one Rx, as there is no additional information from the other receiver. In this case, from $[0, 5]$ s, the PDP shows no path. From $[5, 30]$ s, a presence of fading in the main component indicates the presence of a strong MPCs contained in the LOS. Then, from $[30, 35]$ s a MPCs is extracted from the main path and the fading disappears.

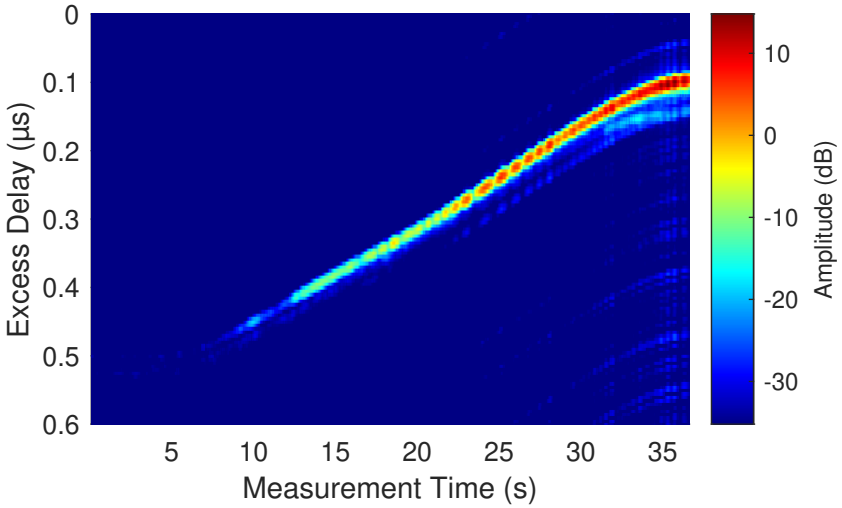

FIGURE 4.27: Evolution of the PDP during the measurement.

Finally, the scattering function is extracted and shown in Fig. 4.28. The appearance and disappearance of MPCs can be seen, especially between $[30, 35]$ s. Moreover,

from $[25, 30]$ s, a distinction can be made between overtaking parked vehicles. The vehicle speed during the measurement was a maximum of 20 km/h, resulting in a Doppler shift of $f_d = v/\lambda = 1110$ Hz, and this value can be retrieved in the scattering function.

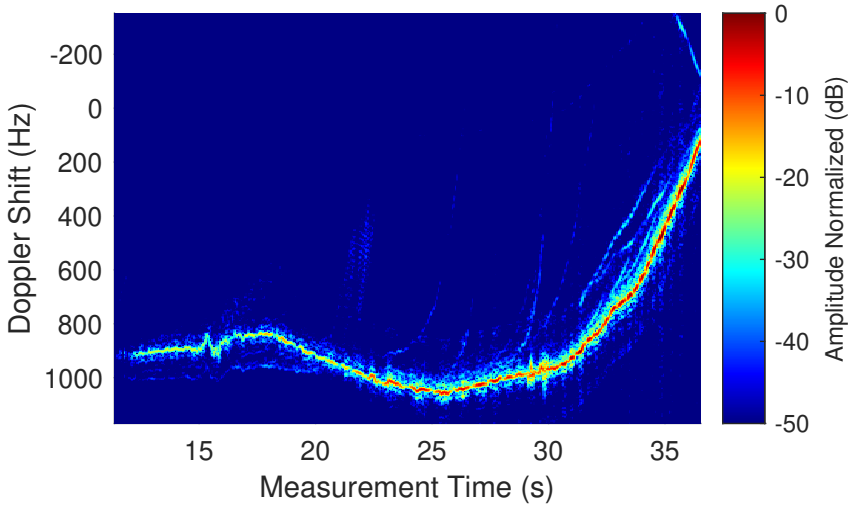

FIGURE 4.28: Evolution of the scattering function during the measurement.

4.4 Limitations

4.4.1 Automatic Gain Control

The main limitation of the developed CS is the lack of Automatic Gain Control (AGC). This implies a fixed attenuation value during the measurement and, in some cases, leads to saturation of the Rx. This limitation is illustrated in Fig. 4.29, where all the data are unusable due to saturation at the beginning of the measurement. Furthermore, the 6 dB step between the two curves is obtained by modifying the calibration value of the second Rx. This difference is realized to show that the saturation occurs on both Rx with the same Rx chain gain value.

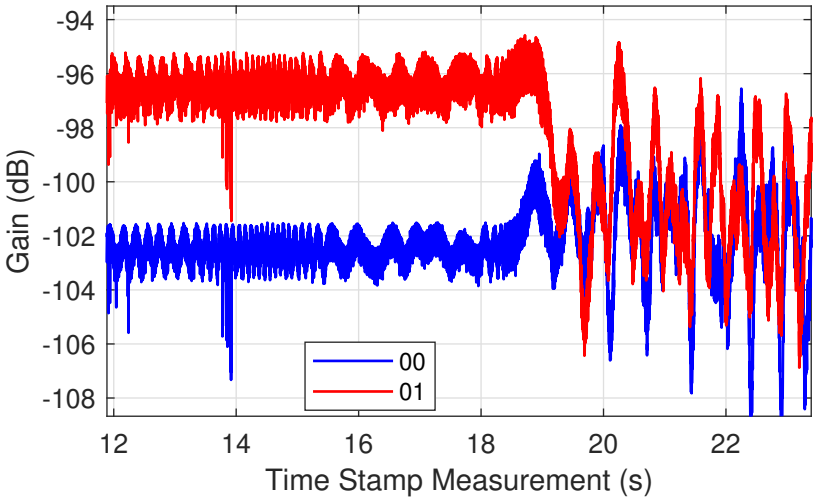

FIGURE 4.29: Example of saturation of the Rx due to fix settings of attenuation.

The AGC is used to correct the gain of the Rx chain so that the measurement is always performed with the best SNR. The simplest way to implement this is to check the power received on each stage of the Rx chain and adjust the attenuation as a function of this value. In our case, the inter-stage signal is not available, but a table to correct the gain in function of the received power can be realized. However, even with this table, the implementation is not trivial due to the update time of the AGC. In fact, in a dynamic scenario, the presence of fading implies a fast fluctuation of the power, and if the AGC rates are too fast, these fluctuations can be compensated. This is even the case for slower fluctuations, and implementing the AGC could be an evolution of the CS.

4.4.2 Speed Information

Another limitation is speed measurement. In fact, collecting data from the speed sensor and storing it synchronously is impossible. The correct use of this sensor is another development perspective for the CS. Nevertheless, the GNSS data gives the relative speed at rates of 1 Hz, which is very low and inaccurate. This leads to difficulties in correctly estimating the Doppler shift implied by the dynamic scenario, especially in the case of acceleration and braking. This limitation is illustrated in Fig. 4.30, where the pink line represents the maximum Doppler shift estimated from the GNSS data and the real one is in red.

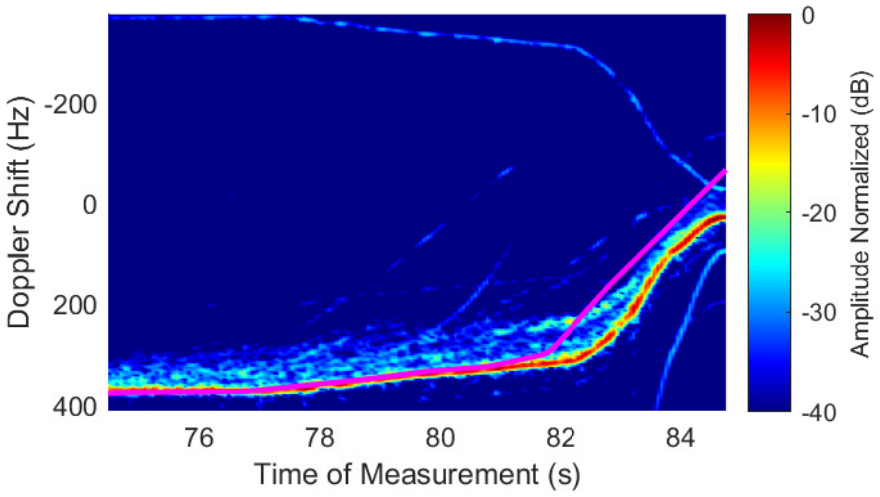

FIGURE 4.30: Example of Doppler shift false estimation from the GNSS data in pink line and the Doppler measured.

4.5 Conclusion

In this chapter, the IMT Atlantique CS has been introduced, as well as the evolution from the Single-Input Single-Output (SISO) version to the upgraded SIMO version, with its features presented in Tab. 4.2.

The CS has been used for several measurement campaigns, which demonstrate its capabilities. Moreover, the various upgrades incorporated in the latest version have been tested in vehicular environments.

In addition, this CS can be used in a variety of environments, including the most complex, such as railways. The radio propagation channel in railways is a hot topic due to the lack of real measurements.

5 Channel Measurement Campaign in Railway Environment

Contents

5.1 Introduction

The purpose of this chapter is to present the measurement campaign carried out in a railway environment. First, the railway environment and its main characteristics are presented. Then, an overview of existing measurements was presented in railway environments, and the results were presented. Next, the railway environment available for our measurements is presented. Finally, the two measurement scenarios are presented: platooning and a scenario comparable to 3GPP HSL. A synthesis of the measurement campaign is then proposed. It presents the number of trips made in each scenario and the data size collected during this measurement campaign. Finally, the first results of the campaign are presented and analyzed.

5.2 The Railway Environment and Related Results

5.2.1 Railway Environment

As mentioned in the introduction, the railway environment can be categorized into six types, as summarized in [148, 149]:

1. Tunnel: this scenario concerns tunnels inserted in open area tracks. Subway scenarios are excluded.
2. Viaduct: this category features long viaducts, such as ones implemented on high-speed lines. On this kind of line, open train stations can be found.
3. Urban area: in urban areas, the surroundings of the tracks are mainly composed of high building density with high height. Moreover, the train stations are located directly on the tracks. These stations can vary from open-area to semi-closed, depending on local conditions.
4. Rural: this scenario includes tracks in rural environments, with and without train stations.
5. Single track: this scenario involves single-track railways with and without viaducts and tunnels present.
6. Subway: this scenario presents the case in which the railway track is under the tunnel at every time. The main difference between tunnel scenarios is the transition possibility between the outside and inside a tunnel.

In any railway scenario, there are several common geometric features. Firstly, the track itself is primarily made of steel. The track is supported by ballast, which consists of rocks of varying size and roughness. At 60 GHz, where the wavelength is only 5 mm, the roughness of these rocks can affect the communication link. In fact, at this frequency, the roughness of the rocks can cause scattering and multiple reflections, resulting in rapid fading. In addition, in some railway environments, such as subways or marshalling yards, the ballast may be replaced by concrete. Furthermore, the roughness of the concrete can also affect the communication link, with the same physical interaction mentioned above. However, the tracks themselves are fixed to the ballast with wooden sleepers, which come in two categories:

1. Complete version: these sleepers fix both tracks securely to the ballast. The complete sleepers cover the track for a short distance but are regularly spaced. Moreover, it covers the ballast and reduces the scattering and the possibility of multiple reflections with the ballast.

2. Reduce version: the wooden sleepers only secure one rail to the ballast. For this version, the sleepers are generally small concrete blocks, a size a little higher than the rail. In this case, the different interactions with the ballast are kept identical during the measurement.

However, due to the natural terrain, railway lines are not always straight; they often cross hills and other mountains with varying gradients. In addition, reflectors such as walls can be found in canyons or railway stations. Depending on their composition, these walls can be highly reflective or allow transmission through them due to their electrical parameters. The Fig. 5.1 shows the common elements found on and in the immediate vicinity of the railway line.

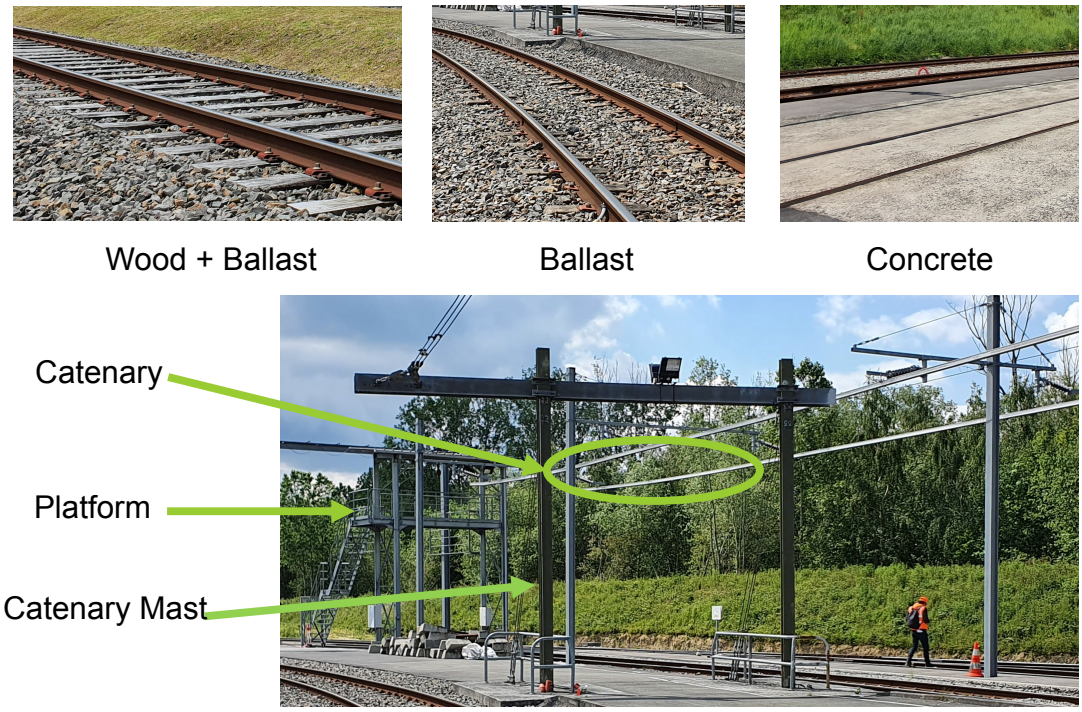

FIGURE 5.1: Representation of the typical railway environment.

Another significant geometric scattering in railway environments is the catenary system and its supporting structure. Modern railway lines are predominantly electrified, and these systems are typically constructed of steel, which acts as a notable reflector in communication links. The Fig. 5.1 shows the typical elements of the railway environment in the immediate vicinity of the tracks. This figure illustrates the regular placement of the catenary masts.

In addition to the geometric scatterers mentioned above, scatterers are also present in various railway scenarios. These scatterers have different probabilities of occurrence depending on the environment. A common example is crossing bridges, which are more likely to be found in open fields and hilly terrain. The material composition of these bridges can have a significant impact on communication links due to multiple reflections and potential shadowing effects. The parameters of such scatterers include their size and the likelihood of their occurrence.

Signalling systems, which are used for safety and to warn drivers of the presence of trains ahead, are usually mounted on separate masts near stations, but can also be found on the catenary structures. Due to their critical role in safety, they are present

in all the environments mentioned above, with their stochastic parameter being the frequency of occurrence. Similarly, vegetation can be found in all these environments, with variations in density, and distance from the track and type (trees or bushes).

Additionally, buildings along the railway tracks can be categorized according to their proximity to the tracks. The closest are the control and command buildings used for train control, followed by electrical transformers that supply power to different sections of track. A final category includes structures that may interfere with communication links, and this impact is increased if either the Tx or Rx heights exceed those of noise barriers or embankments separating the railway tracks from residential areas.

The station environment introduces many stochastic scatterers, including roofs, platforms, and platform obstacles. Variations in their size and orientation can significantly affect the communication channel by introducing MPCs, which can increase the RMS DS, especially depending on the distance between the train and the platform. In addition, platforms can cause diffraction and shadowing effects on the signal.

5.2.2 Existing Measurements Results

5.2.2.a Subway

In [150–153], the author presents the Mobile Hotspot Network (MHN) system, which is a proof of concept system used to measure the Seoul subway. The architecture of this system is divided into several MHN Radio Unit (mRU) connected to a MHN Digital Unit (mDU) itself connected to the internet. The separate mRU realized the mmWave communication with the MHN Terminal Equipment (mTE) placed in the subway. From this measurement, the throughput evolution is presented and leads to a maximum value of 1.2 Gbps. Secondly, in [154], the author adds the results of a measurement campaign in a railway freight depot carried out by the Fraunhofer Institute.

In [8], the author presents a multiband CS used to measure the tunnel environment. This system operates at different frequencies, in particular at 28 GHz, but only to characterize the received power. From these measurements, a single slope PL model, PL_1 is extracted, leading to a PLE lower than in free space due to the wave-guiding effect. This wave-guiding effect is greater at higher frequencies due to the higher specular reflection due to the lower wavelength. However, in this case, it is more appropriate to fit the PL with a double slope separated by a breakpoint where the visibility changes from LOS, PL_{LOS}, to NLOS, PL_{NLOS}, scenario. In this case, the breakpoint distance is fixed at 91 m and all the results can be found in Tab. 5.1.

Table 5.1: PL models obtain from measurement in [8].

Case	PLE	σ	PL_{d_0} (dB)
PL_1	1.47	4.53	70.19
PL_{LOS}	1.29	4.83	72.9
PL_{NLOS}	1.72	4.06	98.11

5.2.2.b Marshalling Yards

These measurements are made in a freight depot in Germany [155]. The time-domain CS used in these measurements operates at 28 GHz with, with a vertically

polarized omnidirectional antenna at the Rx. The CS itself is not installed on a train but on a pickup that follows the track. The Tx remains static in the two positions next to the track, while the Rx moves along the railway track at a constant speed of 1.75 m/s.

From these measures, a model is extracted to extend a channel model. The extracted model extends the PL by two models Floating Intercept (FI) and Fixed Reference (FR). These models were introduced in [156], and are presented in Eq. (5.1), for the FI model and in Eq. (5.2), for the FR model. In Eq. (5.1), α is the FSPL at a reference distance of 1 m, β is the power decay constant, and f_c is the carrier frequency. In Eq. (5.2), $\overline{n}$ represents the PLE. From these equations, it can be seen that the main difference is in the way that the frequency dependence is taken into account. In fact, the FI model has a frequency-dependant factor that can modify the frequency dependence. The parameters obtained for each model are presented in Tab. 5.2.

$$PL_{\mathrm{FI}} = \alpha + 10\beta \log_{10}\left(\frac{d}{1m}\right) \tag{5.1}$$

$$PL_{\mathrm{FR}} = 20\log_{10}\left(\frac{4\pi f_c}{c_0}\right) + 10\overline{n}\log_{10}\left(\frac{d}{1m}\right) \tag{5.2}$$

TABLE 5.2: Resume of the PL model parameters extracted from the measurement campaign in [155].

Parameter		**Value**	
PL FI	β	PL_{d_0}	σ
	2.27	55.7 dB	2.8
PL FR	β	PL_{d_0}	σ
	2.03	61.4 dB	2.8

Then, the RMS DS is calculated with a threshold of 30 dB relative to the strongest MPCs, and to fit with the extended model, the log value is taken into account $\mu_{lg\mathrm{DS}} = log_{10}(\mu_{\mathrm{DS}})$. Finally, the Azimuth Angular Spread of Arrival (aASA) and the Zenith Angular Spread of Arrival (zASA) are modelled to extend the model. All the results are summarized in Tab. 5.3.

TABLE 5.3: Resume of the RMS DS model parameters extracted from the measurement campaign in [155].

Parameter	**Value**
μ_{lgDS}	-7.7
σ_{lgDS}	0.37
μ_{lgaASA}	1.42
σ_{lgaASA}	0.19
μ_{lgzASA}	0.084
σ_{lgzASA}	0.21

In [157], an SDR based CS operating at 28 GHz with a maximum bandwidth of 160 MHz is developed with a phased array antenna capable of scanning the azimuth and elevation plan for 120° with eleven beams available. The Tx part of this CS is

then placed on the top of a bridge over several marshalling yards, where the Tx is located. The measurements are made in a static position. The environment setup allows for several scenarios, the first being an empty track between the Rx and Tx. In the second scenario, a wagon is placed on the track. Finally, the effect of a metal store is studied.

The first presented result is the variation of MPCs as the Rx-Tx distance increases. The authors show that there is no change in the MPCs number as the distance between Rx and Tx increases. There is no real justification for this result from the authors, but it could be explained by the absence of environmental variation. In fact, during the measurement, the environment remains largely the same, due to the repetition of the main obstacles, such as the catenary wires. The second result presents the impact of a typical element of the railway environment, the overhead contact line. Firstly, the author presents the blocking object, which reduces the received power, in different positions and one of the most present is the catenary. The other effect of the catenary concerns the DS, which is increased in the case of a blockage of the link. The increase of the DS can be explained by the increasing number of catenaries when the Rx-Tx distance increases, so the main component is not as much affected as the number of reflections. Finally, the effect of a locomotive is not obvious, on the contrary, the effect of the building shows dramatic random variations.

In [126], the authors present measurement results of a dynamic measurement campaign carried out in a railway environment, with the RUSK CS. This campaign aims to investigate the possibility of a communication system for the coupling maneuvers between two trains. The environment consists of a typical railway track, but the catenary mast line is missing in the environment. The results presented in the paper are the comparison of the received power in the open field area with a two-path model. The two-path losses are modelled with the knowledge of the ground reflection coefficient, $\Gamma(\theta)$ as presented in the Eq. (5.3). In this equation, d_1, ϕ_1 are the length and the phase of the first path, and d_2, ϕ_2 are the same but for the second path. The comparison between the measurement, and the two-path model shows a good correlation, which allows the assumption that the main component comes from the ground reflection.

$$PL_{\text{TP}} = 20\log_{10}\left(\frac{\lambda}{4\pi d_1}\right)e^{-\phi_1} + \Gamma(\theta)20\log_{10}\left(\frac{\lambda}{4\pi d_2}\right)e^{-\phi_2} \tag{5.3}$$

5.2.2.c High Speed Lines

A measurement campaign was carried out in HSL tunnel scenarios, as mentioned in [9, 158]. In this measurement campaign, a sliding correlation CS is operated at 28 GHz, with the Rx part placed inside a HSL and the Tx placed near the track at the tunnel exit. The measurement is divided into two scenarios [9]: inside the tunnel and exit part of the tunnel. In this common railway environment, the PL is modelled with two slopes in [9], PL_A and PL_B, respectively in Tab. 5.4.

TABLE 5.4: PL models obtain from measurements in [9].

Case	β	σ	$\mathbf{PL}_{d_0}$ **(dB)**
PL_A	2.4	1.3	53.8
PL_B	0.38	1.1	99.2

Unlike in [158], where another segment is added before the tunnel, PL uses three slopes and two different models. The result is shown in Tab. 5.5.

TABLE 5.5: PL models obtain from measurements in [9, 158].

Case	β	σ	$\mathbf{PL}_{d_0}$ **(dB)**
PL_{A1}^{AB}	2.43		
PL_{B1}^{AB}	1.43	2.53	51.8
PL_{C1}^{AB}	6.49		
PL_{A1}^{CI}	1.96		
PL_{B1}^{CI}	1.81	2.58	61.4
PL_{C1}^{CI}	6.28		

Another measurement campaign using the Shinkansen HSL is presented in [159]. This campaign only investigates the maximum available throughput at 28 GHz for a specific architecture. From this measurement campaign, the results show a decrease in throughput reduction as the speed increases, but a 1 Gbps can be achieved at 200 km/h.

5.2.3 Simulation Tools

5.2.3.a RapLab

In [160], the author presents a simulation made for the HSL environment using the RapLab simulation tools [19]. The RapLab simulator is a commercial tool that uses the ray launching technique to estimate the coverage and the different propagation paths that exist in a scenario.

The simulation settings are a carrier frequency of 62.5 GHz, a 30° HPBW directional antenna and a transmit power of 30 dBm. The environment consists of two railway tracks with a catenary gantry structure. The portals, cantilevers, and tracks are simulated with a full steel composition, and the ground and fences are fully composed of concrete. However, the body of the train is not included in the simulation, since there is no train modelled in the simulation. Regarding the data, only data above a threshold of 40 dB from the maximum received power path are considered, if this threshold implies a power level higher than -100 dBm.

From this simulation, the mean, RMS DS max, ASA and ASD for both azimuth and elevation angles are extracted and presented in Tab. 5.6.

TABLE 5.6: RMS DS, ASA and ASD for simulation scenario presented in [160].

Parameter	Mean Value	Max Value
RMS DS	0.59 ns	1.56 ns
ASA (azimuth)	0.86°	4.46°
ASA (elevation)	2.01°	5.22°
ASD (azimuth)	0.79°	4.45°
ASD (elevation)	1.03°	2.60°

Finally, this paper aims to present a dynamic SV model for the railway environment. First, from the simulation, the area can be divided into five areas, A, B, C,

D, and E. Finally, the F case covers the entire simulated distance. The parameters of the SV model are detailed as follows, Λ_1, Λ_2 represent the cluster and ray arrival rate, respectively, Γ_1, Γ_2, are the cluster and intra-cluster power decay.

Finally, the AoA are modelled with a Laplace distribution, with mean values θ^{LOS}, ϕ^{LOS}, θ^{NLOS} and, ϕ^{NLOS}, and deviations Ω_1^{θ}, Ω_1^{ϕ}, Ω_2^{θ}, and Ω_2^{ϕ}, are presented. All the results can be found in Tab. 5.7.

TABLE 5.7: SV parameters obtain from the simulation in [160].

Area	$\frac{1}{\Lambda_1}$ **(ns)**	Γ_1 **(ns)**	Ω_1^{θ} **(deg)**	Ω_1^{ϕ} **(deg)**
A	1.39	1.92	5.39	5.89
B	0.89	0.61	3.92	3.54
C	0.55	0.22	3.35	2.44
D	0.36	0.17	3.41	1.64
E	0.29	0.14	3.19	1.42
F	0.50	0.35	3.52	2.61
	$\frac{1}{\Lambda_2}$ **(ns)**	Γ_2 **(ns)**	Ω_2^{θ} **(deg)**	Ω_2^{ϕ} **(deg)**
A	0.18	0.70	2.20	2.10
B	0.15	0.56	1.43	1.23
C	0.11	0.30	0.96	0.91
D	0.01	0.22	0.73	0.70
E	0.06	0.19	0.61	0.56
F	0.09	0.33	1.01	0.86

The results show that the cluster and beam arrival rates decrease as the distance increases. Also, the power decay is weaker at long distances than at short distances. These results indicate that there are fewer MPCs at long distances, and the extra distances made by MPCs are reduced, suggesting that the immediate environment, made up of metallic catenary portals, has the greatest influence on the radio propagation channel.

5.2.3.b Cloud RT

The Beijing Jiaotong University has developed a ray tracing simulator called Cloud RT [20]. This simulator can perform simulations for different environments, especially railways, at different frequency bands, from mmWave to THz. Cloud RT can be used in different railway environments through six different modules representing different scenarios. These scenarios are introduced and detailed in [148, 149], and presented in Tab. 5.8.

TABLE 5.8: Presentation of the six modules of Cloud RT [148, 149].

Module	**Name**
1	Tunnel entrance on the steep wall connecting cutting with crossing bridges
2	Viaduct with open train station
3	Urban with semi-closed train station
4	Rural with cut and cover tunnel
5	Rural connecting double-track tunnel
6	Single-track viaducts

In addition, this simulator has been calibrated by comparing the results obtained with the measurement campaign. The first comparison is made with marshalling yards as presented in [161] and in [162], where the simulation results are validated. The second measurement campaign used to validate the ray tracing operation is carried out with the MHN system. The results of this comparison can be found in [163] and allow the author to validate the correct operation of the ray tracing simulator.

In order to reduce the computation time and the complexity of the scene, a study is carried out to extract the significant objects that most influence the mmWave railway environment. These studies provide the main significant objects and their materials for the different modules, and are presented in [164–166]. Furthermore, some key electromagnetic parameters of the object material have been measured using a VNA and can be selected in the ray tracing. If the material is not characterized, the ITU-recommended parameters are selected by default.

This ray tracing was used to characterize the radio propagation channel for all the scenarios mentioned on Tab. 5.8. The simulation is set to operate at a bandwidth of 8 GHz with a centre frequency of 64.82 GHz and a train speed of 500 km/h. The antennas are chosen to be omnidirectional and the Tx is placed on top of a mast while the Rx is placed in the windscreen of the train. Two antenna setups are realized, setup 1, with both Tx and Rx placed higher than the setup 1. From this simulation, Large Scale Parameter (LSP) are modelled such as PL, the mean value of the RMS DS, noted $\overline{\sigma}_{\text{RMS DS}}$, the mean value of 50% coherence bandwidth, noted $\overline{\mathcal{B}}_{0.5}$, and SSP, as well as the Rician K-Factor and the Shadowing Factor (SF). All the results can be found in Tab. 5.9, Tab. 5.10, Tab. 5.11, Tab. 5.12, Tab. 5.13, and Tab. 5.14.

TABLE 5.9: Results for Module 1.[148, 149]

Visibility	**Antenna Setup**	**Parameter**	**Value**
LOS	1	PLE	1.78
		SF (dB)	4.99
		K-Factor (dB)	-6
		$\overline{\sigma}_{\text{RMS DS}}$ (ns)	7.43
		$\overline{\mathcal{B}}_{0.5}$ (MHz)	74.9
	2	PLE	1.78
		SF (dB)	5.34
		K-Factor (dB)	-6.54
		$\overline{\sigma}_{\text{RMS DS}}$ (ns)	3.97
		$\overline{\mathcal{B}}_{0.5}$ (MHz)	402

TABLE 5.10: Results for Module 2.[148, 149]

Visibility	Antenna Setup	Parameter	Value
LOS	1	PLE	1.57
		SF (dB)	5.26
		K-Factor (dB)	-30.91
		$\overline{\sigma}_{\text{RMS DS}}$ (ns)	31.95
		$\overline{\mathcal{B}}_{0.5}$ (MHz)	76.8
	2	PLE	1.49
		SF (dB)	5.44
		K-Factor (dB)	-19.48
		$\overline{\sigma}_{\text{RMS DS}}$ (ns)	21.71
		$\overline{\mathcal{B}}_{0.5}$ (MHz)	71.33
NLOS	1	PLE	2.34
		SF (dB)	5.26
		K-Factor (dB)	-65.13
		$\overline{\sigma}_{\text{RMS DS}}$ (ns)	41.20
		$\overline{\mathcal{B}}_{0.5}$ (MHz)	106.81

TABLE 5.11: Results for Module 3.[148, 149]

Visibility	Antenna Setup	Parameter	Value
LOS	1	PLE	1.88
		SF (dB)	5.33
		K-Factor (dB)	-38.14
		$\overline{\sigma}_{\text{RMS DS}}$ (ns)	14.90
		$\overline{\mathcal{B}}_{0.5}$ (MHz)	56
	2	PLE	1.76
		SF (dB)	5.85
		K-Factor (dB)	-14.12
		$\overline{\sigma}_{\text{RMS DS}}$ (ns)	12.64
		$\overline{\mathcal{B}}_{0.5}$ (MHz)	99.75

TABLE 5.12: Results for Module 4.[148, 149]

Visibility	Antenna Setup	Parameter	Value
LOS	1	PLE	1.62
		SF (dB)	6.28
		K-Factor (dB)	-27.84
		$\overline{\sigma}_{\text{RMS DS}}$ (ns)	37.61
		$\overline{\mathcal{B}}_{0.5}$ (MHz)	31.80
	2	PLE	1.49
		SF (dB)	4.96
		K-Factor (dB)	-18.32
		$\overline{\sigma}_{\text{RMS DS}}$ (ns)	20.26
		$\overline{\mathcal{B}}_{0.5}$ (MHz)	89.20

TABLE 5.13: Results for Module 5.[148, 149]

Visibility	Antenna Setup	Parameter	Value
LOS	1	PLE	1.86
		SF (dB)	5.82
		K-Factor (dB)	-2.10
		$\overline{\sigma}_{\text{RMS DS}}$ (ns)	1.93
		$\overline{\mathcal{B}}_{0.5}$ (MHz)	113
	2	PLE	1.85
		SF (dB)	6.51
		K-Factor (dB)	-5.64
		$\overline{\sigma}_{\text{RMS DS}}$ (ns)	24.45
		$\overline{\mathcal{B}}_{0.5}$ (MHz)	61.55

TABLE 5.14: Results for Module 6.[148, 149]

Visibility	Antenna Setup	Parameter	Value
LOS	1	PLE	1.69
		SF (dB)	6.08
		K-Factor (dB)	-7.18
		$\overline{\sigma}_{\text{RMS DS}}$ (ns)	1.93
		$\overline{\mathcal{B}}_{0.5}$ (MHz)	113
NLOS	2	PLE	2.57
		SF (dB)	10.92
		K-Factor (dB)	-41.22
		$\overline{\sigma}_{\text{RMS DS}}$ (ns)	7.64
		$\overline{\mathcal{B}}_{0.5}$ (MHz)	294.35

From these results, it can be seen, firstly, that the PLE is always lower than the FSPL coefficient, even in the case where the line has no tunnels. Moreover, the PLE for the NLOS case is not as high as presented in the **Chapter 3**. The author explains these results by the superposition of the LOS path, multiple-order reflections and scattering.

A similar observation can be made for the K-Factor, where it is always negative, which could indicate a Rayleigh channel. The author explains these results by saying that the influence of the environment, which is higher than expected, leads to a higher path power, and the channel behaves like a Rayleigh channel.

There is a huge difference in the RMS DS value. Indeed, for different scenarios, the difference can reach 20 times higher, and for the same scenario, this value can reach 2. This implies that long effective multipath exists in relatively large and open spaces, such as viaducts and rural areas. In contrast, Modules 1 and 5 have the smallest RMS DS, mainly because the semi-enclosed and closed spaces limit the range of multipath.

Another simulation is presented in [167], where the ray tracing tool is used to characterize the tunnel environment in the 30 GHz band with omni and directional antennas. The directional antenna has a HPBW of 8° for a gain of 22 dBi. The tunnel material is considered to be essentially concrete, and it is modelled as a surface made of this single component, with its electromagnetic parameters measured with VNA.

Then, from this measurement, the reflection, and scattering are fitted to have a continuous variation of these as a function of angle.

The simulation area is then divided into two regions to compute the results, with a boundary computed using the following equation, $D = \frac{H_{Tx}-H_{Rx}}{\tan(\theta+\alpha/2)}$, where H_x is the height of the element being considered and $\tan(\theta + \alpha/2)$ is the pointing direction plus half the HPBW.

From this simulation LSP such as PL, RMS DS and RMS Doppler spread are shown. In addition, the cross-polarization factor in both azimuth, XPD_θ, and elevation, XPD_ϕ, and the decorrelation distance, d_m, are shown for two thresholds are presented.

Finally, the Rician K-Factor and the SF, σ, are presented. The results are divided into three setups, **Setup 1**, with directional antenna, **Setup 2**, with directional antenna for the Tx and omnidirectional antenna for the Rx, and **Setup 3**, with both connected to the omnidirectional antenna. The mean value obtained for each extracted parameter is presented in Tab. 5.15.

TABLE 5.15: Mean value of extracted parameters from simulation given in [167].

Parameter	**Setup 1**		**Setup 2**		**Setup 3**	
PLE	1.10		1.10		1.11	
σ (dB)	3.43		3.49		3.47	
Threshold	0.5	e^{-1}	0.5	e^{-1}	0.5	e^{-1}
d_m (m)	2.46	3.36	2.08	3.09	1.89	2.68
Regions	Near	Far	Near	Far	Near	Far
K-Factor (dB)	20.31	-5.80	12.28	-6.54	7.80	-6.85
RMS DS (ns)	2.12	0.47	2.97	0.54	4.42	0.70
RMS Doppler Spread (kHz)	0.95	0.41	1.04	0.41	1.20	0.41
XPD_θ (dB)	26.84	3.13	18.66	2.54	14.34	2.49
XPD_ϕ (dB)	26.90	1.38	18.33	0.80	12.23	0.63

These results show a PLE around 1.1, which the author explains by the tubular structure of the tunnel causing a waveguide propagation effect. The use of directional antennas has an effect on the decorrelation distance, which is increased, and on the RMS DS, due to the resulting spatial filtering. However, it does not affect the RMS Doppler spread and the K-Factor. Finally, the cross-polarization factor shows that vertical polarization is more resistant to depolarization than horizontal polarization.

5.2.4 Conclusion

This section demonstrates the small number of railway measurements required to obtain a realistic railway channel model. In the literature, only one measurement has been realized in the mmWave band for marshalling yards, which is a comparable environment for our purposes.

Furthermore, not only is the number of measurements reduced, but access to the measurement results may be impossible. For example, in [163, 164], the author presents simulation results with a calibrated simulator based on a measurement campaign that is only available for the Asia-Pacific Telecommunity (APT) community.

5.3 Environment Facilities for Measurement Campaign

5.3.1 Tracks And Vehicles

As part of the Millimeter-Wave For Rail (mmW4Rail) ANR project, it has been possible to rent the infrastructure of the Trial Railway Center (CEF) to carry out measurements. The CEF [168] is located in Valenciennes, in the north of France, and has several facilities for testing new trains in real condition. The Fig. 5.2 presents the centre, and its three areas:

1. Static test zone: in this area, three outdoor tracks of 200 m long are installed, two with catenary installation and one without.
2. Endurance ring and speed track: the endurance ring is used to test the train operation for long dynamic runs with a maximum speed of 90 km/h, and 110 km/h for the speed track.
3. Subway line: a 650 m subway line is installed to test the correct operation of the Lille underground. The maximum speed on this line is 70 km/h.

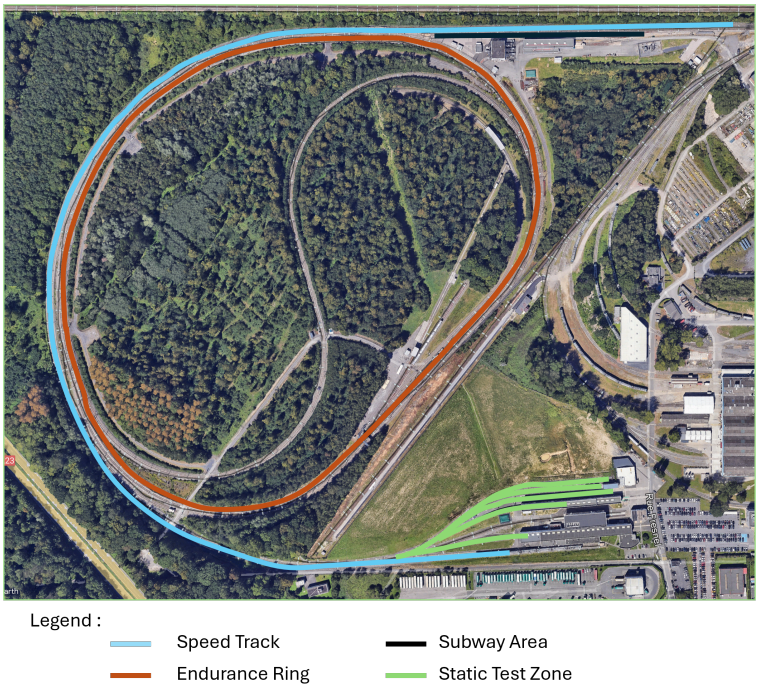

FIGURE 5.2: The CEF map and placement of the different tracks on each area.

To perform the measurements, the CS is placed on the static test area, with three outdoor tracks available. The three tracks are named, **VES1**, **VES2** and **VES3**, with a maximum distance of 200 m, and are shown in Fig. 5.3.

VES1 track is fully made of concrete and has an overhead catenary line with a mast line only on one side of the track. In addition, a metallic warehouse in its direct surroundings is placed on the other side.

VES2 track is located between **VES1** and **VES3**. It is a casual train line with ballast and a reduced version of concrete-made sleepers. On one side the overhead

catenary mast line is presented, and the other side is composed of regularly spaced lampposts with open field area behind them. As for **VES1**, this track ends with NLOS visibility, as the warehouse masks the link.

VES3 track is made with ballast and a complete version of wood-made sleepers, with on the one side the **VES2** track with regularly spaced lamppost. The other side is a completely open field area and there is no overhead catenary or mast line. In the 3 cases, the visibility situation ends with NLOS because of the warehouse, which masks the link.

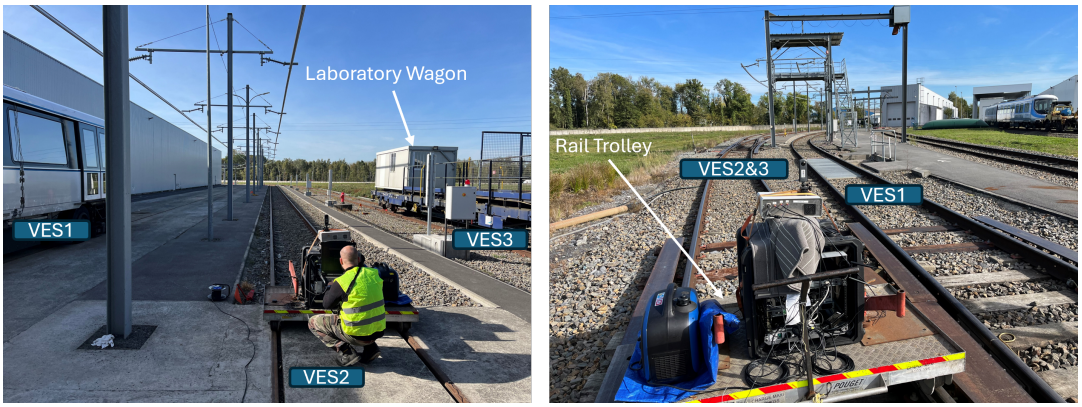

FIGURE 5.3: Environment of the three tracks available for measurements at, on the left, the lower distance and, on the right, at the maximal distance.

Two different vehicles are available to carry out measurements at different speeds, a rail trolley and a laboratory wagon towed by a rail truck and shown in Fig. 5.3. The first is used for low-speed measurements and the second for in situ measurements at higher speeds.

5.3.2 Scenarios

Two main scenarios have been studied, platooning and 3GPP mmWaveHSL. In each scenario, both horizontal and vertical polarization are investigated and, thanks to the dual receiver, cross-polarization can be estimated.

Platooning is the concept of a virtual coupled train. It consists of two steps, first the train approaches the train in front of it. Second, the following train keeps a constant distance. In our case, the first scenario is investigated. This scenario aims to show the influence of the surrounding trains in the platooning scenario, the Fig. 5.4 shows the three realized measurements:

1. Scenario 1: the rail trolley, where the Tx is installed, and the Rx are aligned and on the same track. This is the main coupling scenario, the aim is to investigate the distance impact on the coupling procedure
2. Scenario 2: the rail trolley is placed on **VES1** and the Rx antenna is tilted by 30° in the azimuth plan to cover the distance of the **VES1** track. This scenario simulates the impact of different communication systems in the surroundings of the coupling procedure.
3. Scenario 3: same as Scenario 2 expected that the rail trolley is placed on **VES3**.

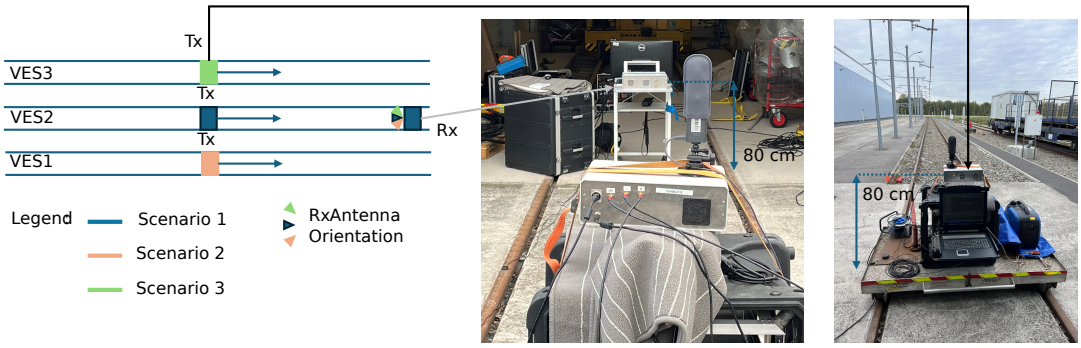

FIGURE 5.4: Platooning scenario configuration.

3GPP HSL scenario introduces an architecture type [169] to ensure the overall coverage of the HSL as shown in Fig. 5.5. This architecture divides the track into different sections, each controlled by a Baseband Processing Unit (BBU) at 1732 m intervals. The BBU control three Remote Radio Head (RRH) spaced 580 m apart, ensuring communication with the train. The RRH are organized with two on the same side and the last one on the other, and the dispositions are alternated.

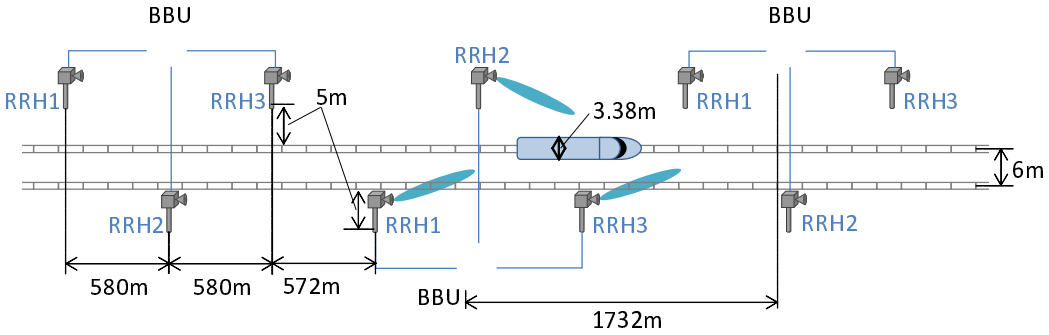

FIGURE 5.5: Illustration of 3GPP mmWave HSL [169].

For this scenario, the Fig. 5.6 shows the two realized measurements, as it can be seen, the Rx, playing the roles of RRH, is not placed at the height mentioned in [169], because the CEF does not allow us to install it close to the catenary for safety reasons. Also, for similar reasons, the maximum speed is limited to a maximum of 20 km/h. The Tx is approximately at the same height as a driver's cab. Scenario 3, presented in Fig. 5.6, is another type of platooning measure. The first results of this measure will be presented in the next section.

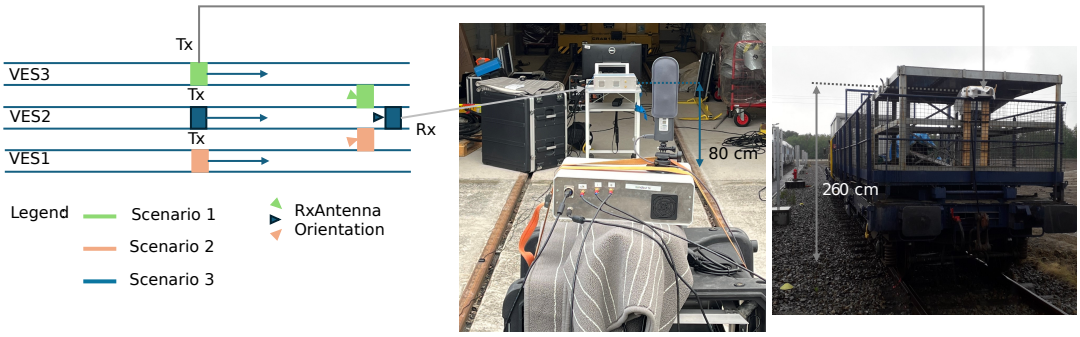

FIGURE 5.6: Illustration of measurements made in the 3GPP HSL scenario.

5.3.3 Measurement Campaign Synthesis

From this measurement campaign, several measurements were made in both scenarios mentioned above. The total number of measurements made during this campaign is 101, resulting in approximately 437 GB of collected data divided between the platooning and 3GPP HSL scenario. Furthermore, in each scenario, the antenna polarization is in co-polarization and cross-polarization. In co-polarization, the measurements are SIMO with both Rx in the same polarization as the Tx. In cross-polarization, the first Rx is in the same polarization as the Tx and the second Rx is in the other polarization.

In the platooning scenario, the measurements were made on each track and resumed in Tab. 5.16.

TABLE 5.16: Synthesis of the measurements made in platooning scenario.

Track	Polar. Config.	No. of Measurements
VES1	Cross-Polar.	6
VES2	Co-Polar.	9
	Cross-Polar.	8
VES3	Co.Polar.	10
	Cross-Polar	8
Total	-	41

For the 3GPP HSL scenario, the number of measurements made on each configuration is resumed in Tab. 5.17.

TABLE 5.17: Synthesis of the measurements made in 3GPP HSL scenario.

Track	Polar. Config.	No. of Measurements
VES1	Co-Polar.	10
	Cross-Polar.	6
VES2	Co-Polar.	15
	Cross-Polar.	16
VES3	Co.Polar.	8
	Cross-Polar	7
Total	-	62

5.4 First Results

5.4.1 Scene Overview

The measurement was made on the **VES2** track at a distance of 200 m distance. The Tx is installed on the laboratory wagon as seen in Fig. 5.6 and the Rx is installed in the front of the metallic warehouse. The Fig. 5.7 shows the localization point obtained from the GNSS RTK for the measurement and a panoramic view of the immediate surroundings.

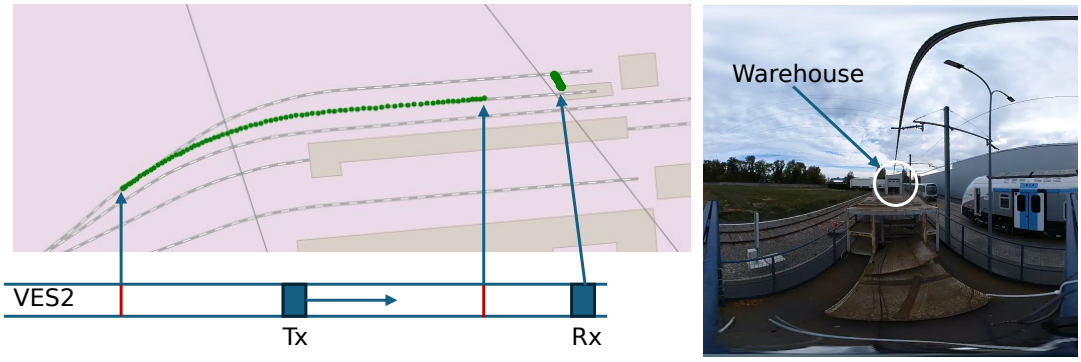

FIGURE 5.7: Measurement run GNSS RTK data and panoramic pictures.

This environment can be divided into three areas as presented in Fig. 5.8 and defined as follows:

1. **Zone 1**: LOS situation, the Rx and Tx are aligned and the train follows the straight track. This section can be seen in the 180° picture of the Fig. 5.7.
2. **Zone 2**: OLOS situation, the track curvature started and the LOS started to be obstructed by the alignment of the catenary mast line.
3. **Zone 3**: NLOS situation, the link is masked by either a train parked in **VES2**, as now, or by the warehouse of the static test area.

FIGURE 5.8: The different visibility situation with in **A**, the OLOS, **B**, the NLOS situation generated by train masking, and **C** generated by the warehouse of the static test area.

5.4.2 Path Gain

The first information derived from the measurement is the path gain. Its evolution and FSPL as a function of distance for both polarization is shown in Fig. 5.9. The first observation that can be made about this figure, is the division range, mentioned above. Indeed, on Fig. 5.9, the area between the beginning and the first black line is **Zone 1**. **Zone 2** is situated between the two black lines, and **Zone 3** is from the second black line to the end. Moreover, the PL is coherent with the FSPL, and the gain higher than the FSPL could be explained by the constructive interference of the MPCs. Another observation that supports this hypothesis is the presence of slow and fast fading, which implies small and large-scale variation due to MPCs.

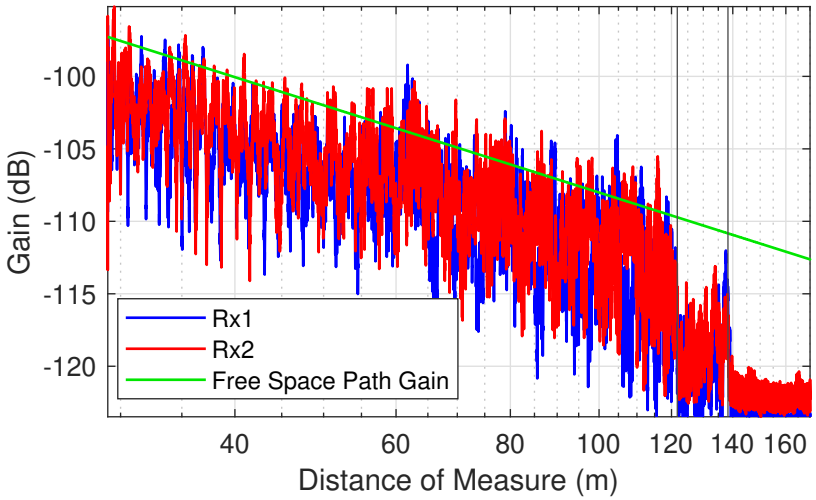

(A) Horizontal polarization.

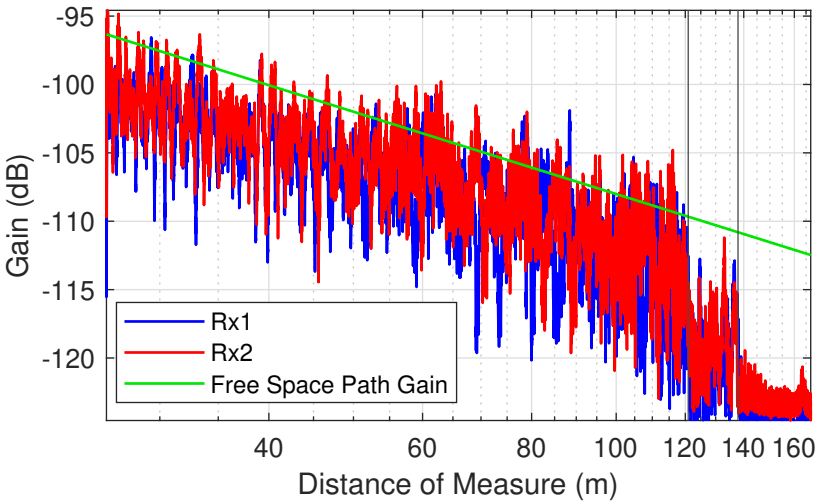

(B) Vertical polarization.

FIGURE 5.9: Path gain, FSPL and the area division of the measurement area.

5.4.3 PDP and Scattering Function

The evolution of the path gain evolution during the measurement leads to the assumption of the presence of MPCs. To study it correctly, it is necessary to calculate the PDP. In our case, the PDP is calculated with interpolated CIR. In fact, the maximum speed was well below the maximum settings of our CS, which leads to oversampling of the radio propagation channel. To correct this, the CIR are interpolated to obtain a spatial sampling of $\lambda/10$. Once this interpolation is done, the PDP calculation window contains 2000 CIR and is intended to measure 20λ. Generally, a larger calculation window of the order of 40λ is maintained, but a window size of 20λ validates the WSS-US assumption.

The Fig. 5.10 shows the PDP obtained for both polarizations, and for a Rx, since in each case, the two PDP are identical. From this plot, the evolution of the main component implies that the train is moving in the direction of the Rx and some MPCs can be seen. In particular, from the beginning to 60 m, two paths have a slope quite different from the other MPCs and are present identically for both polarizations.

This path is visible within both polarizations. The rest of the demonstration will be done only with the vertical polarization. First, the difference in length between the main component and the component with a different tilt is examined. In the Fig. 5.12, the white curve represents a path which comes with an additional distance of 3 times the main component. It can be seen that this curve fits well with the MPCs, and proves that this path is three times longer than the main component. Finally, the origin of this path in the environment must be investigated.

FIGURE 5.10: Interpolated PDP for both polarization

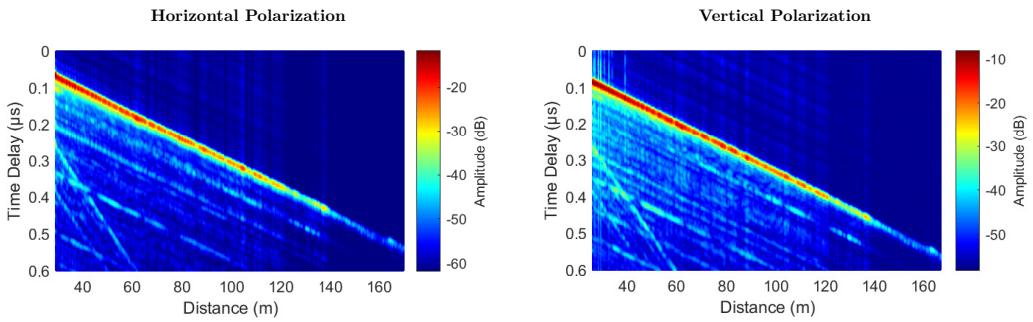

This path, which is three times longer than the main component, can also be found in the scattering function. The Fig. 5.11 shows the normalized scattering function. This plot shows Doppler shifts with higher values than the main component appears. This value shows a path with a velocity that is three times higher than the train or with an increasing distance faster than the main component. This component appears from the beginning of the measurement up to 60 m, as for the paths mentioned above.

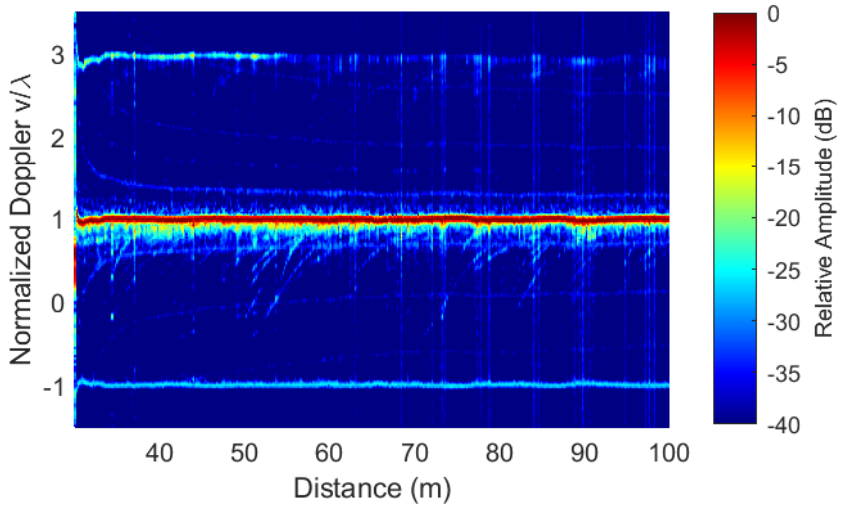

FIGURE 5.11: Normalized scattering function.

To validate the fact that the origin of this path leads to a higher Doppler shift, the scattering function is computed on the main and auxiliary paths. The scattering function is realized on the CIR for a distance size of 1 m size. The Fig. 5.13 shows the interpolated CIR and the study area of the MPCs.

The Fig. 5.14 shows the scattering function for both the LOS and the MPCs. The figure shows a blue line indicating the influence of the main component, and a red line indicating a value of 3. This value is consistent with the previously mentioned results that this path has a distance that increases by a factor of 3.

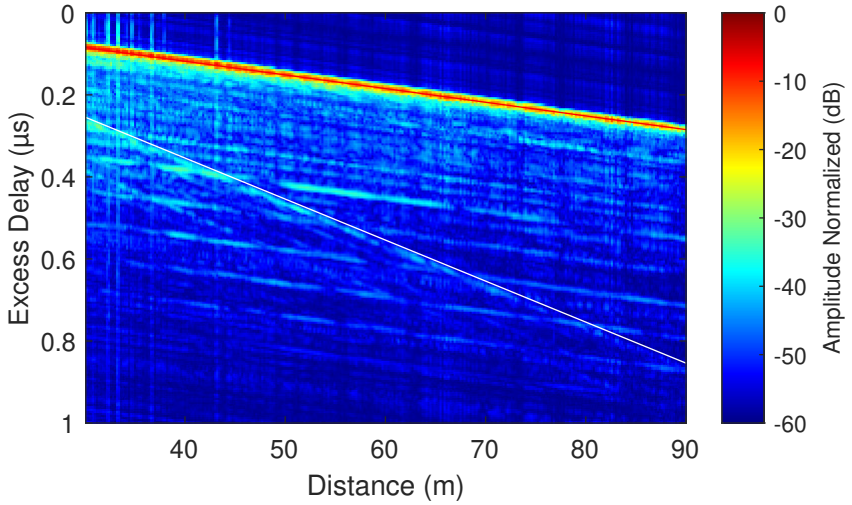

FIGURE 5.12: Interpolated PDP with an estimation of the evolution of the MPCs in white line.

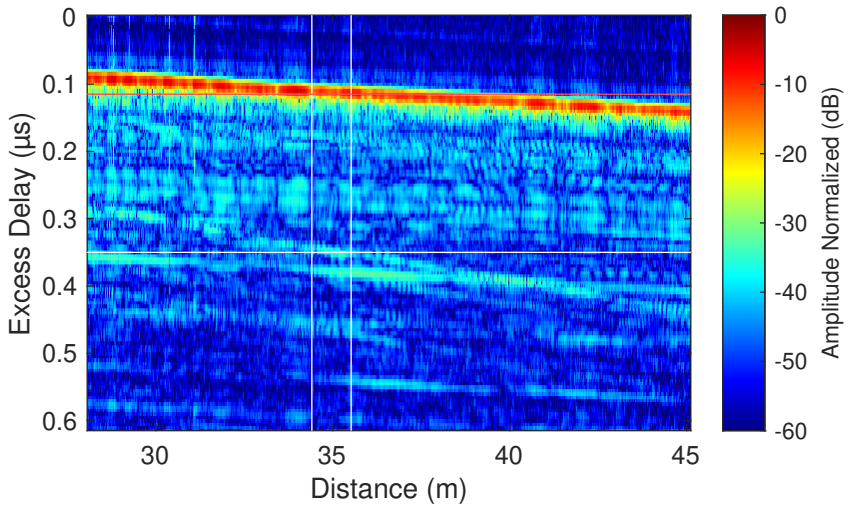

FIGURE 5.13: The CIR with the investigation area between the two vertical white lines. The red line represents the main component and the white horizontal the MPCs investigated.

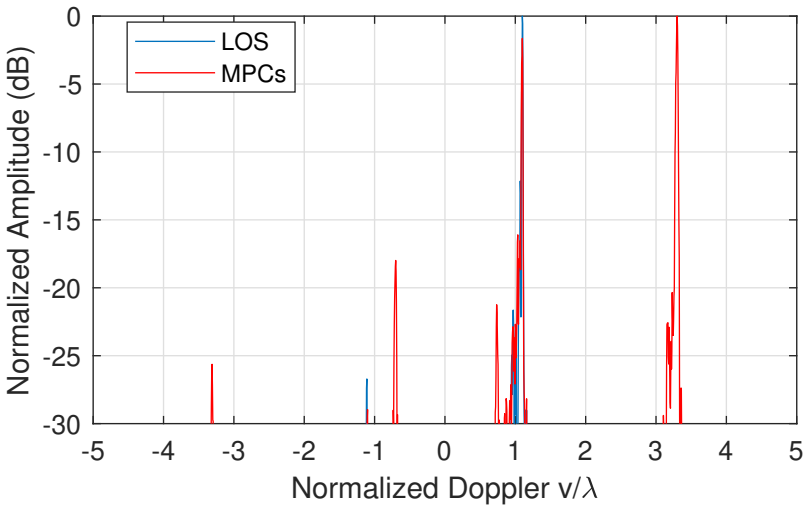

FIGURE 5.14: Scattering function for the MPCs and the main component from the interpolated CIR.

In this scenario, the Rx is placed in front of a warehouse located at the end of the **VES2** track, and the Tx is placed on top of a laboratory wagon resting on a bar with wire mesh underneath and a large metallic structure just behind it. The metallic composition of both components explains the high coefficient of reflection. The evolution of this MPCs with a factor of 3 from the main component is explained by a first reflection on the warehouse, then a second on the train, and finally this path is received at the Rx side. A schematic of the situation is presented in Fig. 5.15.

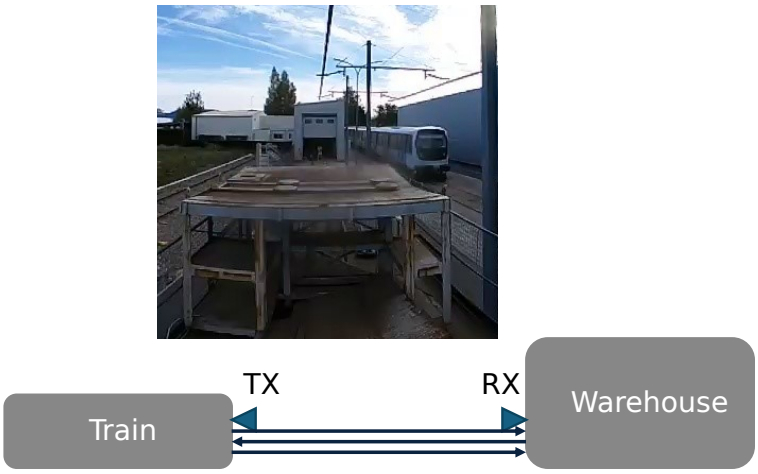

FIGURE 5.15: An illustration of the three times reflection and a picture of the warehouse at the end of VES2 track.

5.5 Conclusion

This chapter introduces the typical railway environment consisting of deterministic and stochastic elements. An overview of existing measurements and simulations made in the railway environment at mmWave band is then presented. This review presents several architectures for the HSL scenario and highlights the lack and complexity of obtaining measurement results. This lack of measurements is mainly due to the impossibility of performing measurements in a real railway environment due to the access restrictions involved.

Thanks to the mmW4Rail ANR project, the CEF infrastructure has been rented to carry out measurements in a real railway environment on different tracks and with various vehicles to perform measurements at different speeds. The three tracks available for the measurements are presented, as well as the immediate surroundings. Furthermore, the two scenarios studied in the measurements, platooning and 3GPP HSL, are presented.

Finally, the first results of a 3GPP HSL scenario are presented, and the presence of MPCs with a different slope different from the LOS appearing in the scattering function is discussed. The result of this investigation shows the influence of the multiple reflections due to the metal bearing and the structure of the train. Moreover, this study demonstrates the high sensitivity of the CS, which can distinguish multiple reflections in some cases.

6 Extraction of 3GPP Kind Model from the Measurement Campaign

Contents

6.1 Introduction

This chapter will present the exploitation of the measurement campaign in railway environment. The main statistical parameters of the radio propagation channel are extracted, and compared to the 3GPP HSL scenario [170] channel models. First, the techniques to estimate the stationary area, are presented. Indeed, the investigation of the size of the stationary area is not always discussed, and often an empirical value is retained. In this chapter, the aim is to provide a technique to estimate this stationary area. Second, this technique is used in our measurement to provide, the first stationary investigation in railway environments at 60 GHz.

Then, the 3GPP HSL scenario [12] provides an architecture for the communication system along the high-speed line. Moreover, they also provide channel models for different environments, and for frequencies between 0.5 to 100 GHz. The 3GPP divides the environment into 3 outdoor and 2 indoor scenarios. The outdoor environments are called RMa, UMa and UMi-street canyon. The indoor environments are called InH-office, and Indoor Factory (InF). In our case, only the outdoor scenarios will be used to compare our results at 60 GHz.

Before providing the statistical parameters, the different visibility situations are discussed. There are two situations: LOS and NLOS, and the estimation method is introduced. The statistical parameters are estimated once this method is introduced, starting with the PL. Moreover, the small-scale fading results are presented, and fitted with different usual distributions such as Rice, Rayleigh and Nakagami. For each distribution, a KS test is realized to validate the use of such distribution. Then, the RMS DS results are compared with the 3GPP model. Nonetheless, the Doppler spread results are presented. Finally, the results for the other measurement environments for a similar scenario are presented.

6.2 Wide Sense Stationarity

6.2.1 Collinearity Estimation

The stationarity area is essential to validate the WSS-US assumption of the radio propagation channel. The WSS validate the second-order statistical properties of the radio propagation channel. In other words, the MPCs obtained with a different delay shift are uncorrelated. Then, the stationary area is mainly limited by the validation of the WSS assumption.

The method is mainly based on the collinearity technique, as presented in [171], to estimate a part of the area where the WSS assumption is validated. Indeed, the main idea is to compare the radio propagation channel parameters between two different distances. If the similarity is below a threshold, then the stationarity is not satisfied any more. However, it is possible to use other metrics to measure the distance over which the channel statistics do not change noticeably, such as the Pearson coefficient as mentioned in [97, 171].

The collinearity matrix can be computed on the LSF, as presented in [172–174]. The equation to obtain the collinearity matrix is presented in Eq. (6.1), where $||\cdot||_F$ denotes the Frobenius norm, and the variables, $k_0 = [f_0, t_0]$, $\Delta k = [\Delta f, \Delta t]$, stand for stationarity analysis in the time and frequency domain, respectively.

$$\mathrm{col}\left(P_s(\nu,\tau;t_0,f_0)\right)[k_0,k_0+\Delta k] = \frac{\sum_{\tau=0}^{\tau_{\max}}\sum_{\nu=-\nu_{\max}}^{\nu_{\max}} P_s[\nu,\tau;k_0]\odot P_s[\nu,\tau;k_0+\Delta k]}{||P_s[\nu,\tau;k_0||_F\cdot||P_s[\nu,\tau;k_0+\Delta k||_F} \tag{6.1}$$

The collinearity can also be computed with the PDP, as presented in [97, 175, 176]. The equation to calculate the collinearity with the PDP is presented in [177], and detailed in Eq. (6.2), where $P_h(x_i,\tau)$ is the PDP at the distance of interest. This technique evaluates the similarity in terms of energy from two PDP at different time instants.

$$\mathrm{col}\left(P_h(x_i,\tau)\right) = \frac{\sum_{\tau=0}^{\tau_{\max}} P_h(x_i,\tau)\cdot P_h(x_i+\Delta x,\tau)}{\max\left\{P_h(x_i,\tau)^2, P_h(x_i+\Delta x,\tau)^2\right\}} \tag{6.2}$$

This metric will be used to estimate the statistical parameters of the radio propagation channel in a railway environment. Indeed, in [171], the author shows that the results for both methods provide similar results in dynamic scenario.

6.2.2 Results From Literature at 60 GHz

In [173], the authors present the stationarity time results for a measurement performed in a vehicular environment at 60 GHz. The proposed scenario is a static Tx placed at 15 m of the Rx placed on the roof of a car, which remains static. Both of them are not directly oriented to be facing each other but tilted with an azimuth angle to illuminate a 3 m width zone to investigate the impact of passing cars. They conclude that the LOS visibility in the V2V link exhibits large stationarity regions compared to a more specular channel. The origin of the specular reflection is due to the passing car, and features a stationarity time of approximately 20 ms. This conclusion can also be used in the NLOS cases. Indeed, in the case of high MPCs scenario, especially on NLOS situation, the stationary time is reduced to 5 ms, which is much lower than a similar scenario but with a dominant path, which leads to a stationary time of 16 ms.

This stationary time can be converted into a stationary area distance by knowing the measurement speed, which is the case in [173]. The results are summarized in Tab. 6.1, for a speed of 7.9 m/s in LOS situation and 15.8 m/s for NLOS.

TABLE 6.1: Stationarity time and distance from the measurements realized in [173].

Visibility	Number of Scatters	Stationarity Time (ms)	Stationarity Distance (λ)
LOS	**High**	>700	>1100
LOS	**Low**	19.7	31
NLOS	**High**	5	8
NLOS	**Low**	16	50.6

6.2.3 Results for our Measurement Campaign

The US part of the assumption is validated for our measurement setup, since the limited temporal resolution does not allow detecting different MPCs from the same scatters. In this section, the results obtained from the measurement campaign will be presented. The obtained results will be illustrated with a measurement performed

on the **VES3** track, with a vertically polarized antenna. The installation of the CS, and the measured localization are presented in Fig. 6.1.

FIGURE 6.1: Measurement localization.

The first step to estimate the stationary area size is to compute the collinearity matrix. In our case, it is computed from the PDP, with Eq. (6.2). For this computation, the first averaging window to compute the PDP is equal to 10λ. This size is commonly used to perform such computation as mentioned in [177]. The collinearity matrix is computed, and plotted in the Fig. 6.2.

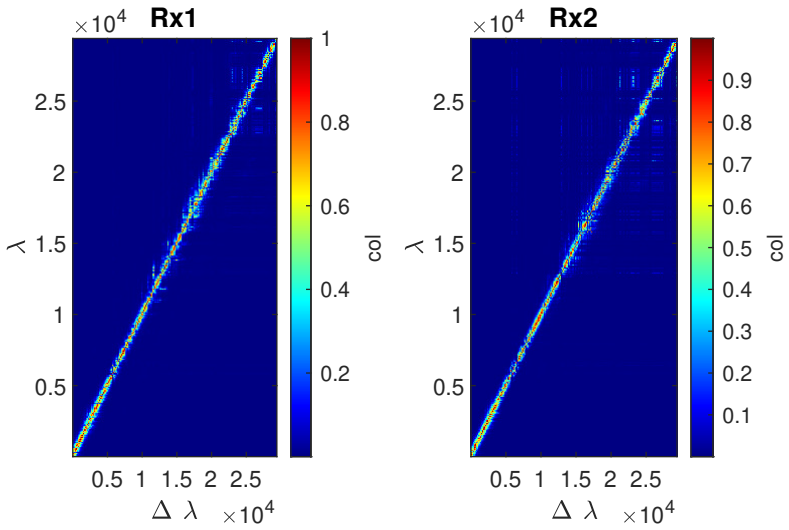

FIGURE 6.2: The collinearity matrix from the measurement made on VES3.

Then, a threshold of 0.9 is chosen as mentioned in [173, 174]. In addition, to reduce the bias value obtained with PDP with low dynamic, due to the presence of noise on this function. For the rest of the development, only the PDP with dynamic higher than 15 dB are kept.

The stationary area for all the **VES1** measurement runs, and for both co-polarization is resumed in the Tab. 6.2. It can be noted that the stationary distance remains approximately identical in function of the polarization. For the rest of the demonstration, the size of the stationary area retained will be 40λ.

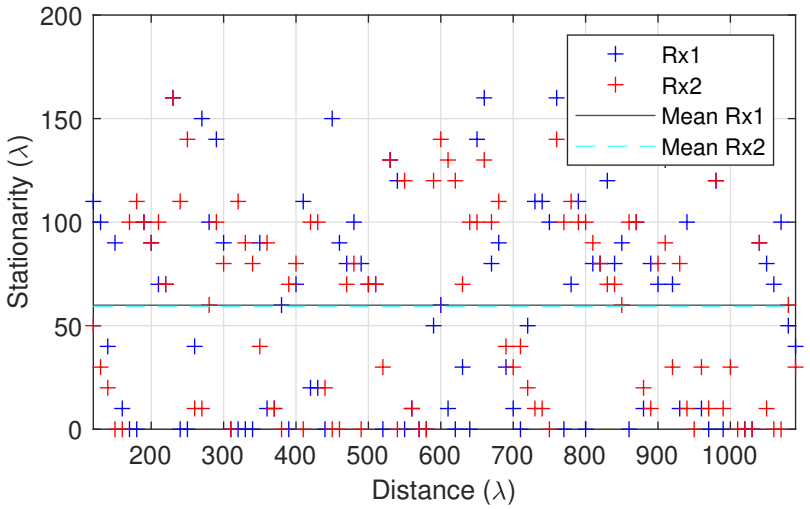

FIGURE 6.3: The stationary area from the measurement made VES3.

TABLE 6.2: Stationary area estimated.

Track	Tx Polarization	Rx Polarization	Stationarity Distance (λ)			
			min	max	μ	σ
VES1	**V**	**V**	53	64	58.63	4.53
VES1	**H**	**H**	56	75	62	7.48

6.3 Extracted Channel Model Parameters

6.3.1 Line-Of-Sight/Non-Line-Of-Sight

The first necessary knowledge is the visibility condition during the measurement trip. The LOS is defined as the absence of physical obstacles inside the Fresnel zone, as presented in the **Chapter 2**. For our purpose, the optical definition will be used. This corresponds to the optical link visibility, and the estimation is realized with the knowledge of the main components of the environment. The position of all the components is extracted from the GNSS augmented localization used in the CS, and a map of the environment, for the concerned measurements, is presented in Fig. 6.4.

The visibility estimation is obtained with a triangle technique. Indeed, each green or black crosses are framed by two crosses, which form with the position of the Rx a triangle. For the warehouse case, the distance between two green crosses is fixed to ensure a continuity triangle realization. This triangle has a shadow zone behind it, which forms a NLOS area. The technique is illustrated in Fig. 6.5. Once this estimation is made, the visibility situation can be plotted above the path loss evolution as presented in Fig. 6.6. It can be seen a good correlation between a losses peak, and the transition between LOS and NLOS situation.

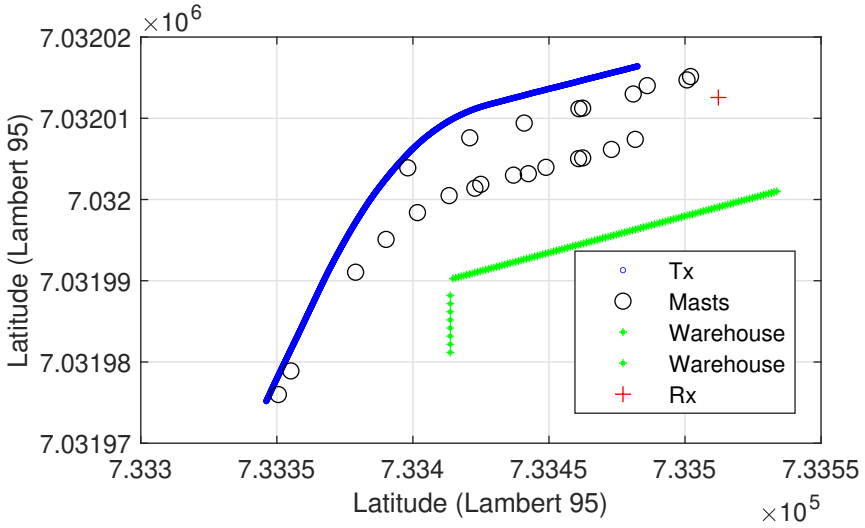

FIGURE 6.4: The map of the measurement field, with VES3 measurement example.

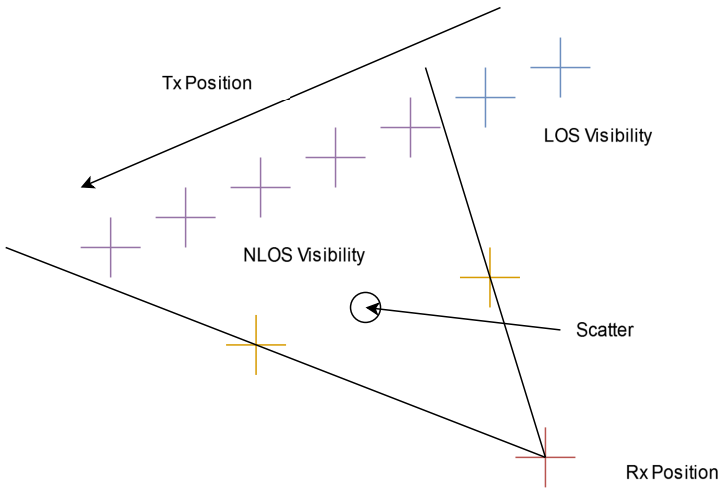

FIGURE 6.5: The triangle technique used to estimate the LOS and NLOS visibility situation.

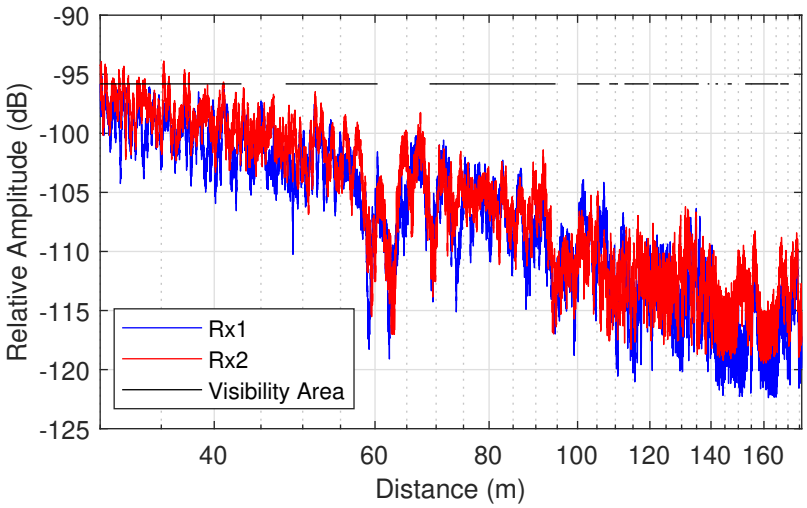

FIGURE 6.6: The evolution of the losses in the function of distance, with the visibility condition, for vertical polarization in VES3 track.

Some limitations appear with the LOS-NLOS estimation techniques due to localization error, as it can be seen in the Fig. 6.6. For example, before 60 m, the cut of the LOS visibility appears before the power drop. This issue leads to keeping NLOS samples as LOS samples, but this error stays in the measured error, and can be kept as it is. With this first-order estimation, it is possible to compute the statistical parameters of the radio propagation channel can be estimated in both LOS, and NLOS.

6.3.2 Path Loss and Shadowing Factor

6.3.2.a Retained Model for Path Loss

The first parameter to be estimated is the PL. The retained model for this purpose has to be comparable to the model mentioned in the 3GPP [12]. In our case, the carrier frequency is $f_c = 60$ GHz, the height of the Tx is $h_{\mathrm{BS}} = 2.5$ m, and the Rx height is $h_{\mathrm{UT}} = 1$ m.

For outdoor environments, the PL is divided into two slopes with a breaking distance $d_{\mathrm{BP}} = 4h_{\mathrm{BS}}h_{\mathrm{UT}}f_c/c$, where $c = 3 \times 10^8$ m/s is the propagation velocity in free space. In our case, this breaking distance is equal to 2000 m which is higher than the maximum measurement distance, which leads us to only use the first PL slope mentioned in [12]. The Tab. 6.3 resumed the different PL, for all the outdoor environments.

TABLE 6.3: Path loss models from the 3GPP [12].

Scenario	Visibility	PL [dB]	SF [dB]
RMa	**LOS**	$20\log_{10}(800\pi d) + 0.4779\log_{10}(d) - 0.7009 + 0.0014d$	$\sigma_{\mathrm{SF}} = 4$
	NLOS	$\max(\mathrm{PL}_{\text{RMa-LOS}}, 67.8015 + 42.1864\log_{10}(d))$	$\sigma_{\mathrm{SF}} = 8$
UMa	**LOS**	$63.5630 + 22\log_{10}(d)$	$\sigma_{\mathrm{SF}} = 4$
	NLOS	$\max(\mathrm{PL}_{\text{UMa-LOS}}, 49.4030 + 39.08\log_{10}(d))$	$\sigma_{\mathrm{SF}} = 6$
UMi	**LOS**	$67.9630 + 21\log_{10}(d)$	$\sigma_{\mathrm{SF}} = 4$
	NLOS	$\max(\mathrm{PL}_{\text{UMi-LOS}}, 60.4246 + 35.3\log_{10}(d))$	$\sigma_{\mathrm{SF}} = 7.82$

As it can be seen, in the LOS visibility cases, the UMi and UMa environments used a log-distance to model the PL. The RMa environment used a more detailed model. The question is, can a single slope log-distance model estimate this scenario? To validate this hypothesis, the 3GPP RMa PL model is plotted in Fig. 6.7, and compared to a single slope log-distance estimation obtained with linear regression. Moreover, the Root-Mean-Square Error (RMSE) between this log-distance single slope estimation and the 3GPP RMa PL model is presented in the same figure, and is negligible in comparison to the measurement error. This verification allows using a single slope log-distance PL for the LOS cases. For the NLOS cases, all the PL models followed the same principle of a log-distance single slope.

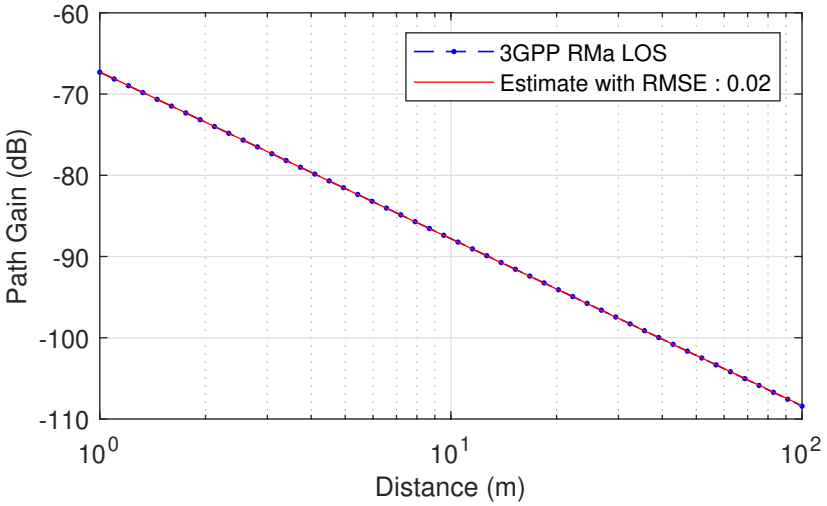

FIGURE 6.7: Comparison between 3GPP RMa PL model, with an estimated single slope.

6.3.2.b Extracted Path Loss

The single slope model is retained, and presented in Eq. (6.3). The coefficient α represent the PLE, and X_σ^{mod} the shadowing factor. The shadowing will be fitted with a normal distribution with a zero mean value and a standard deviation σ_{SF}.

$$\text{PL}_{\text{Mod}} = 10\alpha \log_{10}(d) + X_\sigma^{\text{mod}} \tag{6.3}$$

The PLE estimation is realized with a linear regression on the PL data obtained after averaging the power on a 40λ window. Then, the obtained PL is divided into equal intervals, and the median is computed for each. The choice is made to compute the median instead of the mean, since this metric indicates that 50% of the samples are below and above this value. Then, only the intervals with a median value above the noise threshold are kept. Another technique can be used which only keeps the samples that are above a noise threshold. This technique has the disadvantage of creating a platter which induces a bias for the PLE estimation. With this novel approach, the thinner the intervals, the lower the bias due to the noise.

The losses are firstly divided into LOS and NLOS situations. The Fig. 6.8a shows the PL, and its estimation in LOS condition. As mentioned before, the power samples in the area between 120 and 140 m are in a OLOS area, which is considered in our

case as alternatively LOS and NLOS cases. This absence of OLOS estimation can impact the global PLE, by reducing or increasing it.

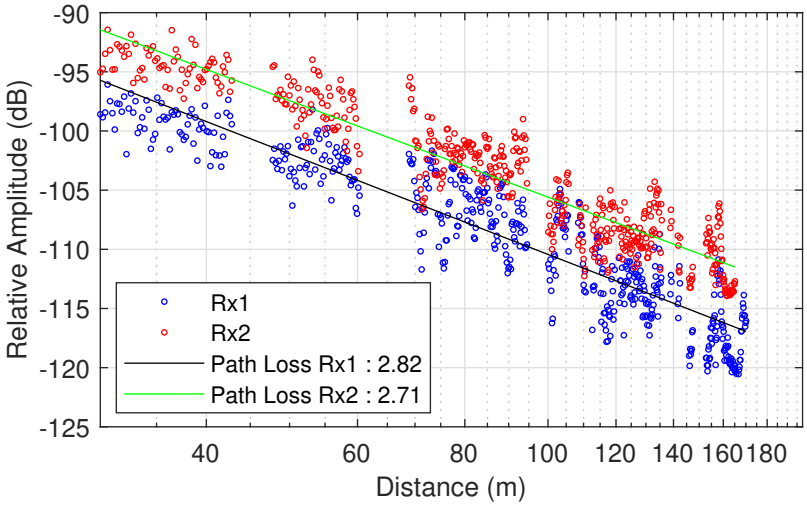

(A) LOS part of the measurement.

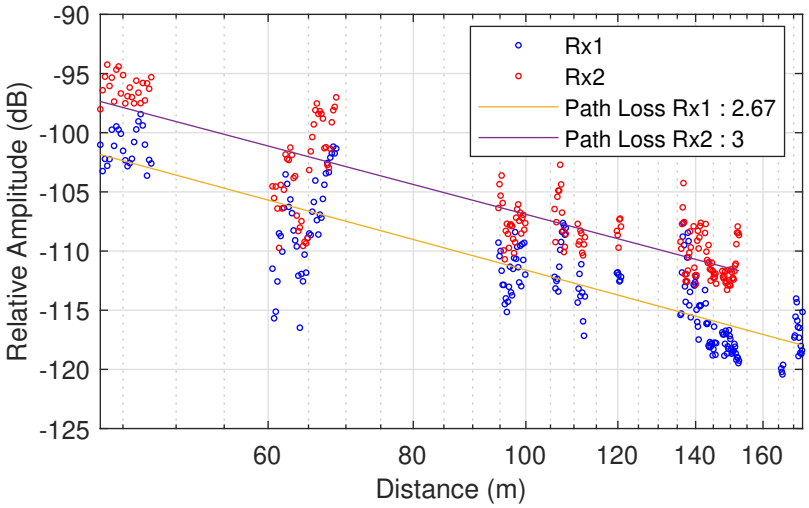

(B) NLOS part of the measurement.

FIGURE 6.8: Path loss evolution for the measurement made in VES3.

The estimation on the NLOS part is realized, and presented in Fig. 6.8b. From this figure, it can be seen that the PLE value, for both Rx is different, but it can be explained by the higher number of samples used to perform the linear regression for the first Rx than for the second one. The second observation is the PLE value which is close to the LOS situation, which can be explained by the environment. Indeed, in our case, the NLOS is due to physical obstacles, which are mainly composed of lampposts and catenary mast lines, and the size of each element is not high enough to completely mask the link as a building could do.

The shadowing fading is estimated by dividing the linear PL with the averaged power over a sliding window of 40λ moved with a step of $\lambda/10$. Then, the PDF distribution of the power in the dB scale is fitted with a normal distribution via the maximum likelihood estimator. As for the PL estimation, the intervals with a median

value below the noise floor plus 3 dB are not taken into account for the SF estimation. The Fig. 6.9 presents the results obtained for the measurement on **VES3** as presented in Sec. 6.2.3, for both visibility situations.

The PLE and SF factors for all the measures are presented in Tab. 6.6.

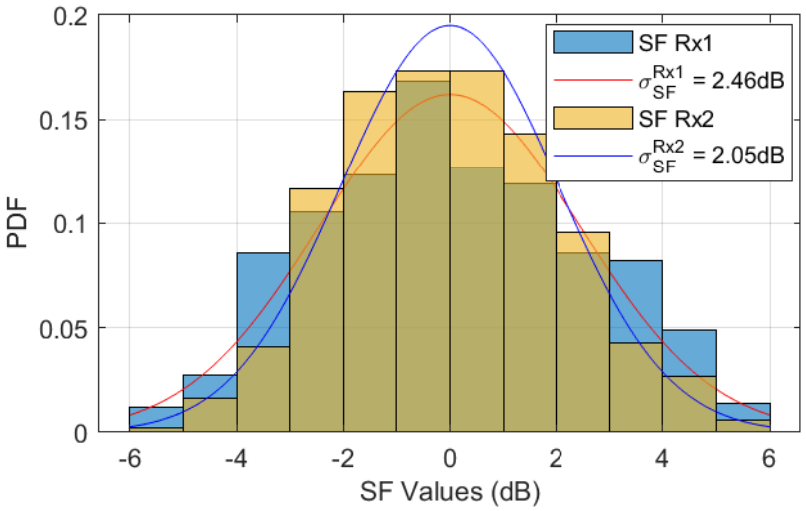

(A) LOS part of the measurement.

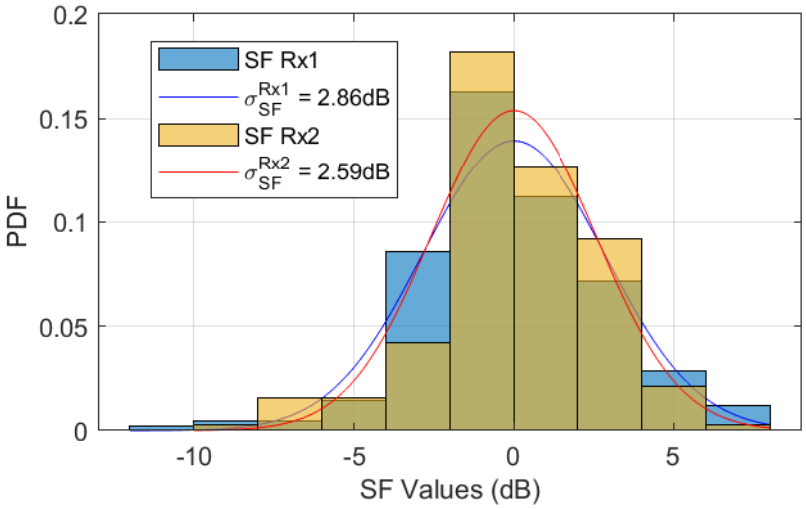

(B) NLOS part of the measurement.

FIGURE 6.9: SF PDF of the measurement made in VES3 for the scenario 3 of the 3GPP HSL environment with vertical polarization.

TABLE 6.4: Path loss estimated for all the measurements.

Track	Tx Polar.	Rx Polar.	Visibility	PLE			
				min	max	μ_{PLE}	σ_{PLE}
VES1	**H**	**H**	**LOS**	2.48	3.06	2.71	0.18
			NLOS	1.98	2.91	2.28	0.31
VES1	**V**	**V**	**LOS**	1.71	2.92	2.41	0.38
			NLOS	2.03	4.63	2.58	0.77
VES3	**H**	**H**	**LOS**	2.58	2.82	2.69	0.09
			NLOS	2.48	3.39	2.76	0.36
VES3	**V**	**V**	**LOS**	2.45	2.96	2.76	0.19
			NLOS	2.27	3.15	2.60	0.16

TABLE 6.5: Shadowing factor estimated for all the measurements.

Track	Tx Polar.	Rx Polar.	Visibility	σ_{SF} [dB]			
				min	max	$\mu_{\sigma_{\text{SF}}}$	$\sigma_{\sigma_{\text{SF}}}$
VES1	**H**	**H**	**LOS**	3.52	4.31	3.82	0.26
			NLOS	3.36	3.82	3.61	0.17
VES1	**V**	**V**	**LOS**	2.43	3.64	3.02	0.43
			NLOS	2.05	3.50	2.87	0.43
VES3	**H**	**H**	**LOS**	2.31	2.59	2.51	0.12
			NLOS	1.85	3.06	2.57	0.44
VES3	**V**	**V**	**LOS**	2.00	2.81	2.43	0.31
			NLOS	2.57	3.04	2.80	0.14

6.3.2.c Comparison with 3GPP Channel Model

This section aims to compare the PL obtained from measurement, and the PL proposed by the 3GPP. To compare the obtained PLE and the one proposed by the 3GPP, the absolute error is computed between the estimated PLE, and the PLE presented in the different 3GPP models. To illustrate the comparison, only the PLE of the different 3GPP models are kept and to compare it, the absolute error between PLE is the retained metric.

The results for all the measurements performed in the 3GPP HSL scenario are noted in Tab. 6.6. The first observation that can be highlighted is that, in the NLOS cases, the 3GPP PL model does not fit at all with the obtained PL. One reason for this could come from the LOS-NLOS estimation, which considers a shadowing zone behind a physical element. The physical elements, in our case, are lamppost or catenary masts, which do not fully block the LOS. This leads to an OLOS than a NLOS situation. But in this case, the distinction between both is not possible.

In the LOS cases, the UMa PL model is the model with the slower absolute error for the PLE, with a shadowing fading close to the mean value obtained from the measurement. In other words, the PL can be modelled with the 3GPP UMa.

TABLE 6.6: RMSE between each 3GPP PL model and estimated PL for all the measurement.

Track	Tx Polar.	Rx Polar.	3GPP scenarios	Mean PLE Abs. Error with 3GPP (LOS/NLOS)
VES1	H	H	RMa	1.81/0.61
			UMa	1.62/0.3
			UMi	1.72/0.08
VES1	V	V	RMa	0.97/1.35
			UMa	0.82/1.04
			UMi	0.92/0.66
VES3	H	H	RMa	0.46/1.65
			UMa	0.31/1.34
			UMi	0.41/0.96
VES3	V	V	RMa	0.38/2.22
			UMa	0.23/1.91
			UMi	0.33/1.53

6.3.3 Delay Spread

6.3.3.a Measurement Results

The RMS DS is the second moment of the PDP, and informs about the duration of the MPCs in the time domain. This parameter is computed with the PDP, and a threshold is retained to compute the RMS DS. Firstly, the method to compute the RMS DS is presented and start with the first step is to remove the noise from the PDP.

The method to remove the noise is detailed as follows, first the PDP instantaneous dynamic is computed, and the PDP are normalized. The Fig. 6.10 presents the obtained PDP for the measurement performed on **VES3**.

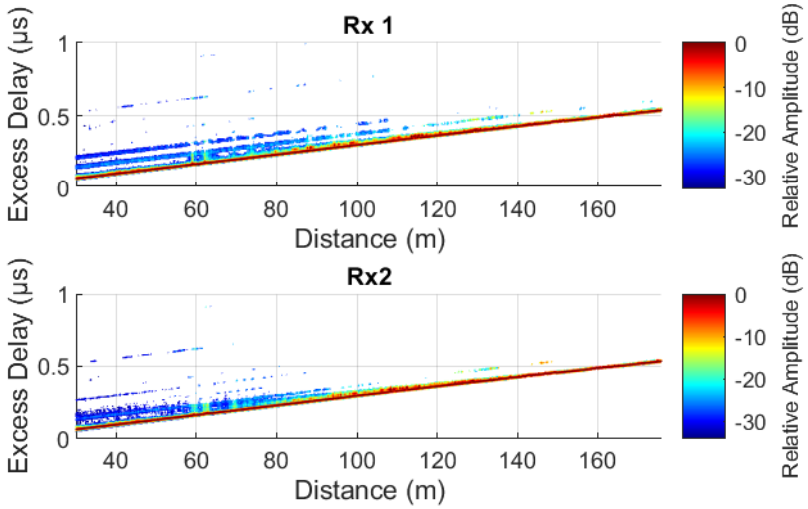

FIGURE 6.10: Normalized PDP without noise, for measurement made in the track VES3 with a vertically polarized antenna.

Then, the PDP samples higher than a threshold of noise floor are kept. This method is realized separately for the LOS and NLOS visibility cases, and the RMS DS is computed, on the normalized PDP without noise, with a threshold value of 30 dB. The RMS DS obtained for both visibility is presented in Fig. 6.11. From this figure, the impact of the lamppost masking can be seen at 60 m. Indeed, at this distance, the RMS DS is increased to reach a maximum value of 30 ns, which can be

explained by the diffraction around the lamppost leading to an increasing number of MPCs.

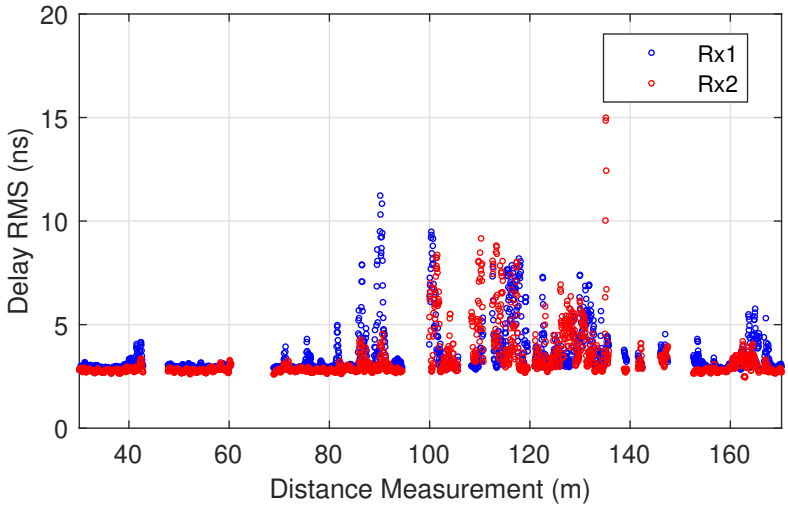

(A) RMS DS for the LOS part of the measurement.

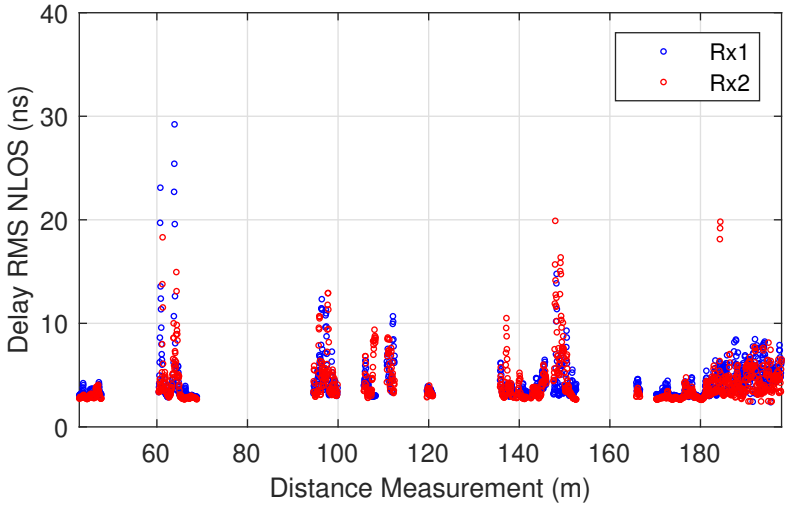

(B) RMS DS for the NLOS part of the measurement.

FIGURE 6.11: RMS DS obtained for the VES3 track measurement realized with a vertically polarized antenna.

6.3.3.b Comparison with 3GPP Channel Model

Once the RMS DS is computed, a statistical distribution is used to model it in the function of distance. To compare with the model provided by the 3GPP, the log value of the RMS DS is computed and the mean, μ_{lgDS}, and standard deviation, σ_{lgDS}, values are extracted

These parameters for the RMS DS are computed, for both LOS and NLOS scenario for the measurement presented in Sec. 6.2.3, and are presented in Fig. 6.12. For the track **VES1**, in the LOS case, the parameter μ_{lgDS} is -8.44 and the parameter σ_{lgDS} is 0.12. In the NLOS case, the parameter μ_{lgDS} is -8.40 and the parameter σ_{lgDS} is 0.12.

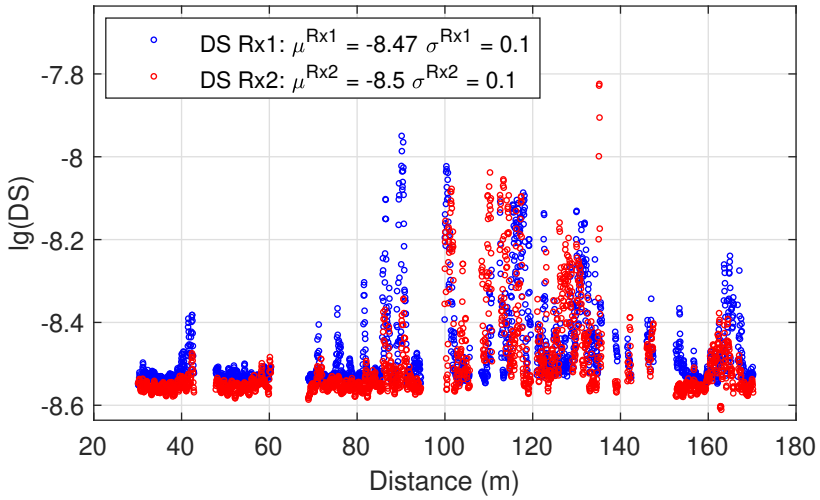

(A) RMS DS distribution and fit for the LOS part of the measurement.

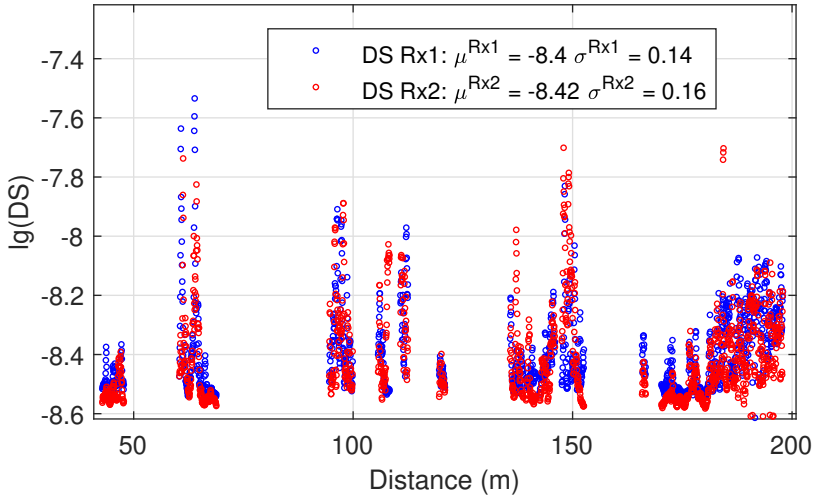

(B) RMS DS distribution and fit for the NLOS part of the measurement.

FIGURE 6.12: RMS DS distribution obtained for the VES3 track measurement realized with vertically polarized antenna, for each Rx and its associated log-normal distribution.

All the results concerning the RMS DS log-normal distribution parameters extracted from measurement data are presented in Tab. 6.7.

TABLE 6.7: RMS DS log-normal distribution parameters estimated for all the measurement made on VES1 track.

Track	Tx Polar.	Rx Polar.	Visibility	μ_{DS}				σ_{DS}			
				min	max	mean	std	min	max	mean	std
VES1	**H**	**H**	**LOS**	-8.45	-8.42	-8.44	0.01	0.10	0.13	0.12	0.01
			NLOS	-8.43	-8.38	-8.40	0.02	0.11	0.17	0.13	0.02
VES1	**V**	**V**	**LOS**	-8.47	-8.40	-8.44	0.02	0.09	0.15	0.11	0.02
			NLOS	-8.44	-8.36	-8.40	0.02	0.10	0.15	0.12	0.02
VES3	**H**	**H**	**LOS**	-8.43	-8.41	-8.42	0.01	0.15	0.15	0.15	0.00
			NLOS	-8.41	-8.40	-8.41	0.01	0.15	0.17	0.16	0.01
VES3	**V**	**V**	**LOS**	-8.49	-8.41	-8.45	0.03	0.10	0.24	0.14	0.05
			NLOS	-8.44	-8.40	-8.42	0.02	0.10	0.16	0.14	0.02

The 3GPP provides the mean and standard deviation for the log-normal distribution of the RMS DS, for frequency higher than 7 GHz only for UMi and UMa scenario. These parameters are presented in the Tab. 6.8. The high difference between the 3GPP models and the obtained parameters can be explained, firstly, by the sparsity of the radio propagation channel. Indeed, as illustrated by the literature, the 60 GHz radio propagation channel is sparser than other frequencies, leading to a lower RMS DS, and a higher mean parameter value in the log scale. This sparsity can be retrieved with the low mean value variation obtained from measurement. Finally, to model the RMS DS for the railway environment, the 3GPP with the lowest error is for the UMi scenario for LOS visibility situation and also for NLOS due to the OLOS situation in our case.

TABLE 6.8: Log normal distribution parameters from the 3GPP for the RMS DS [12].

Scenario	**Visibility**	$\mu_{\mathbf{DS}}$	$\sigma_{\mathbf{DS}}$
UMi	**LOS**	-7.57	0.38
	NLOS	-7.2585	0.57
UMa	**LOS**	-7.12	0.66
	NLOS	-6.6427	0.39

6.3.4 Small-Scale Fading

6.3.4.a Measurement Results

The small-scale fading is the power fluctuations, as defined in the **Chapter 2**, in which the mean power value is divided. The mean power value is obtained with a sliding average window of size 40λ moved with a $\lambda/10$ step. Moreover, the mean power value is computed with the same technique as the one already presented for the PL estimation. The obtained small-scale fading for all the measurements described in Sec. 6.2.3 is presented in Fig. 6.13.

Once these small-scale variations are obtained for both visibility conditions, they are divided into windows with a size of 40λ. For each window, the small-scale distribution is fitted with a Rice, Rayleigh and Nakagami distribution. For the Rice distribution, the K-Factor parameter is given in dB and is obtained with the extracted parameters of the fitting distribution with the equation presented in Eq. (6.4), where s represents the first parameter of the Rice distribution, and σ the second parameter.

$$K_{\mathrm{dB}} = 10\log_{10}\left(\frac{s^2}{2\sigma^2}\right) \tag{6.4}$$

The results, for the first window, in LOS condition are presented in Fig. 6.14. It can be observed that, in this case, the Rayleigh distribution does not fit well the PDF distribution of the small-scale variations. To automatically check the great correspondence between the proposed fit and the small-scale distribution, the KS test is proposed as a metric.

The KS test is a non-parametric statistical test that compares the estimated distribution with a reference probability distribution. The KS test is based on the maximum difference between the empirical CDF of the sample and the CDF of the reference distribution. The test statistic, $\mathcal{D}$, is realized with the equation presented

in Eq. (6.5), where $F_1(x)$ and $F_2(x)$ are the CDF of the two distributions being compared.

$$\mathcal{D} = \max_x |F_1(x) - F_2(x)| \tag{6.5}$$

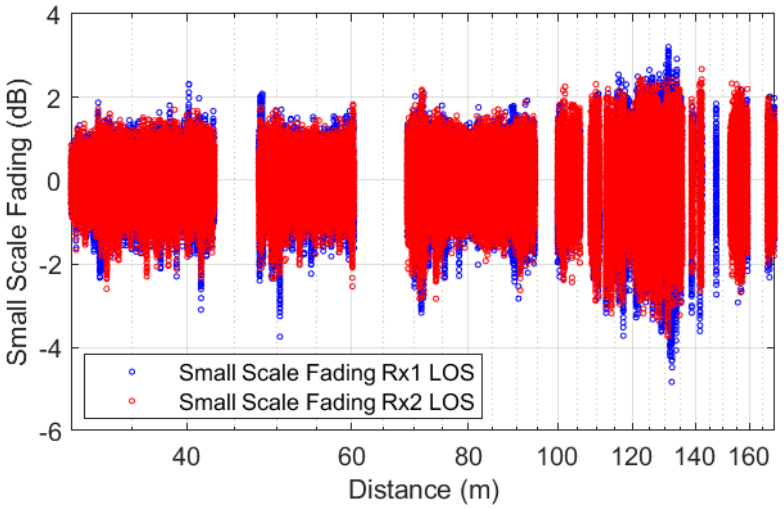

(A) LOS part of the measurement.

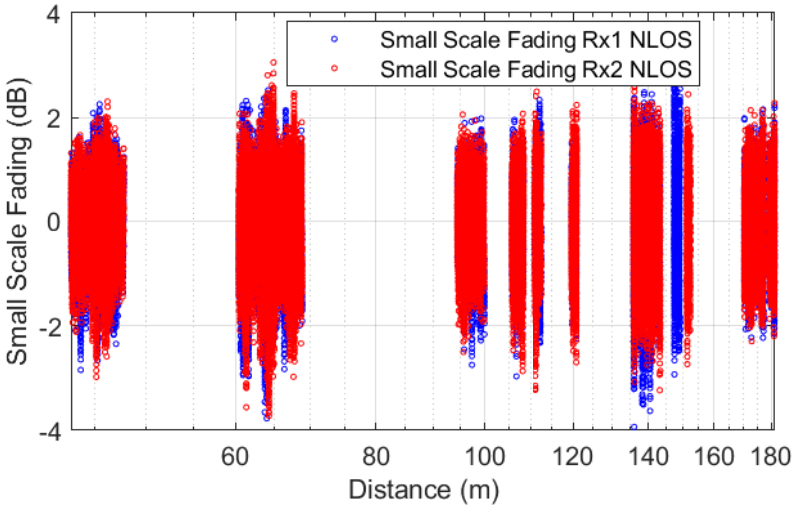

(B) NLOS part of the measurement.

FIGURE 6.13: Small-scale fading for both Rx from the measure made in the VES3 track, for vertical polarization.

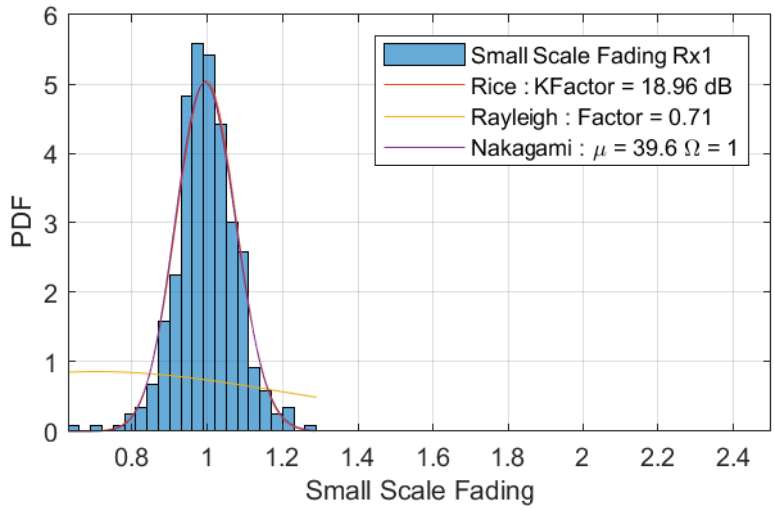

(A) Results for the first Rx.

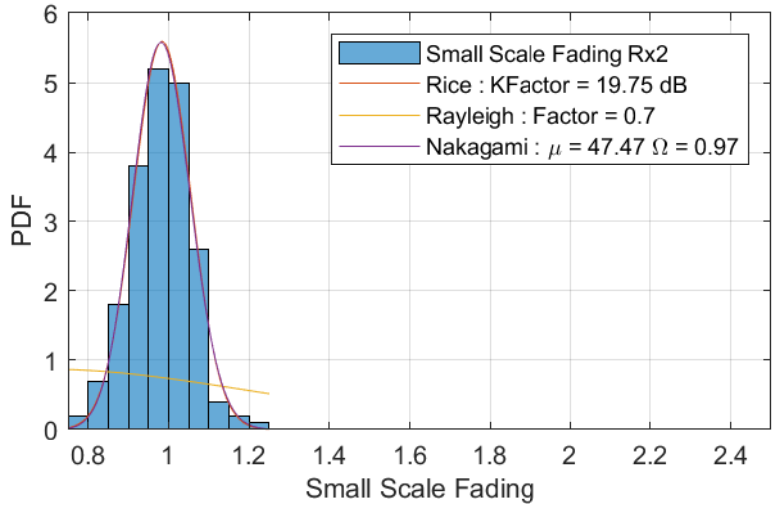

(B) Results for the second Rx.

FIGURE 6.14: Small-scale fading distribution fitting for the first window of 40λ size from the measure made in the VES3 track, for vertical polarization, in LOS case.

The KS test is realized on each estimated distribution and for all the visibility situations. In the following, we will discuss only the results obtained for the LOS situation, and it is presented in Fig. 6.15. The zero value obtained with the KS test validates the hypothesis that the theoretical associated distribution fits well with the empirical distribution, and on the contrary, the one value invalidates this assumption. From the results, it can be noted that in some cases on the first and second Rx the hypothesis of a Nakagami distribution is invalidated, such as the Rice distribution in some cases on the second receiver.

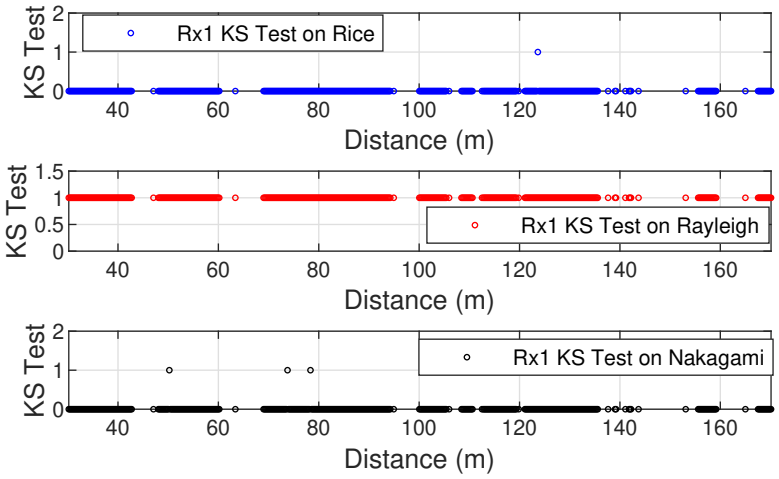

(A) Results for the first Rx.

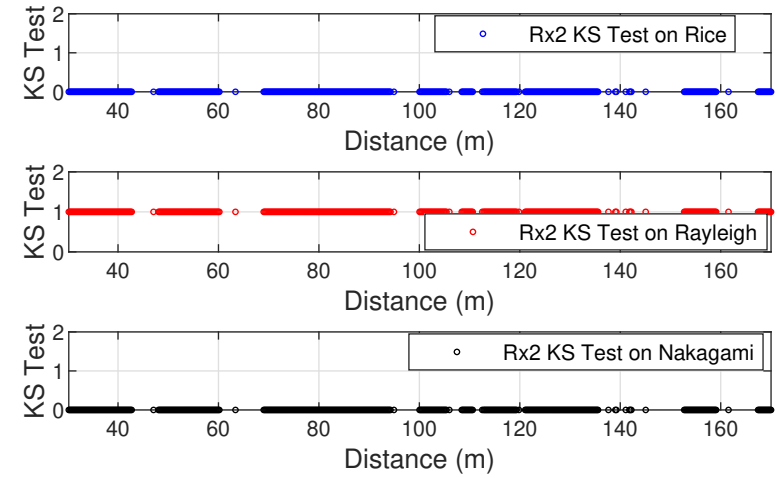

(B) Results for the second Rx.

FIGURE 6.15: Results of the KS test for the LOS condition on measurement made on VES3.

These results show that the Rice distribution for both Rx can be used to fit the small-scale fading distribution. Nonetheless, some questions can be raised about the use of the KS test as a metric to validate the use of a distribution. The first one is about the Nakagami distribution. Indeed, as it can be seen on the Fig. 6.15, for the first Rx in some cases the KS test invalidates the null hypothesis. The null hypothesis is that the investigated CDF distribution fits with the CDF extracted from the data.

Concerning the Nakagami distribution, there are two parameters to accurately fit the CDF. In this case, the hypothesis of a Nakagami distribution which is rejected by the KS test is not usual. For the rest of the thesis, and to compare with the 3GPP, only the K-Factor extracted from the Rician distribution will be computed.

Finally, the K-Factor is computed for all the measurement data in both visibility situations, and the result is presented in Fig. 6.16. From this extraction, the mean value, $\mu_{\text{K-Factor}}$, and the standard deviation, $\sigma_{\text{K-Factor}}$ of the K-Factor are presented and noted in Tab. 6.9.

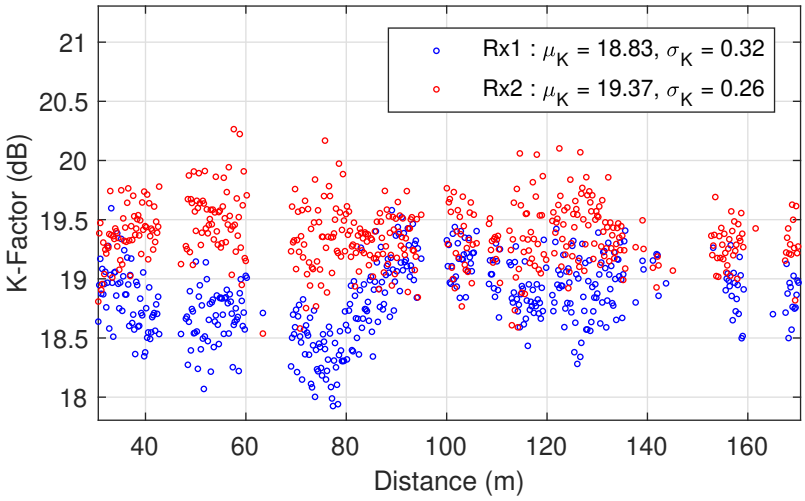

(A) LOS visibility condition.

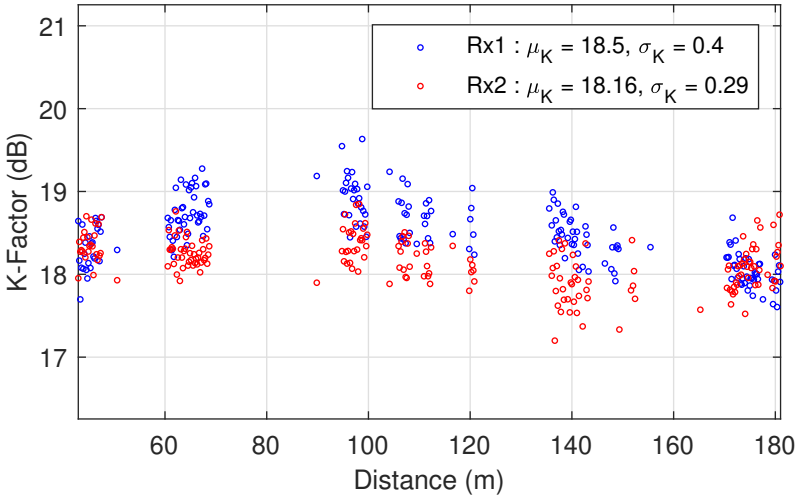

(B) NLOS visibility condition.

FIGURE 6.16: K-Factor computed for all the measurement data made on VES3 track for both Rx with vertically polarized antenna, and for both visibility situations.

TABLE 6.9: Mean and standard deviation for K-Factor parameters estimated for all the measurements made on VES3 track.

Track	Tx Polar.	Rx Polar.	Visibility	$\mu_{\text{K-Factor}}$ [dB]				$\sigma_{\text{K-Factor}}$ [dB]			
				min	max	mean	std	min	max	mean	std
VES1	**H**	**H**	**LOS**	15.36	17.19	16.46	0.63	0.27	0.40	0.33	0.04
			NLOS	14.34	16.07	15.15	0.17	0.26	0.41	0.33	0.06
VES1	**V**	**V**	**LOS**	13.62	18.86	16.20	1.53	0.25	0.42	0.35	0.06
			NLOS	13.69	17.16	15.05	1.03	0.19	0.53	0.34	0.11
VES3	**H**	**H**	**LOS**	17.13	17.62	17.45	0.20	0.27	0.40	0.31	0.05
			NLOS	16.31	18.15	17.58	0.75	0.23	0.33	0.28	0.04
VES3	**V**	**V**	**LOS**	12.68	19.45	16.71	3.04	0.27	0.40	0.34	0.05
			NLOS	13.05	18.54	16.11	2.51	0.13	2	0.55	0.65

6.3.4.b Comparison with 3GPP Channel Model

As mentioned before, the Rice distribution is the retained distribution to model the small-scale fading, for our purpose to be able to compare our results with the 3GPP model. As for the RMS DS, the 3GPP models the small-scale fading for frequency higher than 7 GHz for two environments, the UMi and UMa. In both cases, the mean K-Factor, μ_K, and its standard deviation, σ_K is given, but only for LOS visibility condition. These values, extracted from [12], are reported in Tab. 6.10.

TABLE 6.10: Mean and standard deviation of the K-Factor for the small-scale fading from the 3GPP [12].

Scenario	**Visibility**	μ_K	σ_K
UMi	**LOS**	9	5
UMa	**LOS**	9	3.5

From Tab. 6.9, it can be seen that the mean K-Factor obtained from measurement is higher than one proposed by the 3GPP model, and its standard deviation does not follow the 3GPP model. This situation can be explained by the limited bandwidth of our CS. Indeed, as mentioned earlier, the limited bandwidth led to the integration of MPCs with low excess delay inside the main component. This can explain the presence of a main peak, in terms of power, and lower peaks after. To conclude, the 3GPP model, which achieves the lower error with the measurement result in the railway environment is the UMa, as for the PL.

6.3.5 Doppler Spread

This section will present the Doppler spread computation and results obtained from the measurement performed on **VES3** track. Before, the RMS Doppler spread estimation technique was introduced. This parameter is the second-order statistic, as for the RMS DS, but applied to the scattering function. As for the PDP computation, a first step is realized to delete the sample below the noise threshold. The obtained scattering functions, for both visibility cases, and each Rx are presented in Fig. 6.17.

Once this normalized scattering function is obtained, the RMS Doppler spread is computed by adding a threshold value of 30 dB, and the results obtained for each visibility scenario are presented in Fig. 6.18. It can be seen that the different visibility situation does not affect the RMS Doppler spread, this result can be explained as the NLOS situation is more a OLOS than a fully blocked link. Moreover, just before the first NLOS situation, at 60 m, the RMS Doppler spread increases to reach a value higher than 0.2, which can be explained by the increase of MPCs due to higher diffraction that occurs around the lamppost, or catenary overhead mast. However, the curving part of the measurement does not impact the RMS Doppler spread, as a first idea can be made. This lack of impact can be explained by the lack of dynamic on the CIR, which impacts the number of MPCs on the scattering function.

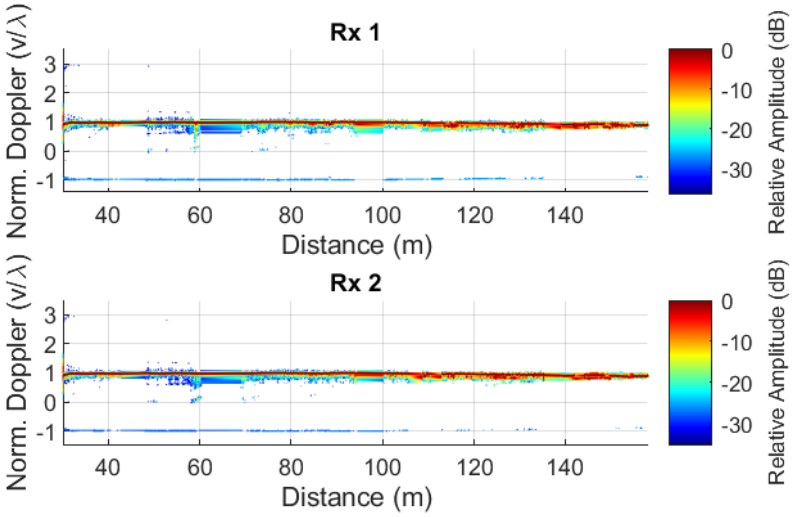

(A) Scattering function for the LOS visibility.

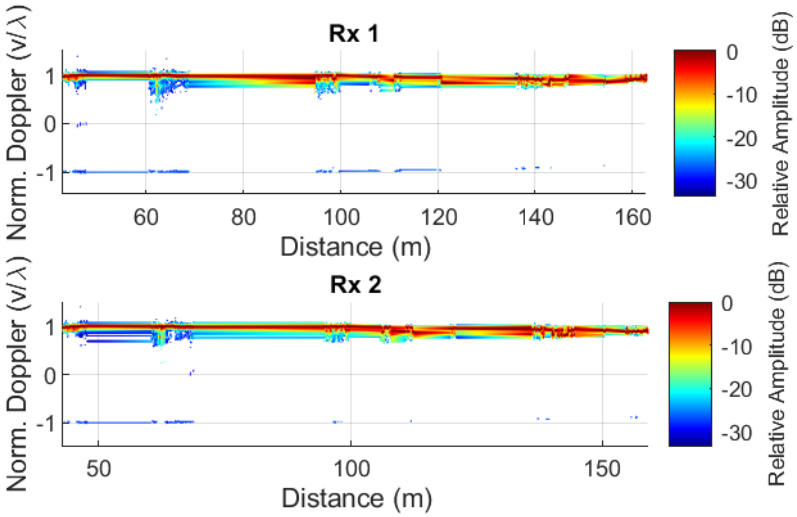

(B) Scattering function for the NLOS visibility.

FIGURE 6.17: Normalized scattering function without noise, obtained from the measurement made in VES3, with the antenna vertically polarized, and for each visibility situation.

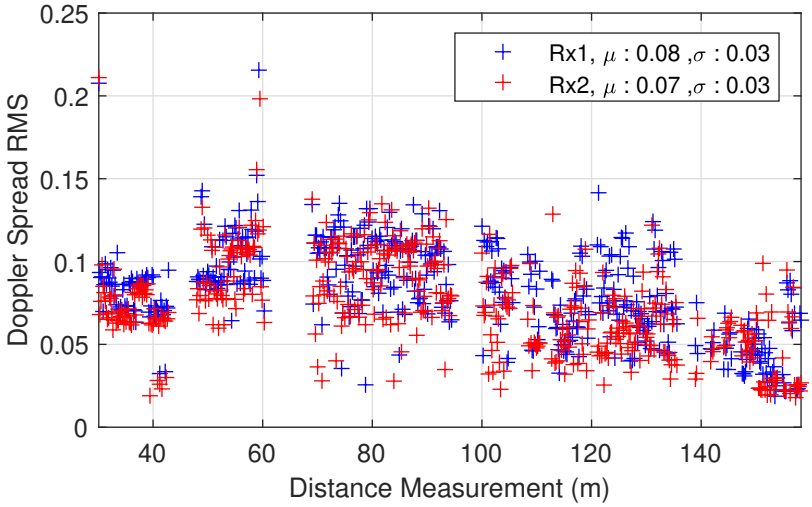

(A) RMS Doppler spread for the LOS visibility.

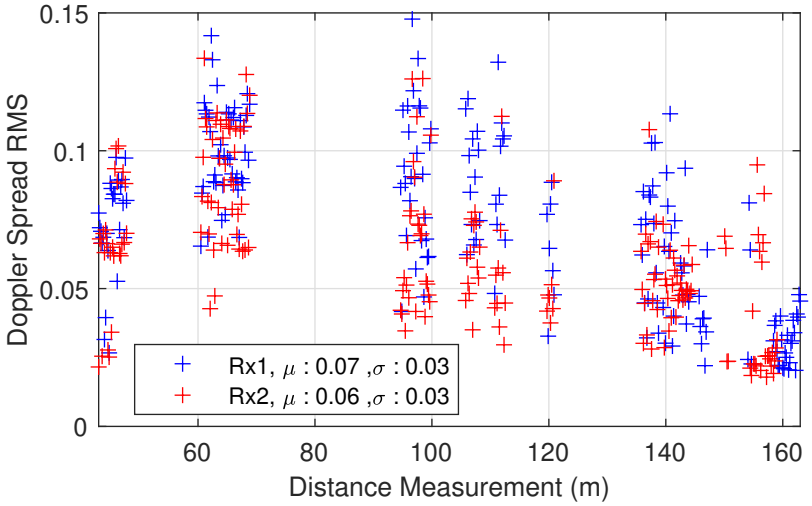

(B) RMS Doppler spread for the NLOS visibility.

FIGURE 6.18: Normalized scattering function without noise, obtained from the measurement made in VES3, with the antenna vertically polarized, and for each visibility situation.

6.4 Conclusion

In this chapter, the statistical parameters of the radio channel propagation at 60 GHz in a railway environment for a 3GPP HSL scenario are presented. First, we discussed the stationary area's size retained to compute the large-scale parameters. To do so, the collinearity matrix is computed with the PDP realized with a 10λ window size. This value is typically retained to perform such computation. Then a threshold value of 0.9 is retained to estimate the stationary area size as a function of the wavelength. From this investigation, it has been concluded that the use of a window size of 40λ is suitable for performing large-scale parameter estimation.

Then, to provide parameters in each visibility case, LOS and NLOS, the triangle shadowing method is applied with the knowledge of scatter's localization obtained with the GNSS augmented system implemented in the CS. This technique presents

some limitations due to the real accuracy of this localization technique, but it is suitable for our purpose since it is not higher than the measurement incertitude.

The PL estimation technique is then presented, and the choice of a single slope log-distance model is justified by comparing the obtained model with 3GPP models. For each track measurement with both co and cross-polarization antennas, the different PLEs are presented. Moreover, the SF estimation technique, and distribution fitting are described and also compared with the 3GPP models. The use of the distribution proposed by the 3GPP is validated by the KS test.

The same presentation methodology is used for the RMS DS, and the small-scale fading estimation. However, for the RMS DS distribution parameters, the 3GPP models do not fit our results and another scenario has to be added to take care of the HSL scenarios. A similar conclusion can be given for the modelling of the small-scale fading.

Finally, our results show that the 3GPP UMa model has the statistical parameters closest to those obtained. However, it should be noted that this model is unsuitable for modelling the RMS DS, since its parameters overestimate the value obtained from the measurement.

7 General conclusion and Perspectives

Contents

7.1 Conclusion

This work has been performed in the framework of the ANR project mmW4Rail. The main objective of this PhD thesis was to provide channel models at 60 GHz in railway environment in order to facilitate system evaluation. A state-of-the-art showed that there is a lack of channel model in this environment in this frequency range. Furthermore, most of the CS in mmWave frequency band are not adapted to do measurements in dynamic and with sufficient recording time. That is why, it has been decided to design and develop our own CS in the framework of the project.

The IMT Atlantique SIMO CS was developed based on an Analog Device COTS for the up-and-down conversion and an SDR platform as a digitizer. This CS features a 180 MHz bandwidth at 60 GHz, and can perform dynamic and long-range measurements (until 6 mins) with co and cross-polarization capabilities. The complex CTF is measured with an independent Rx and a Tx part, based on a front-end, a synchronization unit and a control unit. The baseband sounding sequence is an unmodulated OFDM type with Newman phase between sub-carrier to increase the CF. The synchronization unit is based on GNSS disciplined rubidium clock. Moreover, its architecture allows it to be evolutive by designing and integrating new RF front-end in other frequency bands.

Before doing measurements in railway environments, several measurement campaigns in indoor and outdoor environments have permitted to test the CS and to improve its performance by correcting some parts (phase noise) or adding new functionalities (localization, video, ...).

The railway environment is atypical because it has many differences from vehicular environments, such as the metallic rail, the ballast, and the supplying overhead catenary line. On the contrary, some similarities can be found, such as the presence of an overhead mast line which can be compared to the lamppost in the vehicular scenario, because they are regularly spaced and with similar dimensions. A literature overview showed that there is a lack of real measurements made in the railway environment, due to access and installation complexity. This results in a lack of results from this atypical environment.

Within the mmW4Rail project, we had access to a railway testing facility called CEF near Valenciennes in France. This environment is similar to marshalling yards, and the Tx part of the CS was mounted on a maintenance train to perform measurements. The different scenarios for our measurement campaign are described, and a focus is made on the proposed 3GPP HSL geometry. The correct operation of the CS, and its correct configuration for our scenario, is validated by an investigation, which has led to identifying the causes of multiple reflections.

Then, results obtained for the 3GPP HSL scenarios from the measurements campaign are compared with the model presented in the 3GPP. All parameters are modelled for both LOS and NLOS cases. The visibility situations are defined as the possibility of an optical link between the Rx and the Tx, which is estimated by the knowledge of the surrounding elements. Moreover, the stationary assumption is discussed and concludes that a window size of 40λ is suitable to estimate the large-scale parameters in our case.

Then, the PL is estimated and shows that the PLE for the NLOS situations are similar to the one obtained for the LOS cases. The first hypothesis of this result is the estimation of LOS and NLOS visibility situation. Indeed, in our case, the OLOS

situation is considered as a NLOS situation, which can explain the high RMSE made by comparing the obtained PLE with the 3GPP NLOS model.

To continue, the RMS DS is computed and the mean and standard value of the log RMS DS are extracted. The results indicate that the parameters are stricter than announced by the 3GPP. Indeed, the sparsity of the radio propagation channel led to a low RMS DS. This low RMS DS leads to higher log values, which explains the high mean parameter value. The low value of the standard deviation parameters indicated the low variation of the RMS DS within the same measurement setup.

Furthermore, the small-scale fading distributions are fitted with a Rice distribution. The choice of this distribution is led by the 3GPP, but validated with the KS test. The results show a good correlation between the 3GPP mean K-Factor parameter and the obtained results. Instead of the standard deviation of the K-Factor parameters, which is lower than our measurement results. This can be explained by the limited bandwidth leading to a high power peak, in the main component, and other peaks but with lower power, due to more distant MPCs with higher propagation losses. Finally, the RMS Doppler spread parameter is computed on the normalized scattering function.

7.2 Perspectives

This PhD work opens several interesting perspectives related to the channel sounder itself and then to the exploitation of measured data.

The first perspective is related to the enhancement of the CS operation, which suffers from several limitations such as the lack of AGC, and the speed information, which is limited in vehicle acceleration and braking phases. The realization of the AGC will allow measuring with the high available dynamic possible the radio propagation channel, but it is not trivial to implement. Indeed, the configuration of this AGC has not to be fast enough not to compensate small-scale fading, and not too slow to not compensate the large-scale fading. Moreover, in our case, the front-ends are made with COTS from Analog Device. They are composed of different amplification stages, which can be controlled by computer, but the signal between each stage can not be monitored, and then the AGC will be set following abacus made with laboratory test.

To overcome the speed information limitation, a solution has been developed but has not yet been used in real conditions. Indeed, to monitor the speed, an incremental coder is available at IMT Atlantique, and can be installed on a car wheel. This accurate coder can be connected to the control unit and the instantaneous speed can be saved. This solution has been tested but not yet installed on a train, due to installation issues.

Moreover, the orthomode, which allows the direct measurement of vertical and horizontal polarization from the same antenna, has not been installed in time for the train measurement campaign. Nonetheless, cross-polarization measurement has been made by adding a twist in front of one Rx.

Finally, in the current setup, the use of the SDR component is a limiting factor. Indeed, this type of component is very useful because it proposed a fully integrated Rx chain with a digitizer. Moreover, this solution offers the possibility to easily save

the data in a special format on a simple computer, thanks to the open-source solutions. However, such components have the disadvantage of offering a low available bandwidth. To overcome this limitation, it is possible to change the SDR component by a digitizer card, which will be integrated on a special computer. But this modification is not easy, because it adds developing time to correctly deal with the digitized sample, and the synchronization of such card with the CS has to be investigated.

The second set of perspectives concerns the comparison between the obtained results and the 3GPP model. It showed that there is a necessity to develop a model for this typical scenario, e.g. 3GPP HSL. Moreover, a model for this atypical scenario can be realized, but extra information is needed to do it.

The retained model can be based on SV channel model. To realize such a model, a clustering algorithm needs to be used to obtain a representation of the PDP in a cluster way. Once the size and number of clusters are obtained, the exponential power decay for both, cluster and intra-cluster has to be estimated. Then, the cluster apparition probability has to be estimated and linked to the RMS DS, such as the ray numbers inside each cluster. This part can be realized with the current data obtained from the measurement campaign. To do so, the formatted Matlab file containing the data will be available to the community.

This initial model can be upgraded with knowledge of geometrical information of the measurement environment to achieve a GSCM. To do so, the distribution of each component has to be estimated and fitted with a statistical distribution.

The model has to provide angular information to be used by MIMO system. The angular information is provided by the distribution of the of AoA and AoD. The AoA can be realized by using another Tx, and realized the channel sounding with antenna diversity along both azimuth and elevation angle.

8 Résumé

Contents

8.1 Chapitre 2

Au sein de ce chapitre, les principales caractéristiques du canal de propagation sont présentées. Dans un premier temps, la propagation en espace libre est abordée, avant d'introduire la notion de canal à trajets multiples. De plus, les différentes interactions physiques survenant dans le canal à trajets multiples sont présentées, allant de la simple coupure transmission-réflexion à la diffusion. Cette partie permet aussi de présenter les différents cas de visibilité, allant de la situation où l'ellipsoïde de Fresnel n'est pas obstrué, qui est le cas *Line Of Sight* (LOS), au cas où cette dernière est partiellement obstruée, *Obstructed Line Of Sight* (OLOS), ou totalement, *Non Line Of Sight* (NLOS).

Une fois les bases de la propagation introduites, il est nécessaire de présenter les différentes fonctions mathématiques existantes pour caractériser le canal de propagation. Ces fonctions, au nombre de quatre, ont été introduites par Bello et permettent de représenter le canal dans divers domaines, allant de la représentation amplitude-temps pour la réponse impulsionnelle à la représentation en double fréquence Doppler et largeur de bande du canal. L'ensemble des fonctions est lié par une transformée de Fourier dans les différents domaines. Ces fonctions permettent de décrire le canal de manière complète sur une zone limitée de l'espace.

Effectivement, les fonctions existent sous l'hypothèse d'un canal stationnaire. Autrement dit, les hypothèses de stationnarité au sens large, avec des diffuseurs non corrélés, doivent être validées. Au cours d'un déplacement relatif entre l'émetteur et le récepteur, cette condition ne peut être validée que sur une zone limitée, ou autrement dit dans les zones stationnaires, qui peuvent être de taille variable, allant de la taille de la longueur d'onde jusqu'à plusieurs dizaines de cette dernière.

Le nombre de ces zones peut être assez élevé, surtout lorsque la longueur d'onde devient petite (par exemple, 5 mm pour une fréquence de 60 GHz), ce qui rend l'utilisation d'une description stochastique primordiale. Les fonctions de Bello, présentées ultérieurement, trouvent leurs alter egos via la connaissance des fonctions d'auto-corrélation. De ces fonctions d'auto-corrélation découlent des cas particuliers permettant de connaître l'évolution du canal en termes de puissance reçue, ainsi que de dispersion fréquentielle et temporelle.

Par exemple, la répartition des retards en puissance, plus communément appelée PDP (*Power Delay Profile*), permet d'obtenir la répartition temporelle des retards. La métrique associée à cet étalement des retards est appelée le *RMS Delay Spread* (*Root Mean Square*), qui correspond au moment d'ordre deux du PDP. Il existe son corollaire au niveau fréquentiel, qui permet d'obtenir l'étalement fréquentiel des retards via le *Doppler Spread*.

Après avoir présenté les différentes grandeurs utilisées pour caractériser le canal de propagation, la modélisation de ce dernier peut être abordée. Tout d'abord, la première modélisation qui peut être réalisée est celle des pertes en puissance en fonction de la distance de mesure. Le plus souvent, cette évolution est modélisée via une fonction linéaire dans le domaine log-distance. Cela permet de relier les pertes en décibels (dB) avec la distance via une simple droite linéaire. Bien évidemment, en fonction de l'environnement, cette pente, appelée *Path Loss Exponent* (PLE), varie, allant de moins de 2 à plus de 2. La valeur de 2 correspond aux pertes intrinsèques dues à la propagation en espace libre et obtenues via la formule de Friis.

Puis vient la modélisation à plus petite échelle, où l'on cherche à modéliser le comportement de la réponse impulsionnelle ou du PDP en fonction de la distance. Pour ce faire, Saleh et Valenzuela ont proposé un modèle permettant de caractériser l'évolution du PDP en fonction de la distance. Ils ont proposé de représenter le PDP par la superposition de clusters, qui représentent différents paquets arrivant à des instants très proches. Au sein de ces clusters, différents trajets peuvent être trouvés, arrivant à des instants aléatoires suivant une loi de Poisson. Il en va de même pour l'arrivée des clusters, qui arrivent de manière aléatoire, suivant eux aussi une loi de Poisson. Concernant l'évolution en puissance de ces clusters et des trajets les composant, Saleh et Valenzuela ont proposé de les modéliser chacun avec une pente décroissante de manière exponentielle, mais avec des valeurs de pente différentes.

Néanmoins, la réalisation du modèle précède son implémentation matérielle ou logicielle afin de pouvoir obtenir, par simulation ou mesure matérielle, l'évolution du Taux d'Erreur Binaire (TEB) en fonction du Rapport Signal à Bruit (RSB). Or, lors de l'apparition du modèle de Saleh et Valenzuela, les capacités en termes de calcul informatique n'étaient pas aussi puissantes qu'aujourd'hui, et donc les modèles ont dû s'adapter. Le premier type de modèle à apparaître est le *Tapped Delay Line* (TDL), qui est un modèle permettant de modéliser les trajets par un nombre fini de réalisations normalisées en puissance et en temps par rapport au premier trajet. L'avantage de ce modèle est sa simplicité de réalisation via de simples lignes à retard. En revanche, il ne permet pas de savoir d'où proviennent les multi-trajets, et avec l'avènement des systèmes à plusieurs entrées et plusieurs sorties (MIMO), cette caractéristique est devenue nécessaire.

C'est dans ce contexte que le modèle bidirectionnel est apparu et permet maintenant de prendre en compte les différentes entrées et sorties comme des canaux indépendants avec leurs propres coefficients de canal. La modélisation du canal de propagation elle-même n'en est pas modifiée. En revanche, elle est agrémentée par la connaissance des angles de départ (AoD) et d'arrivée (AoA) des multi-trajets, ainsi que par la connaissance des diagrammes de rayonnement des antennes composant le système MIMO. De plus, la polarisation est prise en compte dans ce modèle et est souvent modélisée par une simple atténuation de la puissance.

Finalement, ce modèle peut être encore amélioré grâce à l'amélioration des temps de calcul en informatique et à la connaissance de l'environnement direct. En effet, les clusters proviennent de diffuseurs de l'environnement qui proposent différents multi-trajets en leur sein. Là encore, les propositions faites par Saleh et Valenzuela se retrouvent dans cette description et sont encore utilisées aujourd'hui dans la modélisation du canal de propagation. Cette modélisation du canal de propagation se retrouve très largement dans les modèles issus de la standardisation, comme l'ITU (Union Internationale des Télécommunications) ou le 3GPP (*Third-generation Partnership Project*). La principale différence entre ces modèles réside dans la découpe des différents environnements que le modèle cherche à représenter.

Les modèles que l'on retrouve dans la standardisation ont été obtenus après diverses campagnes de mesure permettant de tirer un modèle stochastique de l'ensemble de ces mesures. La question qui se pose est la suivante : comment mesurer le canal de propagation ?

8.2 Chapitre 3

Il existe plusieurs techniques pour mesurer le canal de propagation, qui ont toutes en commun l'utilisation d'un sondeur de canal. Ces techniques se déclinent de différentes manières, selon les besoins spécifiques de chaque approche. Tout comme les modèles, les techniques de sondage ont évolué au fil du temps, passant de systèmes uniquement capables de mesurer l'évolution de la puissance reçue en fonction de la distance à des systèmes capables d'obtenir les angles d'arrivée et de départ des multi-trajets. De plus, les bandes de fréquences utilisées par ces systèmes ont évolué, allant de quelques GHz à plusieurs dizaines, voire centaines de GHz, avec l'apparition des sondeurs opérant en THz.

Avant de présenter les différentes techniques de sondage existantes en bande millimétrique, et plus particulièrement à 60 GHz, qui est la fréquence porteuse étudiée dans le cadre de cette thèse, il convient de présenter les prérequis pour réaliser des mesures dynamiques à cette fréquence. Tout d'abord, afin d'obtenir le temps absolu et de pouvoir résoudre la fréquence Doppler, il est nécessaire d'avoir une bonne synchronisation en phase et en temps du sondeur. Cette synchronisation doit être réalisée indépendamment sur l'émetteur et le récepteur afin qu'ils puissent être dissociés. De plus, la résolution du Doppler demande de pouvoir échantillonner spatialement le canal tous les $\lambda/2$, où λ représente la longueur d'onde, qui vaut 5 mm à 60 GHz. Il est donc nécessaire que l'acquisition des réponses impulsionnelles ou des fonctions de transfert soit suffisamment rapide pour répondre à cette problématique. Finalement, il est nécessaire que la dynamique du sondeur soit suffisante pour obtenir des résultats tout au long de la mesure, qui doit être supérieure à la minute dans notre cas.

Une fois cette brève introduction faite, les différentes techniques existantes pour mesurer le canal peuvent être présentées, en commençant par celles nécessitant le moins de matériel. La première technique, très utilisée dans le monde du radar, est le sondeur pulsé. La technique est identique à celle utilisée en radar, à la différence près que l'émetteur et le récepteur sont séparés. Les limites de cette technique sont technologiques, car il est très difficile, même de nos jours, d'amplifier un pulse, ce qui réduit la portée du sondeur. De plus, il est également difficile d'émettre des pulses courts, ce qui permettrait d'avoir une large bande passante. Ensuite, viennent les sondeurs utilisant des instruments de mesure couramment utilisés dans le monde de la radiofréquence. Le premier utilise un simple analyseur de spectre afin de mesurer la puissance reçue par le récepteur. L'utilisation de ce sondeur est limitée, car il ne permet pas la mesure de la phase et donc de différencier les multi-trajets. En revanche, les auteurs ont proposé une technique basée sur la transformée de Hilbert, qui permet de remonter à la phase et ainsi résoudre le problème. La deuxième utilise l'analyseur de réseau vectoriel. Cette technique permet d'analyser les paramètres S d'un élément en test, qui, dans ce cas, est le canal de propagation entre les deux antennes connectées aux deux ports de l'analyseur. L'avantage de cette technique réside dans la "facilité" d'obtention des fonctions de transfert très large bande, jusqu'à plusieurs GHz, mais à plusieurs coûts. Le premier est l'incapacité de faire des mesures sur de longues distances, due à la nécessité de connecter les antennes à un unique appareil par câble. Le deuxième concerne le temps d'acquisition d'une fonction de transfert, qui ne permet pas d'accéder à la résolution Doppler.

De plus, il existe aussi des techniques très largement répandues, car facilement implémentables, il s'agit des sondeurs à base de séquences pseudo-aléatoires. Comme leur nom l'indique, ces sondeurs utilisent des séquences pseudo-aléatoires qui sont

facilement réalisables électroniquement grâce aux bascules. Ces séquences sont émises et, au niveau du récepteur, deux techniques sont possibles. La première consiste à faire une convolution entre le signal reçu et le signal émis. Grâce aux propriétés d'auto-corrélation de ces séquences, il devient donc aisé d'obtenir la réponse impulsionnelle du canal. La deuxième est un dérivé de la première, car elle consiste à convoluer le signal reçu avec le signal de sondage obtenu avec une fréquence d'horloge légèrement différente d'un facteur k. Ce facteur peut aller de quelques dizaines à plusieurs centaines et permet de convoluer la séquence au cours du temps sans action de calcul, ce qui permet au résultat d'apparaître directement sur un oscilloscope. L'inconvénient de ces techniques est double : le premier concerne le temps d'acquisition de la réponse impulsionnelle, qui augmente avec ce facteur k, ce qui rend donc la résolution du Doppler impossible. Le deuxième concerne le calcul de la réponse impulsionnelle, qui prend en compte les effets de l'émetteur et du récepteur.

Afin de prendre en compte les effets de l'émetteur et du récepteur dans le calcul de la réponse impulsionnelle ou de la fonction de transfert, des techniques avancées existent. Elles sont toutes basées sur le même principe : prendre en compte, par calibrage, les fonctions de transfert de chaque élément avant de comparer ce calibrage avec les signaux reçus. La différence se fait sur les différents types de signaux utilisés pour ces techniques. Le meilleur signal en termes de facteur de crête est le signal dit *chirp*. Le deuxième est le signal de type multiplexage par répartition orthogonale de la fréquence (OFDM) sans modulation. Ce signal n'a pas le même facteur de crête que le signal *chirp*, mais avec des phases astucieusement choisies, ce facteur peut s'approcher de celui du *chirp*. De plus, un élément intéressant dans ces sondeurs est l'utilisation de composants commerciaux pour réaliser la partie conversion vers et depuis la bande de base, ce qui permet une architecture globalement moins coûteuse.

De cet état de l'art, il ressort le manque de sondeurs réellement capables de réaliser des mesures en scénarios dynamiques. Parmi ceux qui en sont capables, peu permettent d'être utilisés par une personne tierce. Après cet état de l'art des techniques et des différents sondeurs existants à 60 GHz, il convient de faire de même pour les résultats de mesure proposés par ces mêmes sondeurs. Cet état de l'art réalisé dans le manuscrit montre que le canal de propagation à 60 GHz est bien moins documenté que pour des fréquences plus basses. Un autre constat vient s'ajouter à cela : les pertes sont bien plus importantes à 60 GHz, dû, entre autres, à un pic d'absorption par l'oxygène à cette fréquence. En première approche, ces contraintes peuvent sembler très limitantes, mais elles peuvent être utilisées de manière avantageuse. Dans un premier temps, les pertes plus importantes peuvent être combattues avec des antennes plus directives, ce qui entraînerait des canaux de communication plus étroits, certes, mais qui permettraient une réutilisation de la bande, même pour des zones géographiques plus petites, et ainsi permettre un débit de données plus élevé sans multiplier les systèmes.

En conclusion de ce chapitre, il a été montré que le canal de propagation à 60 GHz est bien moins documenté qu'à des fréquences plus basses, et que cet inconvénient peut être perçu comme un point positif sous un autre angle. Il a également été souligné qu'il n'existe pas de sondeur parfaitement adapté à notre cas d'utilisation. En revanche, il existe des solutions commerciales qui permettent de réaliser des sondeurs à des coûts bien moindres qu'une chaîne d'émission et de réception sur mesure.

8.3 Chapitre 4

Ce chapitre est consacré à la présentation du sondeur de canal développé au sein d'IMT Atlantique dans le cadre de cette thèse. Ce sondeur comprend un émetteur et deux récepteurs, et repose sur une architecture composée de trois grandes parties : le front-end, qui supervise la conversion vers la bande d'intérêt (la bande V dans notre cas, soit autour de 60 GHz), la partie synchronisation, qui assure la synchronisation du front-end et de la partie bande de base de manière identique, et enfin, la partie contrôle, qui englobe la bande de base et l'ordinateur chargé du pilotage de l'ensemble.

La partie front-end, qui supervise la conversion en fréquence, est intégrée au sein d'un boîtier dans lequel se trouve une carte de démonstration provenant d'Analog Devices. Cette carte intègre le composant de la série HMC630x, qui propose une solution intégrée de chaîne d'émission et de réception suivant l'architecture super-hétérodyne. Dans les deux cas, plusieurs étages d'atténuation permettent de régler le gain global de la chaîne d'émission et de réception.

De plus, sur la partie émission, un amplificateur de puissance avec un gain de 23 dB pour un point de compression de 1 dB en sortie de 23 dBm est installé. L'objectif de cet amplificateur est d'assurer une dynamique de mesure suffisante en augmentant la puissance du signal émis. Le réglage du gain de la chaîne d'émission est donc effectué de manière à ne pas saturer l'amplificateur, d'une part, et à éviter que le signal de sondage ne soit saturé au sein de la chaîne d'émission avant son passage dans l'amplificateur, d'autre part.

En ce qui concerne la chaîne de réception, le gain est réglable de 0 à 69 dB, permettant ainsi d'obtenir une dynamique de mesure suffisante pour notre cas. Ces cartes de démonstration peuvent être synchronisées de manière externe via l'apport d'un signal sinusoïdal de référence dont la fréquence est d'environ 71 MHz.

Puis, la synchronisation des deux chaînes est réalisée par une horloge à rubidium, qui peut être disciplinée par des données GNSS (Système Mondial de Navigation par Satellite), par une référence externe ou bien fonctionner sans synchronisation. Cette horloge dispose de plusieurs sorties, dont un signal de référence de 10 MHz et une sortie PPS (*Pulse Per Second*) pour la synchronisation temporelle.

Du côté de l'émission, ce signal de 10 MHz est utilisé pour synchroniser un générateur arbitraire de marque Rohde & Schwarz, qui fournit à la fois le signal de sondage en bande de base et le signal sinusoïdal à 71 MHz pour synchroniser le front-end.

Pour la partie réception, le signal de référence de 10 MHz est d'abord envoyé à un générateur Rohde & Schwarz, chargé de fournir le signal de référence à 71 MHz pour synchroniser le front-end. Il est également envoyé à une plateforme SDR (Radio Définie par Logiciel) qui permet la numérisation du signal de réception en bande de base. Cette plateforme SDR dispose également d'une entrée PPS, utilisée pour synchroniser l'horloge du boîtier avec l'heure GNSS. Cette fonction est assurée par un USRP (*Universal Software Radio Peripheral*) de référence X310, qui permet de numériser des signaux avec une bande passante de 200 MHz.

Enfin, la partie contrôle pilote les différentes cartes Analog Devices ainsi que les valeurs de gain de chaque chaîne. Elle gère également les fonctionnalités supplémentaires ajoutées au sondeur, qui permettent de localiser précisément les mesures et de prendre une photo à 360° de l'environnement pendant la mesure. Cette prise de photo

est assurée par une caméra 360° et permet de capturer une image toutes les secondes lors de la mesure, grâce à la synchronisation avec les données GNSS.

La précision de la localisation est garantie par un boîtier GNSS RTK (*Real-Time Kinematic*). Cette technologie repose sur le principe de correction des données issues des constellations de satellites, effectuée par une station de base. Cette station de base, située à proximité (quelques kilomètres au maximum) du module RTK, est localisée de manière très précise. Grâce à cette proximité, les données reçues par la station de base traversent un canal de propagation similaire à celui du module RTK, ce qui permet à la station de corriger les données de localisation et de renvoyer les corrections apportées.

Dans le cadre de cette thèse, nous avons utilisé des données de station de base fournies par un réseau open-source appelé CENTIPEDE, accessible via une connexion internet. Toutefois, la connexion internet représente un inconvénient pour l'utilisation de la correction RTK, car dès qu'elle disparaît, la précision de la localisation est immédiatement réduite.

En conclusion de la partie sur le sondeur, celui-ci, développé au sein d'IMT Atlantique, présente les spécifications suivantes : une bande passante de 180 MHz, une puissance d'émission de 23 dBm, avec plusieurs options de choix d'antennes (5, 10 et 15 dBi), et une séquence de sondage réalisée à partir d'une séquence OFDM non modulée. Sur cette séquence OFDM, la loi de phase retenue entre les sous-porteuses est celle de Newman, qui a été spécialement étudiée pour tendre vers un facteur de crête similaire à celui d'un signal *chirp* parfait.

Ensuite, le sondeur a été installé dans différents environnements afin de tester son fonctionnement complet. Pour ce faire, il a d'abord été installé dans un couloir du département Micro-Ondes d'IMT Atlantique pour effectuer les premières mesures dynamiques sans contrainte de synchronisation additionnelle, car cette fonction est assurée par un câble dans lequel circule un signal de référence de 10 MHz. Après ce premier test concluant en intérieur, le sondeur a ensuite été installé sur une voiture pour la partie émission, et le récepteur a été placé au bout d'une route sur le campus d'IMT Atlantique. Ce test a permis de valider le fonctionnement global du sondeur dans un environnement véhiculaire, ainsi que l'ensemble des fonctionnalités additionnelles, telles que le module RTK et la prise de photos. Lors de cette dernière campagne, les premiers résultats ont permis de valider, d'une part, que le temps d'enregistrement disponible était suffisant pour ce type de mesure, et d'autre part, que la dynamique du sondeur était suffisante pour effectuer des mesures sur une centaine de mètres.

Cette dernière campagne a permis de mettre en lumière certaines limites du sondeur. La première concerne l'absence de contrôle automatique du gain, qui permettrait d'effectuer des mesures avec la meilleure dynamique possible tout au long de la mesure. Cependant, l'implémentation de cette fonctionnalité n'est pas simple, car elle nécessite l'accès aux différents signaux entre les étages de conversion en fréquence, ce qui n'est pas possible en raison de la solution commerciale retenue. De plus, même après la réalisation d'un abaque permettant de régler les différents étages d'atténuation, la vitesse de réglage de ces derniers impacte la détection du fading, qu'il soit lent ou rapide. La deuxième limite concerne la mesure de la vitesse de déplacement pendant la mesure. En effet, celle-ci est obtenue à partir des données GNSS, mais une limitation apparaît lors des phases d'accélération et de freinage. Cela est dû, en partie, à la fréquence de rafraîchissement des données de localisation,

qui est de 1 Hz. Cela conduit à considérer que la vitesse est constante pendant une seconde, ce qui n'est pas le cas lors des phases d'accélération et de freinage. Une solution est prévue pour pallier ce problème : elle repose sur l'utilisation d'un codeur de roue installé sur une des roues de la voiture. Néanmoins, sa mise en œuvre n'a pas été pleinement validée et n'est donc pas utilisée pour le moment.

8.4 Chapitre 5

Ce chapitre a pour objectif, dans un premier temps, de présenter le milieu ferroviaire ainsi que ses spécificités. Ensuite, un état de l'art des mesures et des différents outils de simulation existants pour la caractérisation du milieu ferroviaire sera proposé. Dans le cadre de ce projet, un emplacement a été loué au Centre d'Essai Ferroviaire (CEF) de Valenciennes afin de réaliser des mesures *in situ*. L'environnement disponible pour effectuer ces mesures, ainsi que les différents véhicules mis à disposition, sont décrits. À partir de cette description, les différents scénarios de mesure réalisés sont détaillés. Enfin, les premiers résultats des mesures effectuées sont présentés.

Comme évoqué précédemment, la première étape consiste à présenter l'environnement ferroviaire. Cet environnement est principalement composé de rails, avec ou sans ballast, et de traverses de tailles et de compositions variées. L'infrastructure ferroviaire est caractérisée par la présence de caténaires, qui permettent l'alimentation électrique des trains, et de mâts de caténaires, qui soutiennent ces dernières. Ces éléments distinctifs différencient l'environnement ferroviaire de l'environnement véhiculaire, notamment par la présence de voies métalliques et de lignes d'alimentation situées directement au-dessus des voies. Bien que certains environnements urbains véhiculaires présentent également des infrastructures telles que des lampadaires ou des pylônes d'alimentation électrique, ils restent très différents du contexte ferroviaire.

En outre, l'accès aux voies ferroviaires est souvent limité ou difficile en raison du trafic constant, ce qui complique la réalisation de mesures dans cet environnement. Ces contraintes se traduisent par un nombre limité de campagnes de mesure en milieu ferroviaire. D'après notre revue de littérature, une seule mesure a été réalisée à 60 GHz dans ce domaine. Cette étude ne visait pas à extraire un modèle de propagation, mais plutôt à évaluer la faisabilité d'un système à 60 GHz pour estimer la distance entre deux trains lors d'une manœuvre de couplage mécanique.

Face à ce constat, l'état de l'art a été élargi aux bandes millimétriques comprises entre 28 GHz et 70 GHz. Malgré cet élargissement, le nombre de mesures effectuées reste très limité, entraînant une rareté, voire une absence, de modèles exploitables. De plus, certains résultats de mesure ne sont pas accessibles en open source, mais réservés à des communautés spécifiques.

Avec les avancées technologiques dans le domaine du calcul informatique, il est désormais possible de simuler la propagation dans le milieu ferroviaire à des vitesses allant jusqu'à plusieurs centaines de km/h. Le simulateur *Cloud RT*, développé par l'université de Pékin, en est un exemple notable. Ce simulateur repose sur la technique du *ray tracing*, permettant d'identifier l'ensemble des réflexions possibles dans un environnement modélisé. Cependant, ce type de simulation nécessite plusieurs éléments. Tout d'abord, une modélisation fidèle de l'environnement est essentielle, ce qui implique une connaissance précise des paramètres diélectriques de nombreux matériaux, notamment en bande millimétrique. Pour répondre à cette exigence, les

auteurs de *Cloud RT* ont mené une étude statistique des propriétés des principaux matériaux présents dans divers environnements ferroviaires. De plus, la validation des résultats de simulation requiert un étalonnage basé sur des mesures expérimentales.

En conclusion, le faible nombre de campagnes de mesure effectuées en milieu ferroviaire limite le développement de modèles de propagation spécifiques, ce qui a un impact direct sur la capacité à simuler efficacement cet environnement.

Afin de pallier ce manque et grâce au projet dans lequel s'inscrit cette thèse, il a été possible de louer une partie du Centre d'Essai Ferroviaire (CEF) pour réaliser des mesures *in situ*. Situé à Valenciennes, dans le nord de la France, le CEF offre divers environnements permettant de tester les trains avant leur mise en circulation. Ces environnements sont divisés en plusieurs zones distinctes.

Tout d'abord, l'anneau d'endurance permet de faire circuler les trains en boucle pendant plusieurs heures afin de réaliser divers tests dynamiques. Ensuite, la ligne à grande vitesse est conçue pour atteindre des vitesses élevées avant de déclencher un arrêt d'urgence, permettant ainsi de valider les distances de freinage. Avant ces tests dynamiques, des tests statiques sont effectués dans une zone dédiée, qui a été mise à disposition pour nos expérimentations.

Cette zone comprend trois voies distinctes dont les compositions varient : une voie en béton, une voie sur ballast avec des traverses complètes en bois, et une autre avec des traverses réduites en béton. L'environnement direct diffère également selon les voies. Certaines disposent de caténaires, permettant l'alimentation électrique des trains à l'arrêt, accompagnées de leurs mâts, tandis qu'une autre voie est dépourvue de toute alimentation, permettant d'étudier l'impact de ces infrastructures.

En outre, différents types de véhicules ont été utilisés pour réaliser des mesures à diverses vitesses. Plusieurs scénarios ont été explorés au sein de cet environnement. Le premier scénario concerne le *platooning*. Cette technique implique un couplage virtuel entre deux trains : contrairement au couplage mécanique, elle permet à deux trains de circuler à courte distance l'un de l'autre sans lien physique. Ce système offre l'avantage d'augmenter le trafic ferroviaire sans nécessiter un temps d'arrêt prolongé en gare pour effectuer un couplage mécanique.

Le deuxième scénario s'appuie sur une architecture proposée par le 3GPP pour intégrer des systèmes de communication sur les lignes à grande vitesse. Selon cette architecture, des stations de base sont réparties le long des voies, tandis que les équipements de communication des trains sont installés sur leurs toits.

Lors de la campagne de mesure, un volume considérable de données a été collecté pour chaque scénario, aboutissant à une quantité totale de 480 Go.

La dernière partie de ce chapitre présente un exemple de mesure réalisée avec une configuration où l'émetteur est installé sur un train laboratoire, tandis que le récepteur est placé à un mètre du sol, en visibilité directe avec le train. Cette mesure permet d'illustrer les différents graphiques pouvant être générés après un premier prétraitement des données.

En outre, elle valide le fonctionnement du sondeur dans ce type d'environnement et confirme la dynamique finale de l'équipement. Lors de cette mesure, un multi-trajet s'éloignant du trajet principal avec un facteur de trois a été détecté. Une analyse géométrique, combinée à la connaissance de l'environnement immédiat et à une analyse en Doppler, a permis de conclure que ce multi-trajet résulte de multiples

réflexions entre l'entrepôt métallique devant lequel le récepteur est positionné et la structure métallique du train.

Ces réflexions, au nombre de trois, génèrent les caractéristiques observées et confirment la capacité du système à détecter ce type de multi-trajet. Cette validation souligne ainsi la précision et la robustesse du sondeur dans des environnements ferroviaires complexes.

8.5 Chapitre 6

Ce dernier chapitre a pour objectif de présenter les différents résultats obtenus concernant le scénario proposé par le 3GPP. Dans un premier temps, une discussion est menée sur la taille de la zone stationnaire à utiliser dans notre cas. Pour cela, plusieurs méthodes issues de la littérature sont présentées, et la version retenue pour notre étude est introduite. Il s'agit d'une méthode basée sur la matrice de colinéarité, calculée à partir du PDP.

Dans ce contexte, le PDP est évalué sur une zone de 10λ, en formulant l'hypothèse que la stationnarité est assurée sur cette étendue. Une fois la matrice de colinéarité obtenue, un seuil est fixé pour estimer la taille de la zone stationnaire. Dans notre étude, ce seuil est établi à 0,9. De plus, seuls les PDP présentant une dynamique suffisante, c'est-à-dire supérieure à 15 dB, sont retenus pour le calcul. Cela permet de réduire le biais introduit par un niveau de bruit trop élevé.

Après cette introduction sur l'estimation de la zone stationnaire, la méthode est appliquée à une mesure d'exemple, et les résultats obtenus pour l'ensemble des mesures sont présentés.

Dans une seconde partie, les paramètres statistiques extraits des mesures et leur méthode de calcul sont présentés. Ensuite, lorsque cela est possible, les résultats obtenus pour notre cas sont comparés avec les modèles présentés dans le 3GPP.

Tout d'abord, l'évolution des pertes de propagation au cours du temps, appelées *Path Loss*, est analysée. Comme mentionné précédemment, le *Path Loss* est modélisé par une pente linéaire en fonction du logarithme de la distance, avec une variable aléatoire appelée *Shadowing Factor*, qui représente les variations non modélisées par la simple pente. Le graphique du *Path Loss* est obtenu en calculant la puissance moyenne sur une zone stationnaire.

Une fois ce graphique établi, deux méthodes sont présentées pour effectuer la régression linéaire. La première consiste à fixer un seuil et à ne conserver que les échantillons au-dessus de ce seuil. Cependant, cette méthode introduit un biais dans la pente, car elle crée un effet de plateau qui modifie les résultats de la régression. Pour pallier cette limitation, une seconde méthode est proposée. Elle consiste, dans un premier temps, à diviser le *Path Loss* en intervalles réguliers. Ensuite, pour chaque intervalle, la médiane est calculée. La médiane est préférée à la moyenne, car elle indique la valeur pour laquelle 50% des points se situent au-dessus et 50% au-dessous. Enfin, seuls les intervalles dont la médiane est inférieure à une valeur correspondant au bruit sont conservés. Cette approche permet de s'affranchir de l'effet plateau tout en améliorant la précision de la régression linéaire en éliminant l'influence du bruit.

Enfin, les résultats obtenus pour chacune des voies mesurées dans le cadre du scénario 3GPP sont présentés et comparés avec le modèle correspondant. Par ailleurs, le

Shadowing Factor, conformément au 3GPP, est modélisé comme une variable aléatoire suivant une loi normale sur une échelle logarithmique exprimée en décibels.

Ensuite, le calcul du *RMS Delay Spread* est présenté. Comme mentionné précédemment, le *RMS Delay Spread* représente la dispersion temporelle des retards et est calculé comme le moment d'ordre deux du PDP. Dans notre cas, le PDP est d'abord normalisé et le bruit est supprimé. Dans certaines situations, lorsque la dynamique du PDP est trop faible, un seuil de 30 dB est ajouté pour le calcul. Finalement, le moment d'ordre deux du PDP est calculé à partir de cette version traitée.

Afin de comparer les résultats avec le modèle proposé par le 3GPP, le *RMS Delay Spread* est reformulé. Plus précisément, le logarithme est appliqué au résultat du PDP, et la valeur moyenne ainsi que l'écart type des*RMS Delay Spread* calculés sur l'ensemble des mesures sont déterminés.

Ensuite, les variations à petite échelle, appelées *small scale fading*, sont calculées. L'objectif est, dans un premier temps, de retirer les variations à grande échelle de l'évolution des pertes observées lors de la mesure. Ces variations peuvent être modélisées par trois distributions bien connues : la distribution de Rice, celle de Rayleigh et celle de Nakagami. La particularité ici réside dans la méthode de détermination, qui est effectuée non pas sur la puissance mais sur le champ. Il est donc nécessaire de convertir la puissance en valeurs de champ avant d'estimer les paramètres des distributions.

Une fois les paramètres extraits, il est observé que la distribution de Rayleigh ne parvient pas à modéliser correctement les variations à petite échelle, contrairement aux distributions de Rice et de Nakagami. Étant donné que les résultats doivent être comparés avec le modèle du 3GPP, il est proposé de conserver la distribution de Rice, mais une métrique est utilisée pour valider ce choix. Pour cela, le test de Kolmogorov-Smirnov est réalisé, et les résultats pour notre exemple sont présentés. Ce test statistique permet de comparer les fonctions de répartition cumulée d'une distribution théorique, dont les paramètres sont connus, avec celle issue des données mesurées. Les résultats de ce test indiquent que la distribution de Rice modélise de manière fidèle les variations à petite échelle et peut donc être utilisée pour les comparaisons avec le 3GPP.

Finalement, un dernier paramètre est présenté : le *RMS Doppler Spread*. Ce paramètre est calculé de manière similaire au *RMS Doppler Spread*, bien que la fonction caractéristique de base soit différente. Dans le cas du *RMS Doppler Spread*, la fonction utilisée est le PDP, tandis que pour le *RMS Doppler Spread*, il s'agit de la fonction de diffusion (*scattering function*), qui représente l'étalement Doppler en fonction de la distance de mesure. Cette fonction est obtenue en moyennant, en puissance, la fonction retard-Doppler sur une zone stationnaire.

Une fois le paramètre calculé, la question de sa modélisation par une variable aléatoire se pose. Cependant, dans le cadre du 3GPP, il n'existe pas de loi statistique permettant de modéliser le *RMS Doppler Spread*. Par conséquent, aucune comparaison avec ce modèle n'est possible. Dans cette thèse, la valeur moyenne et l'écart type du *RMS Doppler Spread* normalisé sont néanmoins présentés.

Bibliography

[1] Ke Guan et al. “5G Channel Models for Railway Use Cases at mmWave Band and the Path Towards Terahertz”. en. In: *IEEE Intelligent Transportation Systems Magazine* 13.3 (2021), pp. 146–155. ISSN: 1939-1390, 1941-1197. DOI: 10.1109/MITS.2019.2926371. URL: https://ieeexplore.ieee.org/document/9006940/ (visited on 10/08/2024).

[2] Bo Ai et al. “Future railway services-oriented mobile communications network”. en. In: *IEEE Communications Magazine* 53.10 (Oct. 2015), pp. 78–85. ISSN: 0163-6804, 1558-1896. DOI: 10.1109/MCOM.2015.7295467. URL: https://ieeexplore.ieee.org/document/7295467/ (visited on 06/26/2024).

[3] Marion Berbineau et al. “Millimetric waves communications for Railways”. en. In: *Transportation Research Procedia* 72 (2023), pp. 1248–1255. ISSN: 23521465. DOI: 10.1016/j.trpro.2023.11.584. URL: https://linkinghub.elsevier.com/retrieve/pii/S2352146523008827 (visited on 07/09/2024).

[4] P. Bello. “Characterization of Randomly Time-Variant Linear Channels”. en. In: *IEEE Transactions on Communications* 11.4 (Dec. 1963), pp. 360–393. ISSN: 0096-2244. DOI: 10.1109/TCOM.1963.1088793. URL: http://ieeexplore.ieee.org/document/1088793/ (visited on 06/27/2024).

[5] R.J.C. Bultitude. “Estimating frequency correlation functions from propagation measurements on fading radio channels: a critical review”. en. In: *IEEE Journal on Selected Areas in Communications* 20.6 (Aug. 2002), pp. 1133–1143. ISSN: 0733-8716. DOI: 10.1109/JSAC.2002.801212. URL: http://ieeexplore.ieee.org/document/1021905/ (visited on 07/01/2024).

[6] T.S. Rappaport. *Wireless Communications: Principles and Practice*. Prentice Hall communications engineering and emerging technologies series. Prentice Hall PTR, 2002. ISBN: 978-0-13-042232-3. URL: https://books.google.fr/books?id=TbgQAQAAMAAJ.

[7] George R. MacCartney et al. “Path loss models for 5G millimeter wave propagation channels in urban microcells”. en. In: *2013 IEEE Global Communications Conference (GLOBECOM)*. Atlanta, GA: IEEE, Dec. 2013, pp. 3948–3953. ISBN: 978-1-4799-1353-4. DOI: 10.1109/GLOCOM.2013.6831690. URL: http://ieeexplore.ieee.org/document/6831690/ (visited on 08/16/2024).

[8] Zhuomin Hu et al. “Channel Measurement for Multiple Frequency Bands in Subway Tunnel Scenario”. en. In: *International Journal of Antennas and Propagation* 2021 (June 2021). Ed. by Renato Cicchetti, pp. 1–13. ISSN: 1687-5877, 1687-5869. DOI: 10.1155/2021/9991758. URL: https://www.hindawi.com/journals/ijap/2021/9991758/ (visited on 07/30/2024).

[9] Jae-Joon Park et al. “28-GHz High-Speed Train Measurements and Propagation Characteristics Analysis”. en. In: *2020 14th European Conference on Antennas and Propagation (EuCAP)*. Copenhagen, Denmark: IEEE, Mar. 2020, pp. 1–5. ISBN: 978-88-312-9900-8. DOI: 10.23919/EuCAP48036.2020.9135221.

URL: https://ieeexplore.ieee.org/document/9135221/ (visited on 07/30/2024).

[10] A.A.M. Saleh and R. Valenzuela. "A Statistical Model for Indoor Multipath Propagation". en. In: *IEEE Journal on Selected Areas in Communications* 5.2 (Feb. 1987), pp. 128–137. ISSN: 0733-8716. DOI: 10.1109/JSAC.1987.1146527. URL: http://ieeexplore.ieee.org/document/1146527/ (visited on 07/11/2024).

[11] Commission européenne and Direction générale de la société de l'information et des médias. *COST 207 : Digital land mobile radio communications*. Publications Office, 1989.

[12] 3GPP. *3rd Generation Partnership Project; Technical Report 5G; Study on channel model for frequencies from 0.5 to 100 GHz (Release 17)*. Tech. rep. TR 38.901 V17.0.0 (2022-04). 3GPP, 2022. URL: https://www.etsi.org/deliver/etsi_tr/138900_138999/138901/17.00.00_60/tr_138901v170000p.pdf (visited on 07/15/2024).

[13] IMT_2000. "M.1225 - Guidelines for evaluation of radio transmission technologies for IMT-2000". en. In: (1997).

[14] M. Steinbauer, A.F. Molisch, and E. Bonek. "The double-directional radio channel". en. In: *IEEE Antennas and Propagation Magazine* 43.4 (Aug. 2001), pp. 51–63. ISSN: 10459243. DOI: 10.1109/74.951559. URL: http://ieeexplore.ieee.org/document/951559/ (visited on 07/11/2024).

[15] ITU. "REPORT ITU-R M.2135-1 - Guidelines for evaluation of radio interface technologies for IMT-Advanced". en. In: ().

[16] Neha Kumari et al. "CDL Channel Model: Revolutionizing Wireless Communication". en. In: 8.7 (2023).

[17] Xuefeng Yin. *Propagation channel characterization, parameter estimation, and modeling for wireless communications*. en. Singapore: Wiley-IEEE Press, 2016. ISBN: 978-1-118-18823-1.

[18] O. Kanhere and T. S. Rappaport. *Calibration of NYURay, a 3D mmWave and sub-THz Ray Tracer using Indoor, Outdoor, and Factory Channel Measurements*. en. arXiv:2302.12380 [cs, math]. Feb. 2023. URL: http://arxiv.org/abs/2302.12380 (visited on 07/15/2024).

[19] *RapLab Rt Simulator*. ja. Mar. 2022. URL: https://network2.kke.co.jp/wireless-products/raplab/ (visited on 07/31/2024).

[20] Ke Guan, Danping He, and Zhangdui Zhong. "CloudRT: A Chinese example of open science infrastructure and services". en. In: *Cultures of Science* 4.4 (Dec. 2021), pp. 217–226. ISSN: 2096-6083, 2633-3287. DOI: 10.1177/20966083221084142. URL: http://journals.sagepub.com/doi/10.1177/20966083221084142 (visited on 07/15/2024).

[21] N. Moraitis and P. Constantinou. "Measurements and characterization of wideband indoor radio channel at 60 GHz". en. In: *IEEE Transactions on Wireless Communications* 5.4 (Apr. 2006), pp. 880–889. ISSN: 1536-1276. DOI: 10.1109/TWC.2006.1618937. URL: http://ieeexplore.ieee.org/document/1618937/ (visited on 04/25/2024).

[22] N. Moraitis and P. Constantinou. "Indoor Channel Measurements and Characterization at 60 GHz for Wireless Local Area Network Applications". en. In: *IEEE Transactions on Antennas and Propagation* 52.12 (Dec. 2004), pp. 3180–3189. ISSN: 0018-926X. DOI: 10.1109/TAP.2004.836422. URL: http://ieeexplore.ieee.org/document/1364132/ (visited on 06/11/2024).

[23] Aniruddha Chandra et al. "60-GHz Millimeter-Wave Propagation Inside Bus: Measurement, Modeling, Simulation, and Performance Analysis". en. In: *IEEE*

Access 7 (2019), pp. 97815–97826. ISSN: 2169-3536. DOI: 10.1109/ACCESS.2019.2924729. URL: https://ieeexplore.ieee.org/document/8744573/ (visited on 04/24/2024).

[24] Petros Karadimas, Ben Allen, and Ernest Okon. "60 GHz time-domain propagation measurement system". en. In: *2012 Loughborough Antennas & Propagation Conference (LAPC)*. Loughborough, Leicestershire, United Kingdom: IEEE, Nov. 2012, pp. 1–4. ISBN: 978-1-4673-2220-1 978-1-4673-2218-8 978-1-4673-2219-5. DOI: 10.1109/LAPC.2012.6403041. URL: http://ieeexplore.ieee.org/document/6403041/ (visited on 02/11/2022).

[25] Seyran Khademi et al. "Channel Measurements and Modeling for a 60 GHz Wireless Link Within a Metal Cabinet". en. In: *IEEE Transactions on Wireless Communications* 14.9 (Sept. 2015), pp. 5098–5110. ISSN: 1536-1276. DOI: 10.1109/TWC.2015.2432755. URL: http://ieeexplore.ieee.org/document/7106513/ (visited on 04/22/2024).

[26] Seyran Khademi et al. *60 GHz Wireless Link Within Metal Enclosures: Channel Measurements and System Analysis*. en. arXiv:1311.4439 [cs, math]. Nov. 2013. URL: http://arxiv.org/abs/1311.4439 (visited on 01/20/2024).

[27] Ismail Ben Mabrouk et al. "Feasibility of a Millimeter-Wave MIMO System for Short-Range Wireless Communications in an Underground Gold Mine". en. In: *IEEE Transactions on Antennas and Propagation* 61.8 (Aug. 2013), pp. 4296–4305. ISSN: 0018-926X, 1558-2221. DOI: 10.1109/TAP.2013.2259454. URL: http://ieeexplore.ieee.org/document/6507244/ (visited on 04/22/2024).

[28] Mohamad Ghaddar et al. "Mm-waves propagation measurements in underground mine using directional MIMO antennas". en. In: *IET Microwaves, Antennas & Propagation* 10.5 (Apr. 2016), pp. 517–524. ISSN: 1751-8733, 1751-8733. DOI: 10.1049/iet-map.2015.0408. URL: https://onlinelibrary.wiley.com/doi/10.1049/iet-map.2015.0408 (visited on 04/22/2024).

[29] Katsuyuki Haneda et al. "Indoor short-range radio propagation measurements at 60 and 70 GHz". en. In: *The 8th European Conference on Antennas and Propagation (EuCAP 2014)*. The Hague, Netherlands: IEEE, Apr. 2014, pp. 634–638. ISBN: 978-88-907018-4-9. DOI: 10.1109/EuCAP.2014.6901839. URL: http://ieeexplore.ieee.org/document/6901839/ (visited on 04/22/2024).

[30] Katsuyuki Haneda et al. "Estimating the omni-directional pathloss from directional channel sounding". en. In: *2016 10th European Conference on Antennas and Propagation (EuCAP)*. Davos, Switzerland: IEEE, Apr. 2016, pp. 1–5. ISBN: 978-88-907018-6-3. DOI: 10.1109/EuCAP.2016.7481455. URL: http://ieeexplore.ieee.org/document/7481455/ (visited on 04/22/2024).

[31] Joni Vehmas et al. "Millimeter-Wave Channel Characterization at Helsinki Airport in the 15, 28, and 60 GHz Bands". en. In: *2016 IEEE 84th Vehicular Technology Conference (VTC-Fall)*. Montreal, QC, Canada: IEEE, Sept. 2016, pp. 1–5. ISBN: 978-1-5090-1701-0. DOI: 10.1109/VTCFall.2016.7881086. URL: http://ieeexplore.ieee.org/document/7881086/ (visited on 04/22/2024).

[32] Dajana Cassioli. "60 GHz UWB channel measurement and model". en. In: *2012 IEEE International Conference on Ultra-Wideband*. Syracuse, NY, USA: IEEE, Sept. 2012, pp. 145–149. ISBN: 978-1-4577-2032-1 978-1-4577-2031-4 978-1-4577-2030-7. DOI: 10.1109/ICUWB.2012.6340429. URL: http://ieeexplore.ieee.org/document/6340429/ (visited on 04/22/2024).

[33] Dajana Cassioli, Luca Alfredo Annoni, and Stefano Piersanti. "Characterization of path loss and delay spread of 60-GHz UWB channels vs. frequency". en. In: *2013 IEEE International Conference on Communications (ICC)*. Budapest, Hungary: IEEE, June 2013, pp. 5153–5157. ISBN: 978-1-4673-3122-7.

DOI: 10.1109/ICC.2013.6655401. URL: http://ieeexplore.ieee.org/document/6655401/ (visited on 04/22/2024).

[34] T. Zwick, T.J. Beukema, and Haewoon Nam. "Wideband channel sounder with measurements and model for the 60 GHz indoor radio channel". en. In: *IEEE Transactions on Vehicular Technology* 54.4 (July 2005), pp. 1266–1277. ISSN: 0018-9545, 1939-9359. DOI: 10.1109/TVT.2005.851354. URL: http://ieeexplore.ieee.org/document/1492680/ (visited on 04/22/2024).

[35] Robert Muller et al. "Ultrawideband multichannel sounding for mm-wave". In: *The 8th European Conference on Antennas and Propagation (EuCAP 2014)*. The Hague, Netherlands: IEEE, Apr. 2014, pp. 817–821. ISBN: 978-88-907018-4-9. DOI: 10.1109/EuCAP.2014.6901887. URL: http://ieeexplore.ieee.org/document/6901887/ (visited on 04/22/2024).

[36] Alexis Paolo Garcia Ariza et al. "60 GHz Ultrawideband Polarimetric MIMO Sensing for Wireless Multi-Gigabit and Radar". en. In: *IEEE Transactions on Antennas and Propagation* 61.4 (Apr. 2013), pp. 1631–1641. ISSN: 0018-926X, 1558-2221. DOI: 10.1109/TAP.2013.2243398. URL: http://ieeexplore.ieee.org/document/6422351/ (visited on 04/22/2024).

[37] Christopher Slezak, Aditya Dhananjay, and Sundeep Rangan. *60 GHz Blockage Study Using Phased Arrays*. en. arXiv:1712.05457 [cs, eess]. Dec. 2017. URL: http://arxiv.org/abs/1712.05457 (visited on 04/25/2024).

[38] Christopher Slezak et al. "Empirical Effects of Dynamic Human-Body Blockage in 60 GHz Communications". en. In: *IEEE Communications Magazine* 56.12 (Dec. 2018), pp. 60–66. ISSN: 0163-6804, 1558-1896. DOI: 10.1109/MCOM.2018.1800232. URL: https://ieeexplore.ieee.org/document/8570041/ (visited on 04/22/2024).

[39] Ruoyu Sun et al. "Design and calibration of a double-directional 60 GHz channel sounder for multipath component tracking". en. In: *2017 11th European Conference on Antennas and Propagation (EUCAP)*. Paris, France: IEEE, Mar. 2017, pp. 3336–3340. ISBN: 978-88-907018-7-0. DOI: 10.23919/EuCAP.2017.7928270. URL: http://ieeexplore.ieee.org/document/7928270/ (visited on 04/22/2024).

[40] Jeanne T. Quimby et al. "Millimeter-Wave Channel-Sounder Performance Verification Using Vector Network Analyzer in a Controlled RF Channel". en. In: *IEEE Transactions on Antennas and Propagation* 69.11 (Nov. 2021), pp. 7867–7875. ISSN: 0018-926X, 1558-2221. DOI: 10.1109/TAP.2021.3083737. URL: https://ieeexplore.ieee.org/document/9445598/ (visited on 04/22/2024).

[41] Jack Chuang et al. "Blind Calibration of Phase Drift in Millimeter-Wave Channel Sounders". en. In: *IEEE Access* 8 (2020), pp. 109557–109567. ISSN: 2169-3536. DOI: 10.1109/ACCESS.2020.3001852. URL: https://ieeexplore.ieee.org/document/9115009/ (visited on 04/22/2024).

[42] Peter B. Papazian et al. "Calibration of millimeter-wave channel sounders for super-resolution multipath component extraction". en. In: *2016 10th European Conference on Antennas and Propagation (EuCAP)*. Davos, Switzerland: IEEE, Apr. 2016, pp. 1–5. ISBN: 978-88-907018-6-3. DOI: 10.1109/EuCAP.2016.7481704. URL: http://ieeexplore.ieee.org/document/7481704/ (visited on 04/22/2024).

[43] Peter B. Papazian et al. "Radio channel sounders for modeling mobile communications at 28 GHz, 60 GHz and 83 GHz". en. In: *Global Symposium on Millimeter-Waves (GSMM)*. Montreal, QC, Canada: IEEE, May 2015, pp. 1–

3. ISBN: 978-1-4673-8063-8. DOI: 10.1109/GSMM.2015.7175448. URL: http://ieeexplore.ieee.org/document/7175448/ (visited on 04/22/2024).

[44] Josef Vychodil et al. "UWB time domain channel sounder". en. In: *2015 25th International Conference Radioelektronika (RADIOELEKTRONIKA)*. Pardubice, Czech Republic: IEEE, Apr. 2015, pp. 268–271. ISBN: 978-1-4799-8117-5 978-1-4799-8119-9. DOI: 10.1109/RADIOELEK.2015.7129028. URL: http://ieeexplore.ieee.org/document/7129028/ (visited on 04/22/2024).

[45] Josef Vychodil et al. "Millimetre wave band time domain channel sounder". en. In: *IET Communications* 13.3 (Feb. 2019), pp. 331–338. ISSN: 1751-8636, 1751-8636. DOI: 10.1049/iet-com.2018.5453. URL: https://onlinelibrary.wiley.com/doi/10.1049/iet-com.2018.5453 (visited on 04/22/2024).

[46] Wilhelm Keusgen et al. "A highly flexible digital radio testbed and 60 GHz application examples". en. In: *2013 European Microwave Conference*. Nuremberg, Germany: IEEE, Oct. 2013, pp. 740–743. ISBN: 978-2-87487-031-6. DOI: 10.23919/EuMC.2013.6686762. URL: https://ieeexplore.ieee.org/document/6686762/ (visited on 04/22/2024).

[47] Wilhelm Keusgen et al. "An NLOS-capable 60 GHz MIMO demonstrator: System concept & performance". en. In: *2011 IEEE 9th International New Circuits and systems conference*. Bordeaux, France: IEEE, June 2011, pp. 265–268. ISBN: 978-1-61284-135-9 978-1-61284-137-3. DOI: 10.1109/NEWCAS.2011.5981306. URL: https://ieeexplore.ieee.org/document/5981306/ (visited on 04/22/2024).

[48] M. Peter and W. Keusgen. "A component-based time domain wideband channel sounder and measurement results for the 60 GHz in-cabin radio channel". en. In: *2nd European Conference on Antennas and Propagation (EuCAP 2007)*. Edinburgh, UK: Institution of Engineering and Technology, 2007, pp. 706–706. ISBN: 978-0-86341-842-6. DOI: 10.1049/ic.2007.1233. URL: https://digital-library.theiet.org/content/conferences/10.1049/ic.2007.1233 (visited on 04/22/2024).

[49] J. Kivinen et al. "Wideband radio channel measurement system at 2 GHz". en. In: *IEEE Transactions on Instrumentation and Measurement* 48.1 (Feb. 1999), pp. 39–44. ISSN: 00189456. DOI: 10.1109/19.755057. URL: http://ieeexplore.ieee.org/document/755057/ (visited on 04/24/2024).

[50] Jarmo Kivinen. "60-GHz Wideband Radio Channel Sounder". en. In: *IEEE Transactions on Instrumentation and Measurement* 56.5 (Oct. 2007), pp. 1831–1838. ISSN: 0018-9456. DOI: 10.1109/TIM.2007.895616. URL: http://ieeexplore.ieee.org/document/4303419/ (visited on 02/10/2022).

[51] S. Guillouard, G. El Zein, and J. Citerne. "High Time Domain Resolution Indoor Channel Sounder for the 60 GHz Band". en. In: *1998 28th European Microwave Conference*. Amsterdam, Netherlands: IEEE, Oct. 1998, pp. 341–344. DOI: 10.1109/EUMA.1998.338175. URL: https://ieeexplore.ieee.org/document/4139230/ (visited on 04/23/2024).

[52] E. Ben-Dor et al. "Millimeter-Wave 60 GHz Outdoor and Vehicle AOA Propagation Measurements Using a Broadband Channel Sounder". en. In: *2011 IEEE Global Telecommunications Conference - GLOBECOM 2011*. Houston, TX, USA: IEEE, Dec. 2011, pp. 1–6. ISBN: 978-1-4244-9268-8 978-1-4244-9266-4 978-1-4244-9267-1. DOI: 10.1109/GLOCOM.2011.6133581. URL: http://ieeexplore.ieee.org/document/6133581/ (visited on 04/23/2024).

[53] Lahatra Rakotondrainibe et al. "Indoor Channel Measurements and Communications System Design at 60 GHz". en. In: ().

[54] Edgar Lemos Cid, Manuel Garcia Sanchez, and Ana Vazquez Alejos. "High speed transmission at 60 GHz for 5G communications". en. In: *2015 IEEE International Symposium on Antennas and Propagation & USNC/URSI National Radio Science Meeting*. Vancouver, BC, Canada: IEEE, July 2015, pp. 1007–1008. ISBN: 978-1-4799-7815-1. DOI: 10.1109/APS.2015.7304891. URL: http://ieeexplore.ieee.org/document/7304891/ (visited on 04/23/2024).

[55] Joseba Osa et al. "A Cost-Effective Directional Millimeter-Wave Channel Sounder for 60 GHz Industrial Wireless Communications". en. In: *2022 IEEE 18th International Conference on Factory Communication Systems (WFCS)*. Pavia, Italy: IEEE, Apr. 2022, pp. 1–8. ISBN: 978-1-66541-086-1. DOI: 10.1109/WFCS53837.2022.9779175. URL: https://ieeexplore.ieee.org/document/9779175/ (visited on 04/23/2024).

[56] Andrew C M Austin et al. "60 GHz Millimetre-Wave Channel Characterisation for Indoor Office Environments". en. In: ().

[57] Jan Erik Hakegard et al. "mm-Wave channel sounding using a fully programmable SoC". en. In: *2016 IEEE 27th Annual International Symposium on Personal, Indoor, and Mobile Radio Communications (PIMRC)*. Valencia, Spain: IEEE, Sept. 2016, pp. 1–6. ISBN: 978-1-5090-3254-9. DOI: 10.1109/PIMRC.2016.7794727. URL: http://ieeexplore.ieee.org/document/7794727/ (visited on 04/23/2024).

[58] Kun Yang et al. "Propagation measurements with regional train at 60 GHz for virtual coupling application". en. In: *2017 11th European Conference on Antennas and Propagation (EUCAP)*. Paris, France: IEEE, Mar. 2017, pp. 126–130. ISBN: 978-88-907018-7-0. DOI: 10.23919/EuCAP.2017.7928494. URL: http://ieeexplore.ieee.org/document/7928494/ (visited on 02/11/2022).

[59] Stuart M Feeney and Sana Salous. "Implementation of a Channel Sounder for the 60 GHz Band". en. In: ().

[60] Mir Ghoraishi et al. "Millimeter wave spread in delay and azimuth for small cell propagation channel at 60 GHz". en. In: *2017 XXXIInd General Assembly and Scientific Symposium of the International Union of Radio Science (URSI GASS)*. Montreal, QC: IEEE, Aug. 2017, pp. 1–4. ISBN: 978-90-825987-0-4. DOI: 10.23919/URSIGASS.2017.8105336. URL: http://ieeexplore.ieee.org/document/8105336/ (visited on 04/23/2024).

[61] E Beller and D J Newman. "AN h EXTREMAL PROBLEM FOR POLYNOMIALS". en. In: ().

[62] Jean-Marc Conrat, Patrice Pajusco, and Jean-Yves Thiriet. "A Multibands Wideband Propagation Channel Sounder from 2 to 60 GHz". en. In: *2006 IEEE Instrumentation and Measurement Technology Conference Proceedings*. ISSN: 1091-5281. Sorrento, Italy: IEEE, Apr. 2006, pp. 590–595. ISBN: 978-0-7803-9360-8 978-0-7803-9359-2. DOI: 10.1109/IMTC.2006.328629. URL: http://ieeexplore.ieee.org/document/4124394/ (visited on 01/20/2024).

[63] Paul Unterhuber et al. "Wide band propagation in train-to-train scenarios — Measurement campaign and first results". en. In: *2017 11th European Conference on Antennas and Propagation (EUCAP)*. Paris, France: IEEE, Mar. 2017, pp. 3356–3360. ISBN: 978-88-907018-7-0. DOI: 10.23919/EuCAP.2017.7928309. URL: http://ieeexplore.ieee.org/document/7928309/ (visited on 02/11/2022).

[64] Minseok Kim et al. "Development of Low-Cost 60-GHz Millimeter-Wave Channel Sounding System". en. In: ().

[65] Minseok Kim et al. “A 24/60-GHz Dual-Band Double-Directional Channel Sounder Using COTS Phased Arrays”. en. In: *2022 IEEE International Conference on Communications Workshops (ICC Workshops)*. Seoul, Korea, Republic of: IEEE, May 2022, pp. 1113–1117. ISBN: 978-1-66542-671-8. DOI: 10.1109/ICCWorkshops53468.2022.9814563. URL: https://ieeexplore.ieee.org/document/9814563/ (visited on 04/23/2024).

[66] E. Zochmann et al. “Measured Delay and Doppler Profiles of Overtaking Vehicles at 60 GHz”. en. In: *12th European Conference on Antennas and Propagation (EuCAP 2018)*. London, UK: Institution of Engineering and Technology, 2018, 111 (5 pp.)–111 (5 pp.) ISBN: 978-1-78561-816-1. DOI: 10.1049/cp.2018.0470. URL: https://digital-library.theiet.org/content/conferences/10.1049/cp.2018.0470 (visited on 04/24/2024).

[67] E. ZOchmann et al. “Statistical Evaluation of Delay and Doppler Spread in 60 GHz Vehicle-to-Vehicle Channels During Overtaking”. en. In: *2018 IEEE-APS Topical Conference on Antennas and Propagation in Wireless Communications (APWC)*. Cartagena des Indias: IEEE, Sept. 2018, pp. 1–4. ISBN: 978-1-5386-6765-1. DOI: 10.1109/APWC.2018.8503750. URL: https://ieeexplore.ieee.org/document/8503750/ (visited on 09/28/2023).

[68] Erich Zochmann et al. “Position-Specific Statistics of 60 GHz Vehicular Channels During Overtaking”. en. In: *IEEE Access* 7 (2019), pp. 14216–14232. ISSN: 2169-3536. DOI: 10.1109/ACCESS.2019.2893136. URL: https://ieeexplore.ieee.org/document/8612933/ (visited on 09/28/2023).

[69] Adrian Loch et al. *A Channel Measurement Campaign for mmWave Communication in Industrial Settings*. en. arXiv:1903.10502 [cs]. Mar. 2019. URL: http://arxiv.org/abs/1903.10502 (visited on 04/22/2024).

[70] Anton Shkel, Alireza Mehrabani, and Julius Kusuma. “A Configurable 60GHz Phased Array Platform for Multi-Link mmWave Channel Characterization”. en. In: *2021 IEEE International Conference on Communications Workshops (ICC Workshops)*. Montreal, QC, Canada: IEEE, June 2021, pp. 1–6. ISBN: 978-1-72819-441-7. DOI: 10.1109/ICCWorkshops50388.2021.9473724. URL: https://ieeexplore.ieee.org/document/9473724/ (visited on 04/22/2024).

[71] Diego Dupleich et al. “Investigations on fading scaling with bandwidth and directivity at 60 GHz”. en. In: *2017 11th European Conference on Antennas and Propagation (EUCAP)*. Paris, France: IEEE, Mar. 2017, pp. 3375–3379. ISBN: 978-88-907018-7-0. DOI: 10.23919/EuCAP.2017.7928451. URL: http://ieeexplore.ieee.org/document/7928451/ (visited on 04/22/2024).

[72] Diego Dupleich et al. “Multi-band Indoor Propagation Characterization by Measurements from 6 to 60 GHz”. en. In: (2019).

[73] D. Dupleich et al. “Multi-band Spatio-Temporal Characterization of a V2V Environment Under Blockage”. en. In: *12th European Conference on Antennas and Propagation (EuCAP 2018)*. London, UK: Institution of Engineering and Technology, 2018, 366 (5 pp.)–366 (5 pp.) ISBN: 978-1-78561-816-1. DOI: 10.1049/cp.2018.0725. URL: https://digital-library.theiet.org/content/conferences/10.1049/cp.2018.0725 (visited on 04/22/2024).

[74] Diego Dupleich et al. “Multi-Band Vehicle to Vehicle Channel Measurements from 6 GHz to 60 GHz at "T" Intersection”. en. In: *2019 IEEE 2nd Connected and Automated Vehicles Symposium (CAVS)*. Honolulu, HI, USA: IEEE, Sept. 2019, pp. 1–5. ISBN: 978-1-72813-616-5. DOI: 10.1109/CAVS.2019.8887794. URL: https://ieeexplore.ieee.org/document/8887794/ (visited on 04/22/2024).

[75] Robert Muller et al. “Simultaneous multi-band channel sounding at mm-Wave frequencies”. en. In: *2016 10th European Conference on Antennas and Propagation (EuCAP)*. Davos, Switzerland: IEEE, Apr. 2016, pp. 1–5. ISBN: 978-88-907018-6-3. DOI: 10.1109/EuCAP.2016.7481757. URL: http://ieeexplore.ieee.org/document/7481757/ (visited on 04/22/2024).

[76] Robert Muller et al. “Ultra-Wideband Channel Sounder for Measurements at 70 GHz”. en. In: *2015 IEEE 81st Vehicular Technology Conference (VTC Spring)*. Glasgow, United Kingdom: IEEE, May 2015, pp. 1–5. ISBN: 978-1-4799-8088-8. DOI: 10.1109/VTCSpring.2015.7146143. URL: http://ieeexplore.ieee.org/document/7146143/ (visited on 04/22/2024).

[77] Peter B. Papazian et al. “A Radio Channel Sounder for Mobile Millimeter-Wave Communications: System Implementation and Measurement Assessment”. en. In: *IEEE Transactions on Microwave Theory and Techniques* 64.9 (Sept. 2016), pp. 2924–2932. ISSN: 0018-9480, 1557-9670. DOI: 10.1109/TMTT.2016.2592530. URL: http://ieeexplore.ieee.org/document/7534832/ (visited on 04/24/2024).

[78] Anmol Bhardwaj et al. “Geometrical-Empirical Channel Propagation Model for Human Presence at 60 GHz”. en. In: *IEEE Access* 9 (2021), pp. 38467–38478. ISSN: 2169-3536. DOI: 10.1109/ACCESS.2021.3063655. URL: https://ieeexplore.ieee.org/document/9367140/ (visited on 04/22/2024).

[79] William Sloane et al. “Measurement-Based Analysis of Millimeter-Wave Channel Sparsity”. en. In: *IEEE Antennas and Wireless Propagation Letters* 22.4 (Apr. 2023), pp. 784–788. ISSN: 1536-1225, 1548-5757. DOI: 10.1109/LAWP.2022.3225246. URL: https://ieeexplore.ieee.org/document/9964460/ (visited on 04/22/2024).

[80] Aidan Hughes et al. “Measuring the Impact of Beamwidth on the Correlation Distance of 60 GHz Indoor and Outdoor Channels”. en. In: *IEEE Open Journal of Vehicular Technology* 2 (2021), pp. 180–193. ISSN: 2644-1330. DOI: 10.1109/OJVT.2021.3067673. URL: https://ieeexplore.ieee.org/document/9382846/ (visited on 04/22/2024).

[81] Chiehping Lai et al. “Methodology for Multipath-Component Tracking in Millimeter-Wave Channel Modeling”. en. In: *IEEE Transactions on Antennas and Propagation* 67.3 (Mar. 2019), pp. 1826–1836. ISSN: 0018-926X, 1558-2221. DOI: 10.1109/TAP.2018.2888686. URL: https://ieeexplore.ieee.org/document/8581503/ (visited on 04/22/2024).

[82] Camillo Gentile et al. “Millimeter-Wave Channel Measurement and Modeling: A NIST Perspective”. en. In: *IEEE Communications Magazine* 56.12 (Dec. 2018), pp. 30–37. ISSN: 0163-6804, 1558-1896. DOI: 10.1109/MCOM.2018.1800222. URL: https://ieeexplore.ieee.org/document/8570037/ (visited on 04/22/2024).

[83] Sung Yun Jun et al. “Penetration Loss at 60 GHz for Indoor-to-Indoor and Outdoor-to-Indoor Mobile Scenarios”. en. In: *2020 14th European Conference on Antennas and Propagation (EuCAP)*. Copenhagen, Denmark: IEEE, Mar. 2020, pp. 1–5. ISBN: 978-88-312-9900-8. DOI: 10.23919/EuCAP48036.2020.9135581. URL: https://ieeexplore.ieee.org/document/9135581/ (visited on 04/22/2024).

[84] Camillo Gentile et al. “Quasi-Deterministic Channel Model Parameters for a Data Center at 60 GHz”. en. In: *IEEE Antennas and Wireless Propagation Letters* 17.5 (May 2018), pp. 808–812. ISSN: 1536-1225, 1548-5757. DOI: 10.1109/LAWP.2018.2817066. URL: https://ieeexplore.ieee.org/document/8319437/ (visited on 04/22/2024).

[85] Michael Peter et al. “Channel Measurement and Modeling for 5G Urban Microcellular Scenarios”. en. In: *Sensors* 16.8 (Aug. 2016), p. 1330. ISSN: 1424-8220. DOI: 10.3390/s16081330. URL: http://www.mdpi.com/1424-8220/16/8/1330 (visited on 04/22/2024).

[86] Richard J. Weiler et al. “Measuring the busy urban 60 GHz outdoor access radio channel”. en. In: *2014 IEEE International Conference on Ultra-WideBand (ICUWB)*. Paris, France: IEEE, Sept. 2014, pp. 166–170. ISBN: 978-1-4799-5396-7. DOI: 10.1109/ICUWB.2014.6958971. URL: https://ieeexplore.ieee.org/document/6958971/ (visited on 04/22/2024).

[87] Richard J. Weiler et al. “Millimeter-wave channel sounding of outdoor ground reflections”. en. In: *2015 IEEE Radio and Wireless Symposium (RWS)*. San Diego, CA, USA: IEEE, Jan. 2015, pp. 95–97. ISBN: 978-1-4799-5507-7. DOI: 10.1109/RWS.2015.7129712. URL: https://ieeexplore.ieee.org/document/7129712/ (visited on 04/22/2024).

[88] Richard J. Weiler et al. “Quasi-deterministic millimeter-wave channel models in MiWEBA”. en. In: *EURASIP Journal on Wireless Communications and Networking* 2016.1 (Dec. 2016), p. 84. ISSN: 1687-1499. DOI: 10.1186/s13638-016-0568-6. URL: https://jwcn-eurasipjournals.springeropen.com/articles/10.1186/s13638-016-0568-6 (visited on 06/12/2024).

[89] Michael Peter et al. “Measurement and Analysis of the 60 GHz In-Vehicular Broadband Radio Channel”. en. In: *2007 IEEE 66th Vehicular Technology Conference*. ISSN: 1090-3038. Baltimore, MD, USA: IEEE, Sept. 2007, pp. 834–838. ISBN: 978-1-4244-0263-2. DOI: 10.1109/VETECF.2007.183. URL: http://ieeexplore.ieee.org/document/4349832/ (visited on 04/22/2024).

[90] Jan M. Kelner et al. “Angular Power Distribution in 60 GHz Wireless Uplink for Vehicle-to-Infrastructure Scenarios”. en. In: *2021 IEEE 32nd Annual International Symposium on Personal, Indoor and Mobile Radio Communications (PIMRC)*. Helsinki, Finland: IEEE, Sept. 2021, pp. 899–904. ISBN: 978-1-72817-586-7. DOI: 10.1109/PIMRC50174.2021.9569535. URL: https://ieeexplore.ieee.org/document/9569535/ (visited on 04/22/2024).

[91] Rajeev Shukla et al. “Deep Learning based Power Delay Profile Trend Generation: A 60 GHz Intra-Vehicle Case Study”. en. In: *2022 IEEE International Symposium on Antennas and Propagation and USNC-URSI Radio Science Meeting (AP-S/URSI)*. Denver, CO, USA: IEEE, July 2022, pp. 1–2. ISBN: 978-1-66549-658-2. DOI: 10.1109/AP-S/USNC-URSI47032.2022.9887316. URL: https://ieeexplore.ieee.org/document/9887316/ (visited on 04/22/2024).

[92] Aniq Ur Rahman et al. “Doppler Characteristics of 60 GHz mmWave I2I Channels”. en. In: *ICC 2019 - 2019 IEEE International Conference on Communications (ICC)*. Shanghai, China: IEEE, May 2019, pp. 1–6. ISBN: 978-1-5386-8088-9. DOI: 10.1109/ICC.2019.8761798. URL: https://ieeexplore.ieee.org/document/8761798/ (visited on 04/22/2024).

[93] Jiri Blumenstein et al. “Measured High-Resolution Power-Delay Profiles of Nonstationary Vehicular Millimeter Wave Channels”. en. In: *2018 IEEE 29th Annual International Symposium on Personal, Indoor and Mobile Radio Communications (PIMRC)*. Bologna, Italy: IEEE, Sept. 2018, pp. 1–5. ISBN: 978-1-5386-6009-6. DOI: 10.1109/PIMRC.2018.8580949. URL: https://ieeexplore.ieee.org/document/8580949/ (visited on 04/22/2024).

[94] Ales Prokes et al. “Multipath Propagation Analysis for Vehicle-to-Infrastructure Communication at 60 GHz”. en. In: *2019 IEEE Vehicular Networking Conference (VNC)*. Los Angeles, CA, USA: IEEE, Dec. 2019, pp. 1–8. ISBN:

978-1-72814-571-6. DOI: 10.1109/VNC48660.2019.9062771. URL: https://ieeexplore.ieee.org/document/9062771/ (visited on 04/22/2024).

[95] Ales Prokes et al. "Time-Domain Broadband 60 GHz Channel Sounder for Vehicle-to-Vehicle Channel Measurement". en. In: *2018 IEEE Vehicular Networking Conference (VNC)*. Taipei, Taiwan: IEEE, Dec. 2018, pp. 1–7. ISBN: 978-1-5386-9428-2. DOI: 10.1109/VNC.2018.8628344. URL: https://ieeexplore.ieee.org/document/8628344/ (visited on 04/22/2024).

[96] Ales Prokes et al. "Time-domain nonstationary intra-car channel measurement in 60 GHz band". en. In: *2016 International Conference on Advanced Technologies for Communications (ATC)*. Hanoi, Vietnam: IEEE, Oct. 2016, pp. 1–6. ISBN: 978-1-5090-2711-8. DOI: 10.1109/ATC.2016.7764753. URL: http://ieeexplore.ieee.org/document/7764753/ (visited on 04/22/2024).

[97] Jiri Blumenstein et al. "Vehicle-to-Vehicle Millimeter-Wave Channel Measurements at 56-64 GHz". en. In: *2019 IEEE 90th Vehicular Technology Conference (VTC2019-Fall)*. Honolulu, HI, USA: IEEE, Sept. 2019, pp. 1–5. ISBN: 978-1-72811-220-6. DOI: 10.1109/VTCFall.2019.8891543. URL: https://ieeexplore.ieee.org/document/8891543/ (visited on 04/22/2024).

[98] D. Cassioli. "UWB Moves up to mmWaves: A channel modeling perspective". en. In: *2011 IEEE International Conference on Ultra-Wideband (ICUWB)*. Bologna: IEEE, Sept. 2011, pp. 521–525. ISBN: 978-1-4577-1764-2 978-1-4577-1763-5 978-1-4577-1762-8. DOI: 10.1109/ICUWB.2011.6058900. URL: http://ieeexplore.ieee.org/document/6058900/ (visited on 06/11/2024).

[99] Mathew K. Samimi and Theodore S. Rappaport. "3-D Millimeter-Wave Statistical Channel Model for 5G Wireless System Design". en. In: *IEEE Transactions on Microwave Theory and Techniques* 64.7 (July 2016), pp. 2207–2225. ISSN: 0018-9480, 1557-9670. DOI: 10.1109/TMTT.2016.2574851. URL: http://ieeexplore.ieee.org/document/7501500/ (visited on 04/23/2024).

[100] Theodore S. Rappaport et al. "38 GHz and 60 GHz angle-dependent propagation for cellular & peer-to-peer wireless communications". en. In: *2012 IEEE International Conference on Communications (ICC)*. Ottawa, ON, Canada: IEEE, June 2012, pp. 4568–4573. ISBN: 978-1-4577-2053-6 978-1-4577-2052-9 978-1-4577-2051-2. DOI: 10.1109/ICC.2012.6363891. URL: http://ieeexplore.ieee.org/document/6363891/ (visited on 04/23/2024).

[101] Sylvain Collonge, Gheorghe Zaharia, and Ghaïs El Zein. "Wideband and dynamic characterization of the 60GHZ indoor radio propagation — future home-WLAN architectures". en. In: *Annales Des Télécommunications* 58.3-4 (Mar. 2003), pp. 417–447. ISSN: 0003-4347, 1958-9395. DOI: 10.1007/BF03001023. URL: https://link.springer.com/10.1007/BF03001023 (visited on 04/23/2024).

[102] M. Z. Zaaimia et al. "60 GHz wireless data center channel measurements: Initial results". en. In: *2014 IEEE International Conference on Ultra-WideBand (ICUWB)*. Paris, France: IEEE, Sept. 2014, pp. 57–61. ISBN: 978-1-4799-5396-7. DOI: 10.1109/ICUWB.2014.6958951. URL: http://ieeexplore.ieee.org/document/6958951/ (visited on 04/22/2024).

[103] M. Z. Zaaimia et al. "60-GHz Statistical Channel Characterization for Wireless Data Centers". en. In: *IEEE Antennas and Wireless Propagation Letters* 15 (2016), pp. 976–979. ISSN: 1536-1225, 1548-5757. DOI: 10.1109/LAWP.2015.2487381. URL: http://ieeexplore.ieee.org/document/7289372/ (visited on 04/22/2024).

[104] Larbi Talbi and Jules LeBel. "Broadband 60 GHz Sounder for Propagation Channel Measurements Over Short/Medium Distances". en. In: *IEEE Transactions on Instrumentation and Measurement* 63.2 (Feb. 2014), pp. 343–351. ISSN: 0018-9456, 1557-9662. DOI: 10.1109/TIM.2013.2280487. URL: http://ieeexplore.ieee.org/document/6601019/ (visited on 04/22/2024).

[105] M. Ghaddar et al. "Experimental analysis of human body effects on NLOS 60 GHz propagation channel". en. In: *2015 IEEE International Symposium on Antennas and Propagation & USNC/URSI National Radio Science Meeting*. Vancouver, BC, Canada: IEEE, July 2015, pp. 1788–1789. ISBN: 978-1-4799-7815-1. DOI: 10.1109/APS.2015.7305283. URL: http://ieeexplore.ieee.org/document/7305283/ (visited on 04/22/2024).

[106] V. Semkin et al. "Static and Dynamic Millimeter-Wave Channel Measurements at 60 GHz in a Conference Room". en. In: *12th European Conference on Antennas and Propagation (EuCAP 2018)*. London, UK: Institution of Engineering and Technology, 2018, 342 (5 pp.)–342 (5 pp.) ISBN: 978-1-78561-816-1. DOI: 10.1049/cp.2018.0701. URL: https://digital-library.theiet.org/content/conferences/10.1049/cp.2018.0701 (visited on 04/22/2024).

[107] Sylvain Ranvier et al. "VNA-based wideband 60 GHz MIMO channel sounder with 3-D arrays". en. In: *2009 IEEE Radio and Wireless Symposium*. San Diego, CA, USA: IEEE, Jan. 2009, pp. 308–311. ISBN: 978-1-4244-2698-0. DOI: 10.1109/RWS.2009.4957340. URL: http://ieeexplore.ieee.org/document/4957340/ (visited on 04/22/2024).

[108] Maria-Teresa Martinez-Ingles et al. "Deterministic and Experimental Indoor mmW Channel Modeling". en. In: *IEEE Antennas and Wireless Propagation Letters* 13 (2014), pp. 1047–1050. ISSN: 1536-1225, 1548-5757. DOI: 10.1109/LAWP.2014.2327054. URL: http://ieeexplore.ieee.org/document/6823110/ (visited on 04/22/2024).

[109] Marc Kacou et al. "Coverage and Throughput Analysis at 60 GHz for Indoor WLAN with Indirect Paths". en. In: *2018 IEEE 29th Annual International Symposium on Personal, Indoor and Mobile Radio Communications (PIMRC)*. Bologna, Italy: IEEE, Sept. 2018, pp. 1–5. ISBN: 978-1-5386-6009-6. DOI: 10.1109/PIMRC.2018.8580903. URL: https://ieeexplore.ieee.org/document/8580903/ (visited on 04/22/2024).

[110] Sucheta Bhaumik, Ales Prokes, and Aniruddha Chandra. "Combined K-Means and Amplitude Clustering of Impulse Response for 60 GHz Vehicular Channels". en. In: *2018 15th International Symposium on Wireless Communication Systems (ISWCS)*. Lisbon: IEEE, Aug. 2018, pp. 1–5. ISBN: 978-1-5386-5005-9. DOI: 10.1109/ISWCS.2018.8491224. URL: https://ieeexplore.ieee.org/document/8491224/ (visited on 04/22/2024).

[111] Xianyue Wu et al. "60-GHz Millimeter-Wave Channel Measurements and Modeling for Indoor Office Environments". en. In: *IEEE Transactions on Antennas and Propagation* 65.4 (Apr. 2017), pp. 1912–1924. ISSN: 0018-926X, 1558-2221. DOI: 10.1109/TAP.2017.2669721. URL: http://ieeexplore.ieee.org/document/7857002/ (visited on 04/22/2024).

[112] Monsij Biswal et al. "On the Characterization of Beam Misalignment in Outdoor-to-Indoor 60 GHz mmWave Channel". en. In: *2021 15th European Conference on Antennas and Propagation (EuCAP)*. Dusseldorf, Germany: IEEE, Mar. 2021, pp. 1–5. ISBN: 978-88-312-9902-2. DOI: 10.23919/EuCAP51087.2021.9411018. URL: https://ieeexplore.ieee.org/document/9411018/ (visited on 04/24/2024).

[113] Amar Al-jzari, Jack Towers, and Sana Salous. "Characterization of Indoor Environment in the 60 GHz band". en. In: *2020 XXXIIIrd General Assembly and Scientific Symposium of the International Union of Radio Science*. Rome, Italy: IEEE, Aug. 2020, pp. 1–4. ISBN: 978-94-6396-800-3. DOI: 10.23919/URSIGASS49373.2020.9232213. URL: https://ieeexplore.ieee.org/document/9232213/ (visited on 04/23/2024).

[114] Amar Al-jzari and Sana Salous. "Millimeter-Wave Indoor Directional Propagation Measurements". en. In: *2021 15th European Conference on Antennas and Propagation (EuCAP)*. Dusseldorf, Germany: IEEE, Mar. 2021, pp. 1–4. ISBN: 978-88-312-9902-2. DOI: 10.23919/EuCAP51087.2021.9410912. URL: https://ieeexplore.ieee.org/document/9410912/ (visited on 04/23/2024).

[115] Sana Salous et al. "Millimeter-Wave Propagation: Characterization and modeling toward fifth-generation systems. [Wireless Corner]". en. In: *IEEE Antennas and Propagation Magazine* 58.6 (Dec. 2016), pp. 115–127. ISSN: 1045-9243. DOI: 10.1109/MAP.2016.2609815. URL: http://ieeexplore.ieee.org/document/7762981/ (visited on 02/11/2022).

[116] S. Salous, A. Cheema, and X. Raimundo. "Radio channel propagation measurements using a multiband agile chirp sounder". en. In: *2014 XXXIth URSI General Assembly and Scientific Symposium (URSI GASS)*. Beijing, China: IEEE, Aug. 2014, pp. 1–4. ISBN: 978-1-4673-5225-3. DOI: 10.1109/URSIGASS.2014.6929650. URL: http://ieeexplore.ieee.org/document/6929650/ (visited on 04/23/2024).

[117] Y. Gao and Salous Sana. "Wideband measurements in the 60 GHz band for short range communication". en. In: *2016 URSI Asia-Pacific Radio Science Conference (URSI AP-RASC)*. Seoul: IEEE, Aug. 2016, pp. 1–3. ISBN: 978-1-4673-8801-6. DOI: 10.1109/URSIAP-RASC.2016.7883522. URL: http://ieeexplore.ieee.org/document/7883522/ (visited on 04/23/2024).

[118] A.C.M. Austin, M.J. Neve, and D. Guven. "Indoor Millimetre Wave Channel Measurements for 5G Wireless Systems". en. In: *12th European Conference on Antennas and Propagation (EuCAP 2018)*. London, UK: Institution of Engineering and Technology, 2018, 20 (4 pp.)–20 (4 pp.) ISBN: 978-1-78561-816-1. DOI: 10.1049/cp.2018.0379. URL: https://digital-library.theiet.org/content/conferences/10.1049/cp.2018.0379 (visited on 04/23/2024).

[119] C.A.L. Diakhate et al. "Antenna Aperture Impact on Channel Delay Spread in an Urban Outdoor Scenario at 17 and 60 GHz". en. In: *12th European Conference on Antennas and Propagation (EuCAP 2018)*. London, UK: Institution of Engineering and Technology, 2018, 633 (5 pp.)–633 (5 pp.) ISBN: 978-1-78561-816-1. DOI: 10.1049/cp.2018.0992. URL: https://digital-library.theiet.org/content/conferences/10.1049/cp.2018.0992 (visited on 12/07/2022).

[120] Minseok Kim, Jun-ichi Takada, and Kentaro Saito. "Multi-Dimensional Radio Channel Measurement, Analysis and Modeling for High Frequency Bands". en. In: *IEICE Transactions on Communications* E101.B.2 (2018), pp. 293–308. ISSN: 0916-8516, 1745-1345. DOI: 10.1587/transcom.2017ISI0003. (Visited on 04/23/2024).

[121] Minseok Kim et al. "Multipath Clusters Observed in Outdoor Open Square Environments at 60 GHz". en. In: *2021 IEEE 94th Vehicular Technology Conference (VTC2021-Fall)*. Norman, OK, USA: IEEE, Sept. 2021, pp. 1–5. ISBN: 978-1-66541-368-8. DOI: 10.1109/VTC2021-Fall52928.2021.9625433. URL: https://ieeexplore.ieee.org/document/9625433/ (visited on 04/23/2024).

[122] Hibiki Tsukada et al. “Millimeter-Wave Channel Model Parameters for Various Office Environments”. en. In: *IEEE Access* 10 (2022), pp. 60387–60396. ISSN: 2169-3536. DOI: 10.1109/ACCESS.2022.3180780. URL: https://ieeexplore.ieee.org/document/9791245/ (visited on 04/23/2024).

[123] H. Groll et al. “60 GHz V2I Channel Variability for Different Elevation Angle Switching Strategies”. en. In: *2020 14th European Conference on Antennas and Propagation (EuCAP)*. Copenhagen, Denmark: IEEE, Mar. 2020, pp. 1–5. ISBN: 978-88-312-9900-8. DOI: 10.23919/EuCAP48036.2020.9135524. URL: https://ieeexplore.ieee.org/document/9135524/ (visited on 09/28/2023).

[124] Herbert Groll et al. *Sparsity in the Delay-Doppler Domain for Measured 60 GHz Vehicle-to-Infrastructure Communication Channels*. en. arXiv:1901.10817 [eess]. Jan. 2019. URL: http://arxiv.org/abs/1901.10817 (visited on 04/22/2024).

[125] Mohammad Soliman et al. “Design and Evaluation of a Millimeter Wave Channel Sounder for Dynamic Propagation Measurements”. en. In: *2018 IEEE 88th Vehicular Technology Conference (VTC-Fall)*. Chicago, IL, USA: IEEE, Aug. 2018, pp. 1–5. ISBN: 978-1-5386-6358-5. DOI: 10.1109/VTCFall.2018.8690620. URL: https://ieeexplore.ieee.org/document/8690620/ (visited on 02/11/2022).

[126] Mohammad Soliman et al. “Dynamic Train-to-Train Propagation Measurements in the Millimeter Wave Band - Campaign and First Results”. en. In: (2019), p. 5.

[127] Paul Unterhuber, Michael Walter, and Thomas Kurner. “Influence of Railway Infrastructure on Train-To-Train Communications”. en. In: *2021 15th European Conference on Antennas and Propagation (EuCAP)*. Dusseldorf, Germany: IEEE, Mar. 2021, pp. 1–5. ISBN: 978-88-312-9902-2. DOI: 10.23919/EuCAP51087.2021.9411407. URL: https://ieeexplore.ieee.org/document/9411407/ (visited on 03/04/2022).

[128] Paul Unterhuber, Michael Walter, and Thomas Kurner. “Localization of Scatterers in Railway Environments for Train-to-Train Propagation”. en. In: *2018 IEEE 88th Vehicular Technology Conference (VTC-Fall)*. Chicago, IL, USA: IEEE, Aug. 2018, pp. 1–5. ISBN: 978-1-5386-6358-5. DOI: 10.1109/VTCFall.2018.8690624. URL: https://ieeexplore.ieee.org/document/8690624/ (visited on 03/04/2022).

[129] Kairui Du et al. “60 GHz Outdoor Propagation Measurements and Analysis Using Facebook Terragraph Radios”. en. In: *2022 IEEE Radio and Wireless Symposium (RWS)*. Las Vegas, NV, USA: IEEE, Jan. 2022, pp. 156–159. ISBN: 978-1-66543-462-1. DOI: 10.1109/RWS53089.2022.9719957. URL: https://ieeexplore.ieee.org/document/9719957/ (visited on 04/22/2024).

[130] Brecht De Beelde et al. “60 GHz Path Loss Modelling Inside Ships”. en. In: *2020 14th European Conference on Antennas and Propagation (EuCAP)*. Copenhagen, Denmark: IEEE, Mar. 2020, pp. 1–5. ISBN: 978-88-312-9900-8. DOI: 10.23919/EuCAP48036.2020.9136047. URL: https://ieeexplore.ieee.org/document/9136047/ (visited on 06/10/2024).

[131] Anton A. Shkel et al. “Comparative Study of 28GHz and 60GHz Propagation Channels in an Outdoor Environment”. en. In: *2021 IEEE Globecom Workshops (GC Wkshps)*. Madrid, Spain: IEEE, Dec. 2021, pp. 1–6. ISBN: 978-1-66542-390-8. DOI: 10.1109/GCWkshps52748.2021.9682150. URL: https://ieeexplore.ieee.org/document/9682150/ (visited on 04/22/2024).

[132] Michele Polese et al. “An Experimental mmWave Channel Model for UAV-to-UAV Communications”. en. In: *Proceedings of the 4th ACM Workshop on Millimeter-Wave Networks and Sensing Systems*. arXiv:2007.11869 [cs, eess]. Sept. 2020, pp. 1–6. DOI: 10.1145/3412060.3418431. URL: http://arxiv.org/abs/2007.11869 (visited on 06/10/2024).

[133] Mohammed Zahid Aslam et al. “Analysis of 60-GHz In-street Backhaul Channel Measurements and LiDAR Ray-based Simulations”. en. In: *2020 14th European Conference on Antennas and Propagation (EuCAP)*. Copenhagen, Denmark: IEEE, Mar. 2020, pp. 1–5. ISBN: 978-88-312-9900-8. DOI: 10.23919/EuCAP48036.2020.9135946. URL: https://ieeexplore.ieee.org/document/9135946/ (visited on 06/10/2024).

[134] Mohammed Zahid Aslam and Yoann Corre. “Simulated Propagation Properties for Future Outdoor sub-THz Networks”. en. In: *2020 IEEE 31st Annual International Symposium on Personal, Indoor and Mobile Radio Communications*. London, United Kingdom: IEEE, Aug. 2020, pp. 1–6. ISBN: 978-1-72814-490-0. DOI: 10.1109/PIMRC48278.2020.9217155. URL: https://ieeexplore.ieee.org/document/9217155/ (visited on 06/10/2024).

[135] Sara Garcia Sanchez et al. “Millimeter-Wave Base Stations in the Sky: An Experimental Study of UAV-to-Ground Communications”. en. In: *IEEE Transactions on Mobile Computing* 21.2 (Feb. 2022), pp. 644–662. ISSN: 1536-1233, 1558-0660, 2161-9875. DOI: 10.1109/TMC.2020.3013575. URL: https://ieeexplore.ieee.org/document/9154517/ (visited on 04/22/2024).

[136] Lorenzo Bertizzolo et al. “mmBAC: Location-aided mmWave Backhaul Management for UAV-based Aerial Cells”. en. In: *Proceedings of the 3rd ACM Workshop on Millimeter-wave Networks and Sensing Systems*. Los Cabos Mexico: ACM, Oct. 2019, pp. 7–12. ISBN: 978-1-4503-6932-9. DOI: 10.1145/3349624.3356763. URL: https://dl.acm.org/doi/10.1145/3349624.3356763 (visited on 06/10/2024).

[137] Han Yan, Benjamin W. Domae, and Danijela Cabric. “mmRAPID: Machine Learning assisted Noncoherent Compressive Millimeter-Wave Beam Alignment”. en. In: *Proceedings of the 4th ACM Workshop on Millimeter-Wave Networks and Sensing Systems*. arXiv:2007.12060 [eess]. Sept. 2020, pp. 1–6. DOI: 10.1145/3412060.3418432. URL: http://arxiv.org/abs/2007.12060 (visited on 06/10/2024).

[138] Muhammad Haroon Tariq et al. “mmWave Massive MIMO Channel Measurements for Fixed Wireless and Smart City Applications”. en. In: *2020 IEEE 31st Annual International Symposium on Personal, Indoor and Mobile Radio Communications*. London, United Kingdom: IEEE, Aug. 2020, pp. 1–6. ISBN: 978-1-72814-490-0. DOI: 10.1109/PIMRC48278.2020.9217375. URL: https://ieeexplore.ieee.org/document/9217375/ (visited on 04/22/2024).

[139] Sara Garcia Sanchez et al. “mmWave Measurement Campaign using Terragraph Channel Sounders”. en. In: ().

[140] TIP. *TIP_mmWave-Networks_Analysis-of-28GHz-and-60GHz-Channel-Measurements-in-an-Indoor-Environment_August-2019.pdf*. Tech. rep. Telecom Infra Project, Aug. 2019. URL: https://telecominfraproject.com/.

[141] S. Salous et al. “Wideband MIMO Channel Sounder for Radio Measurements in the 60 GHz Band”. en. In: *IEEE Transactions on Wireless Communications* 15.4 (Apr. 2016), pp. 2825–2832. ISSN: 1536-1276, 1558-2248. DOI: 10.1109/TWC.2015.2511006. URL: https://ieeexplore.ieee.org/document/7362230/ (visited on 04/23/2024).

[142] Analog Device. *EK1HMC6350*.

[143] Analog Device. *HMC6300 V-Band Transmitter*.

[144] Analog Device. *HMC6301 V-Band Receiver*.

[145] Ettus Research Brand a National Instruments. *USRP X310 High Performance Software Defined Radio*. en. URL: https://www.ettus.com/all-products/x310-kit/ (visited on 08/02/2024).

[146] Minseok Kim, Jun-ichi Takada, and Yohei Konishi. "Novel Scalable MIMO Channel Sounding Technique and Measurement Accuracy Evaluation With Transceiver Impairments". en. In: *IEEE Transactions on Instrumentation and Measurement* 61.12 (Dec. 2012), pp. 3185–3197. ISSN: 0018-9456, 1557-9662. DOI: 10.1109/TIM.2012.2205510. URL: http://ieeexplore.ieee.org/document/6236154/ (visited on 07/08/2024).

[147] Centipede. *Le Reseau Centipede RTK*. en-US. URL: https://docs.centipede.fr/ (visited on 04/29/2024).

[148] Ke Guan et al. "Scenario modules, ray-tracing simulations and analysis of millimetre wave and terahertz channels for smart rail mobility". en. In: *IET Microwaves, Antennas & Propagation* 12.4 (Mar. 2018), pp. 501–508. ISSN: 1751-8733, 1751-8733. DOI: 10.1049/iet-map.2017.0591. URL: https://onlinelibrary.wiley.com/doi/10.1049/iet-map.2017.0591 (visited on 08/01/2024).

[149] Ke Guan et al. "Scenario modules and ray-tracing simulations of millimeter wave and terahertz channels for smart rail mobility". en. In: *2017 11th European Conference on Antennas and Propagation (EUCAP)*. Paris, France: IEEE, Mar. 2017, pp. 113–117. ISBN: 978-88-907018-7-0. DOI: 10.23919/EuCAP.2017.7928471. URL: http://ieeexplore.ieee.org/document/7928471/ (visited on 08/01/2024).

[150] Guangkai Li et al. "Channel Characterization for Mobile Hotspot Network in Subway Tunnels at 30 GHz Band". en. In: *2016 IEEE 83rd Vehicular Technology Conference (VTC Spring)*. Nanjing, China: IEEE, May 2016, pp. 1–5. ISBN: 978-1-5090-1698-3. DOI: 10.1109/VTCSpring.2016.7504155. URL: http://ieeexplore.ieee.org/document/7504155/ (visited on 07/30/2024).

[151] Sung-Woo Choi et al. "Performance Evaluation of Millimeter-Wave-Based Communication System in Tunnels". en. In: *2015 IEEE Globecom Workshops (GC Wkshps)*. San Diego, CA, USA: IEEE, Dec. 2015, pp. 1–5. ISBN: 978-1-4673-9526-7. DOI: 10.1109/GLOCOMW.2015.7414003. URL: http://ieeexplore.ieee.org/document/7414003/ (visited on 07/30/2024).

[152] Sungwoo Choi et al. "Mobile Hotspot Network System for High-Speed Railway Communications Using Millimeter Waves". en. In: *ETRI Journal* 38.6 (Dec. 2016), pp. 1052–1063. ISSN: 12256463. DOI: 10.4218/etrij.16.2716.0018. URL: http://doi.wiley.com/10.4218/etrij.16.2716.0018 (visited on 07/30/2024).

[153] Gosan Noh et al. "mmWave-Based Mobile Backhaul Transceiver for High Speed Train Communication Systems". en. In: *2017 IEEE Globecom Workshops (GC Wkshps)*. Singapore: IEEE, Dec. 2017, pp. 1–5. ISBN: 978-1-5386-3920-7. DOI: 10.1109/GLOCOMW.2017.8269215. URL: http://ieeexplore.ieee.org/document/8269215/ (visited on 07/30/2024).

[154] Junhyeong Kim et al. "A Comprehensive Study on mmWave-Based Mobile Hotspot Network System for High-Speed Train Communications". en. In: *IEEE Transactions on Vehicular Technology* 68.3 (Mar. 2019), pp. 2087–2101. ISSN: 0018-9545, 1939-9359. DOI: 10.1109/TVT.2018.2865700. URL: https://ieeexplore.ieee.org/document/8438925/ (visited on 07/30/2024).

[155] M. Schmieder et al. “Measurement and Characterization of 28 GHz High-Speed Train Backhaul Channels in Rural Propagation Scenarios”. en. In: *12th European Conference on Antennas and Propagation (EuCAP 2018)*. London, UK: Institution of Engineering and Technology, 2018, 363 (5 pp.)–363 (5 pp.) ISBN: 978-1-78561-816-1. DOI: 10.1049/cp.2018.0722. URL: https://digital-library.theiet.org/content/conferences/10.1049/cp.2018.0722 (visited on 07/30/2024).

[156] Katsuyuki Haneda et al. “Frequency-Agile Pathloss Models for Urban Street Canyons”. en. In: *IEEE Transactions on Antennas and Propagation* 64.5 (May 2016), pp. 1941–1951. ISSN: 0018-926X, 1558-2221. DOI: 10.1109/TAP.2016.2536170. URL: https://ieeexplore.ieee.org/document/7421994/ (visited on 10/09/2024).

[157] Yiqun Liang et al. “SDR-Based 28 GHz mmWave Channel Modeling of Railway Marshaling Yard”. en. In: *Sensors* 23.19 (Sept. 2023), p. 8108. ISSN: 1424-8220. DOI: 10.3390/s23198108. URL: https://www.mdpi.com/1424-8220/23/19/8108 (visited on 07/30/2024).

[158] Jae-Joon Park et al. “Large- and Small-Scale Fading Characteristics of mmWave HST Propagation Channel Based on 28-GHz Measurements”. en. In: *2021 15th European Conference on Antennas and Propagation (EuCAP)*. Dusseldorf, Germany: IEEE, Mar. 2021, pp. 1–5. ISBN: 978-88-312-9902-2. DOI: 10.23919/EuCAP51087.2021.9411172. URL: https://ieeexplore.ieee.org/document/9411172/ (visited on 07/30/2024).

[159] Nobuhide Nonaka et al. “28 GHz-Band Experimental Trial at 283 km/h Using the Shinkansen for 5G Evolution”. en. In: *2020 IEEE 91st Vehicular Technology Conference (VTC2020-Spring)*. Antwerp, Belgium: IEEE, May 2020, pp. 1–5. ISBN: 978-1-72815-207-3. DOI: 10.1109/VTC2020-Spring48590.2020.9129578. URL: https://ieeexplore.ieee.org/document/9129578/ (visited on 07/30/2024).

[160] Yuyuan Chang et al. “Propagation Analysis with Ray Tracing Method for High Speed Trains Environment at 60 GHz”. en. In: *2015 IEEE 81st Vehicular Technology Conference (VTC Spring)*. Glasgow, United Kingdom: IEEE, May 2015, pp. 1–5. ISBN: 978-1-4799-8088-8. DOI: 10.1109/VTCSpring.2015.7146034. URL: http://ieeexplore.ieee.org/document/7146034/ (visited on 07/31/2024).

[161] Longhe Wang et al. “Channel characterisation in rural railway environment at 28 GHz”. en. In: *IET Microwaves, Antennas & Propagation* 13.8 (July 2019), pp. 1052–1059. ISSN: 1751-8733, 1751-8733. DOI: 10.1049/iet-map.2018.5811. URL: https://onlinelibrary.wiley.com/doi/10.1049/iet-map.2018.5811 (visited on 08/01/2024).

[162] Danping He et al. “Influence Analysis of Typical Objects in Rural Railway Environments at 28 GHz”. en. In: *IEEE Transactions on Vehicular Technology* 68.3 (Mar. 2019), pp. 2066–2076. ISSN: 0018-9545, 1939-9359. DOI: 10.1109/TVT.2018.2840097. URL: https://ieeexplore.ieee.org/document/8364568/ (visited on 08/01/2024).

[163] Danping He et al. “Channel Measurement, Simulation, and Analysis for High-Speed Railway Communications in 5G Millimeter-Wave Band”. en. In: *IEEE Transactions on Intelligent Transportation Systems* 19.10 (Oct. 2018), pp. 3144–3158. ISSN: 1524-9050, 1558-0016. DOI: 10.1109/TITS.2017.2771559. URL: https://ieeexplore.ieee.org/document/8168415/ (visited on 08/07/2024).

[164] Ke Guan et al. “Towards Realistic High-Speed Train Channels at 5G Millimeter-Wave Band—Part II: Case Study for Paradigm Implementation”. en. In: *IEEE*

Transactions on Vehicular Technology 67.10 (Oct. 2018), pp. 9129–9144. ISSN: 0018-9545, 1939-9359. DOI: 10.1109/TVT.2018.2865530. URL: https://ieeexplore.ieee.org/document/8435937/ (visited on 08/07/2024).

[165] Danping He et al. "Significance Analysis for Typical Objects in mmWave Urban Railway Propagation Environment". en. In: *2017 IEEE Globecom Workshops (GC Wkshps)*. Singapore: IEEE, Dec. 2017, pp. 1–5. ISBN: 978-1-5386-3920-7. DOI: 10.1109/GLOCOMW.2017.8269202. URL: http://ieeexplore.ieee.org/document/8269202/ (visited on 08/01/2024).

[166] Danping He et al. "Influence of Typical Railway Objects in a mmWave Propagation Channel". en. In: *IEEE Transactions on Vehicular Technology* 67.4 (Apr. 2018), pp. 2880–2892. ISSN: 0018-9545, 1939-9359. DOI: 10.1109/TVT.2017.2782268. URL: https://ieeexplore.ieee.org/document/8186199/ (visited on 08/01/2024).

[167] Guangkai Li et al. "On the Feasibility of High Speed Railway mmWave Channels in Tunnel Scenario". en. In: *Wireless Communications and Mobile Computing* 2017 (2017), pp. 1–17. ISSN: 1530-8669, 1530-8677. DOI: 10.1155/2017/7135896. URL: https://www.hindawi.com/journals/wcmc/2017/7135896/ (visited on 08/01/2024).

[168] CEF. *CEF 1 – Petite-Forêt*. URL: https://www.c-e-f.fr/fr/nos-activites/cef-petite-foret (visited on 08/07/2024).

[169] MERCE. "WF on evaluation assumptions for high speed train scenario: Macro + relay at 30GHz". en. In: ().

[170] Fumihiro Hasegawa et al. "High-Speed Train Communications Standardization in 3GPP 5G NR". en. In: *IEEE Communications Standards Magazine* 2.1 (Mar. 2018), pp. 44–52. ISSN: 2471-2825, 2471-2833. DOI: 10.1109/MCOMSTD.2018.1700064. URL: https://ieeexplore.ieee.org/document/8334919/ (visited on 06/26/2024).

[171] Joseph Hoellinger et al. "Channel Correlation and Stationarity in mm-wave V2V Channels". en. In: *2023 17th European Conference on Antennas and Propagation (EuCAP)*. Florence, Italy: IEEE, Mar. 2023, pp. 1–5. DOI: 10.23919/EuCAP57121.2023.10133740. URL: https://ieeexplore.ieee.org/document/10133740/ (visited on 10/16/2024).

[172] Alexander Paier et al. "Non-WSSUS vehicular channel characterization in highway and urban scenarios at 5.2GHz using the local scattering function". en. In: *2008 International ITG Workshop on Smart Antennas*. Darmstadt, Germany: IEEE, Feb. 2008, pp. 9–15. ISBN: 978-1-4244-1756-8 978-1-4244-1757-5. DOI: 10.1109/WSA.2008.4475530. URL: http://ieeexplore.ieee.org/document/4475530/ (visited on 09/26/2024).

[173] Danilo Radovic, Herbert Groll, and Christoph F. Mecklenbräuker. "Evaluation of stationarity regions in measured non-WSSUS 60 GHz mmWave V2V channels". en. In: *2022 56th Asilomar Conference on Signals, Systems, and Computers*. Pacific Grove, CA, USA: IEEE, Oct. 2022, pp. 1212–1216. ISBN: 978-1-66545-906-8. DOI: 10.1109/IEEECONF56349.2022.10052082. URL: https://ieeexplore.ieee.org/document/10052082/.

[174] Danilo Radovic et al. "Stationarity Evaluation of High-mobility sub-6 GHz and mmWave non-WSSUS Channels". en. In: *2023 XXXVth General Assembly and Scientific Symposium of the International Union of Radio Science (URSI GASS)*. arXiv:2304.00870. Aug. 2023, pp. 1–4. DOI: 10.23919/URSIGASS57860.2023.10265539. URL: http://arxiv.org/abs/2304.00870.

[175] R. Wang et al. "Stationarity region of Mm-Wave channel based on outdoor microcellular measurements at 28 GHz". en. In: *MILCOM 2017 - 2017 IEEE*

Military Communications Conference (MILCOM). Baltimore, MD: IEEE, Oct. 2017, pp. 782–787. ISBN: 978-1-5386-0595-0. DOI: 10.1109/MILCOM.2017.8170816. URL: http://ieeexplore.ieee.org/document/8170816/ (visited on 07/03/2024).

[176] Ruisi He et al. "Characterization of Quasi-Stationarity Regions for Vehicle-to-Vehicle Radio Channels". en. In: *IEEE Transactions on Antennas and Propagation* 63.5 (May 2015), pp. 2237–2251. ISSN: 0018-926X, 1558-2221. DOI: 10.1109/TAP.2015.2402291. URL: http://ieeexplore.ieee.org/document/7038157/ (visited on 07/03/2024).

[177] Andreas Gehring et al. "Empirical Channel Stationarity in Urban Environments". In: vol. Proceedings of the European Personal Mobile Communications Conference. Vienna, Austria, 2001, p. 6.

COLLEGES SCIENCES
BRETAGNE POUR L'INGENIEUR
LOIRE ET LE NUMERIQUE

IMT Atlantique
Bretagne-Pays de la Loire
École Mines-Télécom

Titre : Réalisation d'un sondeur de canal en bande millimétrique et extraction de modèle de canal en milieu ferroviaire.

Mot clés : Mesure, Sondeur de Canal, Millimétrique, Ferroviaire, Modéle

Résumé : Le monde des transports connaît aujourd'hui une révolution vers la complète automatisation. Néanmoins, cette automatisation passe par la création de nouveaux systèmes de communication, possédant des débits élevés et une faible latence. Grâce au développement de la 5G, de nouveaux scénarios, tels que la communication entre véhicules ou entre le véhicule et le reste de l'infrastructure, voient le jour. Il en va de même pour des milieux plus complexes, tels que le milieu ferroviaire où une mutation de système de communication est en route avec l'étude d'un nouveau standard de communication, le FRMCS. Néanmoins, pour réaliser de tels systèmes, une connaissance fine du comportement du canal de propagation radioélectrique est nécessaire. Pour répondre à ce besoin, au sein d'IMT Atlantique, un sondeur de canal a été développé, permettant de réaliser des mesures longues pour des scénarios dynamiques et en milieu véhiculaire. Ce sondeur a été installé dans divers environnements pour être testé en conditions in situ, avant d'être utilisé dans le cadre d'une campagne de mesure en milieu ferroviaire. De ces mesures, les paramètres de grandes et petites échelles sont calculés pour différents environnements pour un scénario similaire à l'architecture proposée par le 3GPP. Finalement, ces résultats sont discutés et comparés avec les modèles fournis par ce même 3GPP.

Title: Design of a mmWave Channel Sounder and Channel Model Extraction in Railway Environment.

Keywords: Measurement, Channel Sounder, mmWave, Railway, Model

Abstract: The world of transportation is undergoing a revolution toward full automation. However, this automation requires the creation of new communication systems with high data rates and low latency. Thanks to the development of 5G, new scenarios, such as communication between vehicles or between a vehicle and the rest of the infrastructure, are emerging. The same applies to more complex environments, such as the railway sector, where a transformation of the communication system is underway with the study of a new communication standard, FRMCS. However, to implement such systems, a detailed understanding of the behavior of the radio propagation channel is necessary. To meet this need, at IMT Atlantique, a channel sounder has been developed, enabling long-duration measurements for dynamic scenarios in vehicular environments. This sounder has been installed in various environments to be tested under in-situ conditions before being used in a railway measurement campaign. From these measurements, large-scale and small-scale parameters are calculated for different environments in a scenario similar to the architecture proposed by 3GPP. Finally, these results are discussed and compared with the models provided by 3GPP.